Mass transport aspects of polymer electrolyte fuel cells under two-phase flow conditions

von Dipl.-Ing. (FH) Denis Kramer

geboren am 12. Februar 1977 in Halle/Saale

Pandora, in Greek mythology, first woman on earth. Zeus ordered Hephaestus to create her as vengeance upon man and his benefactor, Prometheus. The gods endowed her with every charm, together with curiosity and deceit. Zeus sent her as a wife to Epimetheus, Prometheus' simple brother, and gave her a box that he forbade her to open. Despite Prometheus' warnings, Epimetheus allowed her to open the box and let out all the evils that have since afflicted man. Hope alone remained inside the box.

The Columbia Encyclopedia, Sixth Edition. 2001.

ACKNOWLEDGMENT - DANKSAGUNG

CONTENTS

LIST OF FIGURES

Nomenclature

Roman symbols

symbol	unit	description
A	$[\text{m}^2]$	area
C	$[\text{F/m}^2]$	capacity, specific
D	$[\text{m}^2/\text{s}]$	diffusion coefficient
E	[eV]	energy
G	[J]	free enthalpy
H	[J]	enthalpy
I	[A]	current, electrical
	$[1/(\text{m}^2 \cdot \text{s})]$	neutron flux
R	$[\Omega]$	resistance, electric
	$[\Omega\,\text{m}^2]$	resistance, specific
S	[J/K]	entropy
T	[K]	temperature
U	[V]	voltage
V	$[\text{m}^3]$	volume
a	[-]	activity
c	$[\text{J/(mol} \cdot \text{K)}]$	heat capacity
	$[\text{mol/m}^3]$	concentration
f	[Hz]	frequency
g	[J/mol]	free enthalpy, specific
h	[J/mol]	enthalpy, specific
j	$[\text{A/m}^2]$	current density
$\dot{n}$	[mol/s]	molar flow
p	[Pa]	pressure
s	$[\text{J/(mol} \cdot \text{K)}]$	entropy, specific
t	[s]	time
x	[-]	relative neutron transmission

Greek symbols

symbol	unit	description
Σ	$[1/\text{m}^2]$	cross-section
Φ	[V]	potential, ionic
γ	[-]	activity coefficient

symbol	unit	description
ϵ	[-]	relative permittivity
	[-]	porosity
η	[V]	potential, over
λ	[-]	stoichiometric ratio
	[-]	water content, membrane
μ	[J/mol]	chemical potential
ν	[-]	stoichiometric coefficient in reactions
ξ	[-]	molar fraction
ρ	$[C/m^3]$	charge density
	$[\Omega\,m^2]$	resistance, specific
σ	[S/m]	conductivity
	[-]	standard deviation
τ	[s]	time, response
	[-]	tortuosity
ϕ	[V]	potential, electronic
φ	[V]	potential, ionic
ψ	$[1/(m^2\,s)]$	neutron flux, angular
ω	[1/s]	frequency, angular

Indices

Subscripts

index	description
$()_0$	unattenuated, reference
$()_{ct}$	charge transfer
$()_{dl}$	double layer
$()_r$	reaction
$()_s$	saturation
$()_E$	energy dependent
$()_F$	faradaic
$()_{ads}$	adsorbed
$()_{in}$	inlet
$()_l$	liquid
$()_{lim}$	limiting
$()_{max}$	maximum
$()_o$	outlet
$()_{ox}$	oxidation / oxidized species
$()_{px}$	pixel
$()_{red}$	reduction / reduced species
$()_s$	secondary, scattering
$()_w$	water

Superscripts

index	description
()°	reference state
()*	pure species
	reference conditions

Constants

symbol	value	unit	description
$\mathcal{F}$	$9{,}648 \cdot 10^4$	[C/mol]	Faradaic constant
R	$8{,}314$	[J/(mol·K)]	universal gas constant
e_0	$1{,}602 \cdot 10^{-19}$	[C]	elementary charge
k	$1{,}381 \cdot 10^{-23}$	[J/K]	Boltzmann constant
ϵ_0	$8{,}854 \cdot 10^{-12}$	[C/(V·m)]	dielectric constant

Abbreviations

abbreviation	description
CV	cyclic voltamogram
DMFC	**d**irect **m**ethanol **f**uel **c**ell
EIS	**e**lectrochemical **i**mpedance **s**pectroscopy
ETFE	poly(**e**thylene-alt-**t**etra**f**luoro**e**thylene)
FEP	poly(tetra**f**luoro**e**thylene-co-hexafluoro-**p**ropylene)
GDL	**g**as **d**iffusion **l**ayer
HOR	**h**ydrogen **o**xidation **r**eaction
ICON	**i**maging with **co**ld **n**eutrons (name of the cold neutron imaging facility at PSI)
MCP	**m**icro-**c**hannel **p**late
MEA	**m**embrane **e**lectrode **a**ssembly
MOR	**m**ethanol **o**xidation **r**eaction
MPL	**m**icro-**p**orous **l**ayer
NCA	**n**on-**c**hanging **a**rea
NEUTRA	**neu**tron **t**ransmission **ra**diography (name of the thermal neutron radiography facility at PSI
OCV	**o**pen **c**ircuit **v**oltage
ORR	**o**xygen **r**eduction **r**eaction
PBI	**p**oly(**b**enz-**i**midazole)
PSF	**p**oint **s**pread **f**unction
PEFC	(hydrogen-fueled) **p**olymer **e**lectrolyte **f**uel **c**ell
PTFE	**p**oly(**t**etra**f**luoro**e**thylene)
SINQ	name of the swiss spallation neutron source at PSI

INTRODUCTION

The modern, industrialized savoir-vivre established in parts of the world is characterized by and depends on the nearly unlimited availability of energy, which is mainly used for heating, manufacture and distribution of products, and individual transportation. As a matter of fact, the majority of nowadays energy demands is satisfied by extraction and combustion of fossil fuels such as oil, natural gas, and coal. It is obvious that the limited availability of these resources becomes increasingly perceptible due to the immense rate of consumption. The rate of global oil deposit exploration per year is exceeded by the annual consumption since the 1980's. Nonetheless, the annual consumption is increasing year after year and is not likely to level off or decrease in the next future—especially if the development of threshold countries such as China is considered. Beside the natural limitation of fossil fuel resources, the release and accumulation of carbon dioxide within the atmosphere needs consideration. A significant change in the planet's thermal balance, caused by anthropogenic carbon dioxide release, is predicted by climatology [1]. The associated bearings on the local and global climate might prove even more restricting non-constrained fossil fuel consumption than the finiteness of resources itself.

Hence, a change in policy of energy supply is inevitable. Future energy scenarios have to be characterized by two major requirements: regenerative sources and environmental sustainability. In that context, hydrogen is intensively discussed as energy carrier. First of all, it can be obtained from regenerative and fossil sources. While the production from natural gas allows the short term supply, the production via electrolysis, powered by photovolatic or solar thermal plants, promises the regenerative production in the long term. This essentially decouples the development of sustainable hydrogen production technologies and the introduction and dispersion of secondary hydrogen-based energy conversion technologies. Secondly, hydrogen as energy carrier intrinsically allows a carbon dioxide free secondary energy conversion, which is essential to meet the requirement of environmental sustainability.

Especially, the automotive industry is recently taking interest in hydrogen as fuel, because hydrogen-based automotive applications promise to enable the sustainable individual mobility. The main disadvantage of hydrogen as energy carrier is the low storage density per volume due to the gaseous state under ambient conditions. This impedes the distribution and entrainment of hydrogen as fuel for automotive applications. Consequently, the conversion of chemically bound energy into traction should be done with the highest possible efficiency. While the maximal efficiency of traditional combustion engines is theoretically limited by the well known CARNOT-factor to approximately 60 % at common operation temperatures, the electrochemical conversion is thermodynamically nearly loss-free at room temperature. Hence, fuel cells are considered as promising propulsion technology. The automotive research and development is focusing on the polymer electrolyte fuel cell (PEFC); this fuel cell type is best suited due to the compact design and low start-up times. The moderate working temperature ($60...80\,°C$), however, implies some serious drawbacks. The need for precious metals as catalysts (predominately platinum or platinum alloys), the dependence of sulfonated polymer electrolytes on a humid environment in order to maintain a sufficient proton conductance, and the possible condensation of water within the assembly are only a few.

The manufactures of portable (mostly electronic) applications show interest in the direct methanol fuel cell (DMFC), which resembles a hydrogen-fueled PEFC in many ways. Yet, the direct anodic feed of diluted methanol separates DMFCs from PEFCs. This fuel cell type promises a higher energy density than batteries ("... a 5-to-1 advantage over similar-size (but heavier) batteries." [2]) in conjunction with a dramatically reduced re-charge time. The complex and, therefore, slow electro-oxidation of methanol limits the power density of DMFC, and the permeability of available electrolytes for methanol and water impedes efficiency and performance. The coexistence of diluted methanol and carbon-dioxide rich gas clusters within the anodic compartment and the high tendency to accumulate liquid within the cathodic compartment are performance impeding mass transport phenomena related to that type of fuel cell.

Within this work, mass transport phenomena in both fuel cell types are investigated experimentally, where emphasis is placed on the occurrence and implications of two-phase flow. While single-phase flow within PEFCs and DMFCs was—and is today—intensively investigated theoretically, theoretical studies of two-phase flow are less common; and, experimentalists have even less frequently contributed to the discussion. To a major extent, this work is motivated by the lack of experimental evidence of two-phase flow within fuel cells. The main objective is the development and adaption of suitable *in situ* diagnostic methods; in particular, the novel diagnostic technique of neutron imaging for non-invasive spatially and temporally resolved detection of liquid is of outstanding importance. Yet, electrochemical methods were likewise explored, improved, and applied. Both routes are joined by combining advanced electrochemical methods, such as spatially resolved current mapping and impedance spectroscopy, with neutron imaging. The availability of a comfortable selection of diagnostic methods permitted some new insights, and of course new questions have been raised. The accumulation of liquid water within PEFC diffusion media and flow fields will be investigated. The impact of material properties and operating conditions onto liquid accumulation and electrochemical characteristics will be explored. The formation of carbon dioxide clusters within the anodic flow field, the formation of liquid within the cathodic flow field, and the influence of membrane materials are phenomena investigated within DMFCs.

Chapter 1

Fuel cell fundamentals

This chapter deals with fuel cell fundamentals. After the work-principle of hydrogen-fueled polymer electrolyte fuel cells (PEFC) and methanol-fueled direct methanol fuel cells (DMFC) is presented, the thermodynamic properties of the devices will be explained. Finally, fundamental processes leading to irrevesibilities and losses are investigated.

1.1 Components and working principle

A schematic of a single polymer electrolyte fuel cell is shown in Figure 1.1 on the following page. Central component is a proton-conducting polymer membrane. Onto each side of this membrane porous electrodes are attached. On top the electrochemically active electrodes, porous electron conducting media are placed. This membrane-electrode-assembly (MEA) named compound is framed by structured end or bipolar plates.

1.1.1 Polymer electrolyte membrane

In the case of PEFCs and DMFCs the electrolyte consists of an acidic membrane, which conducts protons but repels electrons and the gases fed to the anodic or cathodic compartment. Different kinds of polymers have been developed, but still Nafion—the commercial brand for a fluoro-carbon proton exchange membrane by DuPont—is the standard material used today. This polymer consists of a PTFE-like backbone with side chains terminated by a sulfonic acid (SO_3H) group. The sulfonate groups counter-balance the charge of the proton—the charge carrier in fuel cell operation—and ensure electro neutrality. In order to ensure a high conductivity (around $0.1\,S/cm$), these membranes need a high water content (10 to 14 water molecules per sulfonic acid group). Due to the dipole moment of water, protons are hydrated, and their mobility is increased (cf. Ref. [3] for a detailed description of proton transport mechanisms in polymer electrolytes). Among others, the considerable costs, high sensitivity of conductivity towards water content, low thermal stability, and vulnerability of Nafion for hydrogen peroxide (H_2O_2) attacks[1] motivate the development of new membrane materials. An approach, promising materials with similar properties but lower production costs, is radiation grafting of polymers [4]. Radicals are produced in a base polymer by

---

[1] a reaction by-product
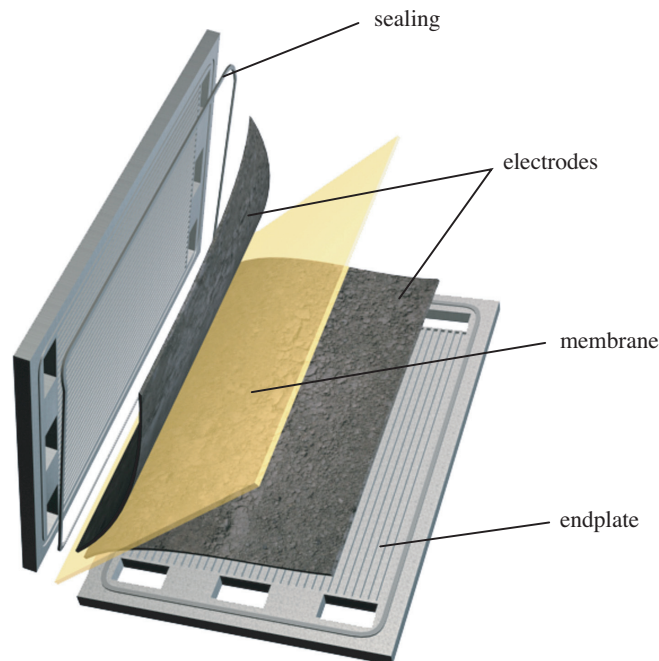
Figure 1.1: Schematic of a polymer electrolyte fuel cell; showing the polymer electrolyte as central component onto which porous electrodes are attached on either side; this assembly is framed by structured end-plates and sealed against ambiance.

irradiation with an electron or gamma beam. Subsequently, the polymer is grafted with styrene and optionally cross-linked. In a final sulfonation step, SO_3H groups are attached to the styrene. These membranes promise higher durability, due to cross-linking. Yet, the thermal stability is not significantly improved. Used base polymers are predominantly ETFE, FEP, or PTFE. The use of SO_3^- as fixed charge implies a similar water content dependence of proton conductivity compared to Nafion. The incorporation of phosphoric acid into a framework of polybenzimidazole (PBI) is considered as high-temperature (above 120 °C) alternative, where a nearly water-free conductance mechanism promises a reduced water content dependence of the proton conductivity [5].

1.1.2 Catalyst layer

Due to the moderate operating temperature of 60...80 °C, the reactions occurring at anode and cathode have to be catalysed by precious metals. Though the search for appropriate catalysts is an active field, only platinum and platinum alloys show a high enough activity for technical application so far. As will be explained in the Sections 1.1.5 and 1.1.6, the catalyst particles need to contact the proton and electron conducting phases. Further on, the accessibility of the reaction educts to the catalyst particles has to be realized. Therefore, the catalyst layers consist of a thin layer (5 to 30 µm thick) of porous materials—either nano dispersed precious metal particles on a carbon substrate or pure but highly porous precious metals—with a certain amount of incorporated ionomer. The ionomer ensures the ionic contact of catalyst particles all over the thickness of the layer. The mixture is brushed or printed as an ink either onto the diffusion medium or onto the membrane. A SEM image of a carbon supported Pt catalyst is shown in Figure 1.2 a). Other fabrication techniques include the dry-spraying of powders [6] and the growth of catalyst-coated whiskers [7].

1.1.3 Diffusion media

Either carbonized cloth or carbon-paper serve as diffusion media, employed with the intension to ensure a homogeneous distribution of reactants over the active area. Further on, they conduct the
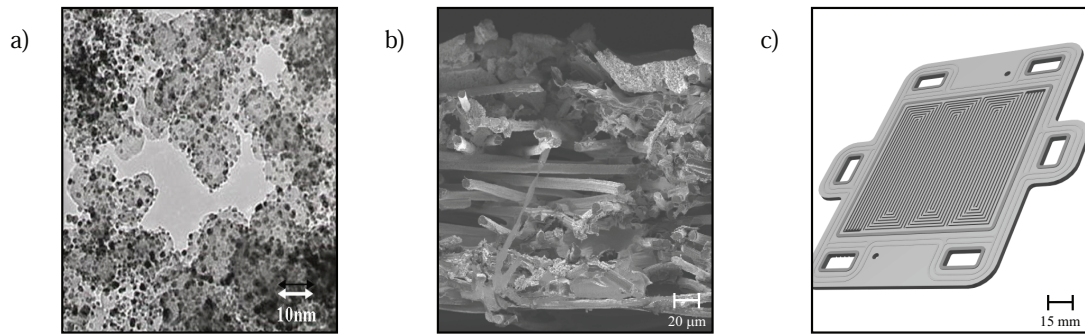
Figure 1.2: Images of different fuel cell components; (a) SEM image of Pt catalyst supported on graphite; (b) REM image of a diffusion medium courteously provided by M. REUM; (c) drawing of a bipolar plate courteously provided by L. GUBLER.

electrons produced/consumed by the reactions from electrode to bipolar plate or vice versa. An microscopic image of a carbon-paper is depicted in Figure 1.2 (b). The 100 to 400 µm thick media are mainly characterized by their porosity, which usually is about 70 %. Further on, the pore size distribution is an important characteristic; usually the most common pore size is about 100 µm. As will be shown later, the condensation of liquid is likely to happen within these layers, and the effective transport towards the flow field is of utmost importance for performance. If this is not ensured, the accessibility of gases to the electrode can be impeded by the presence of liquid. It is common to incorporate a certain amount of PTFE into the structure to influence the wettability of diffusion media. While the measurement of diffusion media characteristics such as porosity, pore size distribution, and gas permeability is generally straightforward in dry state, the exploration of properties under wetted conditions is not as easy. Virtually no *ex situ* data exist for properties such as permeability, diffusivity, and internal wettability (capillary pressure) as function of liquid saturation. The only characteristic obtainable with standard methods is the surface contact angle, which is determined from the shape of droplets. Further on, well-established correlations between *in situ* performance and *ex situ* characterization data are not yet available [8].

1.1.4   Bipolar plates

Stacked cells are separated from each other by bipolar plates, where one plate contacts an anode and a cathode at either side. This bipolar character is missing in the case of single cells, but otherwise the same functionalities have to be fulfilled. The plates have to distribute or guide the reactant flow over the active area. Channels, which form a flow field, are machined into the plate for that purpose. An illsustrating example is given in Figure 1.2 (c). Further on, a good electrical conductivity has to be ensured; therefore, a sufficient land area between the channels (usually around 50 % of the total area) is needed. In many cases, a third flow field is incorporated to pass a coolant through the plates, which is needed to maintain the thermal balance of a stack. Common materials for bypolar plates are graphite and stainless steel. While stainless steel is favorable from a manufacturing perspective, the use of graphite intrinsically avoids corrosion problems. For prototype production, flow field structures are generally milled. Mass production of stainless steel bipolar plates can be done by deep drawing or stamping, and graphite bipolar plates are commonly produced by injection moulding. Although influencing the liquid formation within flow fields (cf. Section 3.1.2), a characteristic often disregarded while choosing between materials is the wettability.
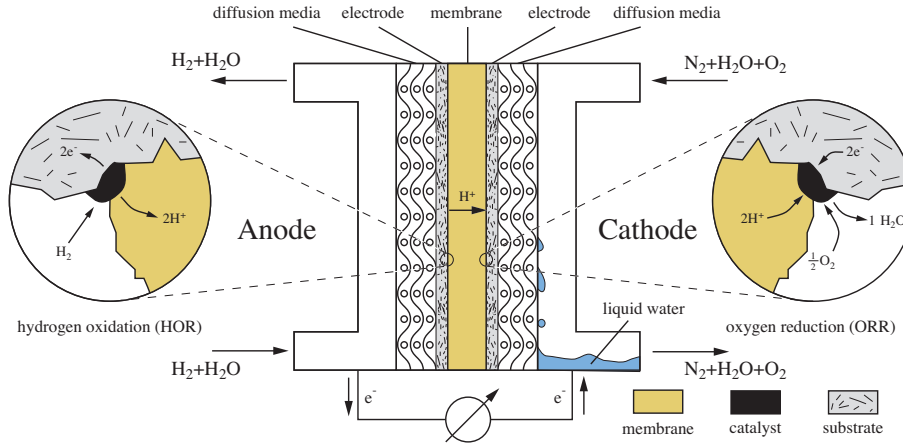
Figure 1.3: Work principle of a PEFC.

1.1.5 Working principle of PEFCs

The working principle of a PEFC is depicted in Figure 1.3. Humidified hydrogen is fed to the anodic flow field by a manifold. After passing the diffusion media, it reaches the anodic electrode. There it is transported within the free pore volume of the porous electrode and reaches the surface of the catalyst particles. Traditionally, it is assumed that the hydrogen oxidation reaction (HOR)

$$H_2 \rightleftharpoons 2H^+ + 2e^- \tag{1.1}$$

only occurs at a triple-phase boundary, which is formed by coexistence of catalyst particle, free pore volume, electron conducting substrate, and ionomer. This is shown in the left inset of Figure 1.3. However, a revised picture has been put forward with the development of agglomerate models. Especially, the direct access of the catalyst particle to the free pore volume is no strict necessity in this model, because a thin ionomer layer, which covers the catalyst particle, can be tolerated without impeding the accessibility of the catalyst surface to hydrogen. If pure platinum is used, the requirement of direct contact between catalyst surface and ionomer can be somewhat relieved; catalyst surface that is not in direct contact with the electrolyte can contribute to the reaction either via fast mobile hydrogen or hydroxyl species at the surface or via surface conductance [9]. The electrons are passed via the diffusion medium to the bipolar or end plate, where they enter an outer electric circuit. The protons are transported through the membrane towards the cathode, where they are recombined with the electrons reentering from the outer circuit in the oxygen reduction reaction (ORR):

$$2H^+ + 2e^- + \frac{1}{2}O_2 \rightleftharpoons H_2O \tag{1.2}$$

The combination of Equation (1.1) and (1.2) gives the overall reaction of a PEFC:

$$H_2 + \frac{1}{2}O_2 \rightleftharpoons H_2O \tag{1.3}$$

The formed water has to be removed either directly via the cathodic diffusion medium and flow field or through the membrane and anodic compartment.

1.1.6 Working principle of DMFCs

As shown in Figure 1.4, diluted methanol—typical concentrations are about $1\,\mathrm{M}$—is fed to the anodic flow field. After diffusion though the anodic diffusion medium, the methanol is oxidized
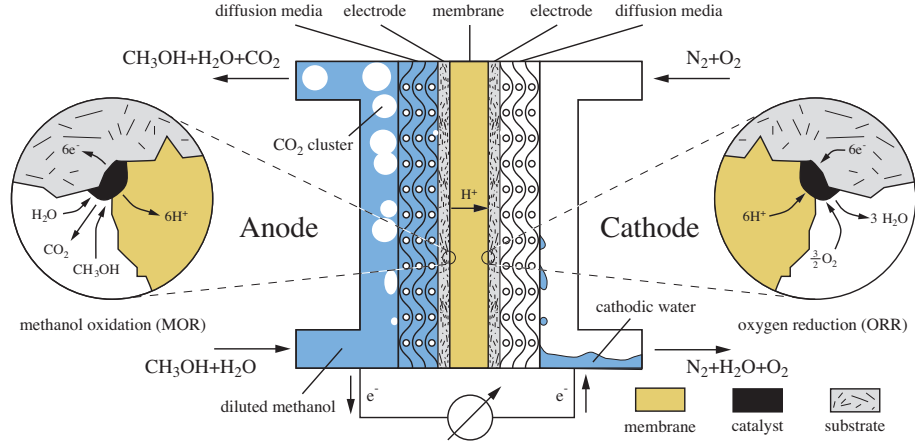
Figure 1.4: Work principle of a DMFC.

according to

$$CH_3OH + H_2O \rightharpoonup 6H^+ + 6e^- + CO_2 \tag{1.4}$$

in the methanol oxidation reaction (MOR). Because the solubility of carbon dioxide (CO_2) in water is limited, a carbon dioxide rich gaseous phase is formed. This causes a two-phase flow pattern in the anodic flow field, which will be investigated in Section 4.1. In analogy to the PEFC, the electrons are passed through an outer electric circuit, while the protons migrate through the membrane. At the cathode, oxygen—fed to the cathodic flow field either as pure gas or as air—is reduced according to

$$6H^+ + 6e^- + \frac{3}{2}O_2 \leftrightharpoons 3H_2O. \tag{1.5}$$
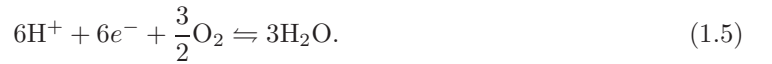
The combination of Equation (1.4) and (1.5) yields the overall reaction of a DMFC:

$$CH_3OH + \frac{3}{2}O_2 \rightharpoonup 2H_2O + CO_2 \tag{1.6}$$
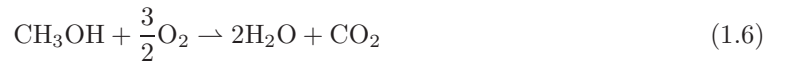
In contrast to the PEFC, the product water is only a fraction of the water to be removed via the cathodic compartment. Due to the liquid state of the anodic feed, more water is permeating through the membrane (cf. Section 4.2). Consequently, the cathodic compartment is usually flooded, which might impede the oxygen diffusion to the cathode. In addition, methanol is readily permeating through the membrane. Because methanol is easily oxidized at cathodic potentials, a parasitic reaction is taking place. This is detrimental to the performance in two ways: (1) a mixed potential is formed (cf. Section 1.3.2.4), and (2) part of the oxygen is consumed.

1.2 Thermodynamics

1.2.1 Standard cell voltages

The theoretical cell voltage can be calculated by applying the first law of thermodynamics (conservation of energy) to the device. The converted energy per unit time (i.e., power) is given by

$$U \cdot I + \Delta h_r \cdot \dot{n} = 0, \tag{1.7}$$

whereas U symbolizes the cell voltage, I the cell current, Δh_r the reaction enthalpy, and $\dot{n}$ the molar flux of the consumed fuel. By introducing FARADAY's first law $I = z \cdot \mathcal{F} \cdot \dot{n}$, Equation (1.7)

can be written as

$$U_{\mathrm{th}} = -\frac{\Delta h_r}{z \cdot \mathcal{F}} \tag{1.8}$$

defining the thermo-neutral voltage. A voltage of $U_{\mathrm{th}} = 1.481\,\mathrm{V}$ for H_2/O_2 (PEFC) and $U_{\mathrm{th}} = 1.254\,\mathrm{V}$ for CH_3OH/O_2 (DMFC) can be calculated under standard conditions.

However, these voltages cannot be achieved in a fuel cell due to the second law of thermodynamics. The reaction entropy reduces the maximal energy convertible into electricity, which is expressed by the free or GIBBS' enthalpy

$$G = H - T \cdot S. \tag{1.9}$$

The achievable voltage under idealized reversible conditions is therefore given by

$$U_{\mathrm{rev}} = -\frac{\Delta g_r}{z \cdot \mathcal{F}}, \tag{1.10}$$

which is $U_{\mathrm{rev}} = 1.229\,\mathrm{V}$ for H_2/O_2 (PEFC) and $U_{\mathrm{rev}} = 1.213\,\mathrm{V}$ for CH_3OH/O_2 (DMFC) under standard conditions.

1.2.2 Temperature, pressure, and concentration dependence

From Equation (1.10) follows that the reversible cell voltage is proportional to the free enthalpy of reaction, which is given by

$$\Delta g_r = \sum_i \nu_i \cdot \mu_i, \tag{1.11}$$

where the stoichiometric factor ν is negative for educts and positive for products, and μ symbolizes the chemical potential. The chemical potential is given by

$$\mu_i = \mu_i^* + R \cdot T \cdot \ln(a_i), \tag{1.12}$$

whereas a_i denotes the activity of the i-th species, and the superscript * indicates the reference state ($a = 1$). Hence, Equation (1.11) can be written as

$$\Delta g_r = \Delta g_r^*(T) + R \cdot T \cdot \ln\left\{\prod_i a_i^{\nu_i}\right\}. \tag{1.13}$$

This is a form of the NERNST equation. Herein, $\Delta g_r^*(T)$ equals the free reaction enthalpy if all activities equal one. The temperature dependence of Δg_r^* is given by

$$\Delta g_r^*(T) = \Delta h_r^*(T) - T \cdot \Delta s_r^*(T) \quad \text{with} \quad \Delta s_r^*(T) = \sum_i \nu_i \cdot s_i^*(T). \tag{1.14}$$

While Δh_r^* is varying only weakly with temperature, Δs_i^* is generally temperature dependent. This can be deduced from the classical definition of entropy

$$s_i^*(T) = \int \frac{dq}{T} = \begin{cases} \int \dfrac{du + R \cdot dT}{T} = c_p \cdot \ln T & \text{for ideal gaseous species,} \\[2mm] \int \dfrac{c \cdot dT}{T} = c \cdot \ln T & \text{for liquids.} \end{cases} \tag{1.15}$$

Herein, c describes the heat capacity of liquids and c_p the isobaric heat capacity of gases. The definition of a reference state, indicated by the superscript $^\circ$, and introduction into Equation (1.14)

			Δh_f° [kJ/mol]	Δg_f° [kJ/mol]	s° [J/(mol·K)]	c [J/(mol·K)]
hydrogen	H_2	(g)	0	-	130.7	28.8
oxygen	O_2	(g)	0	-	205.2	29.4
water	H_2O	(g)	-241.8	-228.6	188.8	33.6
		(l)	-285.8	-237.1	70.0	75.3
methanol	CH_3OH	(l)	-239.2	-166.6	126.8	81.1
carbon dioxide	CO_2	(g)	-393.5	-394.4	213.8	37.1

	Δh_r° [kJ/mol]	Δg_r° [kJ/mol]	Δs_r° [J/(mol·K)]	$\sum \nu_i \cdot c_i$ [J/(mol·K)]
$H_2 + \frac{1}{2}O_2 \rightleftharpoons H_2O$	-285.8	-237.1	-163.3	31.8
$CH_3OH + \frac{3}{2}O_2 \rightharpoonup 2H_2O + CO_2$	-725.9	-702.0	-80.8	62.5

Table 1.1: Thermodynamic properties of PEFC and DMFC.

gives

$$\Delta g_r^*(T) = \Delta g_r^\circ - \left\{ \Delta s_r^\circ \cdot (T - T^\circ) + T \cdot \sum_i \nu_i \cdot c_i \cdot \ln \frac{T}{T^\circ} \right\}. \tag{1.16}$$

Combination of Equation (1.13) with (1.16), and introduction into Equation (1.10) leads to

$$U_{\text{rev}} = U_{\text{rev}}^\circ + \frac{1}{z \cdot \mathcal{F}} \left\{ \Delta s_r^\circ \cdot (T - T^\circ) + T \cdot \sum_i \nu_i \cdot c_i \cdot \ln \frac{T}{T^\circ} - R \cdot T \cdot \ln \prod_i a_i^{\nu_i} \right\}. \tag{1.17}$$

Herein, U_{rev}° is the reversible cell voltage, that would be obtained at reference temperature T°, if all gaseous species would be present at a partial pressure of p° and all liquid species would be pure. Conveniently, standard conditions are chosen as reference state $^\circ$. For gaseous species the activity is given by $a_i = p_i/p^\circ$. For liquid species the activity is related to the molar fraction according to $a_i = \gamma \cdot \xi_i$ with the activity coefficient γ being a function of the molar fraction ξ_i.

The influence of operating conditions onto the reversible cell voltage can be investigated quantitatively with the values given in Table 1.1. As can easily be reconstructed, a reasonable variation of temperature, pressure, or methanol concentration yields in either case (PEFC and DMFC) a minor change of voltage. Within the range of usual operating conditions, the change of voltage is in the order of some mV. Nonetheless, observed voltages are usually well below those calculated—even if no current is generated. The possible permeation of reactants through the electrolyte is commonly stated as a reason. The effect is minor in the hydrogen-fuelled PEFC. The permeation of hydrogen towards the cathode causes a mixed potential at the cathode. The use of $50\,\mu m$ thick Nafion 112 usually results in open circuit voltages (OCV) of around $950\,mV$, which tend to increase by using thicker Nafion membranes, because the rate of permeation is greater for thinner electrolytes. Due to the high permeability of methanol in Nafion, the effect is more pronounced in the DMFC. Hence, this is an active field of research, which will be discussed in more detail in Section 4.2. Typically, the OCV of a DMFC is about $650\,mV$. Yet, as will be shown in Section 4.2.3.3, the formation of a mixed potential at the cathode contributes only partly to the discrepancy.

1.3 Loss mechanisms

In addition to the considerations of Section 1.2, the cell voltage decreases with increasing current. The difference between OCV and actual voltage at a current density j is referred to as
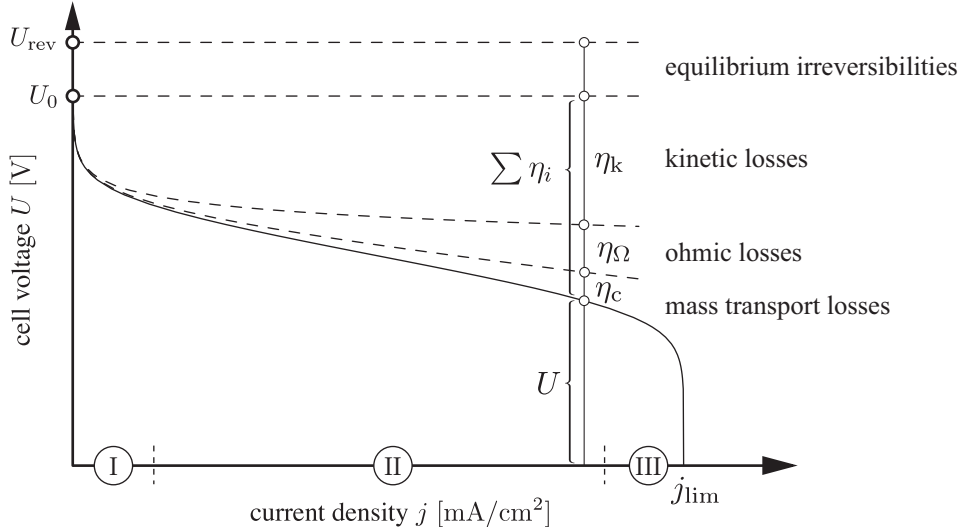
Figure 1.5: Schematic of a current-voltage curve showing the additivity of loss contributions and the separation into characteristic domains.

overpotential η. Therefore, the cell voltage as function of current density j can be written as

$$U(j) = U_0 - \sum_i |\eta_i| . \tag{1.18}$$

The sum is a consequence of different contributing loss mechanisms. However, the strict partitioning into additive losses is somewhat misleading. Fuel cells are highly coupled systems, and the different processes influence each other. A typical relation between current and voltage is schematically given in Figure 1.5. Classically, this current-voltage plot is divided into three regions. The current-voltage curve is dominated by kinetic effects in region I. Mass transport limitations account for the steep voltage decline in region III. The pseudo-linear behavior in region II cannot be attributed to a single effect—although this is frequently done in literature by attributing the linear decline solely to ohmic losses. Sometimes the difference between U_{rev} and U_0 is referred to as equilibrium overpotential.

1.3.1 Ohmic losses

According to Ohm's law

$$\vec{j} \propto \begin{cases} \nabla\phi & \text{for electronic conductors,} \\ \nabla\varphi & \text{for ionic conductors,} \end{cases} \tag{1.19}$$

the transport of charged species (protons and electrons) is coupled with a gradient in electronic ϕ or ionic potential φ. Equation (1.19) implies a voltage loss, which is proportional to the transported current.

While this is valid for the electron transport, the voltage losses due to proton transport are not strictly proportional to the current, because the conductivity of the proton-conducting phase is a function of the water content λ. A possible gradient in liquid content over the thickness of the membrane, which might change as function of current density, causes a dependence of the average conductivity σ on current density (i.e., σ increases with increasing λ). The non-linearity of ionic potential over the thickness of the membrane was experimentally confirmed by Büchi et al. by introducing gold wires as potential probes into a stack of membranes [10], and theoretically this behavior was predicted by Eikerling et al. through description of the membrane as flexible

porous system with variable mean pore radius [11]. Their model is based on a convective description of water transport through the membrane, yielding a better agreement with experiments, if the permeability is a function of water content. The dependence is explained by a swelling of the mean pore radius with increasing liquid content.

Beside the direct correlation between membrane hydration, conductivity, and ohmic losses, processes within the porous electrode are influenced by ohmic losses inside the ionomer of the active layers. ANDREAUS varied the ionomer inside the anodic active layer [12] and showed that the decrease of the ionomer equivalent weight (higher concentration of SO_3H groups) inside the anodic active layer not only decreases the ohmic resistance but also the anodic charge transfer resistance. This beneficial influence on charge transfer was attributed to a higher utilization of catalyst particles. If the ionomer conductivity inside the electrode is too low, proton transport to or from catalyst particles remote from the membrane is hampered, and, therefore, less catalyst particles are contributing to the overall reaction.

Contributions of losses due to electron transport are usually lower than those induced by proton transport. Mainly contact resistances have to be avoided, which is achieved by a reasonable clamping pressure applied to the device. Beside the total clamping pressure, the homogeneous distribution is of importance. By investigating different clamping strategies using a cell capable of locally resolved current mapping WIESER showed that an inhomogeneous clamping pressure influences local electrochemical performance, which is detrimental for overall performance [13]. Modeling results of KULIKOVSKY et al. indicate a detrimental influence of electron transport inside the diffusion media [14]. According to their model, the reaction rate inside the catalyst layer under the channels is greatly reduced because of a hampered transport of electrons to or from this area. Although attempts are presently being made [15, 16], robust experimental evidence for this partitioning due to ohmic losses within the diffusion media could not be obtained yet.

1.3.2 Kinetics

The fundamental equation explaining voltage losses due to a departure of electrochemical cells from the equilibrium state was deduced by BUTLER and VOLMER, and plenty of literature is available. Therefore, only the primary aspects will be recited here in a compressed form (see [17, 18] for further reading). The existence of an activation energy threshold, due to the formation of an activated complex within a thin charged layer near the electrode, is the central aspect of their theory.

The charge of an electrode—expressed by it's potential—is counter-balanced by an increased density of the counter ions within the electrolyte near the electrode-electrolyte interface. As the GOUY-CHAPMAN-theory shows, the density of charged species and potential are related to each other by the POISSON-equation

$$\nabla^2 \varphi(\vec{r}) = -\frac{\rho(\vec{r})}{\epsilon_r \cdot \epsilon_0}, \tag{1.20}$$

where ρ symbolizes the charge density, ϵ_r the relative permittivity of the electrolyte, and ϵ_0 the dielectric constant of the vacuum. The charge density is given by

$$\rho(\vec{r}) = z \cdot \mathcal{F} \cdot [c_+(\vec{r}) - c_-(\vec{r})]. \tag{1.21}$$

Because the negative charge carrier SO_3^- is bound to the polymer, the concentration of the negative charge carrier is space invariant. The concentration of the mobile positive charge carrier H^+ obeys the BOLTZMANN statistic

$$c_+(\vec{r}) = c_0 \cdot \exp\left\{-\frac{z \cdot \mathcal{F} \cdot \varphi(\vec{r})}{R \cdot T}\right\}. \tag{1.22}$$

Joining the Equations (1.22) and (1.21) with Equation (1.20) leads to the POISSON-BOLTZMANN Equation

$$\nabla^2 \varphi(\vec{r}) = -\frac{z \cdot \mathcal{F} \cdot c_0}{\epsilon_r \cdot \epsilon_0} \left[\exp\left\{ -\frac{z \cdot \mathcal{F} \cdot \varphi(\vec{r})}{R \cdot T} \right\} - 1 \right]. \tag{1.23}$$

The exponential term can be linearized for $z \cdot \mathcal{F} \cdot \varphi(\vec{r})/(R \cdot T) \ll 1$. For the one-dimensional case, the linearized POISSON-BOLTZMANN Equation becomes

$$\partial_{x,x}\varphi = \kappa^2 \cdot \varphi(x) \quad \text{with} \quad \kappa^2 = \frac{(z \cdot \mathcal{F})^2 \cdot c_0}{\epsilon_r \cdot \epsilon_0 \cdot R \cdot T}, \tag{1.24}$$

where the proportional constant κ is the inverse of the DEBYE-length[2]. Integration of Equation (1.24) leads to

$$\frac{\varphi(x)}{\varphi_{\mathrm{s}}} = \exp\left\{-\kappa \cdot x\right\}, \tag{1.25}$$

if the ionic potential far away from the electrode is chosen as reference potential $\varphi_\infty = 0$. Further on, φ_{s} symbolizes the potential at the interface, which is defined by the equality of the electrodes surface charge and the electrolytes space charge. The finite layer, where the charge density differs from it's bulk value, is referred to as double layer. The difference in potential between the bulk and the interface is given by $\Delta\varphi = \varphi_{\mathrm{s}} - \varphi_\infty$.

Hence, the ionic potential varies near the electrode-electrolyte interface. This influences the reactions taking place due to the involvement of charged species. According to the theory of the activated complex, the reaction rate is related to the free activation enthalpy $\Delta g^{\neq}(\Delta\varphi)$ by

$$k \propto \exp\left\{ -\frac{\Delta g^{\neq}(\Delta\varphi)}{R \cdot T} \right\}. \tag{1.26}$$

TAYLOR expansion of $\Delta g^{\neq}(\Delta\varphi)$ around the potential difference at equilibrium (OCV) $\Delta\varphi_0$ and truncation after the first order term leads to

$$\Delta g^{\neq}(\Delta\varphi) = \Delta g^{\neq}(\Delta\varphi_0) \pm \alpha \cdot z \cdot \mathcal{F}(\Delta\varphi - \Delta\varphi_0), \tag{1.27}$$

where a negative sign is indicative of a positive influence of the double layer on the reaction, while a positive sign indicates a detrimental influence. The transfer coefficient α can be understood as the relative position of the activated complex within the double layer. For a redox-reaction, the current densities of oxidation and reduction are therefore given by

$$j_{\mathrm{ox}} = z \cdot \mathcal{F} \cdot k_0 \cdot \exp\left\{ \frac{\alpha_{\mathrm{ox}} \cdot z \cdot \mathcal{F}}{R \cdot T}(\Delta\varphi - \Delta\varphi_0) \right\} \tag{1.28}$$

$$j_{\mathrm{red}} = -z \cdot \mathcal{F} \cdot k_0 \cdot \exp\left\{ -\frac{\alpha_{\mathrm{red}} \cdot z \cdot \mathcal{F}}{R \cdot T}(\Delta\varphi - \Delta\varphi_0) \right\} \tag{1.29}$$

with

$$k_0 = A \cdot \exp\left\{ -\frac{\Delta g^{\neq}(\Delta\varphi_0)}{R \cdot T} \right\} \quad \text{and} \quad \alpha_{\mathrm{ox}} + \alpha_{\mathrm{red}} = 1.$$

The net current density is the difference between oxidizing and reducing current densities, and equilibrium is characterized by the equality of both. By taking the definition of the over-potential

---

[2]Due to the mobility of negative and positive charge carriers, κ^2 is doubled in liquid electrolytes.

$\eta = \Delta\varphi - \Delta\varphi_0$ into consideration and setting $\alpha = \alpha_{\mathrm{red}}$, the net current density is given by

$$
\begin{aligned}
j &= j_{\mathrm{ox}} + j_{\mathrm{red}} \\
&= \underbrace{z \cdot \mathcal{F} \cdot A \cdot \exp\left\{-\frac{\Delta g^{\neq}(\Delta\varphi_0)}{R \cdot T}\right\}}_{j_0} \cdot \left[\exp\left\{\frac{(1-\alpha) \cdot z \cdot \mathcal{F}}{R \cdot T}\eta\right\} - \exp\left\{-\frac{\alpha \cdot z \cdot \mathcal{F}}{R \cdot T}\eta\right\}\right].
\end{aligned}
\tag{1.30}
$$

The pre-exponential factor is referred to as exchange current density j_0. Usually, the transfer coefficient α is around $1/2$. For a fully symmetric reaction ($\alpha = 1/2$), Equation (1.30) can be written as

$$
j = 2 \cdot j_0 \cdot \sinh\left\{\frac{z \cdot \mathcal{F}}{2 \cdot R \cdot T}\eta\right\}.
\tag{1.31}
$$

The Equations (1.30) and (1.31) are only valid for a given temperature and non-varying concentrations of the reactants. The influence of varying concentrations will be discussed in Section 1.3.3.

1.3.2.1 Hydrogen oxidation reaction

The hydrogen oxidation (Equation (1.1)) is a simple and therefore fast reaction when using Pt electrodes. Nonetheless, it is a multi-step reaction, because hydrogen needs to be adsorbed on the catalyst surface before the electron transfer can occur. Two mechanisms are proposed [19]: the TAFEL-VOLMER mechanism

$$
H_2 \rightleftharpoons 2H_{\mathrm{ads}}
\tag{1.32}
$$

$$
2H_{\mathrm{ads}} \rightleftharpoons 2H^+ + 2e^-,
\tag{1.33}
$$

and the HEYROVSKY-VOLMER mechanism

$$
H_2 \rightleftharpoons H_{\mathrm{ads}} + H^+ + e^-
\tag{1.34}
$$

$$
H_{\mathrm{ads}} \rightleftharpoons H^+ + e^-.
\tag{1.35}
$$

The favored mechanism depends on the type of electrolyte and catalyst—even the surface orientation of the catalyst (e.g., the reaction proceeds via the TAFEL-VOLMER mechanism on Pt(110), while on Pt(100) the HEYROVSKY-VOLMER mechanism was found [20]). In any case, the reaction is nearly loss-free, enabling the use of electrodes with low catalyst loadings [21]. Due to the simplicity of the reaction, the potential-dependence of hydrogen oxidation currents of porous PEFC electrodes is in good agreement with Equation (1.30)—as long as other effects, such as drying of the catalyst layer, are negligible.

1.3.2.2 Oxygen reduction reaction

According to Ref. [23], the oxygen reduction on Pt surfaces is proposed to follow the reaction scheme displayed in Figure 1.6 b). Oxygen is adsorbed on the catalyst surface. The adsorbed intermediate is either directly reduced to water via a four-electron step or reduced to hydrogen peroxide (H_2O_2) in a two-electron step. Subsequently, the adsorbed H_2O_2 is reduced to water, desorbed from the catalyst surface, or chemically decomposed to water.

In resemblance to the hydrogen reduction reaction, the preference of either pathway depends on the electrolyte, catalyst, and catalyst-morphology. The different reaction pathways are interpreted as a consequence of different adsorption states [22]; this is schematically shown in Figure 1.6 a).

a)

b)
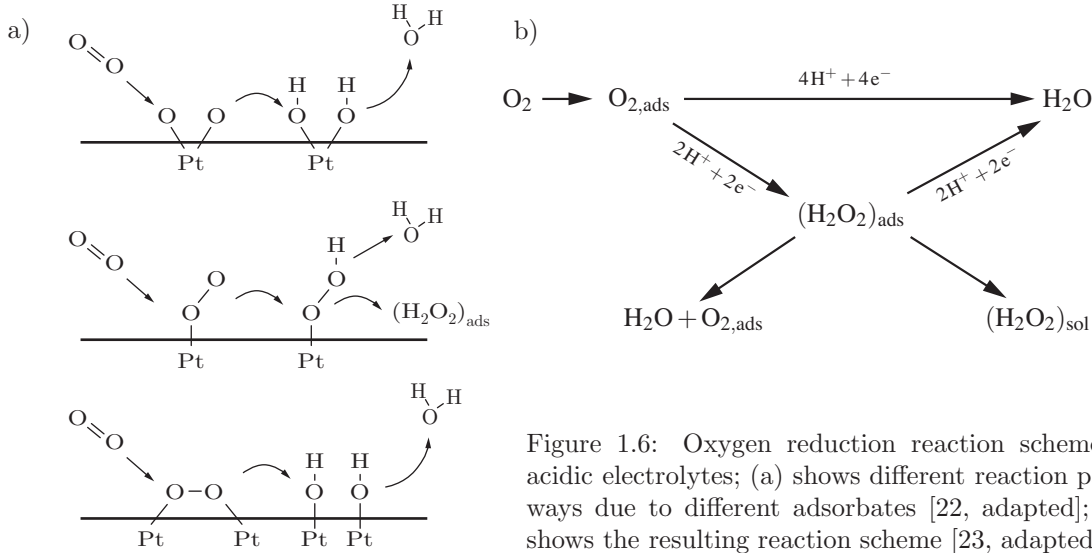
Figure 1.6: Oxygen reduction reaction scheme in acidic electrolytes; (a) shows different reaction pathways due to different adsorbates [22, adapted]; (b) shows the resulting reaction scheme [23, adapted].

Because the different reactions have dissimilar equilibrium potentials:

$$O_2 + 4\,H^+ + 4\,e^- \rightleftharpoons 2\,H_2O \qquad\qquad E^\circ = 1.23\,V \qquad (1.36)$$

$$O_2 + 2\,H^+ + 2\,e^- \rightleftharpoons H_2O_2 \qquad\qquad E^\circ = 0.682\,V \qquad (1.37)$$

$$H_2O_2 + 2\,H^+ + 2\,e^- \rightleftharpoons 2\,H_2O \qquad\qquad E^\circ = 1.77\,V \qquad (1.38)$$

the observable equilibrium overpotential (cf. Section 1.3) in a H_2/O_2 cell is partially attributed to a mixed potential formation at the cathode. As already mentioned in Section 1.1.1, the possible desorption of H_2O_2 impedes the longevity of PEFC, because hydrogen peroxide can attack the polymer electrolyte. Although ORR is a complicated multi-step and multi-pathway reaction, Equation (1.30) is often used to describe its potential-current dependence. However, the pre-exponential factor is allowed to be potential dependent in order to express differences between the BUTLER-VOLMER mechanism and processes occurring in real porous electrodes; for example, theoretical work of JAOUEN et al. [24] predicts an impact of catalyst layer morphology (proton conductivity, oxygen diffusivity) on the pre-exponential factor[3] .

1.3.2.3 Methanol oxidation reaction

The simultaneous transfer of six electrons, as implied by Equation (1.4), is unlikely to happen. On the contrary, it is proposed that methanol is electrosorbed in a complex process analogous to dehydrogenation. Sequential stripping of protons and electrons is believed to take place, leading to the formation of carbon containing intermediates, such as mainly linearly bound CHO_{ads} and CO_{ads}. The adsorbed CO is oxidized via OH_{ads}—formed by the dissociative adsorption of water. Detailed information about the mechanism, which is schematically depicted in Figure 1.7, is given in Ref. [25–28]. IWASITA et al. [28] recorded *in situ* IR spectra showing the presence of bridge bonded and multi bonded CO with bands of COH and $HCOOCH_3$. Further on, the onset of oxidation is not near the thermodynamical equilibrium potential but at much higher potentials (around $400\,mV$). Already in 1964 BOCKRIS et al. demonstrated that the replacement of Pt by PtRu alloys results in much higher oxidation currents at a given potential [29]. Due to the above observation that CO is an adsorbate intermediate, and due to the fact that the oxidation of CO requires a second oxygen atom, and Ru is splitting water easier than Pt at low potentials,

---

[3]They used the simplified TAFEL kinetics.
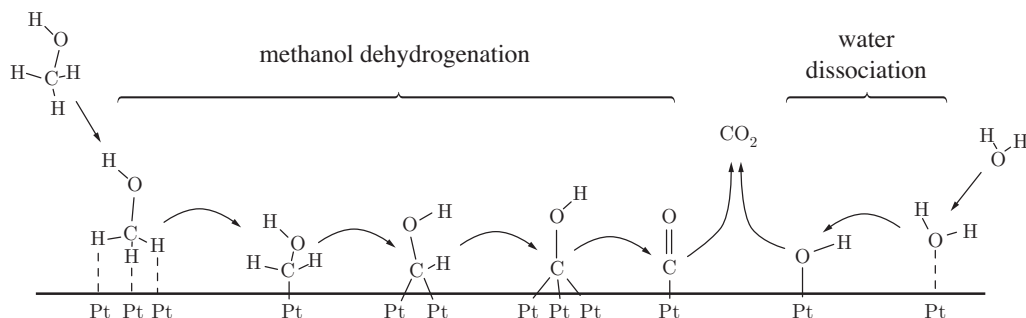
Figure 1.7: A reaction scheme describing the probable methanol electroxidation process within a DMFC anode; adapted from [25].

WATANABE et al. assumed the following bifunctional mechanism [30, mentioned in 28]:

$$Ru\text{-}H_2O \rightharpoonup Ru\text{-}OH + H^+ + e^- \tag{1.39}$$

$$Pt\text{-}CO + Ru\text{-}CO \rightharpoonup Pt + Ru + CO_2 + H^+ + e^-, \tag{1.40}$$
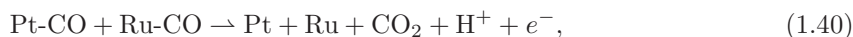
where methanol dehydrogenation is catalysed by Pt and water dissociation by Ru. This model implies a high sensitivity of catalyst activity to the distribution of Pt and Ru sites in the surface, because either $OH_{ads,Ru}$ or $CO_{ads,Pt}$ has to spill over into the area of the other adsorbate before CO_2 can be formed.

1.3.2.4 Mixed potentials

If a multitude of reactions is taking place at an electrode, the resulting current is given by

$$j = \sum_i j_i(\Delta\varphi), \tag{1.41}$$

where the reactions might interfere with each other (e.g., by the blocking of surface sites). The equilibrium potential is defined by

$$0 = \sum_i j_i(\Delta\varphi_0). \tag{1.42}$$

Hence, the equilibrium potential is not determined by a single reaction. This can cause a significant deviation of the observable equilibrium potential from thermodynamical estimations. Further on, there might be a net conversion of species, although no net current is produced.

The cathodic mixed-potential formation in DMFCs is a prominent example. Due to the considerable permeability of available polymer electrolytes for methanol, a parasitic oxidation is taking place at the cathode. This is detrimental to the equilibrium potential, as is illustrated by the simplified schema (any interaction between the reactions is neglected) depicted in Figure 1.8. If no methanol is present, the equilibrium potential is at A', which is given by $0 = j_{ox} + j_{red}$ (equality of $\overline{A'B'}$ and $\overline{A'C'}$). If simultaneous methanol oxidation occurs, the equilibrium potential is given by $0 = j_{ox} + j_{red} + j_c$, where the subscript c indicates the methanol oxidation current. This is expressed by the equality of $\overline{AC} + \overline{AD}$ to $\overline{AB}$, and the equilibrium potential is moved from A' to A. The difference between A and A' is the cross-over overpotential η_c. The methanol oxidation current j_c is shown to be independent on cathode potential in a wide potential range in Figure 1.8. This takes into account that the maximum reaction rate is limited by the transport of methanol towards the electrode. Provided Equation (1.31) describes the oxygen reduction reaction and assuming negligible impact of the cathodic methanol oxidation on the kinetics of the oxygen
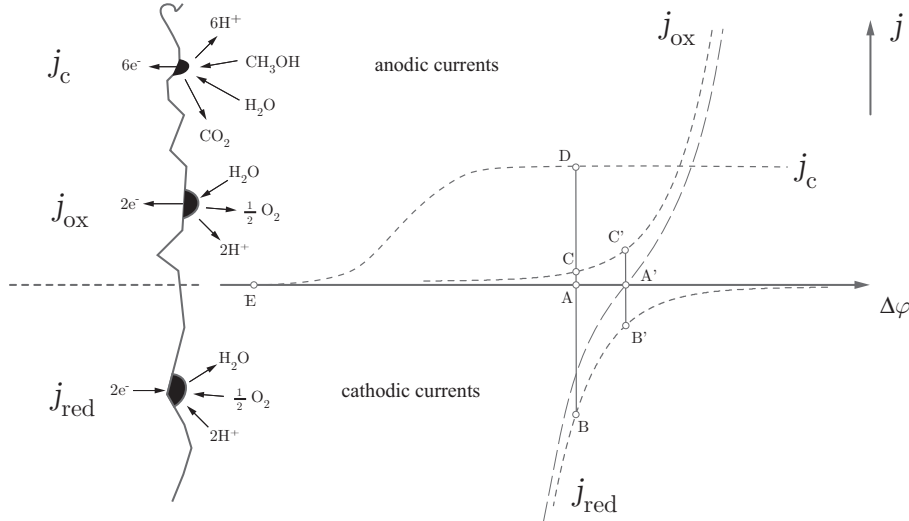
Figure 1.8: Schematic of the mixed potential formation at a DMFC cathode due to methanol cross-over.

reduction[4], the overpotential due to methanol cross-over would be given by

$$\eta_c = \frac{2 \cdot R \cdot T}{\mathcal{F}} \cdot \text{asinh}\left\{\frac{j_c}{2 \cdot j_0}\right\} \quad \xrightarrow{j_c \gg j_0} \quad \eta_c = \frac{2 \cdot R \cdot T}{\mathcal{F}} \cdot \ln\left\{\frac{j_c}{j_0}\right\}, \tag{1.43}$$

where j_0 symbolizes the ORR exchange current density. The cross-over over-potential depends implicitly on net current density because $j_c = f(j)$. If highly diluted methanol is supplied ($c \lesssim 2\,\text{M}$), a higher current density results in less crossing methanol because of the anodic consumption. If less diluted methanol is supplied, more methanol is transported towards the cathode with increasing current density, because the electro-osmotic drag over-compensates the methanol depletion due to anodic consumption. In addition, the competition of methanol oxidation and oxygen reduction for oxygen causes a dependence of j_0 on j_c. The additional consumption of oxygen by methanol oxidation can reduce the oxygen concentration at the cathode, which has an effect on j_0 due to its concentration dependence (cf. Section 1.3.3).

1.3.3 Mass transport losses

Generally, mass transport losses are defined as a detrimental impact of reactant supply to the electrochemical active area on reaction rates[5]. The reaction rate depends on the probability that all reactants needed for the reaction are present. For a first order reaction, this dependence is proportional to the reactant concentration:

$$k \propto \prod_{\text{educts}} c_i. \tag{1.44}$$

To account for this, Equation (1.26) has to be expanded to

$$k = k^\circ \prod_{\text{educts}} \frac{c_i}{c_i^\circ} \cdot \exp\left\{-\frac{\Delta g^{\neq}(\Delta\varphi)}{R \cdot T}\right\}, \tag{1.45}$$

---

[4]This requires a negligible catalyst surface coverage of methanol oxidation intermediates (such as CO_{ads}) and sufficient oxygen supply.

[5]Although the transport of charged species is associated with a displacement of mass, the associated losses are not referred to as mass transport losses but OHMIC losses.

where the superscript $\circ$ indicates reference conditions. The reactant concentrations may vary with current density. Therefore, it is convenient to define equilibrium as reference condition. Following the same derivation as in Section 1.3.2, the net current density is given by

$$j = \underbrace{z\mathcal{F} \cdot k_0^\circ \cdot \exp\left\{-\frac{\Delta g^{\neq}(\Delta\varphi_0^\circ)}{R \cdot T}\right\}}_{=j_0^\circ} \left[\underbrace{\prod_{\text{red.}} \frac{c_i}{c_i^\circ} \exp\left\{\frac{(1-\alpha)z\mathcal{F}}{R \cdot T}\eta\right\}}_{\text{oxidation}} - \underbrace{\prod_{\text{ox.}} \frac{c_i}{c_i^\circ} \exp\left\{-\frac{\alpha z\mathcal{F}}{R \cdot T}\eta\right\}}_{\text{reduction}}\right]. \quad (1.46)$$

Herein, the over-potential is defined as the difference $\eta = \Delta\varphi - \Delta\varphi_0^\circ$. This differs from the usual definition $\eta = \Delta\varphi - \Delta\varphi_0$, but it allows for a common reference in case of inhomogeneous concentrations over the active area. Usually, mass transport effects are relevant far away from equilibrium. This allows to neglect either the oxidizing or the reducing current in Equation (1.46). For a reduction reaction, such as ORR, this yields

$$j = -j_0^\circ \cdot \prod_{\text{ox.}} \frac{c_i}{c_i^\circ} \cdot \exp\left\{-\frac{\alpha z\mathcal{F}}{R \cdot T}\eta\right\}, \quad (1.47)$$

which allows to give an explicit expression for the over-potential:

$$-\eta = \frac{R \cdot T}{\alpha z\mathcal{F}} \ln\left\{\frac{j}{-j_0^\circ}\right\} + \frac{R \cdot T}{\alpha z\mathcal{F}} \ln\left\{\prod_{ox.} \frac{c_i}{c_i^\circ}\right\} \quad (1.48)$$

It has to be kept in mind that reductive currents are defined to be negative, and that also the over-potential is formally smaller than zero. Splitting Equation (1.48) into a concentration dependent and independent part, the over-potentials due to kinetics and mass transport can be separated:

$$-\eta_{\text{k}} = \frac{R \cdot T}{\alpha z\mathcal{F}} \ln\left\{\frac{j}{-j_0^\circ}\right\} \quad \text{and} \quad -\eta_{\text{c}} = \frac{R \cdot T}{\alpha z\mathcal{F}} \ln\left\{\prod_{\text{ox.}} \frac{c_i}{c_i^\circ}\right\} \quad (1.49)$$

The variation of concentrations with current density depends on the mass transport mechanisms. If the transport from flow field to active layer is diffusive, FICK's first law can be assumed as a first order approximation. In that case, the concentration near the electrode depends linearly on the current density, because:

$$\dot{n}_i = \frac{\nu_i \cdot j}{z \cdot F} = -D_{i,\text{eff}} \cdot \partial_x c_i\big|_{x=0} = \frac{D_{i,\text{eff}}}{\delta} \cdot (c_i^\circ - c_i) \quad (1.50)$$

Herein, $D_{i,\text{eff}}$ and δ denote the effective diffusion coefficient and the thickness of the diffusion layer, respectively. If the concentration of any educt near the electrode approaches zero, the overpotential tends towards $-\infty$ because of Equation (1.48). Yet, from Equation (1.50) it becomes obvious that the current density approaches

$$\lim_{c_i \to 0} j = j_{\text{lim}} = \frac{z \cdot F \cdot D_{i,\text{eff}}}{\nu_i \cdot \delta} \cdot c_i^\circ \quad (1.51)$$

The maximum achievable current density, which is independent of the overpotential, is referred to as limiting current density j_{lim}. Its value only depends on mass transport processes. Combination of Equation (1.50) with Equation (1.51) and introduction into Equation (1.47) yields

$$j = \left[\frac{1}{j_{\text{lim}}} - \frac{1}{j_0^\circ} \cdot \exp\left\{\frac{\alpha \cdot z \cdot \mathcal{F}}{R \cdot T}\eta\right\}\right]^{-1}. \quad (1.52)$$

Although a limited qualitative agreement between operative fuel cells and those simple estimations can be assessed, the relation between mass transport and electrochemical performance is far more complex, and modeling of those interactions is an active field [31]. First of all, agglomerate models have been proposed by different authors to account for the structure and morphology of the porous electrodes—inter alia [32–34]. Being of finite thickness, the reactant concentrations may vary over the thickness of the electrode, which might cause varying reaction rates. If the transport of an educt in the porous electrode is not sufficient, the main reaction zone might move from the membrane-electrode interface towards the electrode-diffusion medium interface with increasing current density. Secondly, the need for structured flow fields partitions the geometric area into channel and rib area. Because the diffusion length through the diffusion media is increased under the ribs, it might by possible that those areas are less effectively used than the active layer fraction placed under the channels. Two-dimensional and three-dimensional models have been developed to investigate the influence of channel and rib areas [35–38], and some experimental work was done as well [39]. Especially, the use of computational fluid dynamic (CFD) codes is recently becoming popular [40]. Finally, the likeliness of two-phase flow within PEFCs and DMFCs is highly complicating the mass transport processes. Part of the theoretical literature accounts for the occurrence of two-phase flow; yet, no coherent picture can be obtained, because the predictions vary significantly from author to author.

Chapter 2

Mass transport diagnostics

Diagnostic methods relevant for mass transport investigations are presented within this chapter. After a short introduction and overview of diagnostic methods and their objectives, neutron imaging as a method to detect liquid within PEFCs and DMFCs will be presented in detail. Possibilities and limitations of this novel approach will be shown with special emphasis on quantification. Subsequently, the introduction of a third electrode in order to separate anodic and cathodic contributions to the overall voltage loss is discussed, where emphasis is placed on the application within DMFCs. Electrochemical impedance spectroscopy is reviewed as a method to investigate mass transport losses, and spatially resolved measurements in order to relate inhomogeneous operation with local mass transport phenomena are discussed.

2.1 Principles and objectives

Diagnostics are key elements in research, development, demonstration and production, for the validation of basic theoretical concepts, selection and qualification of materials, as well as evaluation of device and system structures. Fuel cells are highly coupled systems. Hence, the identification of individual loss contributions to the overall performance characteristic is one fundamental task of *in situ* fuel cell diagnostics. Diagnostics cover the whole service life of a fuel cell, as is shown in Figure 2.1. Many diagnostic methods—well known electrochemical standard techniques, as well as innovative, specially developed methods—target on momentary processes, which define the performance of the device at a given time in its service period. The basic method to benchmark a cell is the recording of a polarization curve, whereby the current is recorded as function of cell voltage. Such a polarization curve was already schematically shown in Figure 1.5 on page 10. However, the interpretation of polarization curves is often difficult, and only a limited attribution of losses to processes within a fuel cell is possible with the sole knowledge of the current-voltage relation.

Electrochemical perturbation techniques. The interpretation of the relaxation behavior, caused by a superimposed small perturbation of voltage or current at a given operating point, allows to separate loss contributions by their time constant. The three types of usually applied
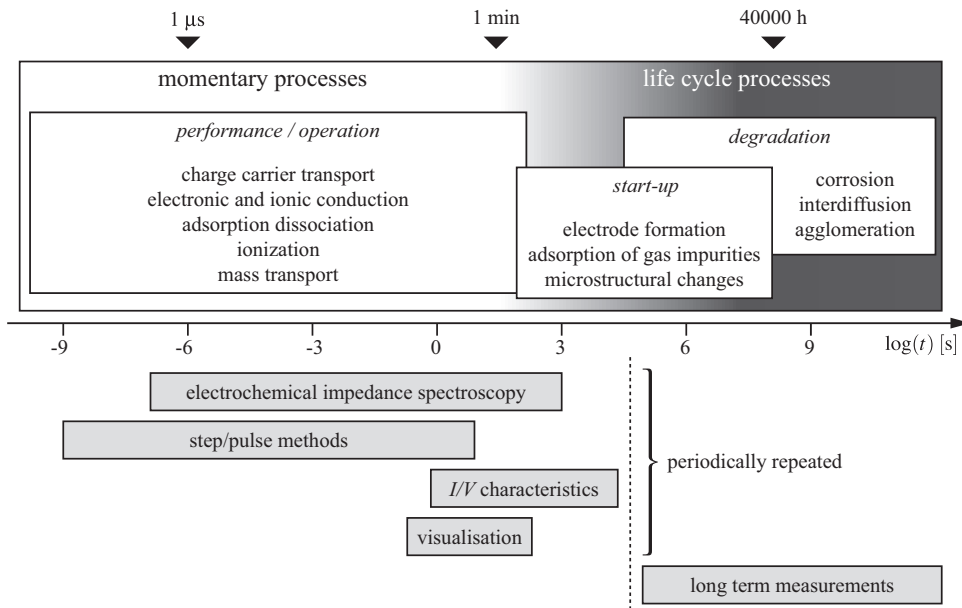
Figure 2.1: Relation of measurement techniques to time-domain events in the service life of fuel cells and stacks [41].

perturbations are shown in Figure 2.2. An abrupt potential step can reveal the time-dependent response of the device through the resulting rate adaption of the current. A current step or abrupt interruption equally induces a voltage relaxation. Repeated potential ramps, alternately positive- and negative-going, detect any redox process on the electrode by a hysteresis effect, a technique known as cyclic voltammetry. Finally, a small amplitude sinusoidal modulation of the electrode potential reveals the behavior of the electrode at the applied frequency. The measured current, in amplitude and phase, is the response of the device at the given frequency, inversely related to its response time. It is complementary to the step methods in that time- and frequency-domain effects are FOURIER-transform related. A frequency sweep can provide the electrochemical impedance spectrum (EIS) of the electrode.

All those methods rely on differences in response-time of superimposed processes in order to discriminate them. Charge displacement is characterized by the shortest response times. Hence, OHMIC contributions are more or less easily distinguishable from other losses. The high frequency resistance ($f \geq 10\,\mathrm{kHz}$) is indicative of OHMIC losses in impedance spectroscopy data. With step or pulse methods, OHMIC losses are determined by the evaluation of the instantaneous response to a perturbation ($\tau < 1\,\mathrm{\mu s}$). Generally, pulse techniques are better suited to measure OHMIC losses, because they resolve faster processes in comparison to impedance spectroscopy. The frequency range of impedance spectroscopy is often limited to approximately $20\,\mathrm{kHz}$ at the upper end due
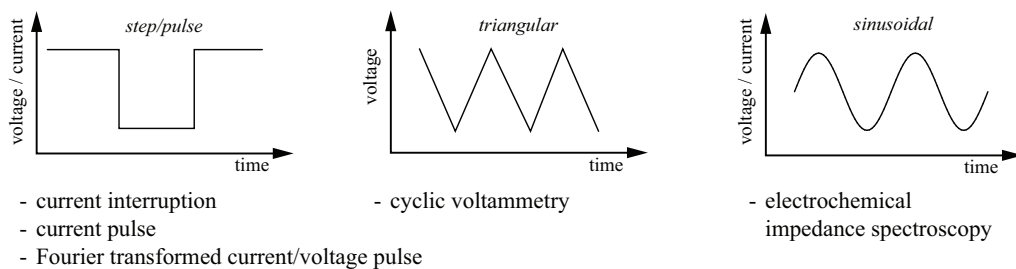
Figure 2.2: Basic perturbations applicable to fuel cells in order to separate superimposed processes by their time constants, and diagnostic methods based on the different types of perturbations.

to inductive influences. In contrast thereto, the investigation of response times below 1 µs, which corresponds to a frequency of 1 MHz, is possible with pulse techniques [42].

The response-time of an electrochemical reaction taking place at an electrode likewise depends on the reaction kinetics and on the double layer capacity. The potential relaxation $\Delta\varphi$, induced by superimposing a small step-like current density perturbation Δj, is given by

$$\Delta j = \underbrace{\partial_\eta j_F \cdot \Delta\varphi}_{\text{kinetics}} + \underbrace{C \cdot \partial_\tau \Delta\varphi}_{\text{double layer}}, \tag{2.1}$$

where the first term on the right-hand side describes the current due to electrochemical reaction Δj_F, and the second term represents the current due to double layer charge/discharge Δj_C, which is characterized by the double layer capacity C. With $1/R_{ct} = \partial_\eta j_F$, the solution of Equation (2.1) is

$$\frac{\Delta\varphi(\tau)}{\Delta j} = R_{ct}\left[1 - \exp\left\{-\frac{\tau}{R_{ct}\cdot C}\right\}\right]. \tag{2.2}$$

Hence, the voltage relaxation is given by an exponential decay with the relaxation time $\tau_k = R_{ct}\cdot C$. If the electrochemical reaction follows Equation (1.31), the relaxation time would be given by

$$\tau_k = j_0 \cdot C \cdot \frac{2\cdot z\cdot \mathcal{F}}{R\cdot T}\cdot\cosh\left\{\frac{\mathcal{F}\cdot z}{2\cdot R\cdot T}\eta\right\}, \tag{2.3}$$

which shows that the relaxation time also depends on the overpotential. This merely exemplifies the principle of step or pulse methods, and a theoretical framework going far beyond those simple considerations might be found in the work of JAOUEN and LINDBERGH [43].

If a sinusoidal perturbation $\Delta j = \Delta\hat{j}\cdot\exp\{i\cdot\omega\cdot t\}$, with $\Delta\hat{j}$ being the amplitude, ω the angular frequency, and t the time, is applied, the solution of Equation (2.1) is

$$\Delta\varphi(t) = \frac{\Delta\hat{j}}{1/R_{ct} + i\cdot\omega\cdot C}\cdot\exp\{i\cdot\omega\cdot t\}. \tag{2.4}$$

In Equation (2.4) ω symbolizes the angular frequency and i the imaginary unit. Hence, the impedance can be written as

$$Z = \frac{\Delta\varphi}{\Delta j} = \left[\frac{1}{R_{ct}} + i\cdot\omega\cdot C\right]^{-1}. \tag{2.5}$$

The phase shift is given by $\beta = \arctan\{-1/(R_{ct}\cdot C\cdot\omega)\}$, and the characteristic frequency $(\tan\beta = 1)$ equals $\omega_k = 1/(R_{ct}\cdot C)$, which is the reciprocal of the relaxation time τ_k. In the popular representation as electrical equivalent circuit, this resembles the parallel connection of a resistance and a capacitance (a so called RANDLES-cell).

As Equation (1.46) implies, the faradaic current Δj_F also depends on the concentration of all participating spezies. In the case of slow mass transport processes, a small current pertubation leads to a change of concentration at the electrode surface. For small current perturbations, the linearization

$$\Delta j_F = \sum_i \partial_{c_i} j_F \cdot \Delta c_i + \partial_\eta j_F \cdot \Delta\varphi \tag{2.6}$$

is valid. Hence, Equation (2.1) has to be expanded to:

$$\Delta j = \sum_i \partial_{c_i} j_F \cdot \Delta c_i + \partial_\eta j_F \cdot \Delta\varphi + C\cdot\partial_\tau\Delta\varphi \tag{2.7}$$

MASS TRANSPORT DIAGNOSTICS

This shows that in resemblance to Section 1.3.3 contributions of mass transport processes to the electrochemical relaxation behavior are additive to those of kinetic origin. However, the Δc_i are dependent variables. The concentration change is a function of the faradaic current Δj_F, and it depends on the mass transport process (diffusion, convection, etc.) and boundary conditions. If FICK's diffusion is assumed, the concentration of species i before the electrode will obey

$$\partial_\tau c_i = D_i \cdot \nabla^2 c_i, \tag{2.8}$$

where D_i symbolizes the diffusion coefficient. Due to the assumed linearity of the system, the concentration field in front of the electrode will oscillate according to

$$c_i(x, \tau) = \langle c_i(x) \rangle + \Delta c_i(x) \cdot \exp \{i \cdot \omega \cdot \tau\}, \tag{2.9}$$

if a sinusoidal perturbation is applied. Herein, $\langle c_i(x) \rangle$ is the steady state concentration profile, which depends linearly on x. Introduction into Equation (2.8) yields

$$i \cdot \omega \cdot \Delta c_i(x) = D_i \cdot \partial_{x,x} (\Delta c_i(x)). \tag{2.10}$$

In the case of infinite diffusion ($\Delta c_i(x \to \infty) = 0$), the solution of Equation (2.10) is

$$\Delta c_i(x) = K \cdot \exp \left\{ -x \cdot \sqrt{\frac{i \cdot \omega}{D_i}} \right\}. \tag{2.11}$$

The integration constant can be derived from mass conservation at the electrode interface:

$$\frac{\Delta j_F}{z \cdot F} = \pm D_i \cdot \partial_x \Delta c_i |_{x=0} \to K = \Delta c_i(0) = \pm \frac{\Delta j_F}{z_i \cdot \mathcal{F} \cdot \sqrt{i \cdot \omega \cdot D_i}} \tag{2.12}$$

A positive sign represents reduced species, whereas a negative sign is valid for oxidized species. Introduction into Equation (2.6) and (2.7) leads to

$$Z_{\mathrm{W}} = \frac{\Delta \varphi}{\Delta j} = \left[\frac{1}{R_{ct}} \left(1 + \sum_i \frac{|\partial_{c_i} j_F|}{z_i \cdot \mathcal{F} \cdot \sqrt{i \cdot \omega \cdot D_i}} \right)^{-1} + C \cdot i \cdot \omega \right]^{-1}. \tag{2.13}$$

Hence, infinite diffusion results in a frequency dependent correction term for the charge transfer resistance. This impedance is named WARBURG impedance. If the diffusion is finite ($\Delta c_i(\delta) = 0$), the concentration field is given by

$$\Delta c_i(x) = 2 \cdot \Delta c_i(0) \cdot \frac{\exp \left\{ -\delta \sqrt{i \cdot \omega / D_i} \right\}}{1 - \exp \left\{ -2\delta \sqrt{i \cdot \omega / D_i} \right\}} \cdot \sinh \left\{ (x - \delta) \sqrt{i \cdot \omega / D_i} \right\}, \tag{2.14}$$

and the same consideration that led to Equation (2.12) yields

$$\Delta c_i(0) = \pm \frac{\Delta j_F}{z_i \cdot \mathcal{F} \cdot \sqrt{i \cdot \omega \cdot D_i}} \cdot \tanh \left\{ \delta \sqrt{i \cdot \omega / D_i} \right\}. \tag{2.15}$$

The resulting impedance

$$Z_{\mathrm{N}} = \frac{\Delta \varphi}{\Delta j} = \left[\frac{1}{R_{ct}} \left(1 + \sum_i \frac{|\partial_{c_i} j_F|}{z_i \cdot \mathcal{F} \cdot \sqrt{i \cdot \omega \cdot D_i}} \cdot \tanh \left\{ \delta \cdot \sqrt{i \cdot \omega / D_i} \right\} \right)^{-1} + C \cdot i \cdot \omega \right]^{-1} \tag{2.16}$$

is refered to as NERNST impedance. Usually, in impedance spectroscopy analysis the Equations (2.13) and (2.16) are compressed by defining a WARBURG parameter

$$\lambda_{\mathrm{W}} = \frac{R_{ct}}{z_i \cdot \mathcal{F}} \cdot |\partial_{c_i} j_F|. \tag{2.17}$$

However, this practice can be misleading, because the WARBURG parameter's kinetic dependence—especially the overpotential dependence—is concealed.

Although useful in electrochemical impedance spectroscopy analysis of fuel cells, these fundamental relations do not account for a variety effects. Mainly, the porous nature and morphology of the electrodes and the heterogeneity of the electrochemical reactions (e.g., adsorbed reactions intermediates) are not covered. A refined theoretical framework is needed to include those. General aspects of the impedance response of porous electrodes are found in the work of DE LEVIE [44]. Focusing more on fuel cells, electrode morphology has been introduced by SPRINGER and RAISTRICK [45] by developing a model which describes the impedance response of porous electrodes on the basis of the flooded-agglomerate model. Another approach to account for structural effects (porous electrode of finite thickness) is the "transmission line" model, which mimics the continuous electrical network of the catalyst layer by a finite number of RC-elements connected in parallel. An equivalent theoretical framework based on the governing differential equations was developed by EIKERLING et al. [46]. Heterogeneous catalysis is covered by generalizing Equation (2.6) according to

$$\Delta j_F = \sum_i \partial_{\xi_i} j_F \cdot \Delta \xi_i. \tag{2.18}$$

The generalized variables ξ_i describe species concentrations, surface concentrations[1], and potential. Additional Equations for all but one $\Delta \xi_i$ are needed in order to relate them to the independent variable—usually the potential. Mass conservation, mass transport, and reaction kinetics (charge-transfer, adsorptions, etc.) provide those equations. This approach has become popular under the term "state-space modeling". Recently, KUHN et al. developed a theoretical framework describing HOR and ORR and provided experimental proof [47].

A general implication of electrochemical fuel cell investigations is the superposition of anodic and cathodic contributions. Commonly, the anodic contribution of a PEFC is considered negligible in comparison to cathodic contributions [48], which simplifies the interpretation—provided the assumption is justified. The validity of this simplification for PEFCs is debatable—especially under dry operating conditions [49]—and is not justified at all within DMFCs, because the kinetics of both (anodic and cathodic) reactions induce significant losses. This calls for a possibility to investigate the electrochemical behavior of each electrode separately. The introduction of a third electrode, which ideally provides a well defined and stable potential, is needed to achieve this. The use of such a reference electrode for DMFC investigations is discussed in Section 2.4, and a suitable pseudo-reference arrangement for the study of PEFC via impedance spectroscopy was developed by KUHN et al. [50].

Direct detection methods. As signified in the last paragraph, the interpretation of electrochemical relaxation behavior is a powerful method to investigate and discriminate mass transport and kinetic phenomena once a valid model is available. However, the analysis of the electrochemical response of fuel cells is complicated by superimposed effects. Additional information is needed in order to ensure the interpretation and to validate model assumptions. The direct detection of

---

[1]Usually, the concentration of adsorbed species is given as surface coverage Θ ($0 < \Theta < 1$).

concentrations, flow compositions, and the state of aggregation is the objective of direct diagnostic methods.

The application of a variety of methods to fuel cells have been reported, and some popular direct methods that are not further discussed in this work are as follows:

- The analysis of effluent composition
  This is a simple yet powerful method to investigate the fluxes within the device. In PEFC investigations mainly the amount of water leaving the cell is measured by condensing and weighing the water mass that was collected in a certain period of time. In relation to durability studies, the fluorine content is determined. This is a measure for the chemical stability of fluorinated membranes and perfluorinated ionomer in the active layer. An infrared absorption method is commonly used to detect the CO_2 concentration of the cathodic effluent in a DMFC. This is a measure for the methanol permeability of the used MEA.

- Spatially resolved gas composition
  The spatially resolved measurement (at different positions along the flow path) of flow composition is an advancement of the effluent analysis. The needed elaborate fuel cell design comprises several (usually around ten) gas probe holes, which are connected to a gas analyzer—either a mass spectrometer (MS) or a gas chromatograph (GC). This allows the detection of oxygen and water vapor concentrations within the flow fields [51]. However, these methods are stricly limited to cells working in the single-phase (dry) regime. Hence, they are not applicable to DMFCs and fail to investigate two-phase flow within PEFCs.

- Transparent flow fields
  Recently, the use of transparent flow field materials has become popular in order to investigate two-phase flow within PEFC flow fields [52–55], and the investigation of carbon dioxide clusters in the anodic flow field of a DMFC was reported in earlier work [56]. Although this approach has several shortcomings, useful information about the formation and transport of liquid droplets has been obtained. The major shortcoming of transparent flow fields is the considerable change of the experimental setup in comparison to non-specialized fuel cells. This influences the thermal balance of the cell. The different surface tension of the transparent material (glass or plexiglass) influences the droplet behavior, and the required extraction of electrical current at the side affects the current density distribution. Despite this, transparent flow fields provide the highest spatial and temporal resolution to study two-phase flow within flow fields.

- Laser-Doppler-Anemometry
  Once an optical access to the cell is realized, the application of a variety of laser-based diagnostics becomes available. Most prominent is the measurement of velocity fields within flow fields via laser-doppler-anemometry. Recently, convective flow through the GDL near a turning of a serpentine flow field could be verified using this technique [57].

- Temperature distribution
  The possibility of even small temperature gradients—either over the cross-section of the MEA or along the flow path—can significantly contribute to the formation of liquid, which calls for spatially resolved temperature measurements. While the introduction of temperature sensors in the bipolar or end-plate is possible without increasing the experimental effort significantly, the measurement of cross-sectional temperature gradients is not as simple.

2.2 Neutron imaging

Most probably, the method best suited to investigate two-phase flow within PEFCs and DMFCs is neutron imaging. Due to the high interaction probability between neutrons and hydrogen nuclei, this technique is ideally suited to detect liquid water within fuel cells. Being a transmitting technique, the detection of liquid within the flow fields and the porous structures becomes possible. Further on, this method avoids some of the shortcomings of transparent flow fields as common housing materials already comply with the neutron instrumentation.

Hence, the increasing popularity of this method is not surprising, and several studies taking advantage of this non-invasive method have been reported recently. The very first report of two-phase flow visualization within PEFCs by neutron imaging was given by VELEV et al. [58] in 1997. They were able to penetrate a fuel cell with neutrons and could detect larger liquid water clusters within the cell. GEIGER et al. reported the first achievements at PSI in 2002 [59]. They were able to clearly identify residual liquid within the flow fields of PEFCs and carbon dioxide-rich clusters within the anodic flow distributor of DMFCs. Later on, SATIJA et al. [60] reported similar activities at NIST[2] and were the first treating the data quantitatively. Advanced quantification—developed at the same time yet reported a year later [61, 62]—originates from the work presented here. Further on, the expansion of the method to study flooding of the GDLs (in addition to liquid accumulations within the flow fields) is an aspect original to this work [63]. Focusing on the two-phase flow within the flow fields, PEKULA et al. [64] communicated first results obtained at the Pennsylvania State University (USA) in 2005, and a recent report of their advancements is found in Ref. [65]. HICKNER et al. [66] took advantage of the facility at NIST, recently, investigating the influence of cell temperature and current density on the liquid accumulation by neutron imaging, and more results obtained at NIST are to be published [67, 68]. Finally, a joint effort at PSI led to the first reported combination of neutron imaging with advanced, spatially resolving electrochemical diagnostics (i.e., current density mapping and local impedance spectroscopy) yielding a powerful set of *in situ* diagnostics to investigate PEFCs and DMFCs [69].

2.2.1 Fundamentals

2.2.1.1 Neutron properties, interaction mechanisms, and transport

Neutrons are electrically neutral elementrary particles. Due to the average lifetime of $886 \pm 2\,\mathrm{s}$, it is possible to extract neutrons from a source as beam. For example, a free thermal neutron ($E \simeq 5\,\mathrm{meV}$) can travel over $1000\,\mathrm{km}$ in vacuum before it decays into a proton, an electron, and an anti-neutrino.

The details of neutron interaction with matter are strictly speaking found in the providence of nuclear and atomic physics, and hence outside the scope of this work. Nonetheless, the well-established cross-section formalism, which will be set down below by examination of the simple slab problem depicted in Figure 2.3, provides a theoretical framework that is sufficiently accurate for the purpose of neutron imaging.

The microscopic and macroscopic cross-section. As illustrated by Figure 2.3, a mono-energetic neutron beam with energy E impinging onto a slab of material with thickness δ will be attenuated. Because the interaction probability of neutrons with nuclei will be proportional to the

---

[2]NIST: National Institute of Standards and Technology, USA
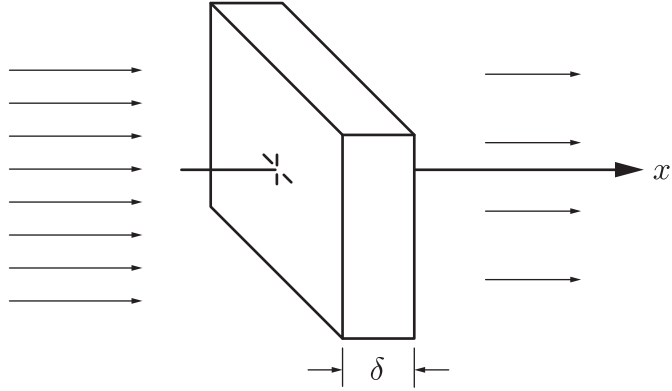
Figure 2.3: Transmission of a beam of neutrons through a slab.

product of neutron flux I_E and nucleus density n, the attenuation of the beam over the length dx is given by:

$$\frac{dI_E}{dx} = -n \cdot \sigma_E \cdot I_E(x) = -\Sigma_E \cdot I_E(x) \tag{2.19}$$

Herein, σ_E denotes the energy-dependent microscopic cross-section; the effective cross-sectional area per nucleus seen by the neutrons. Microscopic cross-sections are typically given in barns ($1\,\text{barn} = 10^{-24}\,\text{cm}$). The macroscopic cross-section Σ_E is obtained by multiplying the microscopic cross-section with the number of nuclei per unit volume. Integration of Equation (2.19) yields the ratio of unattenuated neutrons emerging from the backside of the slab to the intensity of the impinging beam:

$$\frac{I_E(\delta)}{I_E(0)} = \exp\{-\Sigma_E \cdot \delta\} \tag{2.20}$$

If the slab consists of more than one type of nucleus—including isotopes of the same element—the macroscopic cross-section is obtained by the weighted sum of the microscopic cross-sections of each type of nucleus:

$$\Sigma_E = \sum_i n_i \cdot \sigma_{i,E} \tag{2.21}$$

Energy-averaged cross-section. Generally, the neutron beam provided by a source is polychromatic or, in other words, comprises neutrons with different energies. As no energy resolved experiments have been carried-out within this work, the energy-dependence of the cross-section will be neglected by defining an energy-averaged cross-section Σ via

$$\exp\{-\Sigma \cdot \delta\} = \int \exp\{-\Sigma_E \cdot \delta\} \cdot h(E) \cdot dE, \tag{2.22}$$

where $h(E)$ is the normalized energy spectrum of the beam impinging onto the slab. This implies the need to measure the macroscopic cross-section, because it contains characteristics of the used facility. Further on, Equation (2.22) indicates a thickness dependence of the averaged cross-section due to a change of the energy spectrum[3]. If $(\Sigma \cdot \delta) \ll 1$, the exponential function can be linearized by a first-order series expansion around zero: $\exp(-\Sigma \cdot \delta) \simeq 1 - \Sigma \cdot \delta$. Introduction into Equation (2.22) yields

$$
\begin{aligned}
1 - \Sigma \cdot \delta &= \int (1 - \Sigma_E \cdot \delta) \cdot h(E) \cdot dE \\
\Sigma \cdot \delta &= \int \Sigma_E \cdot \delta \cdot h(E) \cdot dE \\
\Sigma &= \int \Sigma_E \cdot h(E) \cdot dE.
\end{aligned}
\tag{2.23}
$$

---

[3]This effect is known as beam-hardening.
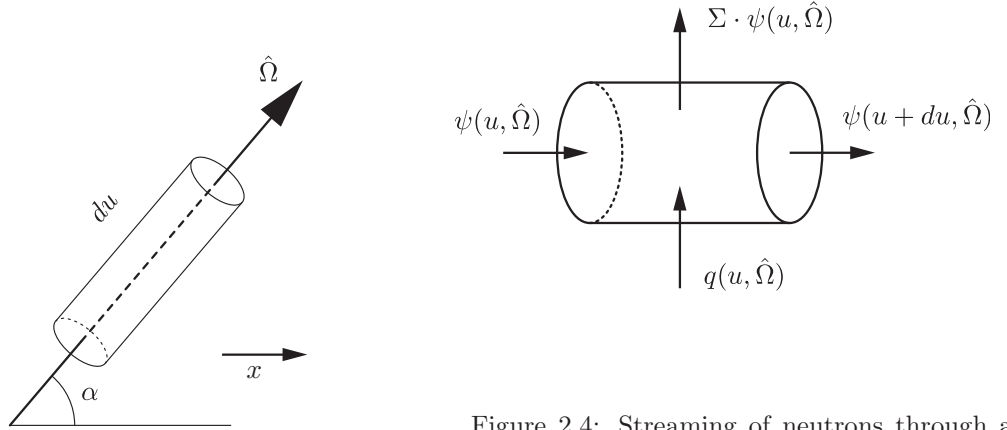
Figure 2.4: Streaming of neutrons through an incremental volume in the direction of $\hat{\Omega}$.

Equation (2.23) bears two important implications: (1) the energy-averaged macroscopic cross-section will be thickness-independent for thin layers, and (2) the energy-averaged macroscopic cross-section will depend on fixture properties such as thickness and material composition. While the first conclusion is obvious, the second needs further explanation. A fuel cell can be seen as a multi-layer object. The beam has to pass through the housing before penetrating the flow field, GDL, and membrane. If the housing alters the energy spectrum strongly (beam hardening), the energy spectrum to be introduced into Equation (2.23) will differ from the spectrum provided by the source, which results in a sensitivity of Σ to the housing material and construction.

Secondary neutron distribution (scattering).   In the context of neutron imaging two different interaction reactions need consideration: a nucleus might interact with a neutron either by absorbing or by scattering it. The scattering might be inelastic or elastic, isotropic or anisotropic. For a perfect absorber, the exponential attenuation law (Eq. 2.20) is strictly fulfilled, and the intensity of unattenuated neutrons equals the measurable neutron intensity behind the slab. A scattering material generates a secondary neutron intensity, because some of the interacting neutrons will emerge from the backside of the slab.

This will be investigated on the basis of a simplified neutron transport equation. The consideration will be one-dimensional and mono-energetic. The sketch of Figure 2.4 shows a small control volume pointing in an arbitrary direction $\hat{\Omega}$ at an angle α to the x-axis. The conservation law requires that

$$\partial_u \psi(u, \hat{\Omega}) + \Sigma \cdot \psi(u, \hat{\Omega}) = q(u, \hat{\Omega}) \tag{2.24}$$

holds. Herein, $\psi(x, \hat{\Omega})$ is the angular neutron flux at position u flying in direction $\hat{\Omega}$. The total cross-section—the sum of scattering and absorption cross-sections—is symbolized by Σ, and $q(u, \hat{\Omega})$ is the flux of neutrons that is directed from any other direction towards $\hat{\Omega}$ at u. With $dx/du = \hat{\Omega} \cdot \hat{e}_x = \cos(\alpha)$ this can be expressed in terms of the spatial coordinate x as

$$\mu \cdot \partial_x \psi(x, \mu) + \Sigma \cdot \psi(x, \mu) = q(x, \mu), \tag{2.25}$$

where $\mu = \hat{\Omega} \cdot \hat{e}_x = cos(\alpha)$ was substituted as angular variable. The source term $q(x, \mu)$ is given as the integral of the probability that neutrons are scattered from a direction $\hat{\Omega}'$ towards $\hat{\Omega}$ over all directions $\hat{\Omega}'$. For isotropic scattering, the probability that a neutron is scattered from $\hat{\Omega}'$ into a small angle $d\hat{\Omega}$ around $\hat{\Omega}$ is $\Sigma_s \cdot d\hat{\Omega}$. In terms of μ this means $q(x, \mu) = \Sigma_s \int \psi(x, \mu') \cdot d\mu'/2$, where

27
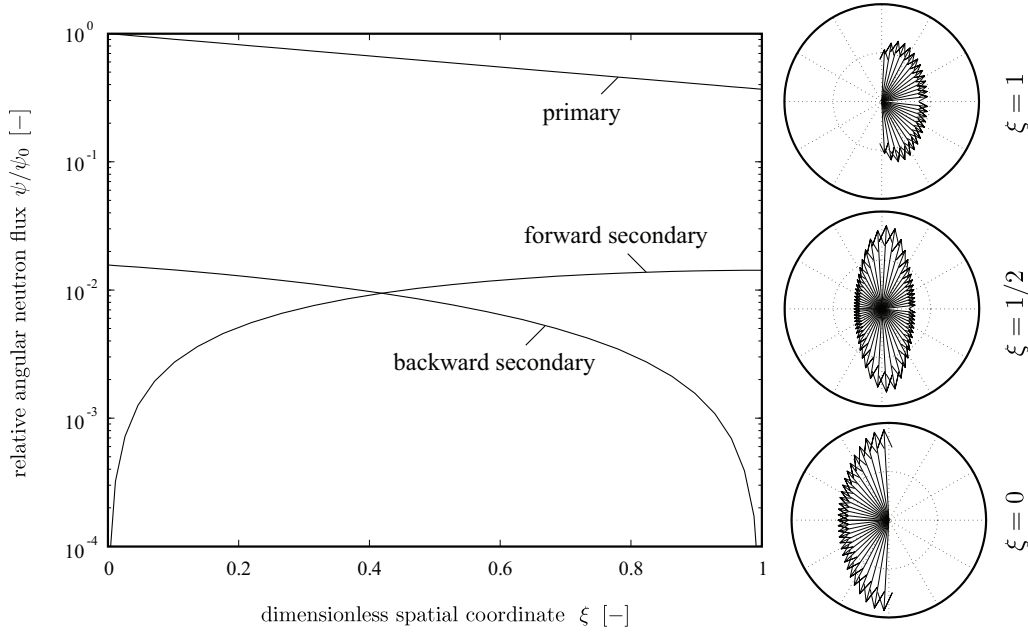
Figure 2.5: Primary and secondary neutron flux for an one-dimensional slab of thickness $\Sigma \cdot \delta = 1$; relative scattering cross-section $\kappa = 1$; polar plots of the secondary neutron flux at selected positions are shown at the right; the diagram shows the secondary angular neutron flux in beam direction (forward) and against beam direction (backward) together with the primary neutron flux.

$\int_{-1}^{1} d\mu' = 2$ has to be respected by normalizing with $1/2$. Hence, Equation (2.25) becomes

$$\mu \cdot \partial_x \psi(x, \mu) = \Sigma_s \int \psi(x, \mu') \cdot \frac{d\mu'}{2} - \Sigma \cdot \psi(x, \mu). \tag{2.26}$$

Herein, Σ_s denotes the scattering cross-section, which is related to the total cross-section by $\Sigma = \Sigma_s + \Sigma_a$ with Σ_a being the absorption cross-section. For computational reasons it is worthwhile to transfer Equation (2.26) into a dimensionless form. This is achieved by changing the spatial variable to $\xi = x \cdot \Sigma$ and defining the relative scattering cross-section to $\kappa = \Sigma_s / \Sigma$. Equation (2.26) reads

$$\mu \cdot \partial_\xi \psi(\xi, \mu) = \kappa \int \psi(\xi, \mu') \cdot \frac{d\mu'}{2} - \psi(\xi, \mu) \tag{2.27}$$

with these transformations. This integro-differential equation is to be solved numerically but for the most trivial cases. Finally, the neutron flux at a position x is obtained from the angular flux by integrating over all directions:

$$I(x) = \int \psi(x, \mu) \cdot d\hat{\Omega} \tag{2.28}$$

To calculate the formation of a secondary neutron distribution within the slab (see Figure 2.3 on page 26), the boundary conditions are found as follows. At the surface facing the impinging beam ($\xi = 0$), the angular flux will be ψ_0 along the x-axis and zero for all angles $0 < \alpha \leq \pi/2$, which can be expressed by $\psi(0, 1) = \psi_0 \cup \psi(0, [0, 1[) = 0$. At the opposite surface located at $\xi = \Sigma \cdot \delta$ the angular flux will be zero for all angles $\pi/2 \leq \alpha \leq \pi$, which means that no neutrons enter the slab from the backside. Hence, $\psi(\Sigma \cdot \delta, [-1, 0]) = 0$ completes the boundary conditions. To compute the secondary neutron flux, equation (2.27) has been solved numerically with a discretized ordinates method [70]. The computational domain consisted of 30 spatial nodes and 30 angular ordinates at every spatial node.

The left-hand diagram of Figure 2.5 shows the primary neutron flux together with selected angles of the secondary neutron flux through a slab of thickness $\Sigma \cdot \delta = 1$ consisting of completely scattering
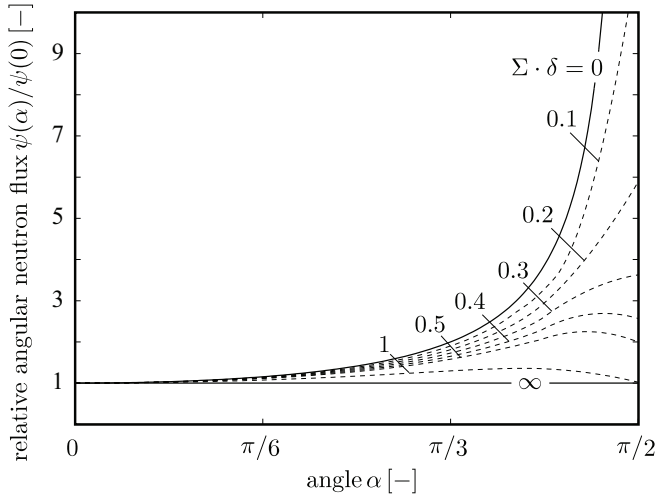
Figure 2.6: Angular secondary neutron flux at the backside of the slab as function of the angle α; relative scattering cross-section $\kappa = 1$.

material $(\kappa = 1)^4$. The primary neutron flux decays according to the exponential attenuation law, which results in a straight line in the semi-logarithmic scaling of the plot. The secondary neutron flux in beam direction is zero at $\xi = 0$ and increases monotonically through the slab. The backward directed secondary neutron flux shows the opposite trend; it is zero at $\xi = 1$ and increases monotonically towards $\xi = 0$. The angular dependency of the secondary neutron flux for three selected positions is shown by the polar plots at the right-hand side. At $\xi = 0$ the angular flux is non-zero only for $\alpha > \pi/2$ due to the boundary condition that no secondary neutron flux enters the slab. Yet, such a restriction has not been imposed for secondary neutrons leaving the surface of the slab. Within the slab, secondary neutrons are present at all angles. At the outlet, no secondary neutrons are directed towards the slab ($\alpha > \pi/2$), which is again a consequence of the boundary conditions.

It is worth noticing that the angular secondary flux is generally a function of the angle, although the scattering was assumed to be isotropic. Further on, the angular dependency at the backside of the slab ($\xi = 1$) is a function of the slab thickness. The two limiting cases can be derived by reasoning. For an infinitesimal thick slab ($\Sigma \cdot \delta \gg 1$), the neutrons will collide several times with the nuclei losing all direction information. The primary neutron flux at the backside of the slab will be zero and the angular secondary fluxes will be equal for all directions. In the case of very thin slabs ($\Sigma \cdot \delta \ll 1$), the chance for multiple scattering is virtually zero and the primary neutron flux will be nearly unchanged. Hence, the chance that neutrons are scattered will be uniform throughout the slab. Consequently, along a given line through the slab, the chance for a neutron to be scattered in the direction of the line will be equal for every unit length. Considering that the length of the line through the slab is proportional to $1/\cos(\alpha)$, the secondary neutron flux will be given by $\psi(\alpha) = \psi(0)/\cos(\alpha)$. The plot of Figure 2.6 shows the relative angular secondary neutron flux at the slab backside surface for different slab thicknesses $\Sigma \cdot \delta$. Already at a slab thickness of $\Sigma \cdot \delta = 1$, the angular flux is nearly homogeneously distributed. Hence, the angular dependency of the secondary neutron flux can be neglected for samples with thicknesses around $\Sigma \cdot \delta = 1$ and above.

The influence of the distance between sample and detector. Scattered neutrons are bothersome from the neutron imaging point of view, because the exponential attenuation law is violated. This complicates the quantitative evaluation significantly and might cause image artifacts. Although possible [71, 72], a correction by adequate data treatment should be circumvented by

---

[4]This is in good agreement with materials common for polymer electrolyte fuel cells, such as aluminium, graphite, or water.
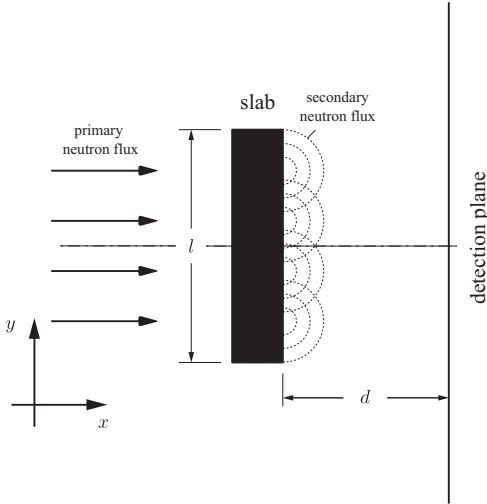
Figure 2.7: Formation of a secondary neutron flux due to scattering within a slab and the influence of the distance between detector and sample.
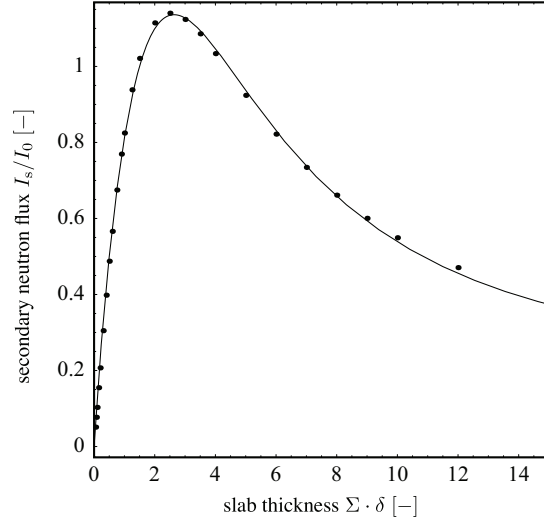
Figure 2.8: Secondary neutron flux at the slab back surface as function of slab thickness; relative scattering cross-section $\kappa = 1$; angular dependency of the secondary neutron flux neglected.

reducing the intensity of scattered neutrons by experimental means. The simplest variation of the experimental set-up influencing the intensity of secondary neutrons is the variation of the distance between the sample and the detection plane. The problem depicted in Figure 2.7,where a slab of equal length and width l in a distance d from the plane of detection is shown, will be explored with the objective to derive a conclusion about the minimum distance between sample and detector that ensures a negligible secondary neutron flux at the plane of detection. The primary neutron flux impinging onto the slab causes a secondary neutron flux emerging from the slab as illustrated by the dashed semi-circles. For the sake of simplicity, the angular dependence of the secondary neutron flux will be neglected by assuming that the secondary neutron flux at the slab surface will be given by

$$I_{\text{s}} \simeq \int \psi(1,0) \cdot d\mu, \tag{2.29}$$

where $\psi(1,0)$ is the angular flux at the slab back ($\xi = 1$) at $\alpha = 0$ (direction of the primary neutron flux). As shown in the last paragraph, this is justified for reasonably thick samples. The diagram of Figure 2.8 shows the intensity of I_{s} at the surface ($d = 0$) normalized to the primary neutron flux before the slab I_0 for a completely scattering material ($\kappa = 1$). As can be expected, the secondary neutron flux increases with slab thickness for $\Sigma \cdot \delta < 2.5$. Yet, for thicker slabs the secondary neutron flux decreases after passing a maximum around $\Sigma \cdot \delta = 2.5$. This is caused by the self-shielding effect, which is a consequence of the increasing probability of multiple scattering events for thicker slabs [72]. For thin layers ($\Sigma \cdot \delta < 0.1$) this is negligible and the secondary neutron flux is virtually equal to $1 - \exp(-\Sigma \cdot \delta)$.

The sketch of Figure 2.9 exemplifies the projection of secondary neutrons onto the plane of detection. The fraction of emitted neutrons that passes through the spherical section A is given by the area ratio of A to the total sphere. Hence,

$$N = \frac{I_{\text{s}}}{4\pi \cdot s^2} \cdot (d\alpha \cdot s) \cdot 2\pi \cdot r \tag{2.30}$$

is the number of neutrons passing through A per unit time. Herein, I_{s} is the emitted scalar secondary neutron flux defined by Equation (2.29). Due to the conservation law, the same number
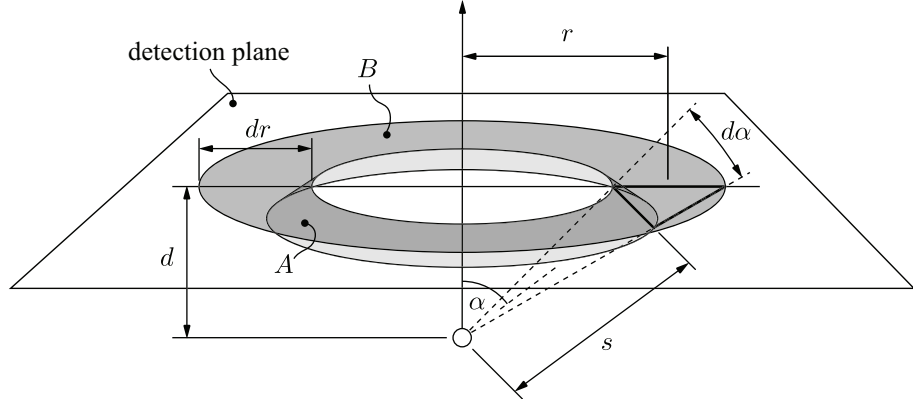
Figure 2.9: Projection of isotropically emitted secondary neutrons at a distance d onto the plane of detection.

of neutrons has to pass through the ring B in the detection plane per unit time, which gives

$$N = I(r) \cdot 2\pi \cdot r \cdot dr. \tag{2.31}$$

Herein, $I(r)$ symbolizes the neutron flux (neutrons per unit time and unit area) passing the detection plane. Combination of Equation (2.30) and (2.31) yields

$$I(r) = \frac{I_\text{s}}{4\pi \cdot s^2} \cdot \frac{d\alpha \cdot s}{dr}. \tag{2.32}$$

With $d\alpha \cdot s = \cos(\alpha) \cdot dr$ and $s = d/\cos(\alpha)$ this becomes

$$I(r) = \frac{I_\text{s}}{4\pi \cdot d^2} \cdot \cos^3(\alpha). \tag{2.33}$$

By taking into account that $\alpha = \tan^{-1}(r/d)$ and that $\cos(\tan^{-1}(x)) = 1/\sqrt{1 + x^2}$, Equation (2.33) can be written in dimensionless coordinates as:

$$P_\text{s}(x', y') = \frac{I(x', y')}{I_s} = \frac{1}{4\pi \cdot \lambda^2} / \left\{ 1 + \frac{x'^2 + y'^2}{\lambda^2} \right\}^{3/2} \tag{2.34}$$

Herein, r was replaced by Cartesian coordinates according to $r^2 = x^2 + y^2$. The dimensionless coordinates are given by $x' = x/l$ and $y' = y/l$. The ratio of slab length to the distance from the detection plane is symbolized by $\lambda = d/l$. Commonly, Equation (2.34) is referred to as scattering point-spread-function (PSF), because the projection of a point-like secondary neutron flux onto the detection plane is described.

The normalized secondary neutron flux which is emitted by the slab as function of position can be expressed as

$$S(x', y') = \Pi\left(x'\right) \cdot \Pi\left(y'\right), \tag{2.35}$$

where $\Pi(x)$ symbolizes the rectangle function. The normalized projection onto the detection plane is then given by the convolution

$$G(x', y') = S(x', y') * P_\text{s}(x', y'). \tag{2.36}$$

Although Equation (2.36) can be solved analytically, the resulting expression will not be given here due to the overall complexity.

Two-dimensional plots of the secondary neutron flux at the detection plane for selected distance
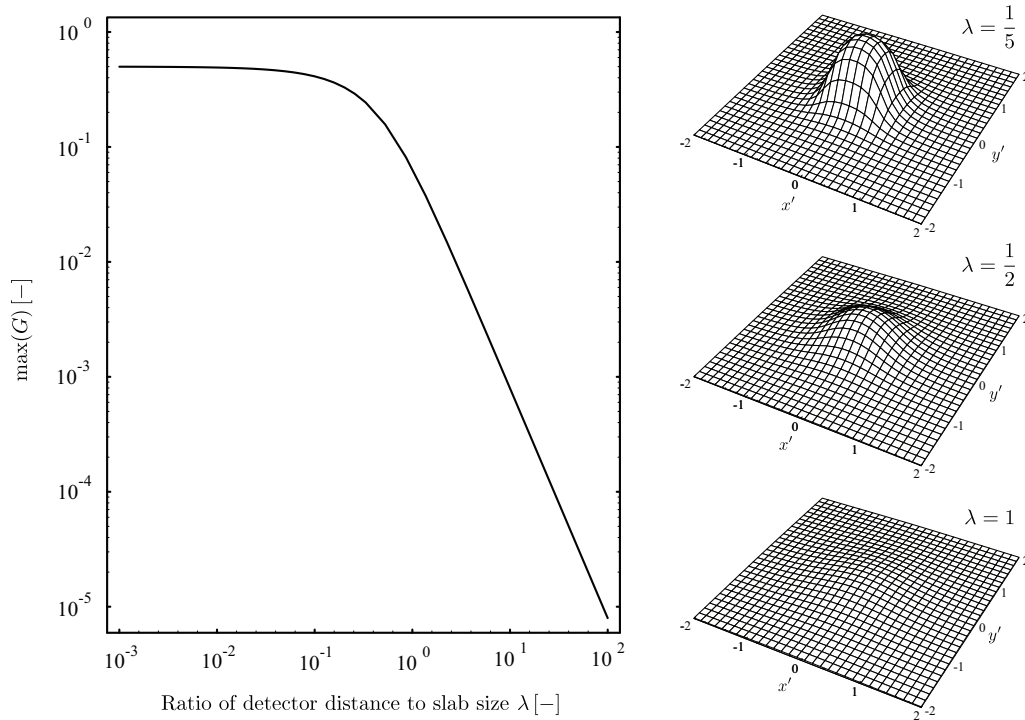
Figure 2.10: The normalized secondary neutron flux at the detection plane G and the influence of the ratio of detector distance to slab length λ.

ratios are given at the right-hand side of Figure 2.10. Placing the detector too near to the sample results in a significant intensity of the secondary neutron flux. By increasing the distance between sample and detector, the secondary neutron flux is effectively diminished. The maximum value, which due to the symmetry of the problem is always located at the center of the sample, is reduced, and the profile is broadened. The left-hand diagram shows the maximum value of the normalized relative neutron flux at the detection plane as function of λ. Even if the detector is placed directly behind the sample, only 50 % of the secondary neutrons are reaching the detection plane, which stems from the definition of I_s (cf. Equation (2.29)), where the angular flux in beam direction was integrated over the full angle (i.e., forward and backward direction). As long as the distance to the sample is ten times smaller than the sample length, only a marginal reduction of the intensity of secondary neutrons is achieved. Choosing the detector distance equal to the sample size reduces the secondary neutron flux to about 6.5 %, and a reduction to 1 % would need a distance ten times the sample size.

However, as will be shown in Section 2.2.7, other concerns limit the distance between sample and detector. Yet, a minimum distance of about the size of the sample between sample and detector should be kept to mitigate the influence of secondary neutrons to a reasonably low level.

2.2.1.2   Detection principles

Neutrons have a mass but no electrical charge. Because of this, they cannot directly produce ionization in a detector, and therefore cannot be detected directly. This means that neutron detectors must rely on a conversion process where an incident neutron interacts with a nucleus to produce a secondary charged particle or secondary radiation. In other words, conversion reactions

are necessary to detect neutrons. The most commonly used reactions are [73]:

$$^{3}\text{He} + {}^{1}\text{n} \quad \rightarrow \quad {}^{3}\text{H} + {}^{1}\text{p} + 0.77\,\text{MeV} \tag{2.37}$$

$$^{6}\text{Li} + {}^{1}\text{n} \quad \rightarrow \quad {}^{3}\text{H} + {}^{4}\text{He} + 4.79\,\text{MeV} \tag{2.38}$$

$$^{10}\text{B} + {}^{1}\text{n} \quad \rightarrow \quad {}^{7}\text{Li}^{*} + {}^{4}\text{He} + 2.30\,\text{MeV} \rightarrow {}^{7}\text{Li} + {}^{4}\text{He} + \gamma(0.48\,\text{MeV}) \tag{2.39}$$

$$^{155}\text{Gd} + {}^{1}\text{n} \quad \rightarrow \quad {}^{156}\text{Gd} + \gamma + e^{-}\,(7.9\,\text{MeV}) \tag{2.40}$$

$$^{157}\text{Gd} + {}^{1}\text{n} \quad \rightarrow \quad {}^{158}\text{Gd} + \gamma + e^{-}\,(8.5\,\text{MeV}) \tag{2.41}$$
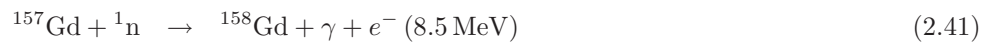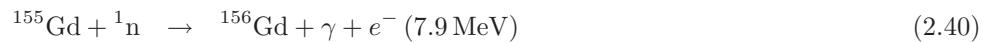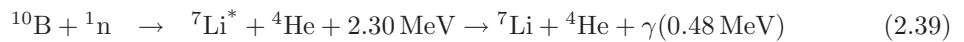
More conversion reactions are listed in [74, page 23], and recent developments as well as detailed analyses of those reactions are found in [75]. Although most frequently used in general, the reaction given by Equation (2.37) is of no use for imaging purposes, because of the range of the secondary particles (6 cm for the proton and 2.5 cm for the triton within He at ambient pressure) that are detected by a gas-filled ionization chamber. Naturally, the spatial resolution of this detector-type is insufficient for imaging applications. The attractiveness of Reaction (2.38) stems from the fact that the released α particles can be converted into liqht by zinc sulfide. Upon impact of α particles, the ZnS emits photons at a wavelength within the visible range of the spectrum ($\simeq 500\,\text{nm}$). Hence, optical detectors can be used to record the emitted light. Further on, the solid state of aggregation of ^{6}Li and ZnS allows manufacturing scintillating screens. This is also beneficial for the spatial resolution, because the range of the secondary particles is significantly reduced to about $40-150\,\mu\text{m}$ for the triton and $5-10\,\mu\text{m}$ for the α particles. However, the moderate cross-section of ^{6}Li leads to rather thick scintillators, which is disadvantageous for the spatial resolution. Gadolinium has a significantly higher cross-section of neutron interaction in comparison to ^{6}Li. Hence, the detection probability is rather high. The emitted conversion electrons are usually detected by photostimulable phosphors[5]. The Reactions (2.40) and (2.41) are advantageous for high spatial resolution (up to $15\,\mu\text{m}$), because the detector can comprise very thin layers of Gd and the conversion electrons are short-lived [74]. Finally, Reaction (2.39) has some interesting properties such as a higher cross-section compared to ^{6}Li. Yet, the emitted γ-ray is detrimental to the spatial resolution due to the long range, and consequently Reaction (2.38) is favored for position-sensitive detectors.

Based on those detection reactions, different types of detectors have been developed. A detailed comparison of the available detector systems at PSI can be found in the last paragraph of Section 2.2.2.4 on page 36.

2.2.2   Neutron imaging facilities at PSI

2.2.2.1   The neutron source (SINQ)

All neutron radiographical experiments within this work have been performed at the neutron source SINQ[6] located at PSI. Principally, the SINQ consists of a central lead target that is surrounded by a moderator tank and concrete shielding. A beam of high energy protons (usually 1.3 mA at 560 MeV) impinges onto a lead target in the center of the source. Due to the collision between protons and lead nuclei, the lead nuclei become exited. The nuclei release the induced energy by emitting spallation neutrons. During the spallation reaction, which is illustrated by the simplified sketch of Figure 2.11, a proton current of 1 mA ($\simeq 6.2{\cdot}10^{15}$ protons/s) is converted into about

---

[5]Here, the term phosphor refers to phosphorescing matter not necessarily containing phosphorus.

[6]This abbreviation refers to the former name of the operating institute "Schweizerische Institut für Nuklear-forschung", which translates into english as "Swiss Institute for Nuclear Research". The "Q" stands for "Quelle", which is german for "source".
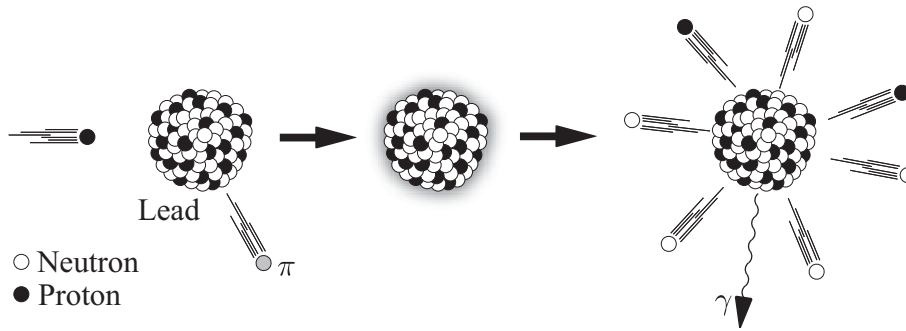
Figure 2.11: Simplified sketch of the spallation reaction that converts high-energy protons into neutrons at SINQ.

$3 - 6 \cdot 10^{16}$ high-energy neutrons. The neutron flux emitted by the source is directly proportional to the proton current. As the target is enclosed by a moderator tank, the neutron energy is reduced with increasing distance from the source, because the neutrons transfer energy to heavy water—the moderating agent—by multiple collisions. Hence, the location of a beam nozzle defines the energy spectrum of the extracted beam. Within the heavy water tank, neutrons are moderated to the thermal energy range (12...100 meV). In order to provide cold neutrons, a second tank is located within the heavy water moderator at the position where the thermal neutron flux is highest. This second tank is filled with liquid deuterium at 25 K. Upon collision with the liquid deuterium, the neutron energy is further reduced. This provides neutrons in the cold energy range (0.12...12 meV).

2.2.2.2 Imaging facility for thermal neutrons (NEUTRA)

The neutron radiography facility NEUTRA was the first of its kind taking advantage of a beam port at a continuously operated spallation source [76]. It was commisioned in 1996 and is operational since. Taking advantage of a thermal beam port at the spallation neutron source SINQ, the facility is characterized by a low γ-background and a high collimation of the beam. The intensity of the provided neutron flux is comparable to that of medium-sized research reactors [76]. The facility is housed by a concrete bunker providing adequate shielding and sufficient space for detector and sample positioning. The sketch of Figure 2.12 displays the principle layout. Neutrons are extracted from the moderator tank by an evacuated aluminium nozzle. The nozzle does not point directly to the target. This ensures a low γ-background, which is important to minimize white-spots[7] at the detector. The neutron beam is guided through an inner collimator before it leaves the concrete shielding of the source. Consisting of several steel-drums, the main shutter is likewise positioned within the source shielding. Subsequently, the neutron beam is passed through an outer collimator (evacuated metal tube with increasing diameter) to the measurement positions. The facility is designed to provide three positions for sample placement at different distances from the source, which implies different beam properties. The main beam properties at the three measurement positions are summarized in Table 2.1. The high neutron flux of the first position is appealing. Reducing the image noise, a high neutron flux is beneficial for the image quality (cf. Section 2.2.5). The small beam diameter, however, restricts the use of this measurement position to samples of about 10 cm length. Furthermore, this position is inferior to the others, if a high spatial resolution (below 100 μm) is required, because of the low collimation ratio[8]. In contrast to position 1, position 3 allows, with a beam diameter of 40 cm, for the investigation of voluminous samples. Further on, this position is equipped with a linear desk enabling the serial scanning of

---

[7]White-spots are points in the image with a significantly increased signal caused by γ-radiation hitting the CCD-chip of the camera system.

[8]The definition of the collimation ratio and its relation to the spatial resolution is discussed in Section 2.2.7.1.
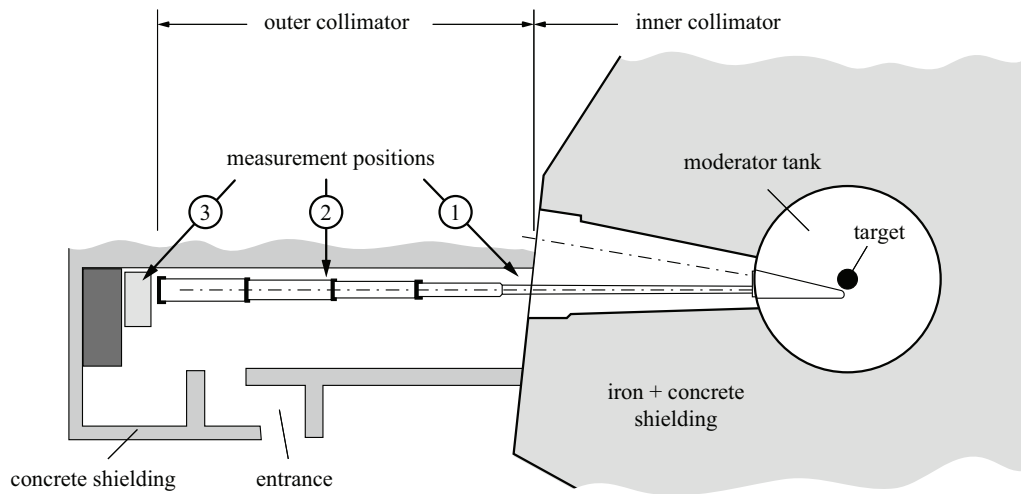
Figure 2.12: Sketch of the thermal neutron imaging beam line NEUTRA; other beam line nozzles and deuterium moderator omitted for clarity.

samples that exceed the beam diameter. Likewise, this position is best suited for investigations where a high spatial resolution is crucial due to the high collimation ratio. The low neutron flux is the main drawback of this position. The middle position (position 2) can be seen as a compromise with average properties regarding neutron flux and beam collimation. This position is mainly used for the investigation of radioactive samples and bears no particular attractiveness for fuel cell investigations.

2.2.2.3 Imaging facility for cold neutrons (ICON)

In 2005 a second facility dedicated to neutron imaging applications was inaugurated at PSI. In contrast to the first radiography station NEUTRA, this facility is located at a cold neutron beam line of the spallation neutron source. The station is named ICON, which is an acronym for "**i**maging with **co**ld **n**eutrons". The general design is similar to that of NEUTRA. Yet, several improvements were made resulting in a very flexible facility with several characteristics that are attractive for the investigation of fuel cells. The beam nozzle points at a tank filled with liquid deuterium at 25 K and located within the heavy water moderator of the SINQ. In similarity to NEUTRA, the neutrons are guided to three different measurement positions via evacuated collimator tubes. While the collimation of the beam is fixed for a measurement position at NEUTRA, a variable aperture with six different openings at ICON allows tailoring of the beam collimation. The geometric beam properties are summarized in Table 2.2. Here, the properties resulting from the smallest aperture

		position 1	position 2	position 3
distance from the source	[m]	6.4	9.9	13.1
distance from the apperture blind	[m]	3.8	7.3	10.5
field of view (beam diameter)	[cm]	$\varnothing15$	$\varnothing29$	$\varnothing40$
neutron flux at 1 mA proton current	$[(cm^2 \cdot s)^{-1}]$	$2.82 \cdot 10^7$	$7.54 \cdot 10^6$	$3.96 \cdot 10^6$
collimation ratio L/D	[-]	200	350	500

Table 2.1: Beam properties of the thermal beam line NEUTRA at the available measurement positions [73].

		position 2			position 3	
distance from aperture	[m]	7.1			12.1	
field of view	[cm]	$\sim 10 \times 10$			$\sim 30 \times 30$	

aperture diameter	[cm]		8	4	2	1	0.1
collimation ratio L/D	[-]	pos. 2	89	178	355	710	7100
		pos. 3	151	303	605	1210	12100
neutron flux	$[(\text{cm}\cdot\text{s})^{-1}]$	pos. 2	$9.6\cdot10^7$	$2.3\cdot10^7$	$5.8\cdot10^6$	$1.4\cdot10^6$	$1.4\cdot10^4$
at 1 mA proton current		pos. 3	$5.4\cdot10^7$	$1.4\cdot10^7$	$2.7\cdot10^6$	$8.5\cdot10^5$	$8.5\cdot10^3$

Table 2.2: Beam properties of the cold beam line ICON at the available measurement positions [73].

were omitted, because this configuration is mainly of interest for phase-contrast imaging [77] and is of no practical interest for fuel cell investigations due to the low neutron flux. Further on, the properties of position 1 (nearest to the source) are not given, because this position is mainly designed to host an energy selector and not forseen for actual measurements. Linear desks are available at the positions two and three. Finally, the concrete bunker shielding the facility is considerably larger than the one housing NEUTRA. This provides plenty of space for experimental equipment—a criterion that can be limiting at NEUTRA under certain conditions.

2.2.2.4   Available detectors and selection criteria

Based on the detection reactions discussed in Section 2.2.1.2 on page 32, different detector technologies have been developed:

Film technology.   Traditionally, the film technique is the standard detector technique. The film consists of $\sim 5\,\mu m$ silver halide grains. It is blackened by the secondary radiation of a converter foil that is usually Gd containing. Alternatively, ^{6}LiF/ZnS can be utilized as converter. Although this technology is still competitive in terms of spatial resolution, many drawbacks are associated with the film technology as well. Mainly, the demand for a high temporal resolution, a wide dynamic range, and quantitative information motivate for alternatives.

Imaging plates.   An alternative with nearly the same spatial resolution are imaging plates. These are plates consisting of a mixture of an neutron converter (usually Gd_2O_3) and a photo-stimulable phosphor (usually $BaFBr : Eu^{2+}$). Upon exposure to neutrons, the secondary radiation emitted by the converter substance excites meta-stable electronic states within the phosphor. After exposure, the imaging plate is transfered into a scanner, where a laser spot invokes the relaxation of the phosphor. The emitted light is recorded by the scanner. The combination of laser spot position and light intensity yields the image information. Afterwards, the imaging plate is erased by bright light and can be reused. The obtainable image quality does not only depend on the imaging plate, because the scanner performance is of equal importance. Beside the intrinsic limitation of the spatial resolution due to the spread of the secondary radiation, the laser spot size defines the spatial resolution of the obtainable image. A pixel size of $50\,\mu m$ is obtained with standard scanners. With high-resolution scanners, the pixel size can be reduced down to $12.5\,\mu m$.

Scintillator with CCD-camera.   Typical neutron sensitive scintillator screens, which are the basis of this detector type, are ^{6}Li-doped ZnS panels. The thickness of these panels influences the

capturing probability of neutrons, where a thicker screen results in a higher capturing probability. However, the practical thickness is limited by the transparency of the scintillator material, because light that is emitted in the volume of the screen has to reach the surface in order to contribute to the detectable signal. Usually, the scintillator is $50 - 400\,\mu m$ thick. As discussed in Section 2.2.7, a thicker scintillator—although beneficial to the light output—is detrimental to the spatial resolution due to light spreading. Hence, the choice of the scintillator is a trade-off between temporal and spatial resolution.

The emitted light is reflected by a mirror that is positioned in an 45° angle to the scintillator and recorded by a "charge-coupled-device" (CCD) camera. This allows to position the CCD-camera outside of the neutron beam. This is necessary, because a direct exposure of the CCD-camera to neutrons would cause early damage to the system. The whole assembly is housed in a light-tight box to avoid recording ambient light. The applied camera system has to be as sensitive as possible, because the light output is rather low. A high quantum efficiency together with a high sensitivity in the spectral range of the emitted light (green-blue at about $500\,nm$) is a pre-requisite for a reasonable temporal resolution. A very important feature of CCD-based detectors with respect to fuel cell investigations is the possible recording of multiple images without changing or moving the detector. This allows to separate the attenuation due to liquid water from the attenuation caused by the housing and structural components (referencing). Usually, the time needed for exposure yielding a reasonable signal to noise ratio is about $1 - 60$ s. In addition, about 2 s are needed for read-out of the CCD-chip and transfer of the data. This is sufficient to resolve slowly varying processes within a fuel cell. Yet, highly dynamic processes such as the movement of droplets within the flow field channels are not adequately resolved.

Amorphous silicon flat panel (A-Si detector). In contrast to the single crystals of CCD-chips, silicon in the amorphous state is considered resistant against neutron radiation. Hence, a light sensor made of amorphous silicon can be situated directly behind the scintillator, and the assembly is directly placeable into the neutron beam without risking damage of the device. This close coupling of scintillator and light detector yields a much higher light gain in comparison to the standard CCD-setup with mirror and optics. However, the effect is somewhat diminished by the lower sensitivity of the sensor material and its reduced capacity per pixel [78]. The detector is read-out continuously, which allows for high frame rates ($1 - 30$ frames per second). Hence, this detector type is best suited for imaging with high temporal resolution [79].

Light-intensified camera. Another approach to overcome the low light output of the scintillator is the combination of photo-multipliers with a CCD-based camera. The intensifier comprises a photocathode input, an electron-multiplying microchannel plate (MCP), and a phosphor screen output. A portion of the incident photons striking the photocathode causes the release of electrons due to the photoelectric effect. These electrons are then accelerated and multiplied within the microchannels of the MCP. By striking the phosphor screen at the output, these electrons cause the release of light with an increased intensity compared to the incident light. The intensifier is coupled to a CCD-camera either by lenses or by fiber-optics. The use of fiber-optics offers a higher light-throughput than lenses, but the coupling is permanent. Fast gating and shutting are advantages of such systems. Yet, the noise magnification and limited dynamic range are limitations that render this detector unattractive for fuel cell investigations. Further on, the time needed to read-out the CCD-chip is comparable to that of the unintensified CCD-camera (around 2 s). Hence, this detector is inferior to the amorphous silicon flat panel for dynamic investigations of fuel cells.

		CCD-camera	amorphous silicon flat panel	imaging plates
spatial resolution	[μm]	$100 - 500$	$127 - 750$	$12.5 - 100$
typical exposure time	[s]	$1 - 60$	< 1	~ 30
detector area	[cm]	10×10	30×40	20×40
dynamic range	[-]	10^5	10^3	10^5
linearity		linear	non-linear	linear
digital format		16 bit	12 bit	16 bit
read-out time	[s]	$2 - 100$	$0.03 - 1$	~ 300

Table 2.3: Performance parameters of different neutron detection systems for imaging purposes; based on the beam conditions at the thermal beam line NEUTRA.

Main figures characterizing the different detectors attractive for fuel cell investigations are compiled in Table 2.3. An graphical overview of the available detectors at PSI is given in Figure 2.13. The range of spatial and temporal resolutions that are obtainable under the conditions of the thermal beam line NEUTRA are compared. Traditional detectors such as track-edge foils and X-ray films are not suited for fuel cell investigations due to the long exposure-times. Dynamic processes occur even in a stationary working fuel cell (no change in current and voltage over time). For example, being a a highly dynamic process, the movement of liquid droplets and slugs within the flow field is accurately resolved only with a temporal resolution well below 1 s. Imaging plates have a higher temporal resolution than track-edge foils or X-ray films. Yet, this is still not sufficient for the investigation of dynamic processes. Nonetheless, they are attractive for investigations where high spatial resolution is necessary. As far as fuel cells are concerned, this is the cross-sectional view of fuel cells in order to discriminate liquid within the anodic and cathodic compartment (cf. Section 3.6). The detection system best suited for the majority of fuel cell investigations is the CCD-based camera with a scintillator. With a temporal resolution in the seconds domain and a spatial resolution of about 100 μm, this detector fits well to standard fuel cell equipment. Further on, this detector type has properties that are advantageous for quantitative measurements, because it has a very good linearity and allows for multiple recordings without exchanging the detector.
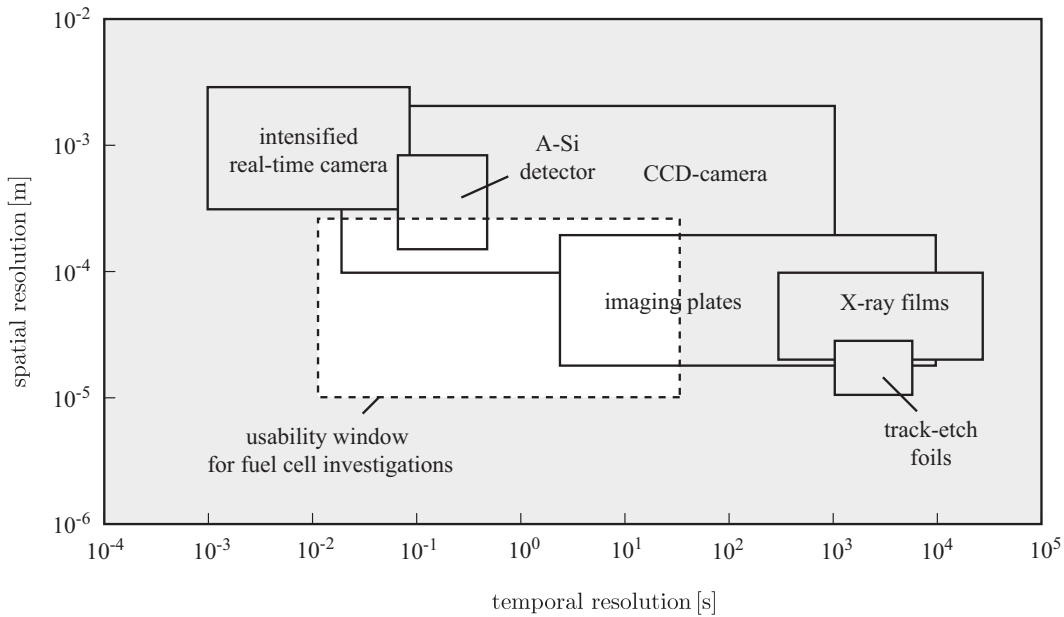
Figure 2.13: Performance characteristics of detectors with respect to spatial and temporal resolution; based on the beam conditions at the thermal beam line NEUTRA; the dashed box indicated the usability window for fuel cell investigations; adopted from [78].
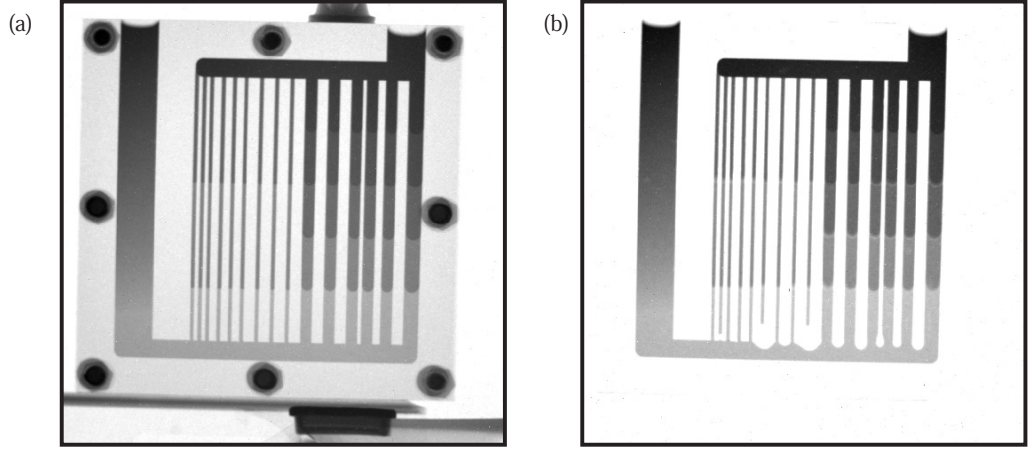
Figure 2.14: Neutron images of a test device to illustrate the process of referencing; image (a) shows the relative neutron transmission with respect to the unattenuated beam; image (b) is referenced to the unfilled device.

2.2.3 Referencing

The investigation of highly structured objects such as fuel cells implies the need to separate the contributions of different materials or layers to the emerging neutron flux behind the object. This is achieved by referencing: the scaling of the recorded neutron flux by a convenient reference.

The relative neutron transmission. The simplest approach is to separate by temporal dependence. Under the assumption of a negligible secondary neutron flux, the time-dependent neutron flux behind the measurement object (at the detection plane) is described by:

$$I(x, y, t) = I_0(x, y, t) \cdot \exp\left\{ -\sum_i \Sigma_i \cdot \delta_i(x, y, t) \right\} \tag{2.42}$$

Herein, the index i sums over all materials and layers with δ_i being the thickness in beam direction. The neutron flux provided by the source is denoted by I_0. If the temporal dependence is expressed as the difference from a given reference state at time t_{ref} according to $\delta_i(t) = \delta_{i,\mathrm{ref}} + \Delta\delta_i$, Equation (2.42) becomes

$$I = I_0 \cdot \exp\left\{ -\sum_i \Sigma_i \cdot (\delta_{i,\mathrm{ref}} + \Delta\delta_i) \right\}. \tag{2.43}$$

Herein, the dependence on the spatial variables is not explicitly given for the conciseness of notation and consistency with the acutual computational procedures. With the neutron flux at reference time $I_{\mathrm{ref}} = I_0 \cdot \{-\sum_i \Sigma_i \cdot \delta_{i,\mathrm{ref}}\}$, this allows to define the relative neutron transmission

$$x = \frac{I(t)}{I_{\mathrm{ref}}} = \exp\left\{ -\sum_i \Sigma_i \cdot \Delta\delta_i \right\}. \tag{2.44}$$

Hence, the division of two images obtained under different conditions allows extracting the difference between both images, and the relative neutron transmission is directly related to the thickness difference of the attenuating materials.

This is illustrated in Figure 2.14, where two images of a sample device are shown. The device consists of an aluminium block, into which channels of different width and depth are machined.

The image on the left hand side shows the neutron transmission of the water-filled device relative to the unattenuated beam. In other words, the obtained image is divided by a so-called openbeam image that is recorded without any sample. To obtain the right hand image, an image of the water-free device was recorded and used as reference. As the openbeam image serves as reference for image (a), all materials contribute to the relative neutron transmission. In addition to the water-filled channels, the fixture is visible with screws and the clamp for fixing. These structuring elements are not contributing to the relative neutron transmission of image (b), because they are spatially invariant and stationary. Hence, only the additional attenuation due to the water within the channels is contributing according to Equation (2.44).

Beam fluctuations. Equation (2.44) was derived under the assumption that the unattenuated neutron flux is constant over time. Strictly speaking, this is an unjustified assumption, because the neutron flux provided by the source is fluctuating slightly (usually the fluctuation is about $1\,\%$ of the beam intensity). To account for this, Equation (2.43) is expanded to

$$I = (I_0 + \Delta I_0) \cdot \exp\left\{-\sum_i \Sigma_i \cdot (\delta_{i,\mathrm{ref}} + \Delta\delta_i)\right\}, \tag{2.45}$$

where ΔI_0 accounts for those fluctuations. The fluctuation of the neutron flux is caused by a slightly fluctuating proton current impinging onto the target. Hence, the neutron flux is scaled evenly at every position and the beam profile is retained qualitatively. This means that at every position the neutron flux fluctuation is proportional to the neutron flux, which allows to set $\Delta I_0 = k_f \cdot I_0$. This leads to a relative neutron transmission of

$$x = \frac{I}{I_{\mathrm{ref}}} = (1 + k_{\mathrm{f}}) \cdot \exp\left\{-\sum_i \Sigma_i \cdot \Delta\delta_i\right\}, \tag{2.46}$$

where k_{f} is a small constant. As k_{f} is independent of the position, it is easily obtained from the image as long as part of the image does not change. The average relative neutron transmission x of this non-changing area (NCA) is equal to $1 + k_{\mathrm{f}}$, because the argument of the exponential term in Equation (2.46) is zero under these conditions. Conveniently, the openbeam fluctuation is compensated by dividing the relative neutron transmission as obtained from the division of images by $1 + k_{\mathrm{f}}$. For example, the openbeam fluctuation for the images of Figure 2.14 is compensated by dividing the images with the averaged relative neutron transmission in an area near the right edge.

Displacement artifacts and compensation. Referencing relies on the immobilisation of sample and detector. This cannot always be guaranteed. For example, the use of linear desks—required for scanning a sample that is larger than the field of view—allows repositioning of the sample only within the accuracy of the desk. Sample displacement results in characteristic artifacts within referenced images. To illustrate displacement artifacts, the impact of a small displacement of the test device is shown by the series of images at the left of Figure 2.15. The images were created artificially by displacing the recorded image of the filled device horizontally before referencing. Another image of the filled device served as reference. Hence, a zero displacement results in a homogeneous gray image, because there is no relative change between the images. Where the neutron flux is rapidly changing (at edges, screws, etc.), the displacement causes light and dark stripes. Where the neutron flux is not changing (openbeam area, at the perimeter of the aluminium fixture, etc.), the displacement has virtually no impact. Hence, the immobilisation gains in relevance, if the object under investigation is highly structured.
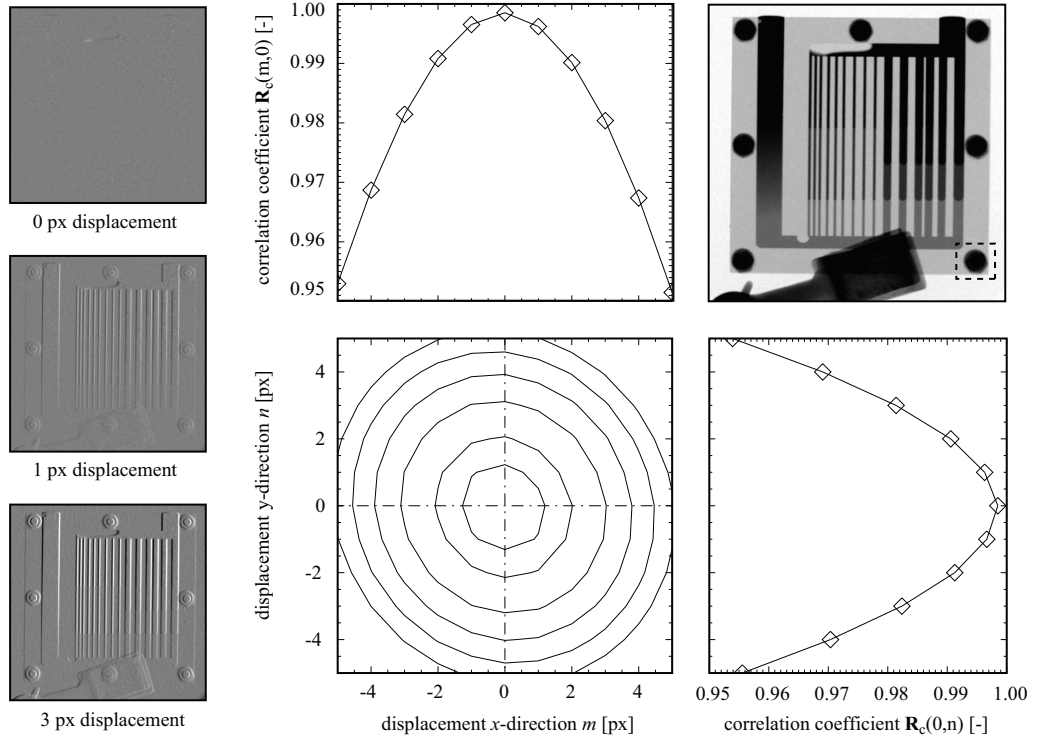
Figure 2.15: Artifacts due to sample displacement and correction via image correlation; the images on the left show the relative neutron transmission for ideally aligned and horizontally displaced references; the image on the top right shows the used test device; the correlation coefficient as obtained from the area marked by the dashed box is shown by the plots.

To some extent, those artifacts can be compensated by displacing the unreferenced image prior to the division. This can be done manually. However, a quantity that allows for an automated correction would be much more reliable and objective than simple trial and error. The theory of image similarities provides such measures [80]. The most widely used quantity is the correlation of two images. The correlation of two continuous functions f and g is defined by

$$f(x,y) \circ g(x,y) = \int \int f^*(\alpha, \beta) \cdot g(x + \alpha, y + \beta) \cdot d\alpha \cdot d\beta, \qquad (2.47)$$

where f^* denotes the complex conjugate of f. The integration is performed from $-\infty$ to $+\infty$. Being closely related to a convolution, the integral can be evaluated in Fourier-space. However, in image processing this is usually not done. In the discrete form, the correlation is computed by

$$\mathbf{R}(m,n) = \sum_x \sum_y \mathbf{F}(x,y) \cdot \mathbf{G}(x - m, y - n), \qquad (2.48)$$

where $\mathbf{F}$ and $\mathbf{G}$ are matrices containing the image information, and m and n denote the displacement in x and y direction, respectively. Near the image edges, accuracy will be lost due to truncation errors. Hence, the image part considered for a correlation should always be significantly larger than the displacement. Further on, the correlation is sensitive to scale changes. To overcome this difficulty, the matching is frequently performed by evaluating the correlation coefficient rather than the correlation itself. The correlation coefficient is computed by

$$\mathbf{R}_c(m,n) = \frac{\sum_x \sum_y \left(\mathbf{F}(x,y) - \langle \mathbf{F} \rangle \right) \cdot \left(\mathbf{G}(x - m, y - n) - \langle \mathbf{G} \rangle \right)}{\left[\sum_x \sum_y \left(\mathbf{F}(x,y) - \langle \mathbf{F} \rangle \right)^2 \cdot \sum_x \sum_y \left(\mathbf{G}(x - m, y - n) - \langle \mathbf{G} \rangle \right)^2 \right]^{1/2}}, \qquad (2.49)$$

where $\langle\mathbf{G}\rangle$ and $\langle\mathbf{F}\rangle$ denote the matrix averages. In its discrete form, Equation (2.49) can be evaluated only for integer values of m and n, because the spatial variables x and y are actually matrix indices. However, displacement in the sub-pixel range is by far the most common displacement encountered. To overcome this, the images are over-sampled by interpolating between the pixels prior to computing the correlation coefficients.

The procedure is exemplified by the right-hand side of Figure 2.15. For computational reasons, it is advantageous to perform the calculation only for a small part of the image. Ideally, a highly structured feature is used. The correlation coefficient matrix shown as contour plot is calculated for the area marked by a dashed box in the Figure at the top right. The additionally shown plots above and to the right of the contour plot are slices through the origin (marked by dash-dotted lines in the contour plot). The maximum correlation, which is virtually one, is obtained at zero displacement. This shows that the original non-displaced images are ideally placed. If either of the images would be displaced, the maximum would be found at a position distinct from the origin. The displacement could then be corrected by moving one of the images in x and y direction by the amount the maximum is displaced from the origin.

This concept of image correlation can be generalized to any kind of image transform by

$$\mathbf{R}_{\mathrm{c}} = \frac{\sum_x \sum_y \left(\mathbf{F} - \langle\mathbf{F}\rangle\right) \cdot \left(\hat{\mathrm{T}}\mathbf{G} - \langle\hat{\mathrm{T}}\mathbf{G}\rangle\right)}{\left[\sum_x \sum_y \left(\mathbf{F} - \langle\mathbf{F}\rangle\right)^2 \cdot \sum_x \sum_y \left(\hat{\mathrm{T}}\mathbf{G} - \langle\hat{\mathrm{T}}\mathbf{G}\rangle\right)^2\right]^{1/2}}, \tag{2.50}$$

where $\hat{\mathrm{T}}$ denotes an operator acting on $\mathbf{G}$. For example, $\hat{\mathrm{T}}$ could be a rotation of $\mathbf{G}$. In this case, the correlation coefficient is a function of the rotation angle and computed for every angle by evaluating Equation (2.50) with the transformed image $\hat{\mathrm{T}}\mathbf{G}$. The dimension of $\mathbf{R}_{\mathrm{c}}$ depends on the degree of freedom of the transformation (e.g., the rotation around one angle results in a vector). However, the compensation of transforms other than translation generally produces rather poor results because interpolation is needed to transform the image. Hence, a good fixation of the sample within beam direction is still of utmost importance.

2.2.4 Relative neutron transmission as function of water layer thickness

It was already mentioned in Section 2.2.1.1 that the macroscopic cross-section depends on the neutron energy, the layer thickness, and the housing. The diagram of Figure 2.16 plots the energy-dependent macroscopic cross-section of H_2O as well as the energy-spectrum of NEUTRA and ICON. The energy-dependent macroscopic cross-section was obtained using Janis [84] from the JEFF library [82] and thermal scattering data for the hydrogen bound in water was taken from the MCNPX library based on [83]. The spectra were measured with the "time-of-flight" method and are courteously provided by G. KÜHNE [81]. According to Equation (2.23) on page 26, an estimate of the energy-averaged neutron cross-section can be obtained from this data. An energy-averaged macroscopic cross-section of about $\Sigma \simeq 3\,\mathrm{cm}^{-1}$ would be obtained for the thermal spectrum provided by NEUTRA, and $\Sigma \simeq 4.6\,\mathrm{cm}^{-1}$ for ICONs cold spectrum, respectively. However, these values are only rough estimates, because effects like the change of the energy spectrum by the housing, the thickness dependence, and the energy-dependent capturing probability of the scintillator are not considered.

In consequence, the macroscopic cross-section needs to be determined experimentally. The experimental conditions to obtain the energy-averaged neutron cross-section Σ should be as near as reasonably possible to the conditions of fuel cell investigations. Especially, the detector and beam
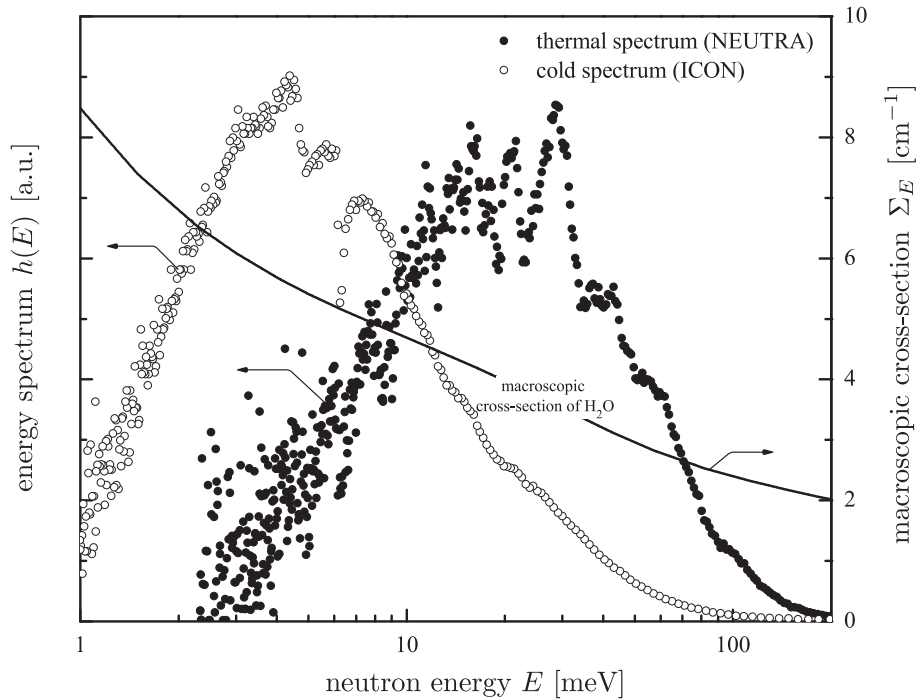
Figure 2.16: Comparison of energy spectra provided by NEUTRA and ICON, and the energy-depended neutron cross-section of H_2O; the spectra are courteously provided by KÜHNE [81]; the energy dependent neutron cross-section is obtained from Ref. [82,83].

have to be equal. In addition, also the structural components of the calibration device should be comparable to a fuel cell. The sketch of Figure 2.17 shows such a calibration device. The device consists of two aluminum blocks with a thickness of 2 cm each. Between these blocks a gap is formed that can be filled with water. The width of the gap is variable and controlled by steel spacers. Further on, the area should be large enough to achieve a statistically meaningful measurement (cf. Section 2.2.6). The relative neutron transmission is measured by taking images of the calibration device with different water layer thicknesses. These images are referenced with the unfilled device after the dark current is subtracted from either image. Finally, the beam fluctuations are corrected before the relative neutron transmission is determined.

Two such calibration curves are compared in Figure 2.18. The same test device and detector (Andor CCD-camera with scintillator) was utilized at NEUTRA and ICON. The decline of the relative neutron transmission with water layer thickness is considerably stronger for the curve obtained at ICON. As already estimated from the energy spectra, the thermal spectrum of NEUTRA results in an lower interaction probability between neutrons and water compared to ICON, and hence the same water layer thickness results in a lower attenuation of the neutron beam. Nonetheless, for both facilities the correlation is linear in the semi-logarithmic scaling of the plot. This proves the validity of the exponential attenuation law and substantiates that the thickness dependence of the effective cross-section can be neglected for thin liquid layers. Fitting of the data with Equation (2.44) on page 39 allows to calculate an effective macroscopic cross-section. For the thermal spectrum of NEUTRA results a value of $\Sigma = 2.76\,cm^{-1}$, and for the cold spectrum of ICON a value of $\Sigma = 4.89\,cm^{-1}$ is obtained. Both values agree fairly well with the estimates. The attenuation at NEUTRA is somewhat weaker than estimated, and at ICON the expectation is somewhat exceeded. The shown calibration curves are not universal. If the experimental conditions differ significantly, some sensitivity of the effective macroscopic cross-section has to be expected. However, the impact is usually not larger than around 10 %.
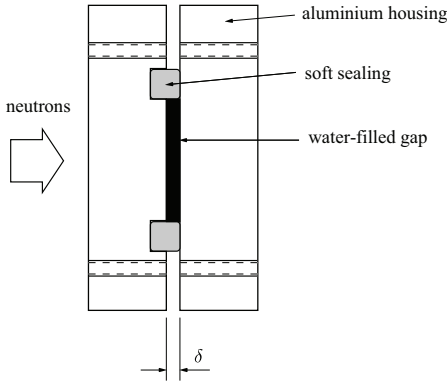
Figure 2.17: Sketch of an calibration device for measuring the relative neutron transmission as function of liquid water layer thickness.
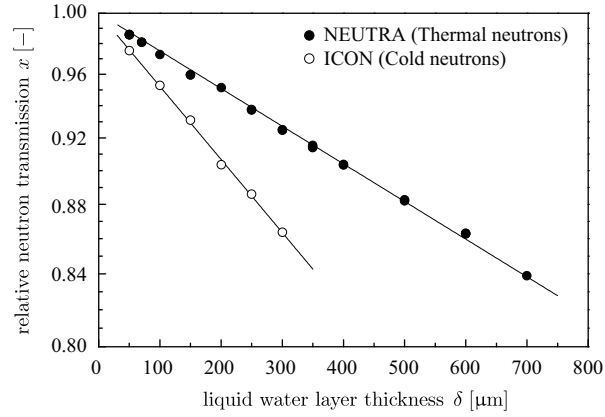
Figure 2.18: Measured relative neutron transmission as function of liquid water layer thickness for NEUTRA and ICON; housing consists of two aluminium blocks with 2 cm thickness each.

2.2.5 Noise and statistics of neutron detection

The statistical properties of neutron detection are explored within this section, and the extraction of quantitive information (e.g., the thickness of a material layer in beam direction) will be discussed in the subsequent sections. The applicability of principles and algorithms depends on the detector technology. As the CCD-camera setup is best suited for quantitative evaluation, the discussion will focus on aspects particular for this detector type. No difference between neutron flux and its observable (e.g., light output of the scintillator screen) has been made so far. Strictly speaking, the statistical properties are different. Nonetheless, the terms neutron flux and relative neutron transmission are used as synonyms for their observables throughout this section to avoid complicated terminology.

2.2.5.1 Noise origin

So far, any image noise was disregarded during the discussion of neutron imaging. However, the lower detection limit for a layer of material is strongly affected by the noise contained within an image, which makes a detailed analysis worthwhile. In general, three contributions to the image noise are distinguished:

- **Thermal noise σ_t**
  Electrons can be emitted from the CCD material itself through thermal excitation and then, trapped in the CCD well, they are indistinguishable from "true" photoelectrons. By cooling the CCD-chip it is possible to significantly reduce the number of "thermal electrons" that give rise to thermal noise.

- **Readout noise σ_r**
  This noise origins from the process of reading a signal from a sensor; in the case of a CCD-chip from the field effect transistor (FET) of the CCD-chip. Readout noise can be reduced to manageable levels by appropriate readout rates and proper electronics.

- **Shot-noise σ_s**
  The registration of light within the CCD-camera is a counting process. As for every counting experiment, the signal is consequently POISSON distributed. This will be discussed in detail below.
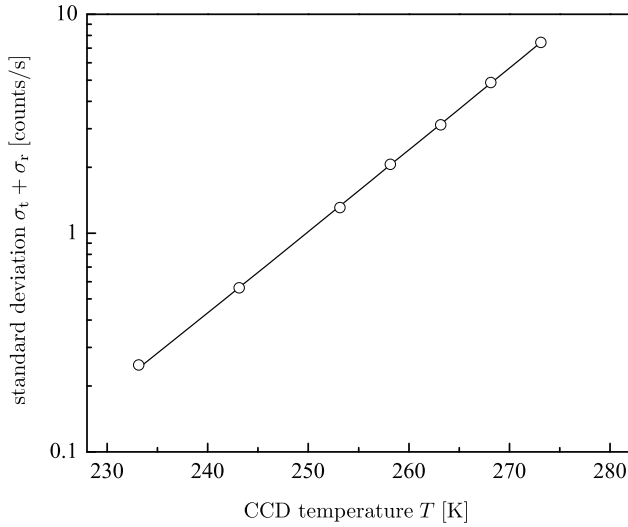
Figure 2.19: Standard deviation of dark frames as function of CCD temperature; CCD-camera: Andor Technologies A-DV434-BV (standard camera at NEUTRA); obtained with an exposure-time of 16 s; adopted from [85].

The different noise contributions are additive, and the total noise is given by

$$\sigma = \sqrt{\sigma_{\mathrm{t}}^2 + \sigma_{\mathrm{r}}^2 + \sigma_{\mathrm{s}}^2}. \tag{2.51}$$

Thermal and readout noise. The sum of readout and thermal noise can be measured from dark frames (the recording of images with closed aperture). The diagram of Figure 2.19 shows the dependence of the standard deviation obtained from dark frames as function of CCD temperature for the CCD-camera used at NEUTRA (Andor Technologies - A-DV434-BV). The used exposure-time was 16 s. However, as the standard-deviation increases linearly with exposure-time [85], the data is given as counts per second. In the semi-logarithmic scaling of the plot the sum of thermal and readout noise increases linearly with temperature. Yet, for a sufficiently cooled CCD-chip ($T < -45\,°\mathrm{C}$), the standard-deviation is reduced to less than 0.3 counts/s. This is several orders of magnitude below the normal count rate, which is of the order of 10^4 counts per pixel. Due to the exponential dependence, a further reduction of the CCD temperature (below $-45\,°\mathrm{C}$) yields no significant improvement in the anyway negligible thermal noise. Hence, for all experiments where the CCD-detector is utilized, the CCD temperature is fixed at $-45\,°\mathrm{C}$.

Shot-noise. As the recoding of light within a pixel of the CCD-chip is basically a counting of photons or—in statistical terms—events, the measurement has an fundamental uncertainty given by the POISSON process. The average or expected number of counts N is proportional to the neutron flux I, the pixel size A_{px}, and the exposure-time τ:

$$N \propto I \cdot A_{\mathrm{px}} \cdot \tau \tag{2.52}$$

The probability to count n events is given by the POISSON distribution

$$P(n|N) = \frac{N^n}{n!} \exp\left(-N\right). \tag{2.53}$$

The first and second central moment are both equal to N. Hence, the mean value increases linearly with the neutron flux, exposure-time, or pixel-size. Yet, the standard deviation follows a square-root law because the second central moment is equal to σ^2. For low expectation values, the POISSON distribution is asymmetric around the expectation value. For sufficiently large expectation values ($N > 200$), the POISSON distribution becomes symmetric and approaches a GAUSSIAN distribution

with mean N and standard deviation $\sqrt{N}$. Hence, the noise of an neutron image is normally distributed, but the mean and standard deviation are not independent from each other.

2.2.5.2 Statistics of referenced images

As shown in section 2.2.3, neutron images are referenced to separate different contributions to the overall attenuation. Hence, the statistics of the relative neutron transmission x are determined by the ratio of two statistically distributed quantities (images). Furthermore, both quantities are normally distributed with a dependence of standard deviation and mean value originating from the POISSON process. The probability density function of the relative neutron transmission will be derived below, where first the ratio distribution is introduced generally by reciting a derivation found in Ref. [86] and than applied to the special case of neutron imaging.

The ratio distribution. Given two statistically distributed quantities W and G (e.g., a neutron image and the corresponding reference image), the probability that both quantities take on certain values w and g simultaneously is the product of the separate probability densities $P_w(w) \cdot P_g(g)$. Hence, the probability that the ratio of w and g is smaller than a given value x is

$$\mathrm{P}\left(\frac{w}{g} < x\right) = \int_0^\infty \int_0^{g \cdot x} P_g(g) \cdot P_w(w) \cdot dg \cdot dw, \tag{2.54}$$

because for any g, the condition $w < g \cdot x$ has to be satisfied in order to obtain a ratio $w/g < x$. Likewise, the probability that w/g is within an infinitesimal small interval dx around x is

$$\mathrm{P}\left(x < \frac{w}{g} < x + dx\right) = \int_0^\infty \int_{g \cdot x}^{g \cdot (x+dx)} P_g(g) \cdot P_w(w) \cdot dg \cdot dw. \tag{2.55}$$

Because $P_g(g)$ does not depend on w, it can be placed outside of the inner integral:

$$\mathrm{P}\left(x < \frac{w}{g} < x + dx\right) = \int_0^\infty P_g(g) \cdot \left[\int_{g \cdot x}^{g \cdot (x+dx)} P_w(w) \cdot dw\right] \cdot dg \tag{2.56}$$

As dx is chosen to be very small, the probability density $P_w(w)$ will be virtually constant and equal to $P_w(g \cdot x)$ within the integration interval, which allows to place it outside of the inner integral as well:

$$\mathrm{P}\left(x < \frac{w}{g} < x + dx\right) = dF(x) = \int_0^\infty P_g(g) \cdot P_w(g \cdot x) \cdot \left[\int_{g \cdot x}^{g \cdot (x+dx)} dw\right] \cdot dg. \tag{2.57}$$

This is labeled $dF(x)$, because it is the incremental change in the cumulative distribution function $F(x)$. The probability density function $P(x)$ of $X = W/G$ is obtained by evaluating the inner integral and dividing both sides of Equation (2.57) by dx:

$$P(x) = \frac{dF_x(x)}{dx} = \int_0^\infty g \cdot P_g(g) \cdot P_w(g \cdot x) \cdot dg \tag{2.58}$$

Equation (2.58) is the general definition of the probability density function of a quantity formed by the ratio of two statistically distributed quantities.

Probability density distribution of the relative neutron transmission. The probability density function of the neutron flux is well approximated by a GAUSSIAN distribution with mean

N and standard deviation $\sigma = \sqrt{N}$ with N being the average event count (cf. Equation (2.52) on page 45). Hence, Equation (2.58) can be written as

$$P(x) = \frac{1}{2\pi \cdot \sigma_w \cdot \sigma_g} \cdot \int_0^\infty g \cdot \exp\left\{ -\frac{(g - N_g)^2}{2 \cdot \sigma_g^2} - \frac{(g \cdot x - N_w)^2}{2 \cdot \sigma_w^2} \right\} \cdot dg, \tag{2.59}$$

where N_w and N_g are the mean values and σ_w and σ_g are the standard deviations of the divided quantities W and G, respectively. Equation (2.59) can be integrated in closed form as long as neither distribution has non-vanishing probabilities at zero. This is fulfilled due to the underlying POISSON process, and integration yields

$$P(x) = \frac{\sigma_w^2 \cdot N_g + \sigma_g^2 \cdot N_w \cdot x}{\sqrt{2\pi} \left(\sigma_w^2 + \sigma_g^2 \cdot x^2\right)^{3/2}} \cdot \exp\left\{ -\frac{(N_w - N_g \cdot x)^2}{2\left(\sigma_w^2 + \sigma_g^2 \cdot x^2\right)} \right\}. \tag{2.60}$$

This can be rewritten, if $\langle x \rangle = N_w/N_g$, $\sigma_g^2 = N_g$, and $\sigma_w^2 = N_w$ is considered, as an expression that explicitly depends on the mean of the relative neutron transmission $\langle x \rangle$, and the mean of the denominator quantity (reference image). The resulting expression is

$$P_{\langle x \rangle}(x) = \sqrt{\frac{N_g}{2\pi}} \cdot \frac{\langle x \rangle + x\langle x \rangle}{\left(\langle x \rangle + x^2\right)^{3/2}} \cdot \exp\left\{ -\frac{N_g}{2} \cdot \frac{\left(\langle x \rangle - x\right)^2}{\langle x \rangle + x^2} \right\}. \tag{2.61}$$

It is important to note that this is not a GAUSSIAN distribution. Hence, the probability distribution of the relative neutron transmission is not normal distributed, although the divided neutron images itself contain GAUSSIAN distributed noise.

The standard deviation of $P_{\langle x \rangle}(x)$ is given by the second central moment

$$\sigma_{\langle x \rangle}^2 = \int_0^\infty P_{\langle x \rangle}(x) \cdot (x - \langle x \rangle)^2 \cdot dx. \tag{2.62}$$

However, before investigating Equation (2.62) generally, it is worthwhile to discuss the special case of $\langle x \rangle = 1$. With this constrain, Equation (2.61) becomes

$$P_1(x) = \sqrt{\frac{N}{2\pi}} \cdot \frac{1 + x}{\left(1 + x^2\right)^{3/2}} \cdot \exp\left\{ -\frac{N}{2} \cdot \frac{(1 - x)^2}{1 + x^2} \right\}. \tag{2.63}$$

Herein, the indices were omitted, because $N_g = N_w = N$ for $\langle x \rangle = 1$. For sufficiently large N, the x containing terms of Equation (2.63) can be expanded into truncated series around $x = 1$, because the probability density will be non-zero only in the neighborhood of $x = 1$. Series expansion and truncation after the first non-zero term yields:

$$\frac{(1 - x)^2}{1 + x^2} = \frac{(x - 1)^2}{2} + O^3$$
$$\frac{1 + x}{\left(1 + x^2\right)^{3/2}} = \frac{1}{\sqrt{2}} + O^1$$

Introduction of the truncated series into Equation (2.63) results in

$$P_1(x) = \frac{1}{\sqrt{2\pi}} \cdot \frac{1}{\sqrt{2/N}} \cdot \exp\left\{ -\frac{(x - 1)^2}{2 \cdot (2/N)} \right\}. \tag{2.64}$$

This is a GAUSSIAN distribution with mean $\langle x \rangle = 1$ and standard deviation $\sigma_1 = \sqrt{2/N}$. Hence, the reciprocal of the standard deviation at an average relative neutron transmission of $\langle x \rangle = 1$ of
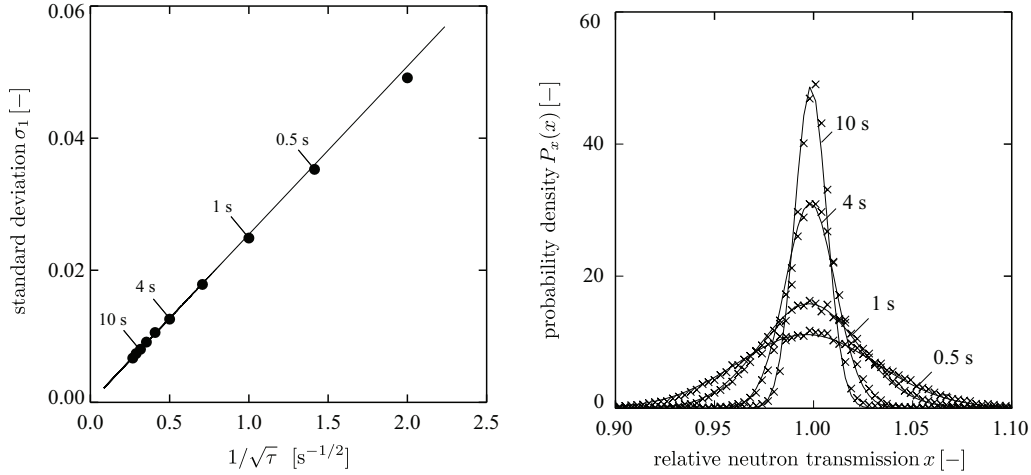
Figure 2.20: Standard deviation and probability density function of the relative neutron transmission at $\langle x \rangle = 1$ as function of the exposure-time; the left diagram compares measured standard deviations σ_1 with the theoretical estimate according to equation (2.65); the right diagram shows corresponding probability densities; measured values are shown as $\times$, and lines show fitted function values according to equation (2.64); measured at NEUTRA position one with standard CCD-detector.

referenced images is proportional to the root of neutron flux, exposure-time, and pixel-size:

$$\sigma_1 \propto 1/\sqrt{I \cdot A_{\mathrm{px}} \cdot \tau} \tag{2.65}$$

The validity of Equation (2.65) is easily substantiated by analyzing openbeam images. The left diagram of Figure 2.20 shows the measured standard deviation as function of exposure-time. The data was collected by taking two openbeam images for every exposure-time, subtracting the dark current value, dividing the images, and performing the beam fluctuation correction. From the referenced images a sub-image of around 200 pixels was extracted where the beam intensity was virtually homogeneous prior to calculating the standard deviation of the pixel values. The experiments were performed at measurement position one at NEUTRA, and the used detector was the Andor CCD-camera A-DV434-BV with scintillator. If the standard deviation is plotted against $1/\sqrt{\tau}$, a straight line is obtained proving the validity of Equation (2.65). Furthermore, the experimentally obtained histograms are compared with Equation (2.64) in the right-hand diagram.

Equation (2.65) imposes important limitations for the improvement of measurements by experimental means. As is shown in Section 2.2.6 on page 50, the noise is of the same order of magnitude as the expectable signal from liquid water within the GDLs (several $10\,\mu\mathrm{m}$ liquid layer thickness). An increase of the exposure-time would be the most obvious approach to minimize the noise. Yet, due to the square-root law, a reduction of the noise by one order of magnitude requires an increase of the exposure-time by two orders of magnitude. This is virtually never feasible due to motion blurring. Furthermore, the neutron flux is decreasing proportionally to the square of the distance from the source. Hence, the measurement position nearest to the source is favorable to achieve the lowest possible noise level. Finally, some improvement can be achieved with amended scintillators that exhibit a higher neutron capturing probability [87].

For the same reasons, the cold imaging facility ICON will bear significant advantages in the future. Because, the capturing probability is higher for low energy neutrons, this facility allows for a much lower noise level although the neutron flux is comparable to NEUTRA. This becomes very clear from the diagram of Figure 2.21. The standard deviation obtained at NEUTRA at measurement position three is compared with data that was recorded at ICONs measurement position
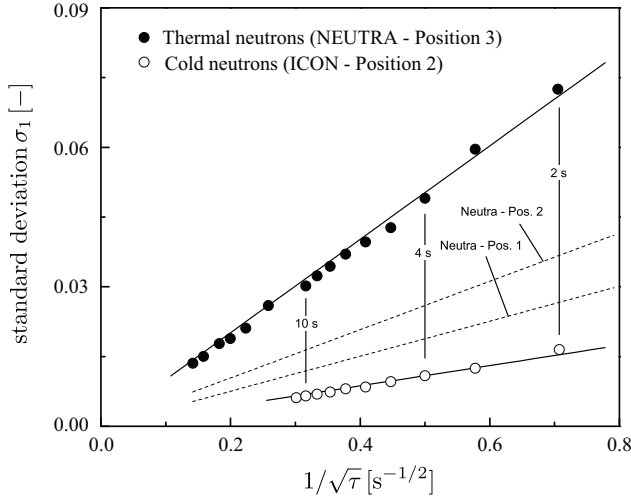
Figure 2.21: Standard deviation as function of exposure-time for thermal and cold neutrons; the dashed-lines show estimates for the other measurement positions at NEUTRA; measured with CCD-camera and in-house scintillator.

two. To ensure comparability, the same detector system was used for both measurements: Andor CCD-camera with scintillator. The dashed lines are estimates for the other measurement positions at NEUTRA calculated from the ratio of neutron fluxes. The standard deviation resulting from ICON is nearly one order of magnitude lower for the same exposure-time compared to NEU-TRAs measurement position three. Even in comparison to measurement position one, a significant improvement can be assessed.

The standard deviation as function of the relative neutron transmission can principally be obtained from Equation (2.62) if Equation (2.61) is introduced into it:

$$\sigma_{\langle x \rangle}^2 = \sqrt{\frac{N}{2\pi}} \cdot \int_0^\infty \frac{\langle x \rangle + x\langle x \rangle}{(\langle x \rangle + x^2)^{3/2}} \cdot \exp\left\{ -\frac{N}{2} \cdot \frac{(\langle x \rangle - x)^2}{\langle x \rangle + x^2} \right\} \cdot (x - \langle x \rangle)^2 \cdot dx. \qquad (2.66)$$

However, the resulting integral has no analytical solution. To overcome this difficulty, the steps that were performed to obtain an expression for σ_1 are repeated. Yet, the series expansion is done around $x = \langle x \rangle$ rather than $x = 1$ yielding

$$\frac{\langle x \rangle + x\langle x \rangle}{(\langle x \rangle + x^2)^{3/2}} = \frac{1}{\sqrt{\langle x \rangle + \langle x \rangle^2}} + \mathrm{O}^1$$

$$\frac{(\langle x \rangle - x)^2}{\langle x \rangle + x^2} = \frac{(x - \langle x \rangle)^2}{\langle x \rangle + \langle x \rangle^2} + \mathrm{O}^3$$

for the x dependent terms. With this approximation, Equation (2.66) becomes again the central moment of a GAUSSIAN distribution with mean $\langle x \rangle$ enabling the analytical solution of the integral. For the standard deviation results:

$$\sigma_{\langle x \rangle} = \sqrt{\frac{\langle x \rangle + \langle x \rangle^2}{N}} = \sigma_1 \cdot \sqrt{\frac{\langle x \rangle + \langle x \rangle^2}{2}} \qquad (2.67)$$

Once more, Equation (2.67) can be validated with openbeam images, whereby different average relative neutron transmissions are achieved by dividing images obtained with different exposure-times because of $N \propto I \cdot \tau$. The relationship between standard deviation and relative neutron transmission is shown is Figure 2.22. The experiment was performed at NEUTRA and ICON with the same detector setup: Andor CCD-camera with scintillator. The standard deviation is normalized with σ_1 and compared to the theoretical prediction according to Equation (2.67). An excellent agreement between experiment and theory can be found. At first thought, it might seem unusual that the standard deviation decreases with lower relative neutron transmissions—

49
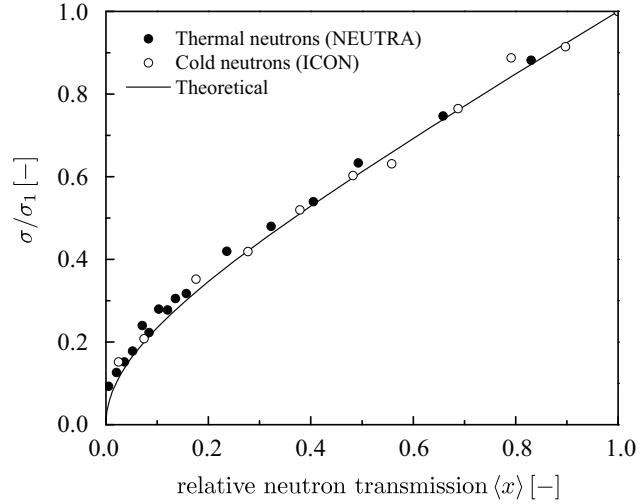
Figure 2.22: Standard deviation of the relative neutron transmission as function of $\langle x \rangle$ for thermal and cold neutrons; normalized to the standard deviation at $\langle x \rangle = 1$; theoretical curve given by Equation (2.67); measured with CCD-camera and scintillator.

especially, if the beneficial impact of a higher event count to σ_1 is recalled. The decline with lower relative neutron transmission origins from the fact that the standard deviation of the unreferenced image is proportional to $\sqrt{N}$. Hence, a lower event count results in a lower standard deviation. Nonetheless, a higher event count is beneficial for σ_1. This stems from the linear scaling of the mean value with N, while the standard deviation increases only with $\sqrt{N}$.

2.2.6 Quantification

2.2.6.1 Single pixel quantification

If the expected neutron transmission for usual amounts of liquid within the GDLs of an fuel cell (cf. Figure 2.18 on page 44) is compared with the achievable image noise (cf. Figure 2.21 on the previous page), it becomes clear that the value of a single pixel is nearly meaningless, because signal and standard deviation are of the same order of magnitude.

To quantify the minimum liquid layer thickness that can be detected on the basis of a single pixel, the confidence interval of the relative neutron transmission Δx has to be translated into a confidence interval of the liquid layer thickness $\Delta \delta$. The confidence interval of the relative neutron transmission is related to its probability distribution $P_{\langle x \rangle}(x)$ by

$$P\left(x \in \langle x \rangle \pm \Delta x\right) = 1 - \alpha = \int_{\langle x \rangle - \Delta x}^{\langle x \rangle + \Delta x} P_{\langle x \rangle}(x) \cdot dx \qquad (2.68)$$

where $P_{\langle x \rangle}(x)$ is well approximated by a GAUSSIAN distribution with mean $\langle x \rangle$ and standard deviation $\sigma_{\langle x \rangle} = \sigma_1 \cdot \sqrt{(\langle x \rangle + \langle x \rangle^2)/2}$. The uncertainty—the probability that x is not found within $\pm \Delta x$—is denoted by α. By changing variables according to $t = (x - \langle x \rangle)/(\sqrt{2}\sigma_{\langle x \rangle})$, this can be transformed into the standard normal distribution, and by considering the symmetry of the standard normal distribution, the probability of finding x in the interval $\pm \Delta x$ is given by

$$1 - \alpha = \text{erf}\left(\frac{\Delta x}{\sqrt{2} \cdot \sigma_{\langle x \rangle}}\right). \qquad (2.69)$$

Inversion of Equation (2.69) and introduction of Equation (2.67) leads to

$$\Delta x = \sigma_1 \cdot \sqrt{\langle x \rangle + \langle x \rangle^2} \cdot \text{erf}^{-1}\left(1 - \alpha\right). \qquad (2.70)$$

In the range of interesting relative neutron transmissions, the exponential attenuation law is fairly well approximated by

$$\delta \simeq \frac{1 - \langle x \rangle}{\Sigma}. \tag{2.71}$$

With this approximation, the error propagation law yields

$$\Delta \delta \quad = \quad \frac{\Delta x}{\Sigma} \tag{2.72}$$

$$= \quad \frac{\sigma_1}{\Sigma} \cdot \sqrt{\langle x \rangle + \langle x \rangle^2} \cdot \mathrm{erf}^{-1} \left(1 - \alpha \right) \tag{2.73}$$

$$= \quad \frac{\sigma_1}{\Sigma} \cdot \sqrt{(1 - \Sigma \cdot \delta) + (1 - \Sigma \cdot \delta)^2} \cdot \mathrm{erf}^{-1} \left(1 - \alpha \right), \tag{2.74}$$

if the macroscopic cross-section is assumed to be known without uncertainty. Because $\Sigma \cdot \delta \ll 1$, the dependence of the confidence interval on the actual thickness δ can be omitted:

$$\Delta \delta \simeq \frac{\sigma_1}{\Sigma} \sqrt{2} \cdot \mathrm{erf}^{-1}(1 - \alpha) \tag{2.75}$$

The confidence interval of the liquid layer thickness is about $\Delta \delta = 93 \, \mu\mathrm{m}$ for typical conditions ($\Sigma = 2.78 \, \mathrm{cm}^{-1}, \sigma_1 = 0.01, \alpha = 0.01$). Hence, the uncertainty is virtually as large as the GDL is thick[9], which renders the value of a single pixel more or less meaningless.

2.2.6.2 Averaging

In order to obtain meaningful values of the water layer thickness, the quantitative accuracy needs improvement. Two approaches are feasible:

- Pixel averaging
  According to Equation (2.65), the standard deviation can be reduced by increasing the pixel size. In practice, this is done by averaging over neighboring pixels (binning). This is either done on-chip or in a post-processing step.

- Image averaging
  The averaging over subsequently recorded images resembles an increase of the exposure-time as long as the read-out noise is negligible. Hence, this allows reducing the standard deviation as well.

In consequence, the quantitative accuracy is improved either by abdication of spatial or temporal resolution.

Image averaging. To analyze the impact of averaging n referenced images is straightforward, because this is identical to increasing the exposure-time by a factor n (provided the read-out noise is negligible). Hence, the standard deviation at $\langle x \rangle = 1$ scales with $1/\sqrt{n}$. The averaging of reference images only is of more practical interest, because this is not detrimental to the temporal resolution. Reference images are characterized by well defined conditions (e.g., completely liquid-free cells). In consequence, the averaging over n images does not lead to effects like motion blurring. Yet, only the standard deviation of the reference image is affected by the number of averaged images, which leads from Equation (2.60) to

$$P_x(x) = \sqrt{\frac{1/\sigma_1}{\pi}} \cdot \frac{1 + x/n}{(1 + x^2/n)^{3/2}} \cdot \exp\left\{ -\frac{1}{\sigma_1^2} \cdot \frac{(1 - x/n)^2}{1 + x^2/n} \right\} \tag{2.76}$$

---

[9]Common thicknesses of GDLs range from $200 \, \mu\mathrm{m}$ to $400 \, \mu\mathrm{m}$.
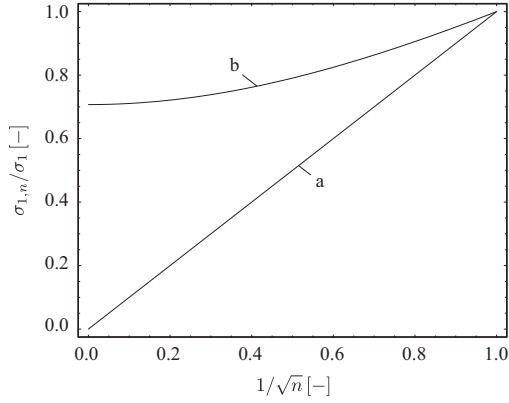
Figure 2.23: Influence of averaging n images onto the standard deviation at $\langle x \rangle = 1$; normalized to the standard deviation without averaging σ_1; averaging of referenced images is shown in (a), and averaging of the reference image only is shown by curve (b).
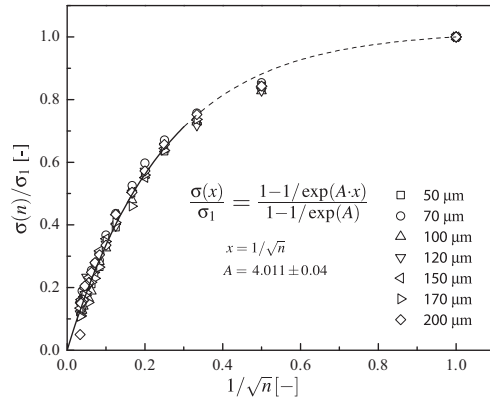
Figure 2.24: Influence of averaging over n pixel onto the standard deviation of the relative neutron transmission for different water layer thicknesses; normalized with the standard deviation of the not averaged images σ_1; the curve shows a phenomenological fit to the data.

for $\langle x \rangle = 1$. In similarity to Section 2.2.5.2, series expansion of Equation (2.76) allows deriving an analytical expression for the standard deviation of the relative neutron transmission at $\langle x \rangle = 1$ in the case of averaging n reference images:

$$\frac{\sigma_{1,n}}{\sigma_1} = \sqrt{\frac{1 + 1/n}{2}} \qquad (2.77)$$

It is inferred from Equation (2.77) and the curves shown in Figure 2.23 that the standard deviation cannot be reduced more than about $30\,\%$ even for an infinite number of averaged images, because the ratio tends towards $\sqrt{1/2}$ for $n \to \infty$, and hardly more than ten images are averaged in practice. Finally, averaging of referenced images (averaging of divided images rather than the reference only) is constrained as well; although the standard deviation can principally be tailored to any accuracy, motion blurring limits the number of averaged images normally to even less then ten.

Pixel averaging. The averaging of pixels allows to enhance the quantification either in conjunction with image averaging or as an alternative approach. It becomes apparent from Equation (2.52) that the reciprocal of the standard deviation principally scales with the square root of the pixel size, because $\sigma_1 = \sqrt{2/N}$ and $N \propto I \cdot A_{\mathrm{px}} \cdot \tau$. However, this is only true if the mean event count is equal for all averaged pixels. This is not accurately fulfilled in the case of neutron imaging, because of scintillator and beam inhomogeneities. In consequence, the dependence of the standard deviation on the number of averaged pixels has to be determined experimentally. The diagram of Figure 2.24 shows the standard deviation as function of the number of averaged pixels n. The plot is normalized with the standard deviations of the original (non-averaged) image σ_1. The data was obtained for different water layer thicknesses with the following detector setup: Andor CCD-camera with scintillator at NEUTRA measurement position three. Under the constraint of negligible inhomogeneities, the plot would show a straight line because the standard deviation is plotted over $1/\sqrt{n}$. Due to the inhomogeneities, the pixel averaging is much less effective than theoretically expected. For example, averaging over 10×10 pixel reduces the standard deviation to about $25\,\%$, which is 2.5 times the theoretical value. As the discrepancy from theory is mainly a detector/beam effect, the mean relative neutron transmission does not affect the curve.
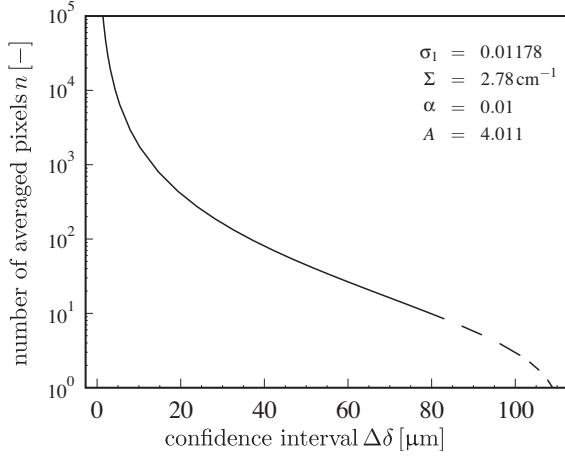
Figure 2.25: Required number of averaged pixels n as a function of the confidence interval $\Delta\delta$; calculated with equation (2.78) using the fit shown in Figure 2.24; parameters are shown in the plot and resemble typical conditions at NEUTRA.

This is shown by the well agreeing points for different water layer thicknesses. In resemblance to Equation (2.75), the confidence interval of the liquid layer thickness is given by:

$$\Delta\delta(n) = \frac{\sigma(n)}{\Sigma} \cdot \sqrt{2} \cdot \mathrm{erf}^{-1}(1 - \alpha), \qquad (2.78)$$

where $\sigma(n)$ denotes the standard deviation for n averaged pixels. To exemplify this, the needed number of averaged pixels as a function of the confidence interval is shown in Figure 2.25 for typical conditions at NEUTRA. The confidence interval of a single pixel is about $110\,\mu\mathrm{m}$. By averaging of 100 pixels, the confidence interval can be reduced to about $40\,\mu\mathrm{m}$. This is still not sufficient for the quantification of water within a GDL because a confidence interval of about $10\,\mu\mathrm{m}$ is adequate for this purpose. Yet, this requires the averaging of more than thousand pixels, which equals an area of about $10\,\mathrm{mm}^2$. This, however, is still a reasonable spatial resolution for most investigations, and pixel averaging is a feasible option as long as the liquid content is not varying strongly in the averaged area.

2.2.6.3 Statistical quantification

Within the last section, averaging over a certain amount of pixels was shown to be a feasible option to achieve sufficient accuracy for quantification purposes. Yet, the consideration was restricted to the special case of non-changing liquid content within the averaged area. In addition, the exponential attenuation law, which links the relative neutron transmission to the liquid water layer thickness, was linearized. If the exponential attenuation law is applied, averaging of the relative neutron transmission prior to calculating the liquid layer thickness brings about a systematic error, because the relative neutron transmission is weighed by the exponential attenuation law. From a statistical point of view, the liquid layer volume V_l within a certain area A is given by

$$\frac{V_l}{A} = \delta_l = \int \delta_w(x) \cdot h(x) \cdot dx. \qquad (2.79)$$

Herein, $\delta_w(x)$ relates the relative neutron transmission to a certain liquid layer thickness. This is a calibration curve that is, in general, experimentally obtainable (cf. Section 2.2.4 on page 42). The average liquid thickness within the considered area A is denoted by δ_l, and $h(x)$ symbolizes the true probability density of the relative neutron transmission, which equals DIRAC's delta function

$$h(x) = \delta_D \left(\langle x \rangle - x \right) \qquad (2.80)$$
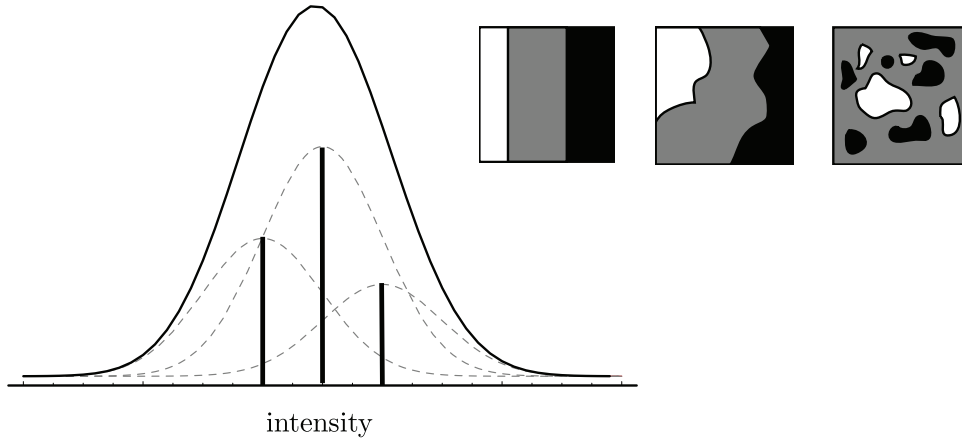
Figure 2.26: Sketch of the composition of the measurable histogram out of convoluted peaks.

if the liquid layer thickness is constant within the considered area. It was shown in Section 2.2.5.2 that a constant true relative neutron transmission causes a distribution of its observable, which is the light intensity emitted by the scintillator and recorded by the CCD-camera, due to the shot-noise effect. The relative neutron transmission x is related to its observable, the relative light intensity $\tilde{x}$, by

$$h(\tilde{x}) = \int h(x) \cdot P_x(\tilde{x}) \cdot dx, \qquad (2.81)$$

where $P_x(\tilde{x})$ is given by Equation (2.61). This is illustrated by Figure 2.26. The three intensity distributions shown at the right result all in the same histogram, because the area ratio of each intensity (white, grey, and black) is equal in each case. Hence, the transition from the actual images to their statistical representation implies always some loss of information. The original probability distribution $h(x)$ consists of three peaks, where the peak height is equal to the area ratio of the related intensity. Each intensity causes a distribution of the observable given by $h(x) \cdot P_x(\tilde{x})$, which are displayed as dashed lines. Finally, the resulting, measurable probability distribution $h(\tilde{x})$ that is shown as black line is the superposition of those distributions.

If the generalized definition of the average liquid layer thickness as defined by Equation (2.79) is compared with the definition according to Equation (2.71)

$$\delta_l = \frac{1 - \langle \tilde{x} \rangle}{\Sigma} = \frac{1}{\Sigma} \left(1 - \int \tilde{x} \cdot h(\tilde{x}) \cdot d\tilde{x} \right),$$

it can be shown that both definitions are equivalent if $\delta_w(x) = (1 - x)/\Sigma$ holds, because

$$\delta_l = \int \underbrace{\frac{1}{\Sigma} \cdot (1 - x)}_{=\delta_w(x)} \cdot h(x) \cdot dx = \frac{1}{\Sigma} \cdot \left(\underbrace{\int h(x) \cdot dx}_{=1} - \underbrace{\int x \cdot h(x) \cdot dx}_{=\langle x \rangle} \right) = \frac{1 - \langle x \rangle}{\Sigma}. \qquad (2.82)$$

Likewise, the mean of the relative neutron transmission $\langle x \rangle$ and its observable $\langle \tilde{x} \rangle$ are equal. To prove this, the definition of $\langle \tilde{x} \rangle$ is expanded with Equation (2.81):

$$
\begin{aligned}
\langle \tilde{x} \rangle &= \int \tilde{x} \cdot h(\tilde{x}) \cdot d\tilde{x} = \int \tilde{x} \left(\int h(x) \cdot P_x(\tilde{x}) \cdot dx \right) \cdot d\tilde{x} = \int \int \tilde{x} \cdot h(x) \cdot P_x(\tilde{x}) \cdot dx \cdot d\tilde{x} \\
&= \int h(x) \cdot \underbrace{\int \tilde{x} \cdot P_x(\tilde{x}) \cdot d\tilde{x}}_{=x} \cdot dx = \int h(x) \cdot x \cdot dx = \langle x \rangle
\end{aligned}
$$
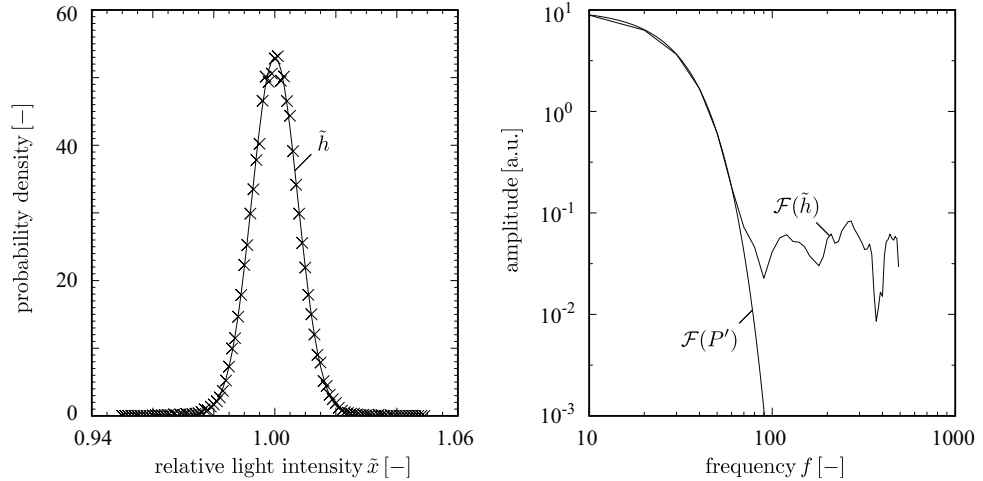
Figure 2.27: Probability density and power spectrum of the relative neutron transmission obtained from openbeam images; the power spectrum shows high frequency scatter that prohibits the application of FOURIER based deconvolution algorithms.

Hence, the requirement of a constant liquid layer thickness within the averaged area can be relaxed. The liquid layer thickness might change within a range that justifies linearizing the exponential attenuation law.

If the relative neutron transmission is changing over a wider range, $\delta_w(x)$ cannot be linearized and averaging is not accurate anymore. To evaluate the liquid layer thickness from Equation (2.79), the probability distribution $h(x)$ has to be obtained from its observable $h(\tilde{x})$. If the dependence of the standard deviation of $P_{\langle x \rangle}(x)$ on $\langle x \rangle$ is omitted, Equation (2.81) can be simplified to the convolution

$$h(\tilde{x}) \simeq \int_0^\infty h(x) \cdot P'(\tilde{x} - x) \cdot dx \;\Leftrightarrow\; \tilde{h} = h * P', \tag{2.83}$$

where P' denotes a GAUSSIAN distribution with standard deviation σ_1 and mean zero. Hence, the probability distribution of the relative neutron transmission can be obtained from its observable by deconvolution. The convolution kernel P' can be measured. For referencing two images obtained from dry cells, it is obvious that $h(x) = \delta_D(1 - x)$ with δ_D denoting DIRAC's delta function. This allows to measure P', since then Equation (2.81) becomes $h(\tilde{x}) = P'(\tilde{x} - 1)$. However, $h(x)$ has still to be determined by deconvolution in order to determine the average liquid layer thickness by Equation (2.79).

Deconvolution in Fourier space. Principally, the deconvolution can be performed in FOURIER space, because

$$\mathcal{F}(\tilde{h}) = \mathcal{F}(h * P') = \mathcal{F}(h) \cdot \mathcal{F}(P') \;\Rightarrow\; h = \mathcal{F}^{-1}\left(\frac{\mathcal{F}(\tilde{h})}{\mathcal{F}(P')} \right). \tag{2.84}$$

Yet, in practice this is not possible for computational reasons. The two diagrams of Figure 2.27 exemplify this. The left-hand diagram shows the histogram (probability density $\tilde{h}$) obtained from two divided openbeam images. The power spectrum of the histograms FOURIER transform is plotted together with the FOURIER transform of the deconvolution kernel P' within the right-hand diagram. As $\tilde{h}$ is obtained from measurement, it contains a small amount of experimental noise. This is reflected within the power spectrum by the high frequency scatter ($f > 80$). At the same time, the power spectrum of P' has extremely small amplitudes at higher frequencies. Because the FOURIER transform of $\tilde{h}$ has to be divided with the Fourier transform of P', the high frequency scatter is extremely magnified. The noise is accelerated by this, which results in a total

information loss. This is a general phenomenon in FOURIER-based deconvolution, and different filtering techniques such as low-pass or WIENER filtering are available to overcome this to a certain extent. Anyhow, all those techniques act on the high frequency part of the FOURIER transform, and the deconvolution results tend to be smoother than the real probability density at best. The case study depicted in Figure 2.27 is an extreme example. As the relative neutron transmission is uniform, the probability density equals a DIRAC delta function. The FOURIER transform of DIRAC's delta function is a constant over frequency. In consequence, the FOURIER transforms of $\tilde{h}$ and P' need to be equal for all frequencies to obtain an accurate result. This is not achievable with any filtering technique. In consequence, FOURIER based deconvolution is not applicable to restore the probability density of the relative neutron transmission x from the measurable probability density of the relative light intensity $\tilde{x}$.

Deconvolution by relaxation methods. The application of linear algebra algorithms becomes possible, if Equation (2.83) is written in discrete form

$$\tilde{h}(i) = \sum_{k=0}^{N-1} P'(i-k) \cdot h(i), \tag{2.85}$$

where N is the number of samples of the vectors $\tilde{h}$ and P'. As P' is the sample of a peak function, $P'(i)$ will be zero for $i < 0$ and $i \geq N$ (zero padding). This allows to write Equation (2.85) in matrix form

$$\tilde{h} = \mathbf{P} \cdot h, \tag{2.86}$$

where $\mathbf{P}$ is a $2N - 1 \times N$ matrix composed of columns that contain the vector P' mutually shifted by one position:

$$\mathbf{P} = \begin{bmatrix} P'(0) & 0 & 0 & \cdots \\ P'(1) & P'(0) & 0 & \cdots \\ P'(2) & P'(1) & P'(0) & \cdots \\ \vdots & \vdots & \vdots & \ddots \\ P'(N-1) & P'(N-2) & P'(N-3) & \cdots \\ 0 & P'(N-1) & P'(N-2) & \cdots \\ 0 & 0 & P'(N-1) & \cdots \\ \vdots & \vdots & \vdots & \ddots \end{bmatrix} \tag{2.87}$$

In this form, $\mathbf{P}$ is not square and h and $\tilde{h}$ are of different length. This imposes limitations for the applicability of matrix algebra. Principally, this is easily overcome by multiplying Equation (2.86) with $\mathbf{P}^\mathsf{T}$. Yet, it is advantageous to multiply with $\mathbf{P}^\mathsf{T}\mathbf{P}\mathbf{P}^\mathsf{T}$ instead. This will be shown below. The adopted equation reads

$$\tilde{h}' = \mathbf{P}' \cdot h \tag{2.88}$$

with $\tilde{h}' = (\mathbf{P}^\mathsf{T}\mathbf{P}\mathbf{P}^\mathsf{T}) \cdot \tilde{h}$ and $\mathbf{P}' = (\mathbf{P}^\mathsf{T}\mathbf{P}\mathbf{P}^\mathsf{T}\mathbf{P})$. Hence, the deconvolution problem has been reformulated into a linear algebra problem. Unfortunately, $\mathbf{P}'$ is almost singular. This prevents direct inversion of $\mathbf{P}'$ to solve for h. The relaxation ansatz

$$h^{k+1} = h^k + \mu \cdot \left(\tilde{h}' - \mathbf{P}' \cdot h^k\right) = \mu \cdot \tilde{h}' + (\mathbf{E} - \mu \cdot \mathbf{P}') \cdot h^k \tag{2.89}$$

is generally chosen to find an approximate solution for h via iteration. In Equation (2.89) the superscript denotes the number of iterations, μ is the relaxation factor, and $\mathbf{E}$ symbolizes the unity

matrix. If $h^0 = \tilde{h}'$ is used as starting guess, successive substitution gives

$$h^k = \mu \cdot \left(\mathbf{E} + \sum_{n=1}^{k} \left(\mathbf{E} - \mu \cdot \mathbf{P}' \right)^n \right) \cdot \tilde{h}'. \tag{2.90}$$

In order to be finite for $k \to \infty$, the sum has to converge. This requires that

$$\lim_{k \to \infty} \left(\mathbf{E} - \mu \cdot \mathbf{P}' \right)^k = [0] \tag{2.91}$$

holds, which implies that the N eigenvalues of $\mathbf{P}'$ satisfy

$$\lim_{k \to \infty} \left(1 - \mu \lambda_i \right)^k = 0, \tag{2.92}$$

where λ_i with $i = 0, 1, ..., N-1$ denote the N eigenvalues of $\mathbf{P}'$. Hence, the relaxation factor needs to satisfy

$$|1 - \mu \cdot \lambda_i| < 1 \tag{2.93}$$

for any λ_i in order to ensure convergence of the iteration. Condition (2.93) is always fulfilled, if all eigenvalues are positive real numbers in the range $]0, 2/\mu[$. The matrix $\mathbf{P}^\mathsf{T}\mathbf{P}$ is symmetric, which means that the eigenvalues are real. The eigenvalues of $(\mathbf{P}^\mathsf{T}\mathbf{P}) \cdot (\mathbf{P}^\mathsf{T}\mathbf{P})$ are squares of the eigenvalues of $\mathbf{P}^\mathsf{T}\mathbf{P}$ and hence are positive real numbers, which is the reason for favoring the multiplication of Equation (2.89) with $\mathbf{P}^\mathsf{T}\mathbf{P}\mathbf{P}^\mathsf{T}$ over $\mathbf{P}^\mathsf{T}$.

Convergence is achieved when $0 < \mu < 2/\max(\lambda_i)$. If the relaxation factor is obtained globally from this inequality, the resulting algorithm is refereed to as VAN CITTERT algorithms [88]. Even better deconvolution results are obtained by localizing the relaxation factor [89]. The local relaxation factor is then obtained from the eigenvalue-like equation

$$\mathbf{P}' \cdot h^k = \lambda \cdot h^k \Rightarrow \lambda_i = \frac{\sum_{m=0}^{N-1} \mathbf{P}'_{i,m} h_m^k}{h_i^k}, \tag{2.94}$$

where λ is a vector of length N. The GOLD deconvolution algorithm results if $\mu_i = 1/\lambda_i$ is chosen as local relaxation parameter. The final iteration rule is obtained by substituting Equation (2.94) into Equation (2.89):

$$h_i^{k+1} = \frac{\tilde{h}_i}{\sum_{m=0}^{N-1} \mathbf{P}'_{i,m} h_m^k} \cdot h_i^k \tag{2.95}$$

As the deconvolution result can be compared with the true histograms, the efficiency of the deconvolution algorithm is best tested with artificial histograms. This is shown for two typical cases in Figure 2.28 on the next page. The left-most diagrams show the initial histograms together with the convoluted histograms that are passed to the deconvolution algorithm. The diagrams to the right compare the deconvolution result with the initial spectra at different iterations. The upper row shows the deconvolution result for two peaks that are convoluted with a Gaussian. Although still overlapping, the peaks are recognizable already after thousand iterations. The deconvolution result improves in quality with an increasing number of iterations, and a stable solution is obtained after $2 \cdot 10^5$ iterations. Both peaks are nearly perfectly restored in terms of position and height. The lower row depicts the deconvolution performance for a rectangular shaped histogram. Again, after thousand iterations, the deconvolution agrees already reasonably well with the initial function and increases in quality with subsequent iterations. The solution stabilizes again after approximately
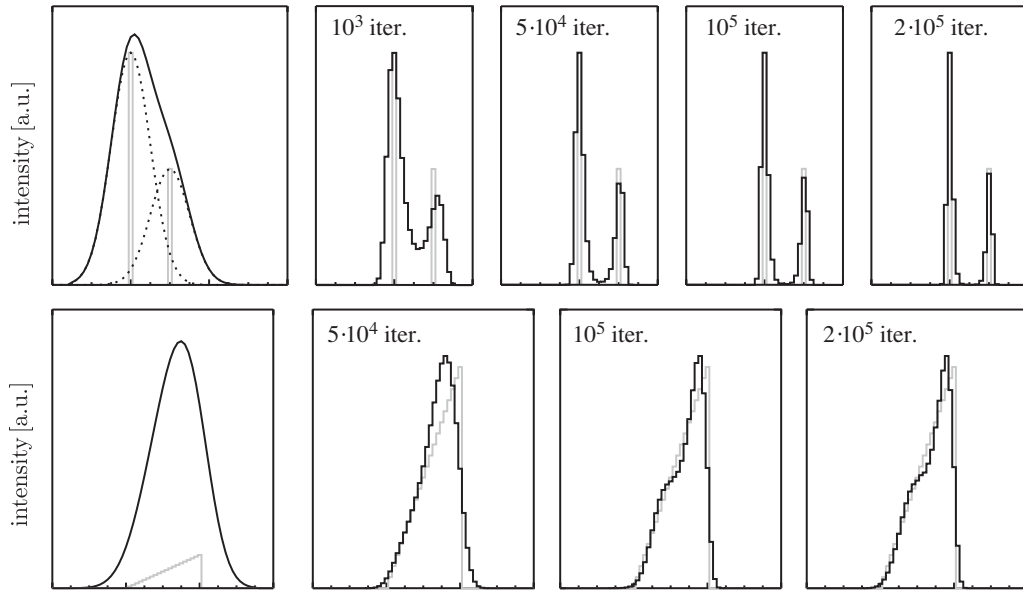
Figure 2.28: Results of Gold deconvolution for two artificially created test problems; the upper row shows the results for two convoluted peaks; the lower row shows the deconvolution result for a step-like function; the original functions were convoluted by a Gaussian as is shown in the left-most diagrams.

$2 \cdot 10^5$ iterations. Although the quality is remarkable, the match is not as perfect as for the two convoluted peaks. The algorithm tends to form separate peaks, which manifests as shoulder in the final result. Notwithstanding, the GOLD deconvolution algorithm works remarkably well.

Although the investigation of the artificial problems is encouraging, an important difficulty encountered in measurement is missing: the functions to be deconvoluted were missing any noise. To test the algorithm with experimental data, it is again convenient to study a case where the probability density of the relative neutron transmission is known in order to rate the deconvolution result. This is shown in Figure 2.29. The shown image, where a $1\,\mathrm{mm}$ thick layer of heavy water was imaged, simulates the expectable small attenuation from water inside a GDL. The experiment was
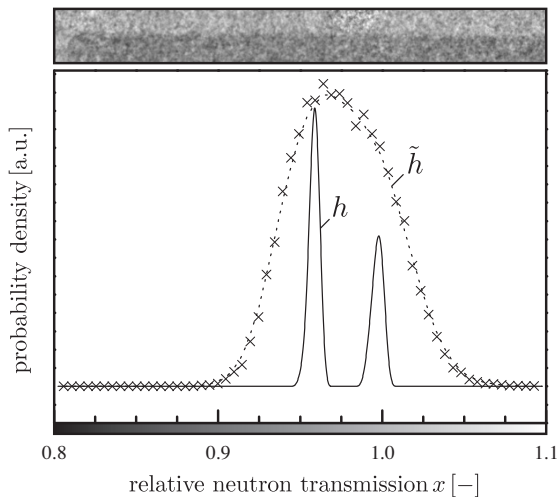
Figure 2.29: Restauration of the probability density h from $\tilde{h}$ in the case of two peaks via Gold deconvolution; the underlying image is shown above the histogram plot.
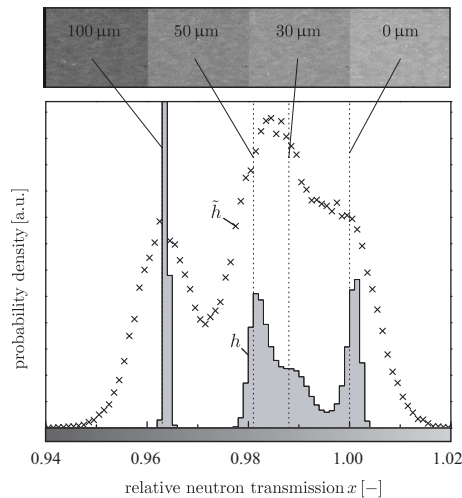
Figure 2.30: Restauration of the probability density h from $\tilde{h}$ in the case of four peaks via Gold deconvolution; the underlying image is shown above the histogram plot.

performed at NEUTRAs measurement position one, and the used detector was the Andor CCD-camera with standard commercial scintillator. Since part of the image (lighter region) is occupied by an aluminium rib, the probability density of the relative neutron transmission has to feature two peaks: one for the heavy water and one for the aluminium. Yet, the noise contained in the observable $\tilde{x}$ smears the probability density of the relative light intensity $\tilde{h}$ into a continuous distribution. The measured histogram is shown by ($\times$) in the diagram. By applying GOLD's algorithm to the histogram, the histogram shown as (—) is obtained. Two well separated peaks are formed, as was expected. Hence, the deconvolution algorithm is tolerant towards experimental scatter and allows to obtain a better representation of h than is given by $\tilde{h}$, if not the true probability density of the relative neutron transmission at all.

However, the capabilities of GOLD deconvolution are limited. This becomes apparent from the example depicted in Figure 2.30. The shown histogram is obtained from polyethylene foils of different thicknesses. The shown image above shows the arrangement of three different foils ($30\,\mu\text{m}$, $50\,\mu\text{m}$, and $100\,\mu\text{m}$) and a foil-free area. The measured histogram shows three peaks: one for the $100\,\mu\text{m}$ foil, one representing the foil-free area, and one with contributions from the $30\,\mu\text{m}$ and $50\,\mu\text{m}$ foils. In addition, the peak at $x = 1.0$ is merged with the peak formed from the foils of intermediate thickness. The deconvolution procedure is able to recover clear peaks for the $100\,\mu\text{m}$ foil and the foil-free area. Yet, the merged peak in-between is not clearly separated, although the existence of the $30\,\mu\text{m}$ peak might be anticipated from the shoulder connected to the peak at $50\,\mu\text{m}$.

Nonetheless, it can be concluded that the deconvolution algorithm produces results with reasonable accuracy, which allows deriving quantitative information from neutron images with an accuracy that is better than given by the noise limitation.

Parallelized computation. The low convergence speed is a major drawback of the relaxation ansatz. The rather time-consuming computation of 10^5 iterations is rather time-consuming motivates to parallelize the computation algorithm. Unfortunately, Equation (2.95) has only moderate parallelization properties. In addition to the N multiplications and N summations needed to evaluate the denominator, one division and one multiplication is needed to compute a single element of h during an iteration. Hence, $2 \cdot (N^2 + N)$ floating-point operations are needed to calculate one iteration. If the computation is performed in parallel, h^k has to be communicated between the nodes after every iteration. This results in $2 \cdot N$ communications, because the values have to be send forth and back. Hence, the calculation time can be estimated by

$$t = 2 \cdot \frac{N^2 + N}{n} \cdot t_{\text{calc}} + 2 \cdot N \cdot n \cdot t_{\text{comm}}, \tag{2.96}$$

if n is the number of nodes, t_{calc} the typical time to perform a floating-point operation, and t_{comm} the average time to communicate this number. The number of optimal processors is found from $\partial_n t = 0$ to be

$$n_{\text{opt}} = \sqrt{\frac{1 + N^2}{N} \cdot \frac{t_{\text{calc}}}{t_{\text{comm}}}} \simeq \sqrt{\frac{N}{t_{\text{comm}}/t_{\text{calc}}}}. \tag{2.97}$$

The average computational time per iteration is shown in Figure 2.31 in dependence of the number of processors for histograms of different length. The calculation was performed on the Linux computation cluster Merlin at PSI with 10^5 iterations per histogram. The lines show the theoretical prediction according to Equation (2.96). The ratio of $t_{\text{comm}}/t_{\text{calc}}$ was found to be around eighty by fitting with Equation (2.96). Because the communication time is eighty times the computation time, parallelized computation bears no attractiveness for small histograms ($N < 300$), and even for
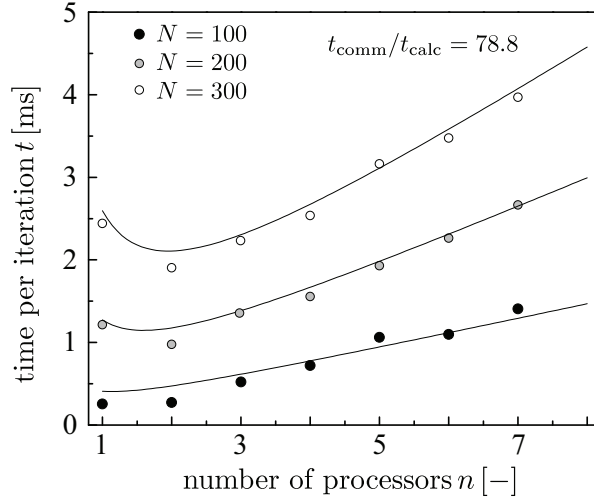
Figure 2.31: Computational time for parallelized Gold deconvolution; computation performed at the Linux cluster Merlin at PSI; N denotes the length of the histograms; the lines show the function values of equation (2.96) fitted to the data.

larger histograms the benefit in computational time is moderate (e.g., deconvoluting a histogram with thousand samples on four processors would reduce the computation time by approximately 50% compared to the time needed on one processor). Notwithstanding, the utilization of a cluster is reasonable, if a series of histograms needs deconvolution. In that case, many histograms can be deconvoluted simultaneously, whereby each calculation is performed on some few processors.

2.2.7 Instrumental broadening

Instrumental broadening causes differences between the observable relative light intensities $\tilde{x}$ and the relative neutron transmission x, which become apparent as unsharpness within the images. This is exemplified in Figure 2.32. The light intensity as recorded by the CCD-camera is shown for a step-like change of the neutron intensity. The step was created by placing a Gd-strip (strong neutron absorber) such that it occupies part of the image. The image, which is referenced with a corresponding openbeam image, is shown as inset in Figure 2.32. The step-response that is shown as averaged profile causes a region of roughly eight pixel ($\simeq 750\,\mu\mathrm{m}$), where the light intensity is continuously increasing. The inherent unsharpness depends on several parameters like the collimation ratio (L/D), the quality of the optical system, and the scintillator unsharpness. These will be addressed in more detail in Section 2.2.7.1 on the facing page.

To derive a mathematical framework which describes the instrumental broadening, it is useful to describe the experimental setup as linear system. This is illustrated in Figure 2.33 on the next page. The unattenuated neutron beam $\mathbf{I}_0$ is attenuated by the fuel cell, which results in the
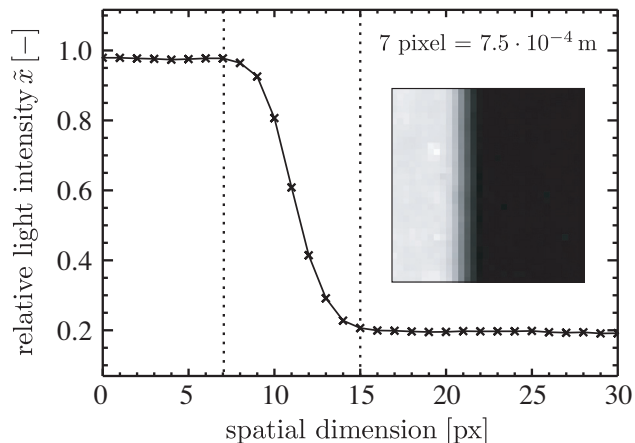
Figure 2.32: Light intensity generated by a stepwise change of the neutron intensity; standad CCD-detector with commercial scintillator; ($\times$) denotes the mean of forty columns; the inset shows the corresponding image.
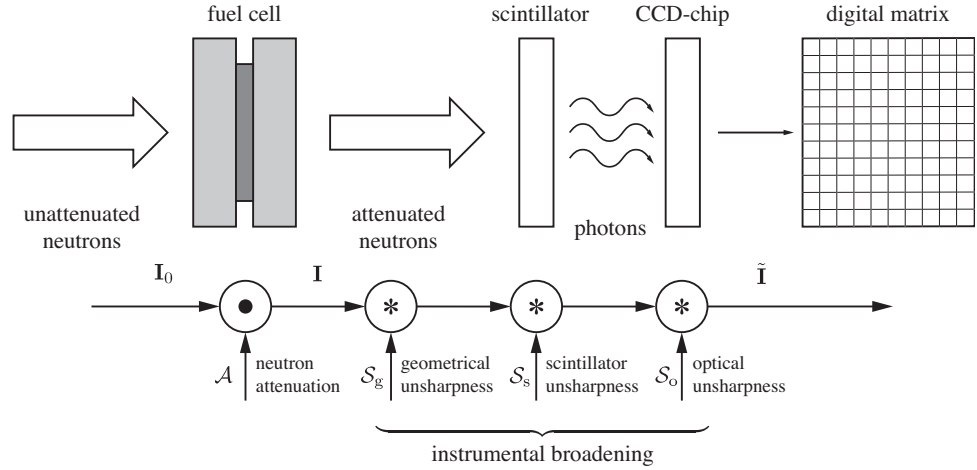
Figure 2.33: Description of the experimental setup for neutron imaging as linear system.

neutron beam $\mathbf{I}$ leaving the fuel cell. The difference between $\mathbf{I}$ and $\mathbf{I}_0$ contains the information about attenuating matter and its distribution within the fuel cell. However, the observable light intensity as recorded by the CCD-chip $\tilde{\mathbf{I}}$ differs from $\mathbf{I}$ due to several broadening effects, which are expressed by several point-spread-functions (PSF) $\mathcal{S}$. The most prominent contributions to the intrumental broadening are: the geometrical unsharpness (beam divergence), the scinitllator unsharpness, and the optical unsharpness of the lenses. These are explicitly shown in Figure 2.33 and denoted by the subscripts g, s, and o, respectively. If scattering is neglected, the exponential attenuation law holds and the relation between $\mathbf{I}$ and $\mathbf{I}_0$ is multiplicative such that $\mathbf{I} = \mathbf{I}_0 \cdot \mathcal{A}$ with $\mathcal{A} = \exp\left\{-\sum(\delta_i \cdot \Sigma_i)\right\}$. Hence, the light intensity recorded by the CCD-chip is given by

$$\tilde{\mathbf{I}} = (\mathbf{I}_0 \cdot \mathcal{A}) * S + \mathcal{C}, \tag{2.98}$$

where $\mathcal{S}$ symbolizes the system PSF and $\mathcal{C}$ denotes the noise accompanying the measurement. Due to the associativity of the convolution operation, several PSF can be combined to a system PSF according to

$$\mathcal{S} = \mathcal{S}_{\mathrm{g}} * \mathcal{S}_{\mathrm{s}} * \mathcal{S}_{\mathrm{o}} * \ldots \tag{2.99}$$

Formally, the relative light intensity $\tilde{x}$ is given by

$$\tilde{x} = \frac{(\mathbf{I}_0 \cdot \mathcal{A}) * \mathcal{S} + \mathcal{C}}{(\mathbf{I}_0 \cdot \mathcal{A}_{\mathrm{ref}}) * \mathcal{S} + \mathcal{C}} = \frac{(x \cdot \mathbf{I}_0 \cdot \mathcal{A}_{\mathrm{ref}}) * \mathcal{S} + \mathcal{C}}{(\mathbf{I}_0 \cdot \mathcal{A}_{\mathrm{ref}}) * \mathcal{S} + \mathcal{C}}, \tag{2.100}$$

because the broadening acts on both images separately. Equation (2.100) can be simplified to

$$\tilde{x} = x * \mathcal{S} + \mathcal{C} \tag{2.101}$$

in the limiting case of a constant reference $(\mathbf{I}_0 \cdot \mathcal{A}_{\mathrm{ref}}) = const.$, which is nearly fulfilled, if an open-beam image serves as reference. However, even for a non-homogeneous reference, Equation (2.100) is well approximated by Equation (2.101) as long as the inhomogeneity of the reference is not too strong (intensity variations of less than about 10 %).

2.2.7.1 Selected broadening contributions

Geometrical unsharpness. As illustrated in Figure 2.34, geometrical unsharpness has its origin in the finiteness of the aperture opening at the source-facing end of the collimator. The source
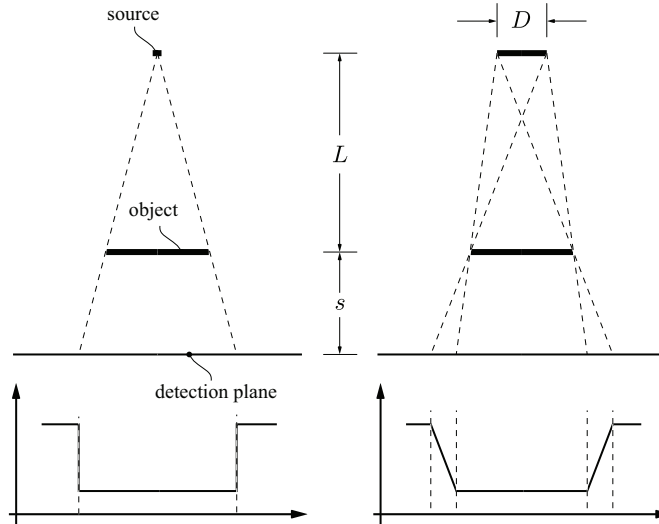
Figure 2.34: Geometry of image formation for a point source at the left and a source with finite aperture at the right.

distribution (neutron flux at the aperture opening) is projected onto the detection plane. An object placed between source and detector causes a shadow on the detection plane. The area directly behind the object, which is completely contained within the shadow of the object is referred to as umbra. Similarly, the area that has a partial view of the aperture spot is refereed to as penumbra[10]. In some literature, the penumbra is called the edge gradient. If $\mathcal{S}_{\mathrm{g}}$ denotes the normalized neutron flux distribution within the aperture plane (focal spot), the noise-free neutron flux on the detection plane is given by

$$\mathbf{I}(x,y) = I_0 \cdot \mathcal{A}\left(\frac{x}{M}, \frac{y}{M}\right) * \mathcal{S}_{\mathrm{g}}\left(-\frac{x}{M-1}, -\frac{y}{M-1}\right), \tag{2.102}$$

where I_0 denotes the average neutron flux of the unattenuated beam at the detection plane, and M is refereed to as the object magnification, which is given by

$$M = \frac{L+s}{L}. \tag{2.103}$$

The term $M-1$ is called the source magnification. The scaling of the spatial coordinates at the different planes is easily derivable from the theorem of intersecting lines. The minus signs in argument of $\mathcal{S}_{\mathrm{g}}$ stems from the spatial reversal of the source distribution on the detection plane.

A reasonable approximation for the source distribution is a uniform distribution of either circular (NEUTRA) or rectangular (ICON) shape. The PSF of a uniform circular source distribution is expressible in terms of the rectangle function $\Pi(r)$ by

$$\mathcal{S}_{\mathrm{g}} = \frac{4}{\pi \cdot D^2} \cdot \frac{1}{(M-1)^2} \cdot \Pi\left(\frac{r}{D \cdot (M-1)}\right) \quad \text{with} \quad r^2 = x^2 + y^2. \tag{2.104}$$

Herein, D symbolizes the aperture diameter. The spread of the penumbra at the detection plane is given by $s/(L/D)$. Hence, the distance between object and detection plane is limited. The nearer the object is placed to the detector, the less geometrical unsharpness is found in the images. For example, the L/D at NEUTRAs measurement position one is about 200 (see Table 2.1 on page 35), which means that the object should not be placed further away from the detector than 2 cm to reduce the penumbra to about 100 μm, which is the pixel size of the standard CCD-camera. On the other hand, the distance between sample and detector should at least be one times the sample size to minimize the influence of scattered neutrons. This is shown in Section 2.2.1.1. Investigated fuel cells are typically about 10 cm in size, and keeping the same distance between fuel cell and

---

[10]Umbra is Latin for shadow, and paene is Latin for almost.

detector results in a penumbra of about $500\,\mu\text{m}$ ($\simeq 5\,\text{pixel}$) under the conditions of NEUTRAs measurement position one.

Similarly, the PSF corresponding to a rectangularly shaped aperture is given by

$$\mathcal{S}_{\text{g}} = \frac{1}{A \cdot B} \cdot \frac{1}{(M-1)^2} \cdot \Pi \left(\frac{x}{A \cdot (M-1)} \right) \cdot \Pi \left(\frac{y}{B \cdot (M-1)} \right), \tag{2.105}$$

where A and B are the length and width of the aperture opening, respectively. The penumbra is different in x and y direction and given by $s/(L/A)$ and $s/(L/B)$, respectively.

Scintillator unsharpness. Unsharpness is likewise caused by "light diffusion" in the scintillator screen. When neutrons are captured in the depth of the scintillator, the emitted light is irradiated isotropically in any direction. A thicker screen will increase the probability of neutron capture. Yet, the thicker screen will allow more "light diffusion" at the same time. The geometric consideration that describes the propagation of scattered neutrons—depicted in Figure 2.9 on page 31—is also valid for the propagation of light from the depth of the scintillator to its surface. Hence, the emitted light from a neutron capturing event in the depth of the screen will cause a symmetrically spread light intensity at the screen surface, which can be expressed by

$$\tilde{\mathbf{I}} = \mathbf{I} * \mathcal{S}_{\text{s}}, \tag{2.106}$$

with $\mathcal{S}_{\text{s}}$ being the scintillator characterizing PSF that is given by

$$\mathcal{S}_{\text{s}} = \frac{\lambda}{2\pi} \Big/ \left(\lambda^2 + r^2 \right)^{3/2} \quad \text{with} \quad r^2 = x^2 + y^2. \tag{2.107}$$

Herein, λ denotes the distance between the scintillator surface and the point of neutron capture in the depth of the screen. The division by 2π rather than 4π as in equation (2.34) ensures proper normalization.

Optical unsharpness. The third major contribution to the instrumental broadening is introduced by the optical system (CCD aperture and lenses). A principal limitation of all optical systems is given by light diffraction. It can be shown that a planar wavefront that passes through an aperture causes an interference pattern at the detection plane (CCD-chip), which is described by an Airy disc [90]. The RAYLEIGH-criteria for diffraction limited optics gives the minimal distance between discriminable points. It is defined by

$$\Delta x_r = 0.61 \cdot \frac{f}{r} \cdot \lambda, \tag{2.108}$$

where r denotes the radius of the aperture, λ the wavelength of the light, and f is the focal length. As the light output of the scintillator is very low, the aperture is normally fully opened (large r), and diffraction is usually no limitation. As the wavelength of the light is about $500\,\text{nm}$, it can be estimated that the diffraction limit is well below $1\,\mu\text{m}$.

Another source for optical unsharpness is caused by an off-focus configuration of the scintillator plane. If the position of the scintillator is not exactly matching the focal plane of the optics, a point is projected as circle on the CCD-chip. Hence, the PSF of the off-focus unsharpness is again a circle:

$$\mathcal{S}_{\text{o}} = \frac{1}{\pi \cdot \epsilon^2} \cdot \Pi \left(\frac{r}{2 \cdot \epsilon} \right) \quad \text{with} \quad r^2 = x^2 + y^2. \tag{2.109}$$

As illustrated in Figure 2.35, the radius of the unsharpness circle is given by $\epsilon = r \cdot z/d$, where r
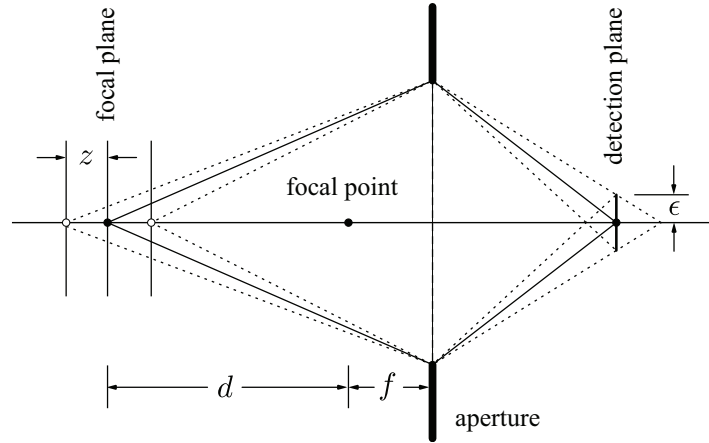
Figure 2.35: Illustration of the formation of off-focus unsharpness.

is the radius of the aperture, z the displacement from the focal plane, and d is the distance of the focal plane from the focal point of the optical system.

Phenomenological PSF. The broadening contributions that were discussed so far cover a wide range of experimentally encountered broadening. Yet, some effects like broadening by not perfectly manufactured optical components are not covered by those PSFs. Several phenomenological PSFs have been formulated to account for broadening that is not otherwise mathematically describable. The most prominent representative of this class of PSFs is the GAUSSIAN

$$\mathcal{S} = \frac{1}{\sqrt{2\pi} \cdot \sigma} \exp\left(-\frac{r^2}{2 \cdot \sigma^2}\right) \quad \text{with} \quad r^2 = x^2 + y^2. \tag{2.110}$$

Yet, also a LORENTZIAN is frequently used.

2.2.7.2 Determination of the system PSF

The actual PSF of the detection system is composed of several broadening influences, some of them might be describable by the equations given in the last section, and generally the real detector system has to be characterized experimentally. The most obvious approach is the direct measurement of the PSF by realizing a point-like intensity. However, this is technically difficult, because an infinitesimal point object cannot be produced perfectly but only approximated. Further on, the aperture of the point object needs to be small in comparison to the spatial resolution of the system (some few micrometers). This implies that very few neutrons are transmitted through the aperture, which forces a lengthy exposure-time.

The measurement of the edge-spread-function (ESF) is experimentally easier. The edge is formed by an object that transmits neutrons on one side of the edge but is perfectly attenuating on the other side. An example of such an experimental arrangement was already given in Figure 2.32. The ESF associated with a particular PSF is given by

$$\mathcal{E}(x) = \int\limits_{-\infty}^{x} \int\limits_{-\infty}^{\infty} S(x, y) \cdot dy \cdot dx, \tag{2.111}$$

where the edge is located at $x = 0$. This relation allows fitting the experimentally obtained edge response with appropriate ESF in order to obtain the parameters for the PSF.

The most important PSFs and their FOURIER transforms are summarized in Table 2.4. In addition, the corresponding ESFs, as obtained with Equation (2.111) are listed. The ESFs are normalized
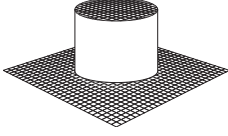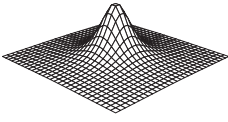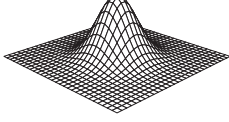
	circle	scintillator	gaussian
PSF $\mathcal{S}$	$\frac{1}{\pi \cdot R^2} \cdot \Pi(\frac{r}{R})$	$\frac{\lambda}{2\pi} / \left(\lambda^2 + r^2\right)^{3/2}$	$\frac{1}{2\pi \cdot \sigma^2} \cdot \exp\left(-\frac{r^2}{2\sigma^2}\right)$
ESF $\mathcal{E}$	$\frac{1}{2} + \frac{x}{\pi} \cdot \frac{\sqrt{R^2-x^2}}{R^2}$ $-\frac{1}{\pi} \cdot \tan^{-1}\left(x \cdot \frac{\sqrt{R^2-x^2}}{x^2-R^2}\right)$	$\frac{1}{2} + \frac{1}{\pi} \cdot \tan^{-1}\left(\frac{x}{\lambda}\right)$	$\frac{1}{2} + \frac{1}{2}\mathrm{erf}\left(\frac{x}{\sqrt{2}\cdot\sigma}\right)$
LSF $\mathcal{L}$	$\frac{2}{\pi R^2}\sqrt{R^2 - x^2}$	$\frac{\lambda}{\pi} / \left(\lambda^2 + x^2\right)$	$\frac{1}{\sqrt{2\pi}\sigma} \exp\left(-\frac{x^2}{2\sigma^2}\right)$
PSF $\mathcal{F}\{\mathcal{S}\}$	$\frac{R}{\rho} \cdot J_1\left(2\pi R\rho\right)$	$\exp\left(-2\pi\lambda|\rho|\right)$	$\exp\left(-2\pi\sigma^2\rho^2\right)$

Table 2.4: Common PSFs, LSFs, and ESFs and their FOURIER transforms; formula are given in polar coordinates; transformation into Cartesian coordinates by $r^2 = x^2 + y^2$; likewise the conjugate spatial-frequency variables of the Fourier transforms are given by $\rho^2 = u^2 + v^2$; functions are normalized; J_1 denotes BESSEL functions of the first kind.

to stretch from zero to one. If the edge response of the system is dominated by one broadening contribution, the parameter of the PSF is easily found by fitting the measured profile with the appropriate $\mathcal{E}$. If the edge response is composed out of more than one broadening contribution, the parameter determination is slightly more complicated. The ESF is then given by

$$\mathcal{E}(x) = H(x) * \mathcal{L}(x), \tag{2.112}$$

where $H(x)$ denotes the HEAVISIDE step function, and $\mathcal{L}$ is the system line-spread-function (LSF). A LSF is defined by

$$\mathcal{L}(x) = \int_{-\infty}^{\infty} \mathcal{S}(x,y) \cdot dy, \tag{2.113}$$

and the system LSF is just the convolution of all contributing line-spread-functions:

$$\mathcal{L} = \mathcal{L}_\mathrm{g} * \mathcal{L}_\mathrm{s} * \mathcal{L}_\mathrm{o} * ... \tag{2.114}$$

Finally, the FOURIER transform of the line spread function is related to the FOURIER transform of the PSF by

$$\mathcal{F}\{\mathcal{L}\}(u) = \mathcal{F}\{\mathcal{S}\}(u,0). \tag{2.115}$$

Hence, the FOURIER transform of the LSF is the FOURIER transform of the PSF in one dimension. Consequently, the system ESF can be calculated by multiplying the one-dimensional FOURIER transforms of the single PSFs, transformation into real space of the resulting expression, and convolution according to Equation (2.112). Because the convolution operation is associative, the calculation can alternatively be performed by starting with the analytical ESF of either contribution and subsequent convolution with the other LSFs.

The PSF parameter determination is exemplified in Figure 2.36, where the edge response of one of the liquid-filled channels of the test device already in Section 2.2.3 described is shown. The measured profile is shown by ($\times$). The profile is fitted with the ESF for scintillator unsharpness (—), which shows very good agreement with the measurement. In the shown example, the parameter estimate was performed by investigating a gap rather than a single edge, which bears the advantage that twice as many points of the transient region enter the fit. The procedure outlined before can be applied nonetheless, because the gap is just the super-position of two edges.
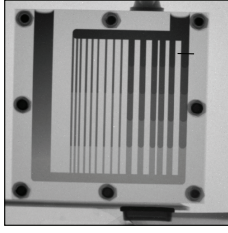
Figure 2.36: Determination of the system PSF parameters from edge responses; measured profile shown by (×); fitted ESF shown as (—); profile obtained from marked slice in the image; standard CCD-detector with commercial scintillator.
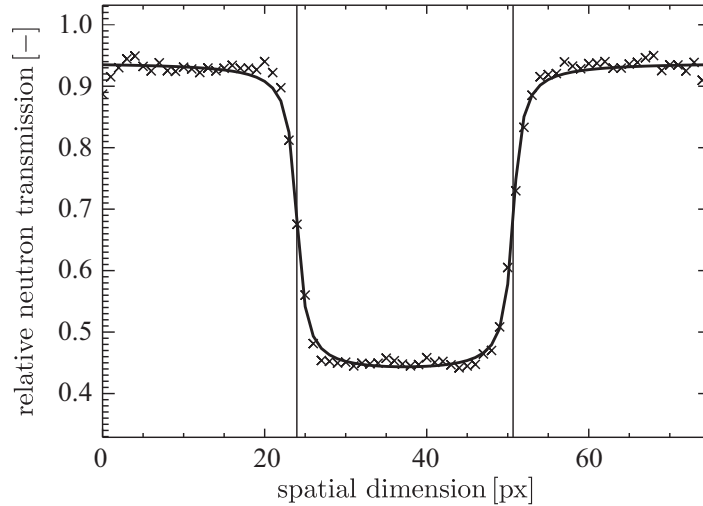
2.2.7.3 Filtering techniques and image reconstruction

Once the experimental setup is characterized and the system PSF is known, the instrumental broadening can be compensated to some extent by appropriate filtering techniques. From Equation (2.98), it becomes clear that the compensation of instrumental broadening is a two-dimensional deconvolution problem. Similar to the deconvolution problems discussed in Section 2.2.6.3, direct inverse filtering in FOURIER space according to

$$\mathcal{F}\left\{\mathbf{I}\right\} = \frac{\mathcal{F}\{\tilde{\mathbf{I}}\} - \mathcal{F}\{\mathcal{C}\}}{\mathcal{F}\{\mathcal{S}\}} \tag{2.116}$$

is not possible due to numerical instabilities. The FOURIER transform of the PSF $\mathcal{F}\{\mathcal{S}\}$ usually drops off rapidly as a function of distance from the origin of the frequency plane. The noise term—denoted by $\mathcal{F}\{\mathcal{C}\}$ in Equation (2.116)—on the other hand usually drops off much slower or—as in the case of white noise—is constant throughout the frequency plane. Hence, the division by $\mathcal{F}\{\mathcal{S}\}$ will accelerate the noise, which will result in a total information loss.

Again, a variety of filtering techniques is available to obtain a better representation for x than given by $\tilde{x}$. Many of them operate in FOURIER space. Yet, also methods like the family of maximum likelihood algorithms are available [91], which do not rely on FOURIER transforms. A two-dimensional formulation of GOLD's deconvolution algorithms, which is very powerful for one-dimensional data, is also found in the literature [92]. Nonetheless, the majority of filtering techniques is FOURIER-based. The simplest filter allowing for deconvolution of noisy images is the WIENER filter. If the FOURIER transform of a function f is denoted by $\mathcal{F}\{f\} = \hat{f}$, the WIENER filter may be written in shortened form as

$$\hat{\mathbf{I}} = \left[\frac{\hat{\mathcal{S}}^*}{|\hat{\mathcal{S}}|^2 + K}\right] \cdot \hat{\tilde{\mathbf{I}}}, \tag{2.117}$$

where $\hat{\mathcal{S}}^*$ denotes the complex conjugate of $\hat{\mathcal{S}}$ and $|\hat{\mathcal{S}}|^2 = \hat{\mathcal{S}}^*\hat{\mathcal{S}}$. Hence, the WIENER filter circumvents the acceleration of noise by adding a constant K to the PSF, which prevents the division by nearly zero values. The parameter K is tunable; a value of about twice the noise variance ($K = 2\sigma^2$) is a good practical starting value.

The WIENER filter is optimal in a global sense, because the parameter K acts equally on the whole

frequency plane. Local optimality is obtained by the expansion

$$\hat{\mathbf{I}} = \left[\frac{\hat{\mathcal{S}}^*}{|\hat{\mathcal{S}}|^2 + \gamma|\hat{\mathbf{P}}|^2} \right] \cdot \hat{\tilde{\mathbf{I}}}, \tag{2.118}$$

where $\hat{\mathbf{P}}$ is obtained from some measure of local optimality and $|\hat{\mathbf{P}}|^2 = \hat{\mathbf{P}}^*\hat{\mathbf{P}}$. A possible measure is the smoothness of $\mathbf{I}$. In that case, $\mathbf{I} * \mathbf{P}$ has to be minimized, where

$$\mathbf{P} = \begin{bmatrix} 0 & 1 & 0 \\ 1 & -4 & 1 \\ 0 & 1 & 0 \end{bmatrix} \tag{2.119}$$

is the convolution kernel associated with the second derivative. Hence, $\hat{\mathbf{P}}$ is the Fourier transform of $\mathbf{P}$ padded with zeros to match the size of $\tilde{\mathbf{I}}$. A viable optimization criterion, from which γ can be obtained, is

$$\|\tilde{\mathbf{I}} - \mathbf{I} * \mathcal{S}\|^2 = \|\mathcal{C}\|^2, \tag{2.120}$$

where $\|\mathbf{I}\|^2$ denotes the square matrix norm of $\mathbf{I}$. Generally, γ is adjusted in an iterative manner by choosing a starting guess, calculating $\mathbf{I}$ with Equation (2.118), and adjusting γ according to the optimization criterion (Eq. (2.120)). To evaluate Equation (2.120) some knowledge about $\|\mathcal{C}\|^2$ is required. As $\mathcal{C}$ denotes the split-off image noise, it will have mean zero. Further on, the variance of neutron images is well defined and investigated in detail in Section 2.2.5.2. Hence, the square norm of $\mathcal{C}$ can be estimated by

$$\|\mathcal{C}\|^2 = (M - 1)(N - 1)\sigma^2, \tag{2.121}$$

if σ denotes the standard deviation of the noise, and N and M are the dimensions of $\tilde{\mathbf{I}}$, respectively. This filtering technique is referred to as "constrained-least-square" filter and a detailed derivation is found in [80]. Equation (2.121) is a good measure but not the only constrain that needs consideration. Generally, a low value of γ will cause noise acceleration, because Equation (2.118) approaches the inverse filter (Eq. (2.116)) for $\gamma \to 0$. A large value of γ will bias the high frequency part of the FOURIER transform in a way that the noise is diminished together with a blurring of the image. The blurring originates from a too strong weighting of the smoothness criteria that is associated with a large γ. Hence, it is natural to define the noise acceleration as a second criteria. Mathematically, this leads to

$$0 = \frac{\sigma(\mathbf{I})}{\sigma(\tilde{\mathbf{I}})} - 1 \tag{2.122}$$

as optimality criteria, where $\sigma(\mathbf{I})$ symbolizes the standard deviation obtained from an unstructured part of the filtered image (non-changing area), and $\sigma(\tilde{\mathbf{I}})$ denotes the standard deviation of the same image region as obtained from the unfiltered image. Equation (2.122) always results in a higher value for the optimal γ than Equation (2.120), because geometric improvement is not weighted. Hence, both criteria can be interpreted as boundaries for a range of optimal parameters. If γ is chosen according to Equation (2.120), the blurring will be compensated nearly completely, but the noise level will increase. If γ is obtained by Equation (2.122), the noise level is kept constant, but the blurring is not compensated completely.

The algorithm is exemplified in Figure 2.37. The diagram (a) illustrates the determination of the PSF. The measured profile ($\times$) is obtained from one of the water channel edges of the original image and fitted with a PSF model. The resulting ESF is shown as line. The inset shows the corresponding PSF as surface plot. The determination of the optimal filter parameter γ is illustrated in diagram (b). For larger values of γ, the noise of the filtered image is reduced, which

original image

reconstructed image
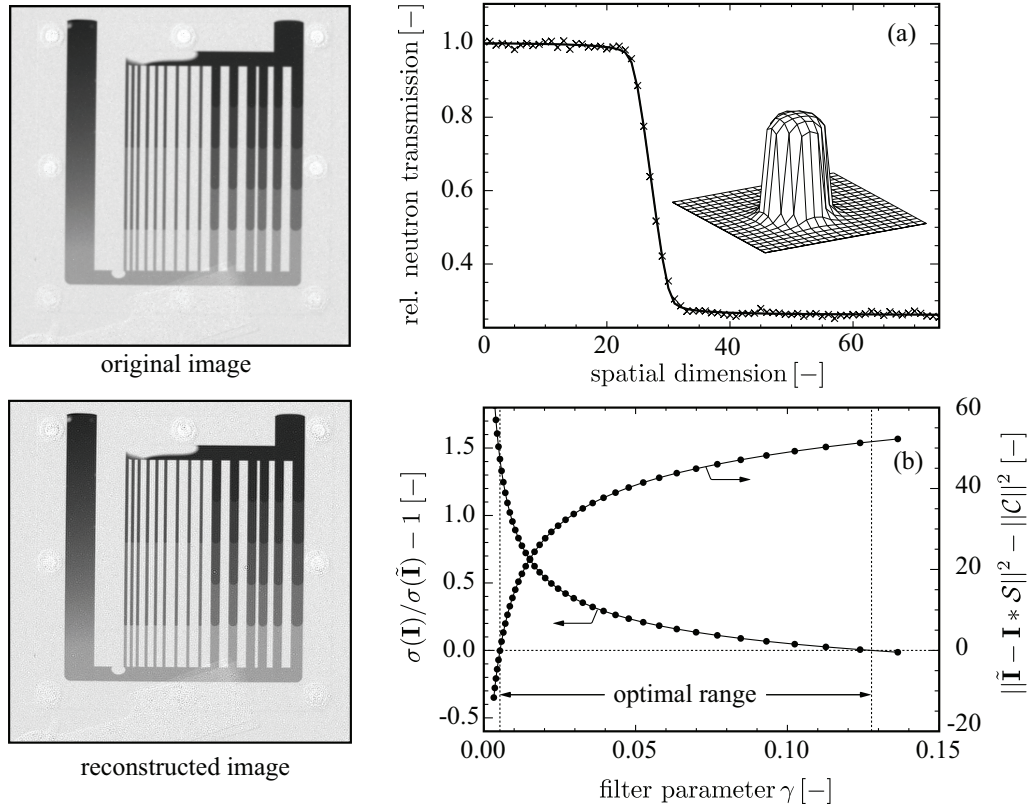
Figure 2.37: Illustration of image restoration with the "constrained least square filter"; the diagram (a) shows the determination of the PSF from an edge response together with the resulting PSF as inset; the determination of the optimal filter parameter according to the equations (2.120) and (2.122) is shown in diagram (b); original and reconstructed image are shown to the left.

results in a negative value of the optimality criteria (2.122). If γ is chosen too small, the noise is strongly amplified and tends towards the results obtained by inverse filtering. Comparison of the images at the left, shows that the reconstructed image is sharper in a qualitative sense. The filter parameter was set according to the middle of the optimal range. Although the visible effect is not very pronounced for the shown test device, the quantitative analysis is strongly affected. This will be shown in detail in the next section.

2.2.7.4 Instrumental broadening and quantification

Quantitative evaluation is significantly influenced by the instrumental broadening, if the feature under investigation is of approximately the same size as the broadening. Because typical flow field structures (channels and ribs) are of about the same size as the broadening, this needs consideration.

Figure 2.38 compares profiles of the relative neutron transmission of water-filled channels with different width but equal thickness. The compared channel widths are 1 mm and 3 mm, respectively. The channels were machined into aluminium blocks. As the thickness of 4 mm is the same in both cases, the neutron attenuation is the same. Ideally, the profiles should be rectangularly shaped and with equal attenuation. Yet, the profiles are blurred due to the instrumental broadening. Furthermore, the apparent attenuation of the smaller channel is much lower than that of the thicker channel (higher values of the relative neutron transmission in the center of the channel). Hence, the amount of liquid within the smaller channel would be underestimated. Fitting of the profiles with two superimposed ESFs allows to estimate the error. The fits are shown as continuous lines. The edge-responses that would result from a single-sided edge are shown as dashed lines.
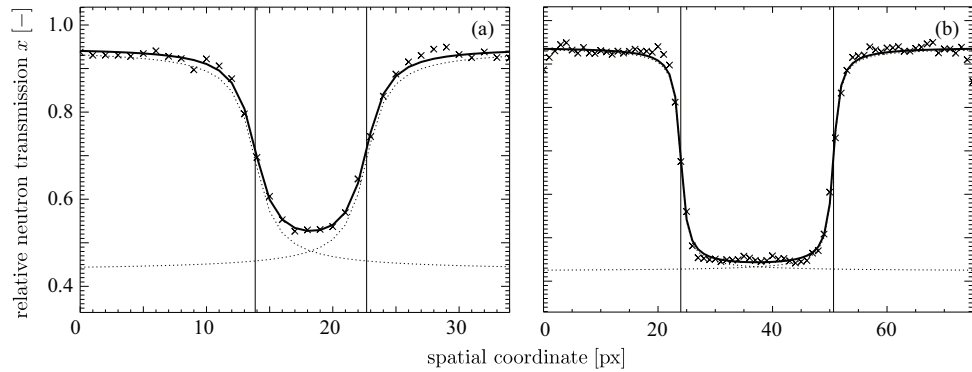
Figure 2.38: Influence of instrumental broadening onto water-filled channels of different width; diagram (a) shows the profile for 1 mm and (b) for 3 mm width, respectively; channel depth is 4 mm; measured profiles are shown by ($\times$), (——) show fitted ESF, and (- - -) shows ESF for a single-sided edge; structuring material is aluminium; the detector is the standard CCD-camera with commercial scintillator; data obtained at NEUTRAs measurement position one.

The relative neutron transmission of these lines far away from the edge corresponds to the true relative neutron transmission caused by the water-filled channels. In the case of the wide channel, the match is quite close, and the calculation of the water layer thickness from the relative neutron transmission would be fairly accurate. By contrast, the attenuation of the smaller channel would be underestimated by roughly 20 %.

The application of the filtering technique described in Section 2.2.7.3 allows to compensate for the instrumental broadening to some extent. This enables a significantly improved quantification of small features as exemplified by Figure 2.39. The Figure compares histograms obtained from an unfiltered and a filtered image of water-filled channels with the histogram obtained from a continuous water layer of the same thickness. The histograms of the structured images show two peaks: one at $x = 1.0$ for the structural material, and one for the water-filled channels at lower values. Naturally, the histogram of the continuous water layer has only one peak. Comparison of the peak positions of the original image with the continuous water layer case shows that the peak is shifted to higher values. As discussed above, this is due to the instrumental broadening. The well agreeing peak positions between the histograms obtained from the filtered image and the image of the continuous water layer are evidence of the improved quantification after filtering. Unfortunately,
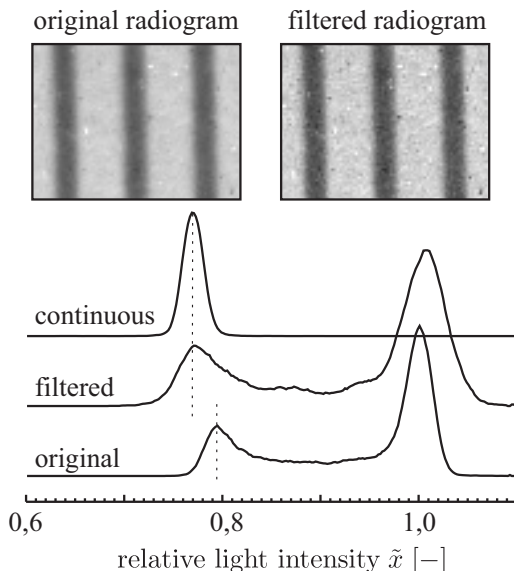
Figure 2.39: Improved quantification of small features by compensating the instrumental broadening with appropriate filter techniques; histograms obtained from unfiltered and filtered images of water-filled channels with 1 mm width and thickness are compared with the histogram of a continuous water-layer of the same thickness; corresponding images are shown above the histograms.

application of the instrumental broadening compensation alters the noise of the images even if the magnitude of the noise is kept constant by choosing the appropriate filter parameter. By this, the noise looses any physical meaning. In consequence, the statistical quantification (cf. Section 2.2.6.3) and broadening compensation are not simultaneously applicable to obtain quantitative information from the images.

2.2.8   Summary

Neutron imaging is a highly suited method for the spatially resolved *in situ* detection of liquid water within polymer electrolyte fuel cells. Being non-invasive, neutron imaging enables the study of two-phase flow phenomena without major interference between the measurement object (i.e., the fuel cell) and the measurement. Being a transmitting technique, neutron imaging provides access to liquid within the porous structures as well as liquid within the flow fields. The possible detection of liquid water within the porous structures is a unique feature separating neutron imaging from other approaches such as the use of transparent flow fields.

Quantitative studies are enabled by proper design of the experimental setup and adequate post-processing. In general, three aspects have to be addressed: the impact of scattered neutrons, the instrumental broadening, and the signal-to-noise ratio. The impact of scattered neutrons, which significantly complicates the interpretation, is mitigated by adjusting the distance between sample and detector (cf. Section 2.2.1.1). As highlighted in Section 2.2.7.4 by investigating water-filled, narrow channels, the instrumental broadening, which is a function of the used detector and facility, has bearings on the quantification, motivating the development of adequate post-processing techniques to compensate the instrumental broadening (cf. Section 2.2.7.3). Likewise, the experimentally achievable signal-to-noise ratio, which is mainly given by shot-noise, requires consideration. Especially, the quantification of liquid water within the porous structures (i.e., the GDLs) is limited by experimental noise. Intending an improved quantification of thin liquid water layers, averaging (cf. Section 2.2.6.2) and statistical quantification (cf. Section 2.2.6.3) were investigated. Though reducing the spatial and/or temporal resolution, both approaches enable the quantification with sufficient accuracy to study flooding of the GDLs while maintaining a sufficient spatial and/or temporal resolution.

Finally, neutron imaging is combinable with other spatially resolving, advanced diagnostics, such as current density measurements (cf. Section 3.3) or local impedance spectroscopy (cf. Section 3.4), and hence complements the suite of diagnostics for fuel cell research.

2.3   Spatially resolved electrochemical measurements

As shown in Chapter 1, the electrochemical current is influenced by temperature, species concentrations, material properties, and reaction characteristics. Either or all of these might change as a function of position in a fuel cell; especially, if the fuel cell is operated under technically relevant operating conditions. Hence, inhomogeneities of either or all these parameters map to the locally generated current. In consequence, measurement of the local electrochemical current generation is a crucial task to develop an understanding of the functional device as a whole. As a variety of processed influences the local electrochemical performance, the separation of different contributions is a logical, desirable extension to the measurement of the local current generation. The dynamic response as obtained by impedance spectroscopy is a well established method to separate processes by their time constant (cf. Section 2.1). Hence, locally applied impedance spectroscopy
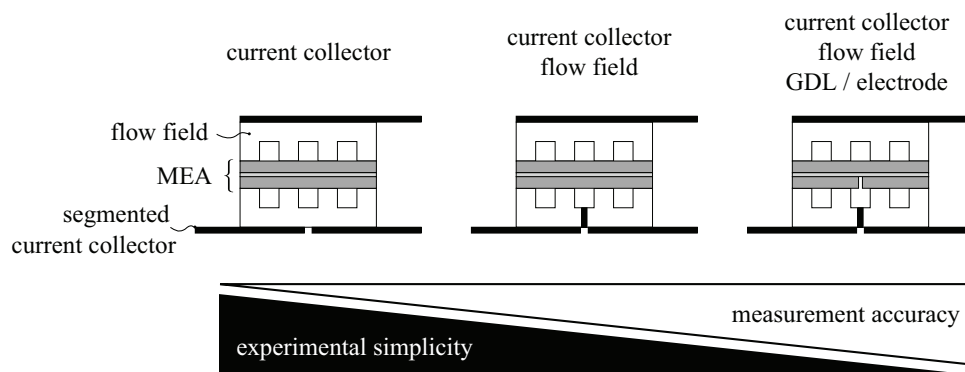
Figure 2.40: Different levels of cell segmentation allowing for tailoring the accuray of current distribution measurements; the compromise between experimental simplicity and accuracy is illustrated.

provides a route to even further understand the complex relation between inhomogeneities and local performance.

2.3.1 Current distribution

As formulated by WIESER [13], the measurement of the current distribution has to fulfill the following requirements to minimize systematic errors:

- No modification of the MEA as current generating component

- Sufficient spatial resolution to map gradients with reasonable resolution

- Applicability to the device independent of operating conditions and without influencing the fuel cell

The majority of approaches realized so far was inspired by techniques that were developed to investigate electrolysis cells. A common characteristic of nearly all locally resolving methods[11] is the need to extract and measure current generated in different areas of the cell separately before the separated currents are combined. This implies the need to segment the fuel cell into electrically insulated parts. As illustrated in Figure 2.40, the level of segmentation might vary and allows for tailoring the accuracy. Electrical insulation of current collector, flow field, and GDL/electrode enables the highest precision, because no lateral currents between the insulated segments are possible. Unfortunately, this configuration requires an elaborate cell design and handling. Especially, the alignment of the components is critical. The segmentation of flow field and current collector can be seen as a compromise between experimental simplicity and accuracy. Yet, the outer measurement circuit requires careful design in order to minimize lateral currents over the GDL. This requirement is even more stringent, if only the current collector is segmented. This experimentally simplest setup—from the cell design point of view—has the highest tendency to allow lateral currents, because current can be exchanged between segments over GDL and flow field.

2.3.1.1 Selected cell segmentation techniques

Printed circuit board. This approach, which was first applied to PEFCs by CLEGHORN et al. [93], comprises a segmented printed circuit board (PCB) into which the flow field structure is

---

[11]The exception is magnetotomography (see the end of Section 2.3.1.3)
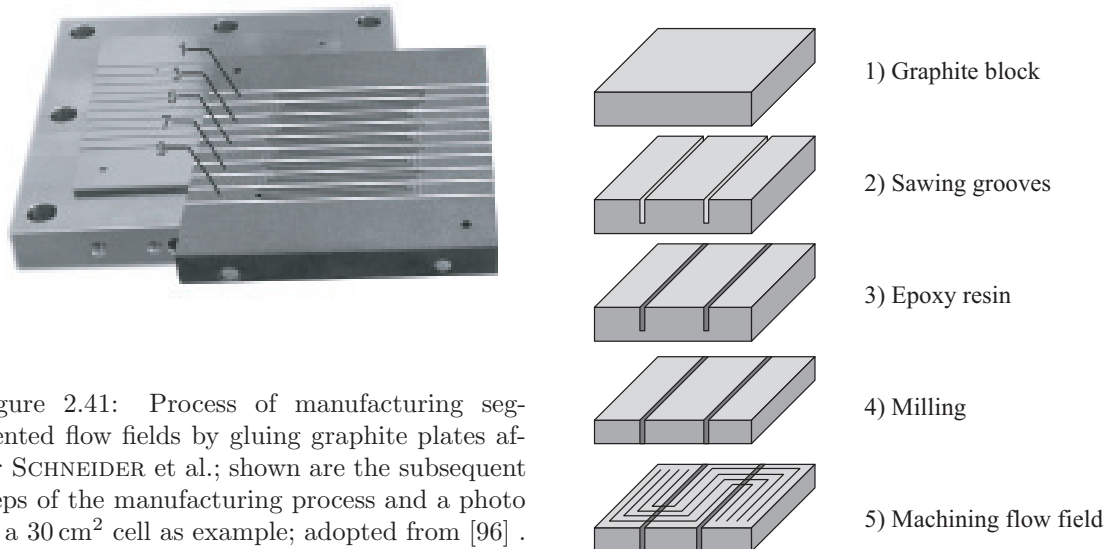
Figure 2.41: Process of manufacturing segmented flow fields by gluing graphite plates after SCHNEIDER et al.; shown are the subsequent steps of the manufacturing process and a photo of a 30 cm^2 cell as example; adopted from [96] .

machined. A PCB with isolated copper segments in the desired configuration was first fabricated, the flow field structure was machined into the PCB, and the copper segments were gold plated to provide a good corrosion resistance. Their cell configuration was fully segmented, meaning that they segmented the GDL and electrode as well. A refinement of the PCB-based approach was presented by SCHÖNBAUER et al. [94]. They replaced the copper segments by a non-conductive matrix with plated-through holes. This enables a higher flexibility, because several different flow field structures are realizable with the same base plate design. A general disadvantage of these approaches is the use of copper. The used copper is shielded from the electrochemical active components by a thin gold plating only. If this coating is not completely tight, copper ions might migrate into the MEA over time, which either poisons the electrodes or damages the membrane by exchanging protons.

Glued flow fields. Another segmentation approach was first presented by BENDER et al. [95]. They manufactured a segmented flow field by placing graphite segments in a polyetherimide frame using a two-component epoxy for sealing and attachment. The current collector, the GDL, and the electrode were segmented as well. The exclusive use of materials common for non-segmented cells is the main advantage of this configuration.

A similar technology was developed by GEIGER et al. [97] and improved by SCHNEIDER et al. [96] at PSI. They developed a method to segment graphite-made flow fields by sawing grooves in a plate, which are subsequently filled with a Epoxy resin. Afterwards, the base is milled until no electrical connection between the segments remains. In a final step, the flow field structure is machined into the segmented graphite plate. The process is illustrated in Figure 2.41. This technology is especially attractive for manufacturing cells that are suitable for neutron imaging, because the thickness of the flow field plate is easily adjustable by the milling process. The thickness of the plates is limited by the structural integrity of the glued segments. If the plate thickness is reduced too much, the adherent surface becomes too small to withstand the mechanical stress (e.g. introduced by cell heating due to slightly different coefficients of expansion) during operation. Nonetheless, a thickness that allows sufficient neutron transmission can be realized, and the investigations shown in the Sections 3.4 and 3.5 utilize this type of segmented flow field.

A variation of the glued flow field concept was realized by MENCH et al. [98]. In order to construct a segmented flow field, they embedded forty eight gold-plated stainless steel ribs into a polycarbonate
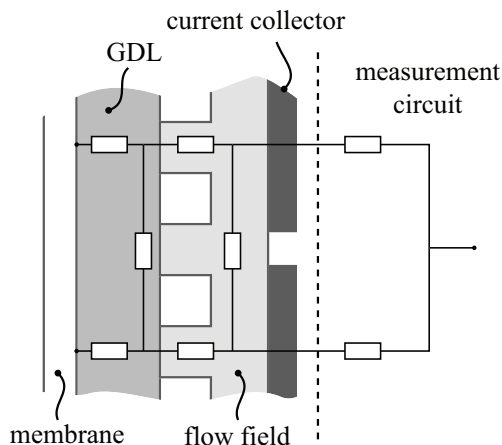
Figure 2.42: Illustration of the formation of lateral currents in semi-segmented cells and simplistic modeling by electrical circuits.

slab. The ribs were arranged to produce a single-pass serpentine structure. However, this concept lacks the flexibility to construct flow field geometries other than single-pass serpentines.

2.3.1.2 Semi-segmented cells and lateral currents

If GDL and/or flow field are not segmented, the current passed to the measurement circuit of a segment might be different from the current generated by the electrode within the area governed by the segment due to lateral currents. Lateral currents are caused by different electrical potentials within adjacent segments of the current collector. This is illustrated in Figure 2.42 by a simplistic electrical circuit representation. The potential is fixed behind the current measurement where the segment currents are combined. If the resistance of the measurement circuit is large, differences of the segment currents will result in different potentials in the upper and lower current collector segment. Depending on the lateral resistances and geometric configuration, a current will flow between the segments through flow field and GDL. Hence, a minimal resistance of the measurement circuit including contact resistances is crucial for minimizing lateral currents.

In order to obtain an estimate for the error induced by lateral currents, it is helpful to approximate flow field and GDL by a continuous potential field and calculate the dispersion of sample current distributions at the electrode side. This means that the structure that is formed by the channels is neglected in this first order approximation. A suitable current distribution is a step-like change of the current density from a value j^* to zero in the middle of the gap formed by the current collector segments. The geometry on which the POISSON equation is solved with appropriate boundary conditions is shown in Figure 2.43. The potential field is given by

$$0 = \partial_{x,x}\varphi + \tau \cdot \partial_{y,y}\varphi \tag{2.123}$$

due to charge conservation. Herein, φ denotes the electric potential and $\tau = \sigma_y/\sigma_x$ accounts for
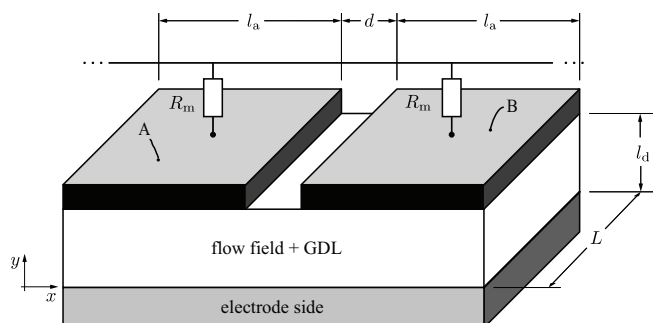
Figure 2.43: Computational domain for the estimation of lateral currents in semi-segmented cells.

a possible anisotropy of the electric conductivity. For computational reasons, it is worthwhile to transform Equation (2.123) into a dimensionless form by changing variables according to

$$\varphi' = \varphi \cdot \frac{j^* \cdot d}{\sigma_y}, \quad y = d \cdot y' \quad \text{and} \quad x = d \cdot x', \tag{2.124}$$

where d is the gap width formed by the current collector segments. The boundary condition for the electrode facing side of the computational domain is given by OHM's law:

$$x \in [0...l_a + d/2], y = 0 \quad : \quad \sigma_y \cdot \partial_y \varphi = j^* \rightarrow \partial_{y'} \varphi' = 1 \tag{2.125}$$

$$x \in]l_a + d/2...2l_a + d], y = 0 \quad : \quad \sigma_y \cdot \partial_y \varphi = 0 \rightarrow \partial_{y'} \varphi' = 0 \tag{2.126}$$

Boundary conditions for the left and right edge of the computational domain are found by symmetry considerations:

$$\partial_x \varphi = 0 \rightarrow \partial_{x'} \varphi' = 0 \tag{2.127}$$

Likewise, the boundary condition for the gap area is given by

$$\partial_y \varphi = 0 \rightarrow \partial_{y'} \varphi' = 0, \tag{2.128}$$

because there current is not allowed to pass the boundary of the computational domain. The boundary conditions for the current collector area need some consideration. Because all the current that is collected within one segment needs to pass the measurement circuit, the potential of the current collector segments, which by itself are considered equipotential, might differ. If the common potential behind the measurement circuit is arbitrarily chosen as reference point (zero potential), the potential at the edge of any current collector is given by

$$\varphi_{A,B} = R_m \cdot I = R_m \cdot L \int_{A,B} j \cdot dx = -R_m \cdot L \cdot \sigma_y \int_{A,B} \partial_y \varphi \cdot dx, \tag{2.129}$$

where L is the length of a current collector segment. With the definition of the parameter κ by

$$\kappa = R_m \cdot L \cdot \sigma_y \tag{2.130}$$

Equation (2.129) reads in dimensionless form

$$0 = \varphi'_{A,B} + \kappa \int_{A,B} \partial_{y'} \varphi' \cdot dx'. \tag{2.131}$$

Under ideal conditions, all current would pass through segment A. Hence, the current passing through segment B for a given configuration resembles the lateral current error associated with a step-like change of the current density distribution. This can be calculated from

$$\frac{I}{I^*} = \frac{1}{l_a/d + 1/2} \int_B \partial_{y'} \varphi' \cdot dx'. \tag{2.132}$$

The problem is self-similar for the following set of parameters: κ, τ, l_a/d, and l_d/d, which means that either combination of geometric lengths and material properties that yields these parameters results in the same lateral error I/I^*.

To illustrate the calculation, the potential field and current densities resulting from a typical set of parameters is shown in Figure 2.44. The total current collected by segment A is much larger than
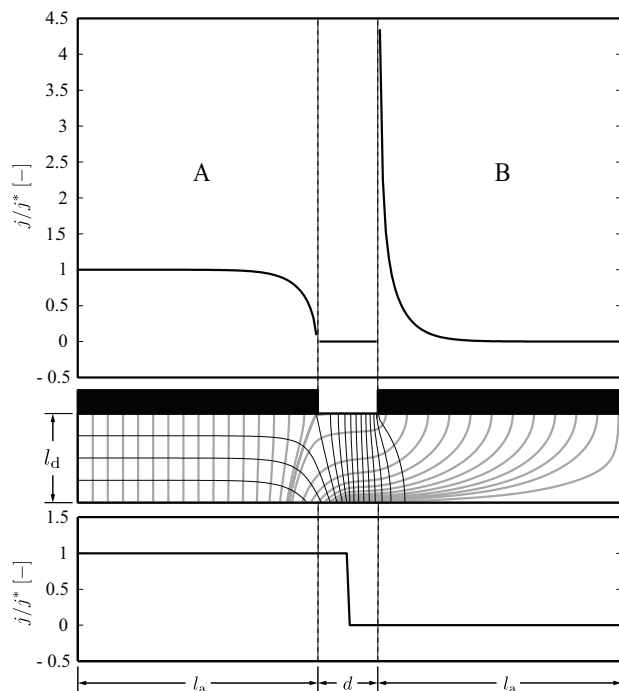
Figure 2.44: Example of the potential field and current distribution in the flow field/GDL of semi-segmented cells; the potential field is shown as contour plot in the middle; the current density at the collector side is shown in the upper plot, and the current density at the electrode side is shown below the contour plot; the parameters for the shown example are: $\kappa = 0.5$, $\tau = 1$; $l_a/d = 4$, $l_d/d = 0.5$.

that of segment B. Hence, the potential near this edge is higher than near the edge of the current collector B. Due to this potential difference, some of the current introduced at the electrode side is directed towards the collector B. Most of the current collected by B is reaching the collector near the gap (shortest way). This results in a rather high current density near the gap, which fades away to zero with increasing distance from the gap. The opposite is true for the current density at the edge of collector A. Far away from the gap, the current is undisturbed and the current density is equal to the current density that is introduced at the electrode side. Near the gap, the current density is diminished, because some current from the electrode side area facing A is flowing towards B due to the larger potential difference.

The lateral error as function of κ is shown in diagram (a) of Figure 2.45 for an isotropic electric conductivity and an anisotropy[12] of $\tau = 5$. For the given set of geometric parameters, $\kappa \leq 2.5$ is needed to reduce the lateral error to less than 10 %, if the flow field material is anisotropic. For the isotropic case, $\kappa < 0.5$ is required to achieve a similar accuracy. Being highly sensitive towards κ, the lateral error increases rapidly with increasing κ. From Equation (2.130), it becomes obvious that a small κ can be achieved by minimizing the resistance of the measurement circuit, choosing a

---

[12]A high anisotropy of the electric conductivity is usually found for carbon-based flow field materials; e.g., the value of $\tau = 5$ resembles SGL Sigracet BMA5 [99], which is a common flow field material.
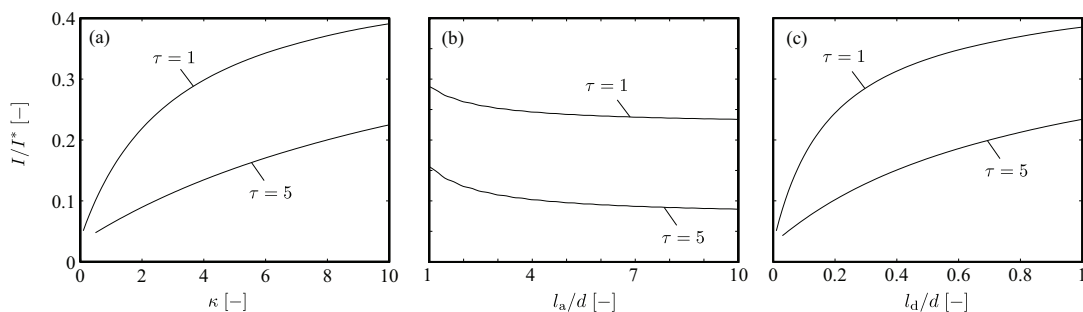
Figure 2.45: Parameter sensitivity of the lateral current error in semi-segmented cells; the variation of κ is shown in diagram (a), the variation of l_a/d in (b), and the variation of l_d/d in (c), respectively; non-changed parameters are $\kappa = 2.5$, $l_a/d = 4$, and $l_d/d = 0.2$.

flow field material with rather low electric conductivity, or minimizing the length of the segments.

An increase of the ratio l_a/d results in a moderate error reduction as seen in diagram (b). If the ratio is larger than about four, the error is nearly constant. On the other side, as illustrated by diagram (c), changing the thickness of the flow field (i.e., changing the ratio l_d/d) allows for a considerable reduction of the lateral error.

From the diagrams of Figure 2.45 it can be inferred that an anisotropic material bears nearly no improvement in terms of minimizing the lateral current compared with an isotropic material of equal conductivity in lateral direction. If the anisotropic material is characterized by $\kappa = 5$ and $\tau = 5$, the corresponding isotropic material would be represented by $\kappa = 1$, because the through-plane conductivity is reduced by a factor of five, and $\tau = 1$. It becomes apparent from diagram (a) that in both cases nearly the same lateral current is expectable.

Generally, it can be concluded that a lateral error of about $10\,\%$ to $15\,\%$ is reasonably achievable, if the measurement circuit is carefully designed and an appropriate material choice is made. For example, a conductivity of $\sigma_y = 5\,\text{S/mm}$ together with a measurement circuit resistance of $R_m = 10\,\text{m}\Omega$ and a segment length of $50\,\text{mm}$ results in $\kappa = 2.5$, which yields an error of $10\,\%$ in the anisotropic case for the geometric parameters given in Figure 2.45. In many situations, the geometry—meaning l_a and L—is more or less defined by the flow field structure and therefore not adjustable in order to minimize the lateral currents. However, the flow field thickness should be reduced as much as the mechanical integrity allows[13].

Finally, it should be mentioned that larger potential differences have to be avoided even if lateral currents are inhibited by full segmentation. Otherwise, the influence of the measurement onto the cell operation will be too strong for comparing the results with unsegmented cells, and the obtained results loose significance.

2.3.1.3 Current distribution measurement technologies

The vast majority of current distribution measurements carried out so far utilized segmented or semi-segmented cells. The experimental setup for current distribution measurements is completed by combining the segmented or semi-segmented cell with a suitable current measurement hardware. Three different concepts are popular in the literature:

- Measurement of the segment currents by a shunt array

- Measurement of the segment currents by a Hall sensor array

- Individual control of the segments by a multi-channel potentiostat

A common aspect of the first two approaches is the operation with a single, conventional load connected to the cell, and the segment currents are measured without actively controlling any of the segments individually. Introducing virtually no additional resistance, Hall sensors are generally favorable in comparison to shunts[14] due to the requirement of the lowest possible resistance of the measurement circuit. This concept was first applied to PEFCs by WIESER et al. [100] and was utilized in PEFCs studies several times by others in adopted form [95, 97, 101]. Nonetheless, shunt arrays are frequently used to measure the segment current [93, 102]. A comparison of this approach with more traditional alternatives is found in the pioneering report of STUMPER et

---

[13]This is also true from the neutron imaging point of view, because thinner flow fields ensure lower attenuation of the structural components.

[14]High precision resistors for current measurements

al. [103]. Circumventing the need to minimize the electrical resistance of the measurement circuit, the use of a multi-channel potentiostat allows controlling the potential of each segment individually. Unfortunately, this approach implies a rather elaborate and expensive setup compared to the passive current measurements. In addition, the cell cannot be operated galvanostatically, which significantly complicates stochiometric operation. Nonetheless, this concept is frequently employed [53, 98, 104–107].

A novel approach to measure current locally resolved was reported by HAUER et al. [108]. They measured the magnetic field around a complete fuel cell by displacing a sensor via a four-axis positioning system. In similarity to other tomography methods, the current density is calculated from the magnetic field data by inversion of a matrix equation. Because the technique does not rely on cell segmentation and is non-invasive, it bears a high attractiveness. The communicated results, however, show only a qualitative agreement with validation data obtained with the segmented cell approach.

2.3.2 Electrochemical impedance spectroscopy

Once the local current generation is characterized, knowledge about the local electrochemical performance is obtained. Yet, the processes contributing to the actual local characteristic are not separated. Hence, it is a logical step to apply impedance spectroscopy on a local scale to obtain further insight. A segmented cell—similar to those applicable for current distribution measurements—is connected to a multi-channel control and measurement hardware. Each segment is perturbed by a small sinusoidal and the local perturbation response is measured. Weather voltage or current is the perturbing signal depends on the actual measurement hardware. In any case, the local impedance is formed by the ratio

$$Z_s(\omega) = \frac{\delta U}{\delta I_s}, \qquad (2.133)$$

where δU and δI_s are the complex-values FOURIER-transform of the cell voltage and segment current, respectively. Usually, the cell hardware is segmented on only one side, and the sum current is fed back to the measurement and control hardware.

The first measurements of local impedance spectra of a PEFC utilizing a segmented cell were reported by BRETT et al. [109] and KUHN et al. [110] in 2003. While BRETT utilized a rack of loads to control each segment individually, KUHN expanded upon an available current density measurement hardware [97] by applying a single current perturbation with a commercial impedance device and measured the part of the total current perturbation accessing each segment by an array of Hall sensors. Recently, HAKENJOS and HEBLING published first results [106] with an experimental setup similar to that of BRETT.

Significant progress was achieved in 2004 by SCHNEIDER in our group [111]. The realisation of a low impedance current measuring circuit [96] enabled the application of locally resolved impedance spectroscopy to technical cells with an active area of serval hundred square centimeter [112] and hence represents a major advancement compared to the measurement hardware set up by BRETT et al. [109], which is not as easily scaled from small-scale model cells to technical cells. A simplified block diagram of the measurement hardware is shown in Figure 2.46. The segmented cell hardware is connected in series to a conventional load and auxiliary power supply. The load is controlled by a sine wave generator in order to modulate the total cell current. The current passing through each segment is measured individually by an array of Hall sensors. Likewise, the voltage is obtained for each segment to improve the measurement accuracy; although the voltage is virtually equal for all segments, small differences that might occur (some few mV) are respected by this. Both signals
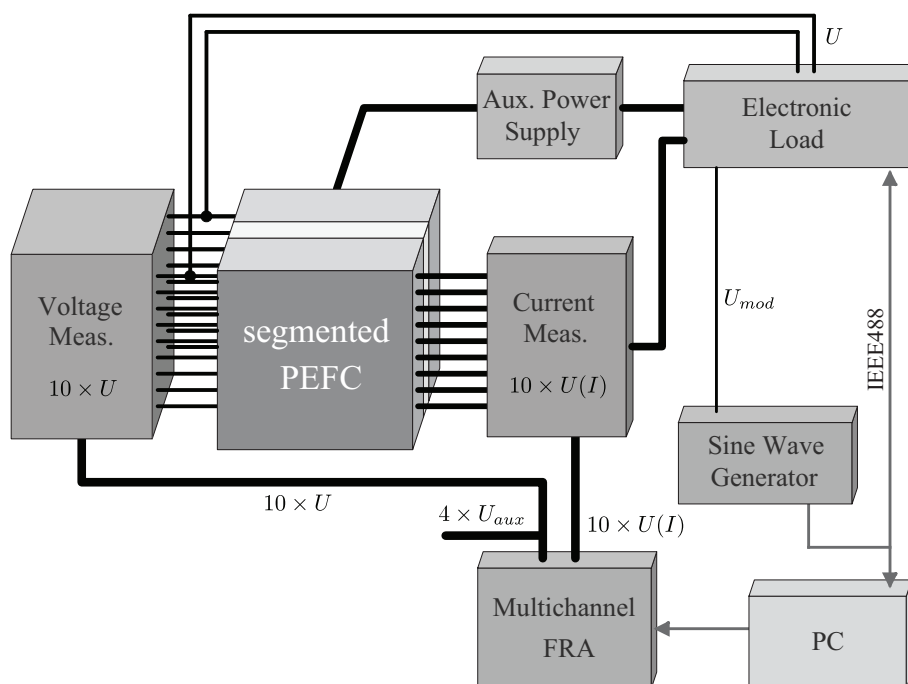
Figure 2.46: Simplified block diagram of the system for fast parallel EIS in PEFCs employing a segmented cell; adopted from [96].

(ac and dc part) are passed to an in-house build multichannel frequency response analyzer and the impedance in amplitude and phase is calculated. The whole setup is controlled by a PC via an in-house made software, which controls the sine wave generator and displays and records the impedance obtained from each segment.

A complete impedance spectrum is obtained by recording a frequency ramp usually ranging from some few mHz to $10\,\mathrm{kHz}$. Though potentiostatic operation is principally possible, the cell is usually operated galvanostatically, and the amplitude and frequency of the current perturbation generated by the load is controlled by the sine wave generator. This setup is characterized by a significantly higher flexibility than that proposed by BRETT, because a scaling to different cell sizes is easily achieved by replacing the load circuit. Further on, the galvanostatic operation, which is not possible with the multi load approach, is another important advantage of SCHNEIDER's approach. A detailed description of the system utilized for the studies related in the Sections 3.4 and 3.5 is found in Ref. [96].

2.4 Reference electrode for DMFCs

Every electrochemical cell comprises two electrodes. Hence, the voltage-current relation obtained from the whole cell contains voltage losses incurred by the processes at both electrodes. In connection with PEFCs, it is often argued that the anodic contribution to the total voltage loss is small compared to the cathodic contribution, because hydrogen is readily oxidized. Although this assumption is debatable under dry conditions, it is a reasonable approximation under humid conditions—especially, if air is used as the cathodic supply. This argumentation cannot be extended to DMFCs, because the oxidation of methanol is a complex reaction and therefore causes voltage losses that are comparable to those incurred by the cathodic oxygen reduction. Hence, a separation of anodic and cathodic voltage losses is highly attractive in order to develop a refined understanding of the cell polarization.
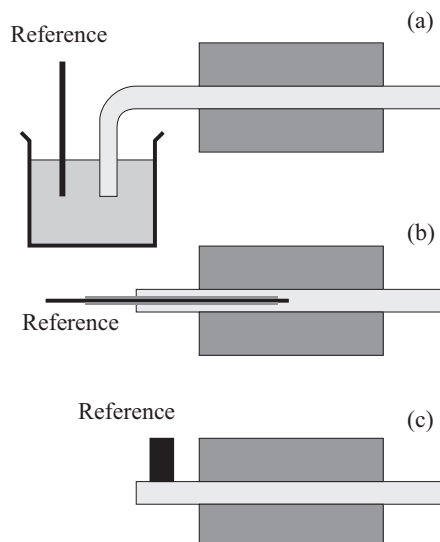
Figure 2.47: Sketch of possible reference electrode placement in a DMFC; (a) shows the introduction of a standard reference electrode via an electrolyte bridge; (b) shows the introduction of a potential probe between the electrodes; (c) shows the placement of a reference at the perimeter of the cell.

To achieve this, a third electrode is introduced into the system. Ideally, this electrode provides a stable and reproducible reference potential against which the potential of each electrode is probed separately. Three principles are sketched in Figure 2.47. The setup shown in (a) comprises a standard electrode, which is connected to the solid electrolyte of the fuel cell by a liquid electrolyte bridge [113]. The applicability of well characterized standard reference electrodes is the main advantage of this approach. The main drawback stems from the necessity to pass the electrolyte out of the cell hardware, where the solid electrolyte has to be wetted in order to maintain a sufficient conductivity. Further on, the effect of Donnan-potential (liquid/membrane junction potential) has to be accounted for [114]. Further on, this setup is influenced by the same geometric effects that are discussed in Section 2.4.2 as setup (c). The configuration shown in (c) circumvents the need to extract the electrolyte potential from the cell by placing a reference at the perimeter of the fuel cell. This reference is operated such that a reliable potential is formed; usually, a reversible hydrogen electrode (RHE), or a dynamic hydrogen electrode (DHE) is favored. However, a reliable measurement requires the compensation of artifacts incurred by the geometric configuration. This is discussed in Section 2.4.2. The design depicted in (b) bears the advantage of probing the electrolyte potential directly between the electrodes. This is achieved by placing a potential probe between two membranes. This potential probe, which consists of thin graphite or gold wires, is insulated with exception of the tip. The diameter of the probe has to be small compared to the thickness of the electrolyte. This is not easily achieved, because common electrolytes may be as thin as $30\,\mu$m. Hence, the introduction of a real reference electrode is highly complicated, and normally the potential is probed by a simpler "pseudo-reference"—an electrode that provides a stable yet not precisely defined potential. Recently, remarkable insights into the single electrode characteristics of PEFCs could be obtained by KUHN et al. [47,50] by following and improving this approach. However, this setup requires the stacking of two electrolytes, which is a considerable adaption of the MEA and hence an intrinsic short-coming.

The perimeter-placed reference electrode configuration is favorable for DMFC investigations, because an electrode providing a reliable (normalizable) potential can be realized, and edge effects can be minimized due to the relatively thick electrolytes utilized in DMFCs. This will be explored in detail within the following sections.
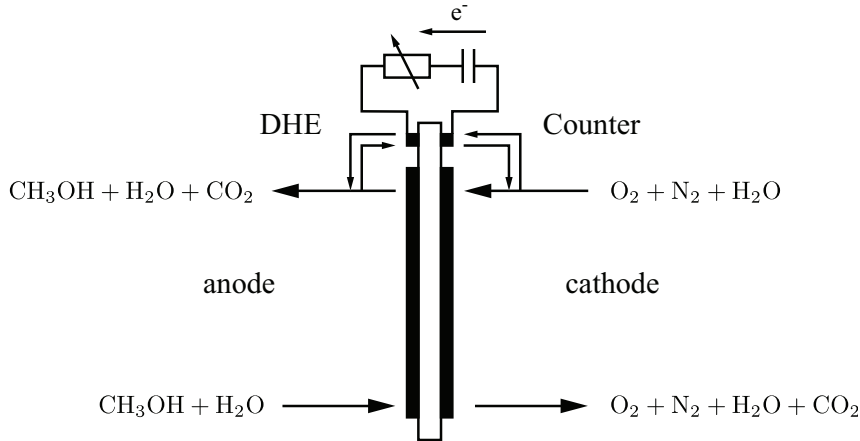
Figure 2.48: Schematic sketch of the experimental setup comprising a DHE and its counter electrode at the perimeter of a DMFC.

2.4.1 Reliability of the dynamic hydrogen electrode within a DMFC

The configuration of a dynamic hydrogen electrode (DHE) is depicted in Figure 2.48. The DHE is a hydrogen evolving porous Pt electrode, which is connected to a counter electrode via a potentiostat. Both electrodes, are placed at the perimeter of the DMFC opposing each other. A small percentage of the main feed is redirected from the flow fields and is passed over the active area of the DHE and its counter electrode, respectively. On the anodic side, this ensures the removal of the generated hydrogen. On the cathodic side, a sufficient hydration of the electrolyte is ensured.

Potential stability against methanol. The DHE current and the associated evolution rate of hydrogen according to

$$2H^+ + 2e^- \longrightarrow H_2 \tag{2.134}$$

has to be sufficiently large to minimize the accessibility of methanol to the electrode. If methanol accesses the DHE, a CO-like adsorbate is readily formed. This has a considerable impact onto the DHE potential as can be concluded from Figure 2.49. The depicted polarization curves where obtained by measuring the voltage difference between DHE and it's counter electrode as function of the DHE current. Both electrodes, which were circularly shaped with a diameter of 4 mm, consisted of Pt-black (unsupported porous Pt) electrodes with an precious metal loading of 4 mg/cm^2. They were incorporated at the perimeter of a 30 cm^2 single cell DMFC with a single-channel serpentine flow field. Because the cathode was flushed with hydrogen, the DHE and counter electrode operate
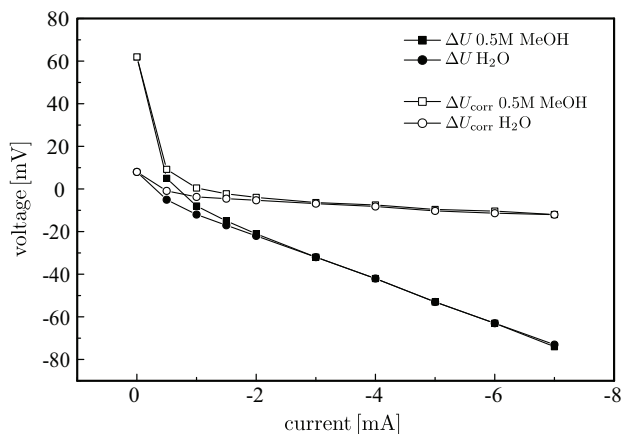
Figure 2.49: Potential of the DHE against the hydrogen flushed counter electrode as function of the DHE current; the cell is operated at 90 °C and 2 bar(a) on both sides; the cathode is flushed with 500 ml/min H$_2$; the anode is supplied with 20 ml/min H$_2$O or 0.5 M methanol solution, respectively.
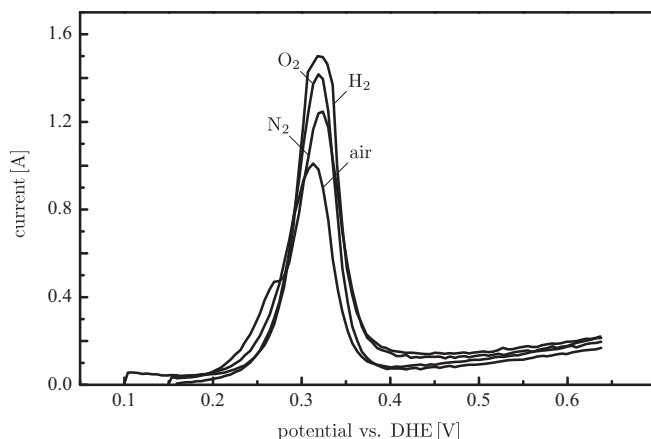
Figure 2.50: Stripping voltamograms of the anode for various cathodic supply gases showing a negligible influence of the cathodic supply onto the DHE potential; anodic potential measured against DHE; the cell is operated at 90 °C and 2 bar(a); sweep-rate is 10 mV/s.

as a "hydrogen-pump": hydrogen is oxidized at the counter electrode, and the resulting protons are recombined to hydrogen at the DHE by reduction. The polarization curves as obtained are shown by (●) and (■), respectively. The IR-corrected polarization curves are shown by (○) and (□), respectively. The ohmic resistance was measured by obtaining the high frequency impedance at 10 kHz. The curves obtained with 0.5 M methanol solution and water coincide for DHE currents larger than about 3 mA. As expected, a considerable voltage difference is observed for smaller currents, because methanol poisons the DHE. Nonetheless, the DHE current should be chosen as small as possible, because otherwise the ohmic resistance of the electrolyte influences the DHE potential strongly. Because the electrolyte resistance might change as a function of the operating condition, this is a source of uncertainty which should be kept as small as possible.

Potential stability against the cathodic supply. In addition to the stability of the DHE potential against methanol, the stability against different cathodic supply feeds has to be investigated. This is not as strait forward as the proof of the methanol tolerance, because the cathode has to be supplied with different gases. Hence, no a priori well-defined potential is available at either electrode (anode, cathode, or counter) to validate the DHE potential. However, stripping voltametry provides an indirect measure. If the anode is fixed at a potential of about 150 mV vs. RHE, methanol is readily dehydrogenized to $(CO)_{ads}$ or similar adsorbates, which form a stable mono-layer at the anodic active surface (cf. Section 1.3.2.3 on page 14). This adsorbate layer can be preserved, while the anode is flushed with water, if the anode potential is kept constant during the removal of excess methanol. Afterwards, a positive potential sweep results in an increase of current, because the adsorbate is oxidized after a critical potential is passed. Yet, oxidation can only occur as long as adsorbed species are available. Consequently, the current will not increase unbounded with increasing potential but will nearly drop to zero after passing a peak due to the lack of adsorbates. The generated charge is a measure for the amount of bound adsorbates and might, therefore, be used to evaluate the active surface of the anode (cf. Section 4.3.3.1). However, the position of the peak is of relevance here. If this stripping is repeated while the cathode is supplied with different gases, a change of the current peak position would be indicative for a shift of the DHE potential. The stripping voltamograms obtained from a DMFC with an active area of 30 cm² are depicted in Figure 2.50. The cell was operated at 90 °C and 2 bar(a). After poisoning the electrode with 0.5 M methanol, the excess methanol was removed by flushing the anodic compartment for 20 min with water. During this, the anode was held at a constant potential of 150 mV measured against the DHE. Afterwards, the adsorbate layer is oxidized by a positive potential sweep up to 650 mV. It can be concluded from the well agreeing peak positions that a variation of the cathodic supply bears no significant implications onto the DHE potential.
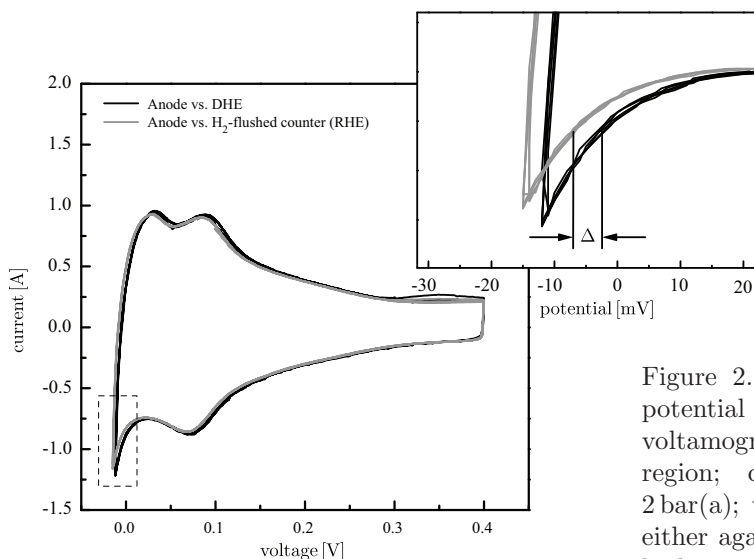
Figure 2.51: Normalization of the DHE potential by measuring the shift of cyclic voltamograms obtained in the H-UPD region; cell is operated at $90\,°C$ and $2\,bar(a)$; the anodic potential is measured either against the DHE or the current-free hydrogen-flushed counter serving as RHE; sweep rate is $25\,mV/s$.

Normalization of the DHE potential. Because the effective DHE potential is influenced by the ohmic drop of the electrolyte and the kinetics of the hydrogen evolution, the potential obtained from different cells might be slightly different (some few to some ten mV). Also a drift of the DHE potential with time, incurred by a degradation of the DHE, cannot be excluded. Hence, a normalization to a more well-defined potential is desirable. A modus operandi similar to that utilized in the last section allows to measure the DHE potential against a RHE. Although stripping voltametry would be applicable, a faster procedure is the measurement of the hydrogen under-potential deposition (H-UPD). The H-UPD causes a characteristic cyclic voltamogram (CV) of Pt and Pt-alloy electrodes near the reversible hydrogen potential [19, 22, 115]. If the cathode is supplied with hydrogen, the current-free counter electrode might serve as RHE. Hence, a shift of CVs obtained by probing the anode potential either against the DHE or the hydrogen-flushed current-free counter electrode allows estimating the DHE potential relative to the RHE potential. This is exemplified in Figure 2.51, where two CVs showing the H-UPD region are compared. The CV shown in grey was recorded by probing the anodic voltage against the hydrogen-flushed, current-free counter electrode. In this way, the counter electrode operates as RHE and hence provides a standard potential. The black CV was recorded by taking the DHE as reference. Both CVs are similar, yet the grey CV is shifted slightly towards lower potentials. The shift is shown more clearly in the inset of Figure 2.51, where the region enclosed by a dashed box is magnified. The black CV is shifted towards positive potentials, because the DHE is more negative than the RHE; hence, the voltage difference between DHE and anode is larger than between RHE and anode for the same anodic potential. This results in a positive shift of the potential. As can be seen, the shift is rather small ($< 10\,mV$ in the shown example). Depending on the ohmic drop resulting from the DHE current, the DHE usually has a potential that is some ten millivolts lower than the corresponding RHE potential.

2.4.2 Edge effects

Primary current distribution. Figure 2.52 displays the electrolyte potential Φ near the electrode edges under idealized conditions: a perfect placement of the electrodes and isotropic conductivity of the electrolyte. Further on, it was assumed that the ionic potential in front of the electrodes is uniform, which is known in literature as primary current distribution [116]. With
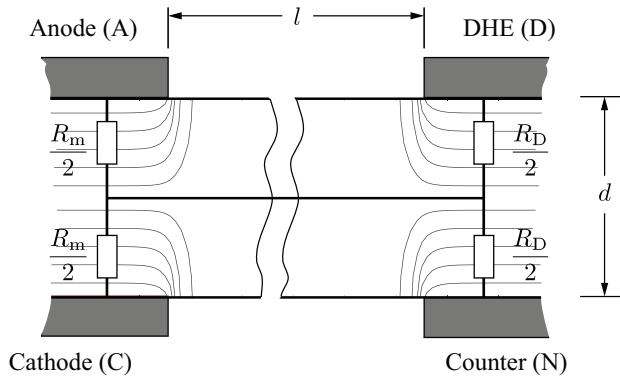
Figure 2.52: Sketch of the ionic potential within the electrolyte for perfectly aligned electrodes and simplistic electric circuit representation.

these assumptions, the potential field is given by the POISSON equation

$$\nabla^2 \Phi = 0 \tag{2.135}$$

with the boundary conditions

$$\Phi = const. \text{ on } A, C, D, N \quad \text{and} \quad \partial_y \Phi = 0 \text{ elsewhere.} \tag{2.136}$$

Under these conditions, the voltage between anode and DHE is given by

$$\Delta U|_\mathrm{D}^\mathrm{A} = \Delta\varphi_\mathrm{A} + \Delta\varphi_\mathrm{D} + \frac{1}{2} \cdot \rho \left[j + j_\mathrm{D} \right], \tag{2.137}$$

where $\Delta\varphi_\mathrm{A}$ and $\Delta\varphi_\mathrm{D}$ denote the potential difference between electronic and ionic phase (cf. Section 1.3.2 on page 11) at the anode and DHE, respectively. The specific resistance of the electrolyte is symbolized by ρ, The current density passing between anode and cathode is given by j, and j_D denotes the current density applied to the DHE. Because the potential field opens symmetrical at the perfectly aligned edges, half of the ohmic drop between anode and cathode is included in the voltage difference between anode and DHE. This is easily expressed by an equivalent circuit, which is likewise shown in Figure 2.52.

If the electrodes are not perfectly aligned, the field will open asymmetrically near the edges. This means that the ionic potential at the perimeter is not matching the potential in the middle between anode and cathode. In consequence, the ohmic drop included in the voltage difference between
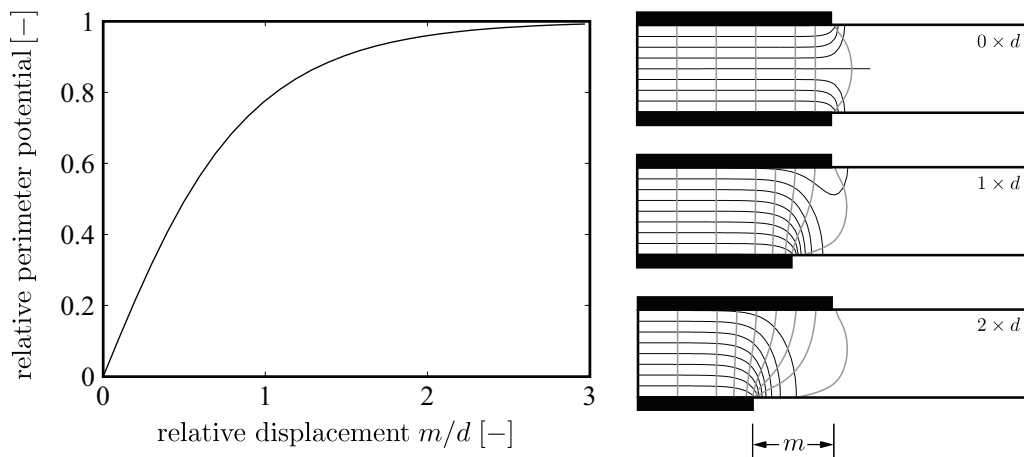
Figure 2.53: Influence of the electrode placement onto the field opening near the edges; the diagram shows the relative shift of the perimeter potential as function of the electrode misplacement; selected potential distributions are shown at the right.

anode and DHE is not exactly half the total ohmic drop. Yet, in the primary current distribution approximation, the perimeter potential is bounded to be between the ionic potential in front of the cathode and in front of the anode, respectively. The dependence of the field asymmetry on the displacement m is shown in Figure 2.53. A displacement of $m/d = 0$ corresponds to perfectly aligned electrodes. A relative perimeter potential of zero is equivalent to the middle of the membrane, and a value of one corresponds to the potential in front of either electrode, meaning that either the total or no ohmic drop between anode and cathode is included in the potential difference between anode and DHE. The calculation reveals a high sensitivity of the field asymmetry with respect to the electrode placement. Already a misplacement of one times the membrane thickness results in a considerable asymmetry. Hence, it can not be assumed generally that half the ohmic drop between anode and cathode enters the difference between anode and DHE.

Secondary current distribution. A major simplification that leads to the primary current distribution is the negligence of any kinetic influence by assuming the ionic potential to be constant in front of the electrodes. A refined model is obtained, if the boundary condition describing the areas that are occupied by electrodes is adopted such that kinetics are respected. Assuming symmetric BUTLER-VOLMER reactions, this leads with Equation (1.31) to

$$\partial_y \Phi = -\frac{j}{\sigma} = -\frac{2 \cdot j_0}{\sigma} \cdot \sinh\left(\frac{\varphi - \Phi}{b} - \frac{\Delta\varphi_0}{b}\right), \tag{2.138}$$

where $\Delta\varphi_0$ is the voltage drop over the double layer at OCV. Further on, Φ and φ denote the ionic potential in front of the electrode and the electronic potential of the electrode, respectively. In resemblance to the argumentation given in Section 2.3.1.2, it is advantageous to reformulate the problem, achieving a dimensionless formulation by the variable transformations:

$$x' = \frac{x}{d}, \quad y' = \frac{y}{d}, \quad \Phi' = \frac{\Phi}{b}, \quad \text{and} \quad \varphi' = \frac{\varphi}{b}, \tag{2.139}$$

where d denotes the thickness of the electrolyte, and b is the TAFEL slope. If the discussion is restricted to symmetrical reactions[15] (same kinetic parameters for anode and cathode), this allows to formulate a single parameter κ describing the kinetics, because

$$\partial_{y'}\Phi' = -\underbrace{\frac{2 \cdot j_0 \cdot d}{\sigma \cdot b}}_{=\kappa} \cdot \sinh\left((\varphi' - \Phi') - \Delta\varphi_0'\right). \tag{2.140}$$

Further on, the geometry is fully described by the ratio m/d, where m denotes the displacement of the electrodes.

To illustrate the difference between primary and secondary current distribution, the potential field and current densities resulting from a certain set of parameters are shown in Figure 2.54. The case of perfectly aligned electrodes is shown at the left-hand side. As for the primary current distribution, the field opens symmetrically and the perimeter potential is the average between the potential in front of the anode and cathode. The current density is slightly increased at both electrode edges. This stems from the fact that the current is able to "spread out" at the edge and hence produces a lower ohmic drop, which results in a current density increase. An example of misaligned electrodes is shown at the right. The current density of the protruding electrode is gradually reduced towards the electrode edge, while the opposite is true for the facing electrode.

---

[15]See [114, 116] for the influence of kinetic asymmetry.
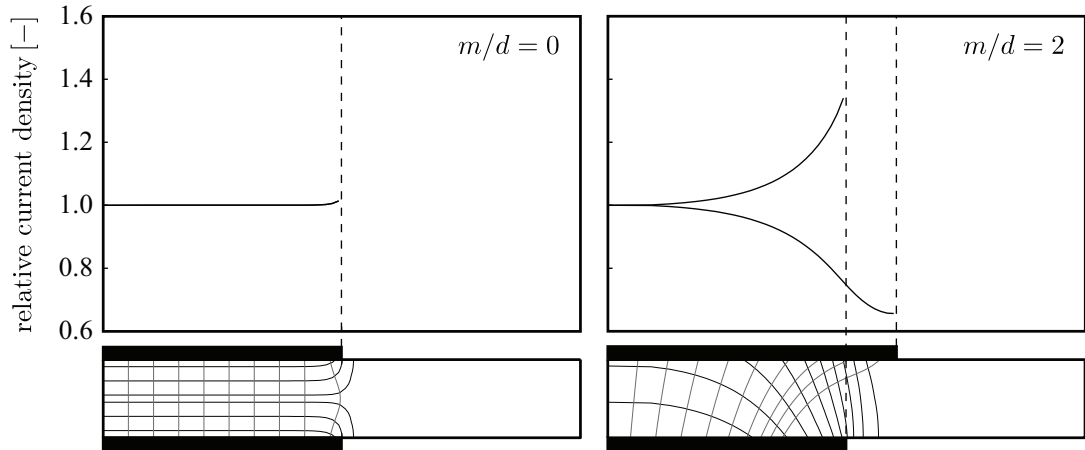
Figure 2.54: Influence of electrode misplacement onto the current density and electrolyte potential field near the edges with secondary current distribution approximation; equal kinetics on both electrodes; kinetic parameter: $\kappa = 0.04$, $\varphi'_C - \varphi'_A = 16$; current density normalized to the current density far away from the edges.

The current density is diminished, because the current has to pass over an increased length to reach the edge of the facing electrode, which implies a higher ohmic drop. The current density at the edge of the facing electrode is increasing, because current from all over the protruding area is collected there. The potential field opens asymmetrically. Yet, in contrast to the primary current distribution the perimeter potentials in not restricted to be between the potential in front of the anode and cathode, respectively. The relative perimeter potential is defined by

$$1 - 2 \cdot \frac{\Phi_A - \Phi_P}{\Phi_A - \Phi_C}, \tag{2.141}$$

where Φ_P denotes the perimeter potential and the potential in front of the electrodes is symbolized by Φ_A and Φ_C, respectively. The sensitivity of the relative perimeter potential towards electrode misplacement is shown in Figure 2.53. The corresponding result obtained from the primary current distribution approximation is shown as thick line for comparison. The perimeter potential is insensitive towards the current density, if the electrodes are precisely aligned. However, even a small misalignment (about half the membrane thickness) leads to a significant shift of the perimeter potential, whereby the sensitivity is stronger at higher cell voltages (lower currents) and approaches the primary case for high currents. Hence, the perimeter potential changes as function of the
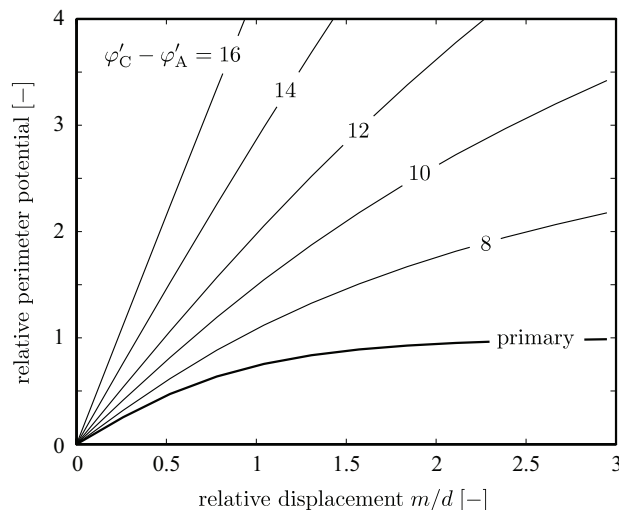
Figure 2.55: The relative perimeter potential as function of the electrode misplacement; the parameter $\varphi'_C - \varphi'_A$ represents the cell voltage, and a lower value results in higher current densities; kinetic parameter: $\kappa = 0.04$.
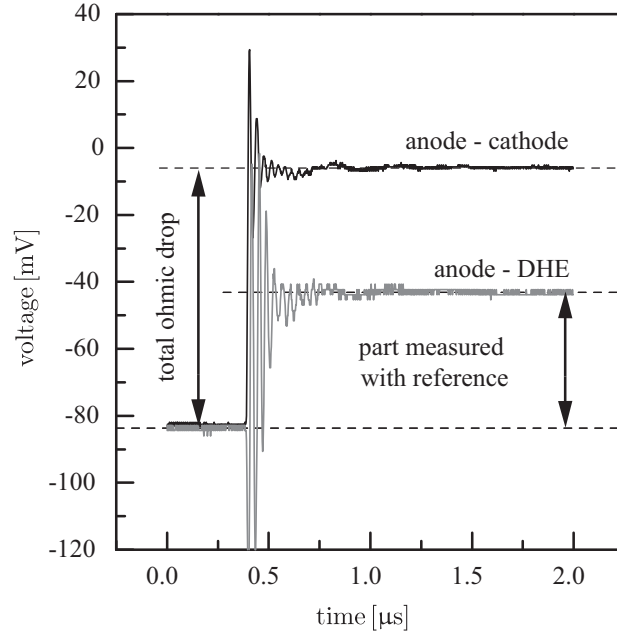
Figure 2.56: Voltage response upon a current step measured simultaneously between anode and cathode and anode and DHE; the active area is $30\,cm^2$; the current step is $5\,A$; the electrolyte is Nafion 117; the DHE has a diameter of $4\,mm$ and is placed at the anodic side.

operating conditions, if the electrodes are significantly misaligned.

In consequence, a reference electrode that is placed at the perimeter of the cell is highly susceptible to edge effects, if the electrodes are misaligned. The perimeter potential—and therefore the DHE potential relative to the anode or cathode—might easily shift several times the ohmic drop. The tendency of potential shifts is diminished with increasing current density. This is beneficial, because the absolute ohmic drop will be larger at higher currents and therefore the same relative perimeter potential would translate to a higher absolute potential shift. However, in order to gain confidence in measurements and enable a viable ohmic compensation, the electrode alignment has to be characterized *in situ* for every cell to ensure that the electrodes are nearly perfectly aligned. Because the ratio of electrode displacement to membrane thickness is critical, it is beneficial that common electrolytes for DMFCs are several hundred micrometer thick. Hence, there is a fair chance to align electrodes with sufficient precision.

2.4.3 Measurement of electrode alignment and ohmic compensation

Unfortunately, it is not possible to probe the perimeter potential directly. The adoption of transient techniques that are applicable to obtain the ohmic drop between anode and cathode (high frequency resistance or pulse techniques) seems obvious. From a mathematical point of view, it is more convenient to investigate the possibility of impedance measurements. Yet, the conclusions derived below are also valid for pulse techniques, because both techniques are FOURIER transform related.

If a sinusoidal voltage perturbation is applied between anode and cathode, the resulting current perturbation of either electrode is given by

$$j + \Delta j = 2 \cdot j_0 \cdot \sinh\left(\frac{(\varphi + \Delta\varphi) - (\Phi + \Delta\Phi)}{b} - \frac{\Delta\varphi_0}{b}\right), \tag{2.142}$$

which for $j \gg 0$ and small perturbation values $\Delta\varphi$ and $\Delta\Phi$ can be approximated by

$$j + \Delta j = j_0 \cdot \exp\left(\frac{\varphi - \Phi}{b} - \frac{\Delta\varphi_0}{b}\right) \cdot \left(1 - \frac{\Delta\Phi}{b}\right) \cdot \left(1 + \frac{\Delta\varphi}{b}\right). \tag{2.143}$$

FOURIER transform and negligence of steady-state and higher order terms leads to

$$\delta j = \underbrace{\frac{j_0}{b} \cdot \exp\left(\frac{\varphi - \Phi}{b} - \frac{\Delta\varphi_0}{b}\right)}_{=1/R_{ct}} \cdot (\delta\varphi - \delta\Phi), \tag{2.144}$$

where δj, $\delta\varphi$, and $\delta\Phi$ denote the FOURIER transforms of the faradaic current, the electric electrode potential, and the ionic potential in front of the electrode. Because the current passed over the electrode interface is the sum of farradaic and double layer current, OHMS law requires that

$$\partial_y(\delta\Phi) = \frac{1}{\sigma}\left[\frac{1}{R_{ct}} + i \cdot \omega \cdot C_{dl}\right] \cdot (\delta\varphi - \delta\Phi). \tag{2.145}$$

holds at the electrodes. Herein, $\omega = 2\pi \cdot f$ is the perturbation frequency and C_{dl} denotes the double layer capacitance. In the high frequency limit ($f \geq 10\,\mathrm{kHz}$), the charge transfer reaction is negligible compared to the double layer charging, and Equation (2.145) simplifies to

$$\partial_y(\delta\Phi) = i \cdot \frac{\omega \cdot C_{dl}}{\sigma} \cdot (\delta\varphi - \delta\Phi). \tag{2.146}$$

Equation (2.146) provides the boundary condition in front of the electrodes for the oscillating part of the potential field inside the electrolyte, which obeys

$$\nabla^2(\delta\Phi) = 0. \tag{2.147}$$

For all other boundaries $\partial_y(\delta\Phi) = 0$ is valid. Neither Equation (2.146) nor Equation (2.147) contain any term originating from the steady-state solution[16]. In fact, the high frequency field propagates similar to the steady-state potential field within the primary current distribution approximation. Hence, the ratio

$$1 - 2 \cdot \frac{|\delta\Phi_A - \delta\Phi_P|}{|\delta\Phi_A - \delta\Phi_C|}, \tag{2.148}$$

which is experimentally accessible by sensing the voltage perturbation between anode and DHE and anode and cathode, is a measure for the misalignment of the electrodes. The relation between electrode displacement m/d and this quantity is exactly the same as shown in Figure 2.53 for the steady-state case. As shown in Figure 2.55, the actual perimeter potential might be significantly different from the primary current distribution approximation for misaligned electrodes. In consequence, an ohmic compensation is strictly speaking only precisely possible on the basis of perturbation techniques, if the electrodes are perfectly aligned. However, the difference between primary and secondary current distribution is tolerable, if the misalignment is small enough (about 50% of the membrane thickness). This provides a tolerance band that is experimentally achievable by reasonable measures.

The experimental validation of the electrode alignment by a current step technique [42] is exemplified in Figure 2.56. An operating $30\,\mathrm{cm}^2$ cell was perturbed by a $5\,\mathrm{A}$ auxiliary current pulse. Shown is the voltage relaxation after pulse termination. The instantaneous voltage jump of about $80\,\mathrm{mV}$ measured between anode and cathode is indicative for the ohmic drop over the electrolyte and corresponds to the high frequency impedance measurable with a sinusoidal perturbation. The voltage relaxation of the anode relative to the DHE is half as strong. This shows that the potential field opens symmetrically at the electrode edges, and hence the DHE provides a reliable reference potential. The polarization curves shown in Figure 2.57 provide further proof. Compared is the

---

[16]The steady-state solution would have entered the equations via R_{ct}, which is negligible in the high frequency limit.
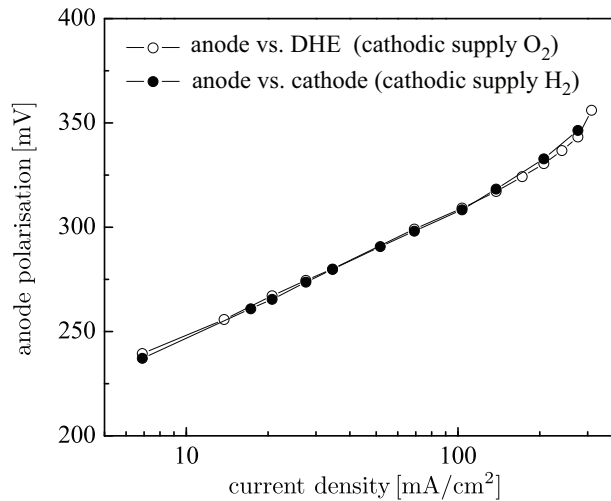
Figure 2.57: Anodic polarization curves obtained by sensing the anodic voltage once against the DHE and once against the hydrogen-supplied cathode; the data is IR-compensated.

anodic polarization of the same cell obtained by utilizing the DHE ($\circ$) and by using the cathode, which is supplied with hydrogen rather than air or oxygen, as reference potential ($\bullet$). The MEA consisted of a Nafion 117 membrane, a commercial supported Pt-Ru electrode with $1.5\,\mathrm{mg/cm^2}$ precious metal loading at the anode, and a Pt-black electrode with $4.0\,\mathrm{mg/cm^2}$ platinum loading at the cathode from the same supplier. The anode was supplied with $20\,\mathrm{ml/min}$ of $0.5\,\mathrm{M}$ methanol. The cathode was supplied with $500\,\mathrm{ml/min}$ oxygen and hydrogen, respectively. In both cases, the cathode gas was fed dry to the cell. The cell was operated at $90\,^\circ\mathrm{C}$ and $2\,\mathrm{bar(a)}$. If hydrogen is fed to the cathode, this electrode operates as hydrogen evolution electrode and hence provides a rather stable potential, which is similar to that of the DHE. The ohmic drop, as obtained from the current pulse technique (voltage relaxation between anode and cathode), was subtracted from the measured cell voltage, and the resulting polarization curve is shown by ($\bullet$). Under normal DMFC operation (cathodic supply with oxygen), the anodic polarization was obtained by sensing the anodic potential relative to the DHE. The resulting voltage was corrected for the included ohmic drop on the basis of the voltage relaxation between anode and DHE, and the resulting polarization curve is shown by ($\circ$). The well agreeing curves substantiate that the perimeter-placed DHE provides a reliable reference voltage under varying operating conditions as long as a symmetric opening of the potential field is ensured, and hence can be used to resolve anodic, cathodic, and ohmic losses contributing to the cell voltage.

CHAPTER 3

POLYMER ELECTROLYTE FUEL CELLS

The occurance of liquid water formation within PEFCs of different size and structure will be investigated. First, the presence and transport of liquid water accumulations within different flow field structures and the influence of surface properties will be examined. Afterwards, the discussion will turn to flooding within the gas diffusion layers. The influence of operating conditions and material choice will be explored within simplified differential cells. On this basis, the discussion will return to cells operating under technically realistic operating conditions, and the relation between liquid distribution and local performance is investigated. Subsequently, co- and counterflow operation is compared by showing differences in liquid distribution and local performance. The concluding sections deal with methodologic aspects. The influence of oxygen concentration oscillations within flow fields during locally resolved impedance spectroscopy is evaluated, and the possible discrimination of liquid accumulation within anode and cathode by high-resolution neutron imaging is shown.

All studies presented within the Sections 3.1 to 3.3 and Section 3.6 originate from a lasting cooperation with Nissan Motor Co. (Japan). While the actual samples (i.e., cells and MEAs) were provided by Nissan, all experiments were performed at PSI. Though the diagnostic methods and provided interpretation of the results is original to this work, many fruitful discussions and a deliberate planing of experiments are only some contributions of various co-workers at Nissan which were indispensable.

The results presented in Section 3.4 originate from a cooperation with I.A. Schneider, who investigated the internal water household of PEFCs by means of localized impedance spectroscopy before [117]. A joint effort was undertaken to combine both methods to gain even further insight than obtained by separately applying each method. Hence, the availability of localized impedance spectroscopy in our group originates from his work. Likewise, the results related in Section 3.5 were obtained jointly with I.A. Schneider. Here, the development of the two-dimensional, mathematical model describing the local impedance response of an air-fed PEFC is original to this work, while the physical model and the experiments, which were performed jointly, were proposed by I.A. Schneider.

3.1 Two-phase flow within flow fields

As the reactants fed to a PEFC are distributed over the active area by the flow fields, a close relation between the processes occuring in the channels and the electrochemical characteristics seems natural. Beside the distribution of reactants, the removal of product water (either as vapor or as liquid) is a central functionality of the flow field. An ideal flow field is characterized by the ability to remove product water from the cell without impeding influence on the distribution of reactants.

In contrast to the gas diffusion layer, mass transport processes in the flow field channels are experimentally accessible by means of optical diagnostics. By choosing an optically transparent flow field material, the transport of liquid can be imaged directly, and the more advanced application of laser-based diagnostics is possible (e.g., laser-doppler-anemometry). Recently, some studies of liquid transport within flow field channels were published utilizing transparent cells. The optical approach is attractive, because a high spatial and temporal resolution can be achieved. This enables detailed studies of the nature of two-phase flow within PEFC. The first reports concerning liquid formation and transport in such a transparent PEFC was given by TÜBER et al. [55] in 2003 and YANG et al. [52] in 2004. Investigating the cathodic flow field of a linear cell with seven channels and an active area of $14\,cm^2$, ZHANG et al. [118] presented a detailed study of liquid removal from PEFCs. They observed the formation of small droplets on the GDL surface at preferential sites. These droplets grew in diameter until they were either removed by the shear force of the gas flow (high flow rates) or by capillary wicking onto the neighboring channel wall, which was hydrophilic due to a gold-coating needed to realize a sufficient corrosion resistance of the flow field. Eventually, a liquid layer was formed at the channel wall enabling liquid removal via this film. However, they also observed that this film becomes unstable for higher water production rates (high current densities) resulting in a transition of the annular film flow into a slug flow.

Yet, the need for transparent flow fields entails a significant intrusion into the cell hardware, and proof of the occurrence of phenomena observed within transparent cells in non-specialized cells has to be given. This calls for a less intrusive experimental approach such as neutron imaging.

Selected aspects of the complex relation between geometry, material properties, liquid transport, and electrochemical performance will be explored within the following sections using neutron imaging. However, to structure the discussion, it is useful to propose a water transport/removal mechanism first. A possible mechanism derived from observations reported in literature (see above) and experimental findings communicated in the following sections is given in Figure 3.1. Following this scheme, water droplets initially protrude from the GDL surface and subsequently grow in size. If the shear forces of the gases are large enough, these droplets are removed from the GDL providing the first removal mechanism. If the shear forces acting on droplets are not sufficient for droplet acceleration, the droplets might grow until contact with the flow field wall. Depending on the flow field properties, a liquid layer might form at the flow field wall, and transport within this film provides the second removal mechanism. If the removal rate by film transport is lower than the water production rate, these films will grow and spread at the flow field wall, which ultimately leads to clogged channels. After channel clogging, the pressure drop between inlet and outlet side of the water plug provides the third removal mechanism.

A multitude of parameters influence the formation and transport of liquid within flow fields; some of them are shown on the left of Figure 3.1. A confined discussion, therefore, requires favoring a selection of parameters. Consequently, the study of the first removal mechanism is omitted for experimental and practical reasons: (1) the study of droplet removal in the sub-millimeter range
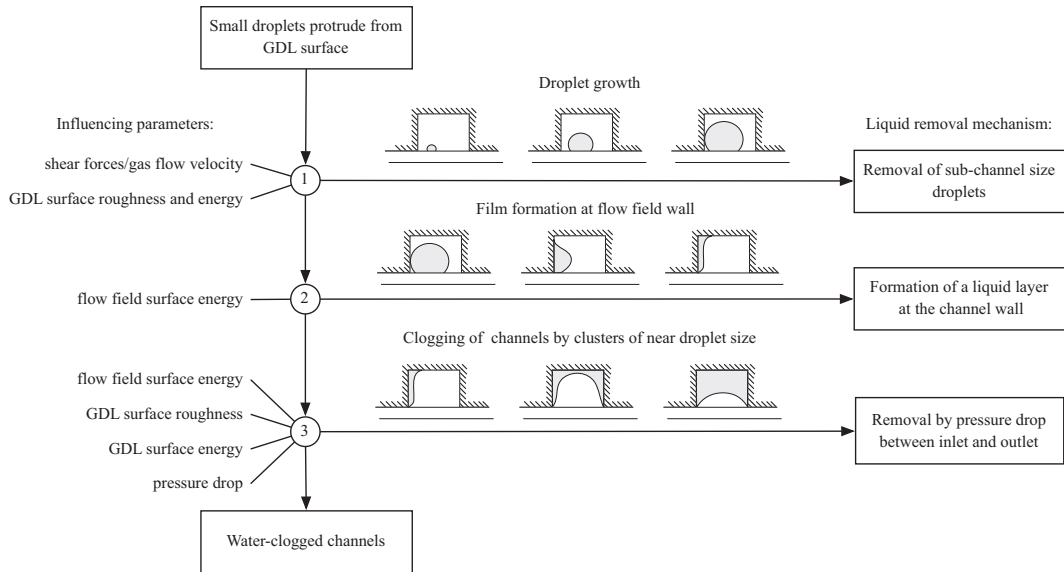
Figure 3.1: Possible mechanism of liquid formation, accumulation, and removal within PEFC channels and a selection of influencing parameters.

requires a temporal and spatial resolution well beyond the capabilities of neutron imaging, and (2) the droplet detachment diameter is easily reaching typical channel dimensions [118] for technically relevant operating conditions (near stoichiometric operation). This increases the relevance of the second and third removal mechanism for technical cells.

3.1.1 Comparison of flow field geometries

Numerous flow field geometries have been proposed over the years ranging from the most simplest geometries to highly complicated structures. Nonetheless, most of them can be grouped into three categories: (1) channel geometries providing a continuous pathway from inlet to outlet, (2) channel geometries without direct connection between inlet and outlet, and (3) open structures without channels[1]. A typical representative of the first category is the serpentine flow field, where a number of parallel channels is folded several times over the active area. The classical representative of the second group is the interdigitated flow field, which usually comprises two interlocked combs with a number of fingers (channels). One comb is connected to the inlet and the other to the outlet, respectively. These two geometries will be compared hereinafter.

---

[1]This includes nets, porous materials such as metal foams, and pin-structures.
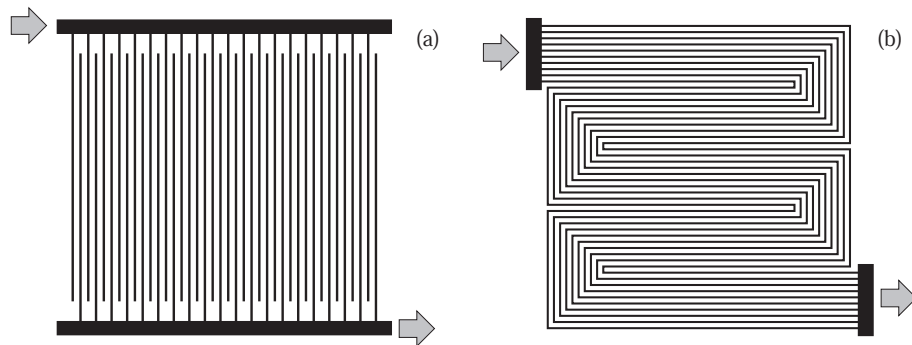
Figure 3.2: Sketch of the compared flow field structures; (a) shows a interdigitated structure with two interlocked combs formed by fifty fingers each; (b) shows a tenfold serpentine folded five times.
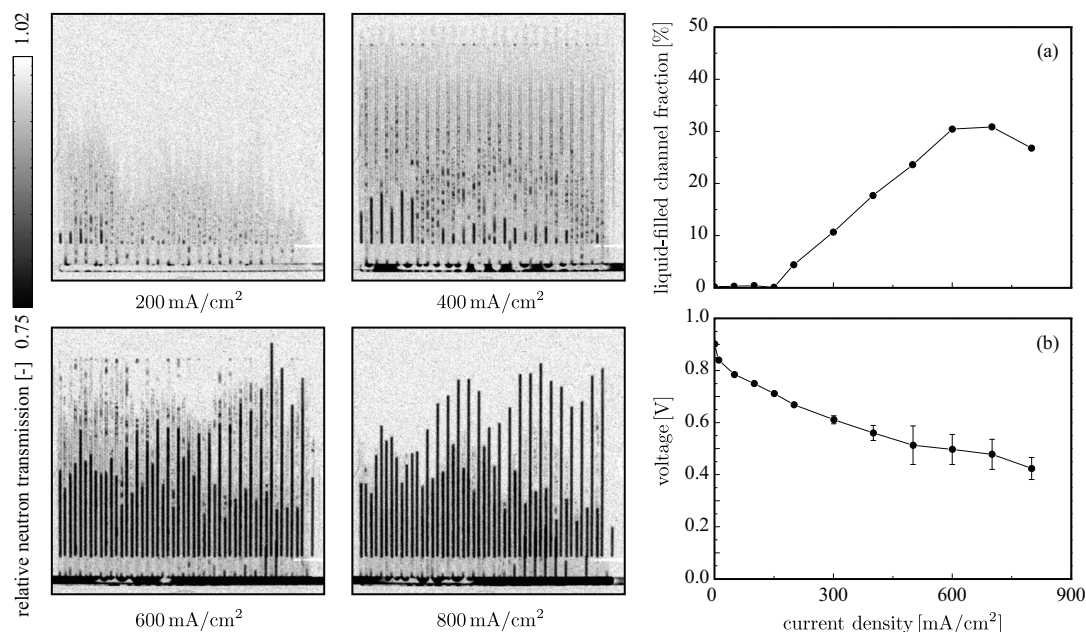
Figure 3.3: Liquid water accumulation as a function of current density within interdigitated flow fields; the diagram (a) shows the percentage of liquid-filled channels as function of current density; the corresponding polarization curve is given in diagram (b); selected neutron images are shown on the left; the cell was operated at 80 °C and near ambient pressure; anodic inlet dew-point is 75 °C; cathodic inlet dew-point is 65 °C; anodic and cathodic SR is 1.5; cathodic supply is air.

For this purpose, two square cells with an active area of $100 \, cm^2$ were manufactured[2]. The cells consisted of 4 cm thick aluminium blocks into which the flow field structures were directly machined. A sketch of the chosen structures is given in Figure 3.2. The interdigitated flow field comprised two interlocked combs; each comb consisted of fifty vertical fingers that were connected by horizontally aligned manifolds. The width and depth of the fingers was 1 mm each. Likewise, the land formed between adjacent channels was 1 mm wide. Anodic and cathodic flow fields were identical, and the inlet comb of the anode was placed over the outlet comb of the cathode and vice versa. Ten parallel channels folded five times formed the serpentine flow field. The channels were again 1 mm wide and deep, and a land of 1 mm width separated adjacent channels. Again, anodic and cathodic flow fields were alike for the sake of simplicity. The structured blocks were coated with a relatively thick gold-layer to avoid passivation and ensure a good contact resistance. Four electrical heaters are placed at the circumference of the cell controlling the cell temperature, whereby the temperature was sensed by a thermocouple in the center of the active area. Both cells housed commercial MEAs of similar type comprising a $30 \, \mu m$ thick membrane and paper-type GDLs. The cells were sealed by a soft sealing and assembled with torque wrench fastened screws. The cells were investigated at NEUTRAs measurement position 1 (nearest to the source) with the standard CCD-detector.

Interdigitated flow field. The liquid accumulation within interdigitated flow fields as function of current density is exemplified in Figure 3.3 for a set of operating conditions. The cell was investigated by recording a galvanostatically controlled polarization curve starting from load-free operation. The resulting polarization curve is shown in diagram (b); the percentage of liquid-filled channels[3] is shown in diagram (a), and some of the underlying neutron images are shown on the left-hand side. An equilibration time of at least 3 min after changing the current was granted before images and voltage were recorded. For the shown operating conditions, no liquid is accumulated if

---

[2]cf. first paragraph on page 89
[3]cf. Section 4.1.2 for a description of the algorithm for quantifying the void fraction in channels.
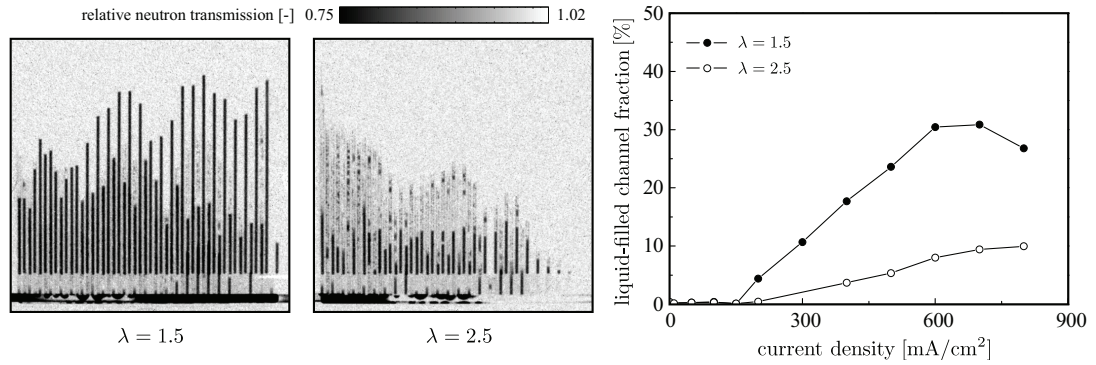
Figure 3.4: Influence of the cathodic stoichiometric ratio onto slug formation within interdigitated flow fields; cathodic stoichiometry λ as indicated in the diagrams; other operating conditions as for Figure 3.3; the images show the conditions at $800\,\mathrm{mA/cm^2}$.

the current density is below $200\,\mathrm{mA/cm^2}$. At $200\,\mathrm{mA/cm^2}$ first droplets appear in the lower half[4] of the active area. With increasing current density, the amount of liquid water increases and larger slugs start to form at the end of the inlet fingers (at $400\,\mathrm{mA/cm^2}$ and higher). It is worth noting that anodic and cathodic inlets contain droplets. However, the fraction of liquid-filled channels is still below $20\,\%$ and the cell is producing a stable potential. By increasing the current density, this changes seriously. The cell voltage starts to fluctuate, which is reflected in the polarization curve by increasing error bars. Likewise, the fraction of liquid-filled fingers exceeds $30\,\%$. With the assumption that no liquid is contained in the outlet fingers, this translates into a blockage of more than half of the active area. Further on, the droplets have grown in size and huge slugs are formed; again, the cathodic and anodic inlet structures are both flooded. Also the GDL is flooded to a significant degree at $600\,\mathrm{mA/cm^2}$. This can be seen from the medium gray shades in the corresponding image. At $800\,\mathrm{mA/cm^2}$, the GDL flooding is reduced due to the higher flow rate passing through the porous structures. Yet, the slugs in the inlet fingers persist.

The shown example highlights the major drawback of interdigitated structures. Following the mechanism depicted in Figure 3.1, droplets emerging from the GDL surface grow within the fingers until slugs are formed. Obviously, the pressure drop between inlet and outlet fingers, which is a consequence of the gas flows passing convectively through the GDLs, is not sufficient to force enough liquid through the GDLs to avoid liquid accumulation and slug formation.

Naturally, a higher cathodic stoichiometry λ increases the pressure drop between inlet and outlet structure, which supports the liquid removal resulting in a lower tendency to accumulate liquid. This can be extracted from the diagram of Figure 3.4, where the fraction of liquid filled channels is compared for a cathodic stoichiometry of 1.5 and 2.5, respectively. The corresponding neutron images obtained at $800\,\mathrm{mA/cm^2}$ are shown on the left-hand side for illustration. Only about $10\,\%$ of the fingers are clogged at $800\,\mathrm{mA/cm^2}$, if air is supplied at a stoichiometry of 2.5. The significantly reduced liquid content within the flow field in conjunction with the higher average oxygen concentration yields an improvement in electrochemical performance. A subtlety becomes apparent by inspecting the neutron image corresponding to $\lambda = 2.5$. The liquid is predominantly located in the lower left corner, which is a preference that is not as obvious under lower stoichiometry operation. It is likely that this is a consequence of the inlet conditions. The gases are fed to the manifold from the top left corner, and obviously the gas feed is not distributed evenly between the fingers. Due to the higher dynamic pressure within the manifold near the inlet (higher flow velocity), the static pressure, which is the driving force for the gas flow through the fingers, is lower. This results in

---

[4]The gases were supplied from the top (cf. Figure 3.2).
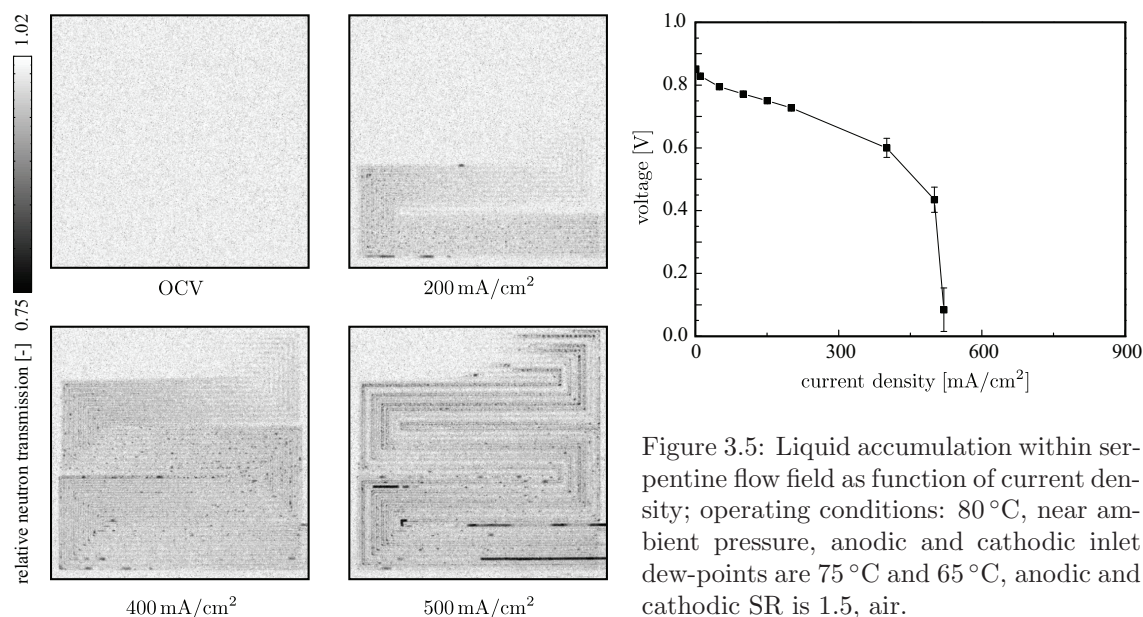
Figure 3.5: Liquid accumulation within serpentine flow field as function of current density; operating conditions: 80 °C, near ambient pressure, anodic and cathodic inlet dew-points are 75 °C and 65 °C, anodic and cathodic SR is 1.5, air.

an impeded supply of the fingers near the inlet (left side in the images) and consequently causes a higher liquid content in this region.

It can be concluded that interdigitated flow fields provide reasonable functionality under high stoichiometric operation. However, as this is costly from a balance of plant perspective, interdigitated flow fields are not attractive for technical application.

Serpentine flow field. The use of flow field geometries that provide a continuous pathway from inlet to outlet, such as serpentines, circumvents the necessity to convectively force liquid accumulating within the channels through the GDLs. Hence, an improved removal of liquid from the flow field structures can be expected in comparison to interdigitated structures. The neutron images depicted in Figure 3.5 show the liquid accumulation within the serpentine flow fields. The channel width and depth of anodic and cathodic flow field is 1 mm each. Likewise, the land formed between the ten parallel channels is 1 mm wide. The operating and experimental conditions are the same as for the investigation of the interdigitated flow field shown in Figure 3.3. Comparison of the images given in Figure 3.5 with those of Figure 3.3 shows that indeed the utilization of a continuous serpentine enables an efficient removal of liquid, and, generally, slug formation is prevented. The images are characterized by small droplets (black speckles), which are located predominantly at the channel walls. Some of them stretch over the full channel width. Yet, larger slugs are rare. Following the mechanism depicted in Figure 3.2, the second removal mechanism—the removal by film transport—is obviously effective. Because direct liquid transport to the outlets (without the need of passing through the GDL) is possible, the slug formation typical for interdigitated flow fields is inhibited. Hence, serpentine flow fields are superior to interdigitated structures, especially under low stoichiometric operation.

This, however, does not directly translate into an improved electrochemical performance. Although the flow fields are nearly liquid free, the polarization curves exhibit a drastic voltage decline around $500\,\mathrm{mA/cm^2}$. As indicated by the medium gray shades in the images, a substantial percentage of the GDL is flooded. Because neither the liquid nor the gases are forced convectively through the GDL, the transport of oxygen from the channel towards the GDL is dominated by diffusion. Obviously, the diffusive transport of oxygen towards the electrode, which might be hampered by the presence of liquid within the porous structures, is not sufficient to enable a current density larger

than $500\,\mathrm{mA/cm^2}$. This points towards the importance of the mass transport within the porous structures, which is studied in detail in Section 3.2. Before focusing on GDL flooding, however, the next section will complete the discussion of flow field related two-phase flow by inspecting the implications of technically more realistic flow field materials than gold-coated structures.

3.1.2 The influence of surface properties

A close interaction driven by capillary forces between the liquid within the flow field channels and the channel walls is shown within the last section. Gold-coated flow fields were utilized for the shown study. Gold surfaces are generally hydrophilic, which supports the spreading of droplets upon contact with the wall and enables the transport of liquid within a film. However, because of the high material and manufacturing costs, gold-coating is generally not an option for technical cells. Hence, the implications originating from the use of technically more relevant materials is a question to be addressed.

Owing to its good corrosion resistance, graphite is an attractive material choice and consequently widely used. Generally, graphite surfaces are more hydrophobic than gold surfaces, and with the proposed mechanism in mind (Figure 3.1), an influences on the transport of liquid within flow field structures can be expected. In order to investigate graphite-made flow fields, a modified cell design was realized[5]. The cell size (active area) and geometry of the serpentine flow field have been retained unchanged. Yet, the flow field structures were machined into thin graphite plates rather than directly into aluminum blocks. These graphite plates were clamped between gold-coated aluminium blocks. Because graphite attenuates neutrons significantly stronger than aluminium, the end plates were thinned over the active area to compensate for the additional neutron attenuation incurred by the graphite plates. Yet, the thinning was moderate to ensure a homogeneous compression force and isothermal cell conditions [63].

The cells with graphite-made flow fields were investigated at NEUTRAs measurement position one with the standard CCD-detector setup. Galvanostatically controlled polarization curves were obtained by starting from load-free operation, step-wise increase of the current up to a maximal current, and subsequent decrease of the current back to OCV. An equilibration time of at least 5 min was granted at every current prior to taking images. Before every polarization curve, the cells were purged with dry nitrogen until the high frequency resistance (measured at 1 kHz) gained at least one order of magnitude, indicating that even the membrane was significantly dried. Images recorded at the end of the purge served as reference images for the subsequent experiment.

A typical result of such an experiment is depicted in Figure 3.6. The gray scale of the shown neutron images is adjusted such that mainly liquid within the flow fields is reflected. Generally, there is a higher tendency of slug formation within the channels compared to gold-coated flow fields. Already during the down-sweep (increasing current) an increased number of liquid clusters that stretch over the full width of the channel is observed in comparison to the experiments utilizing gold-coated flow fields. With increasing current, the slugs grow in size and liquid clusters of several centimeter length are easily found. Taking reference to the liquid formation and removal mechanism proposed in Figure 3.1, this is attributed to the different wetting properties of graphite and gold. Because of its hydrophobicity, graphite inhibits the wicking of droplets to the channel wall deactivating the second removal mechanism. Consequently, less hydrophilic or hydrophobic surface properties of the flow field material imply a higher tendency to form clusters stretching over the full width of the channels. Nonetheless, the liquid removal rate matches the production rate, and the flow fields are not as drastically filled as observed for the interdigitated structures.

---

[5]cf. first paragraph on page 89
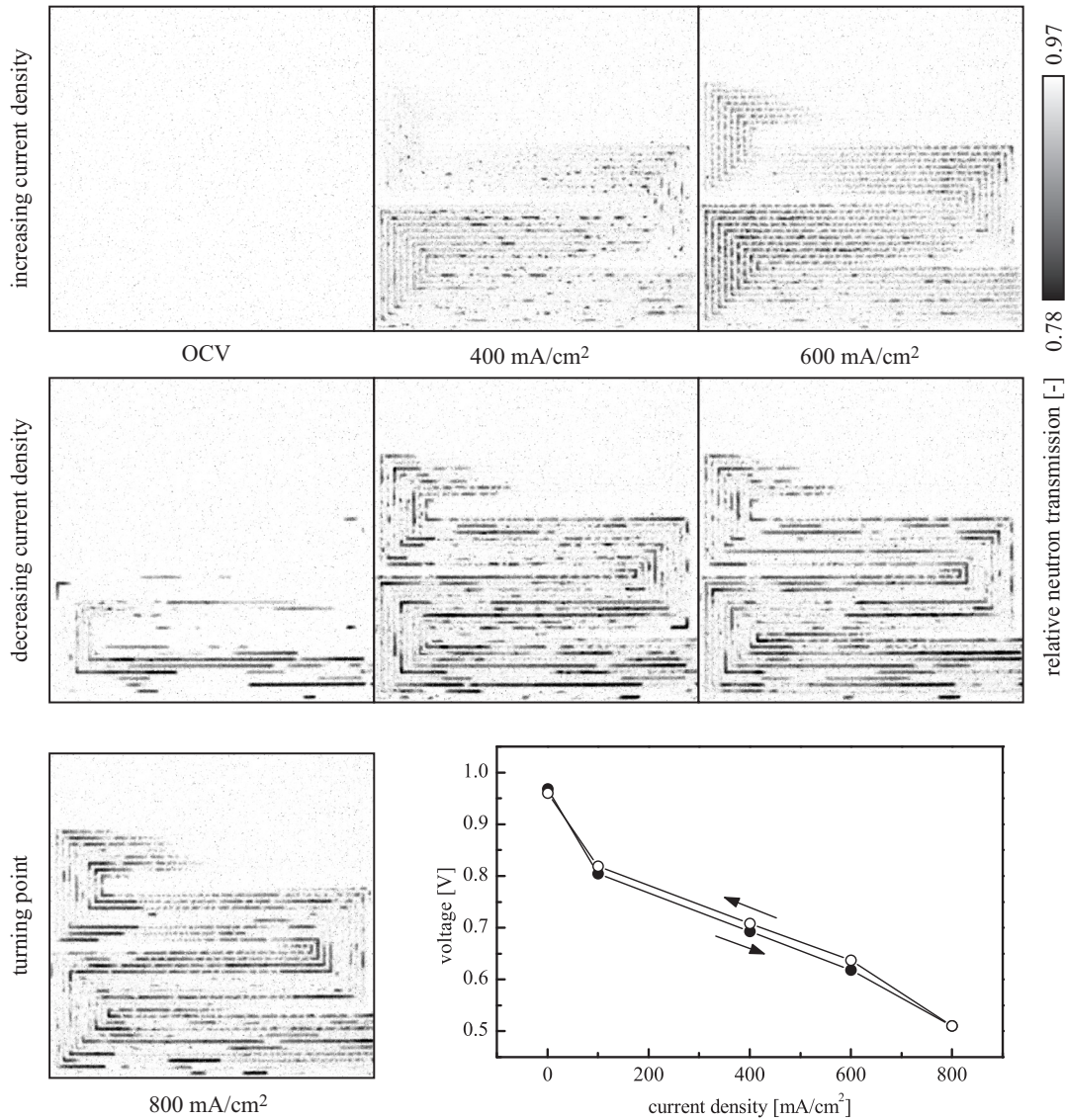
Figure 3.6: Neutron images and corresponding polarization curve showing a hysteresis in liquid content; (●) increasing current; (○) decreasing current; the cell was operated at 70 °C under near ambient pressure; the relative humidity at the anodic and cathodic inlet is 80 %; the anodic stoichiometry is 1.5; the cathodic stoichiometry is 2.5; the flow field material is graphite.

Further on, a hysteresis in liquid content between down- and up-sweep is seen. Large clusters that are formed at higher current densities ($\geq 800 \, \text{mA/cm}^2$) persist, if the current density—and because of the stoichiometric operation, the flow rate—is decreased. Even at OCV, clusters remain within the flow field. Comparison of the neutron images at $400 \, \text{mA/cm}^2$ shows the hysteresis very clearly. During down-sweep (increasing current), the liquid is removed in reasonable time and no large clusters are formed. During up-sweep (decreasing current) large clusters are present within the channels originating from the history of operation. However, why the large clusters persist and are not removed from the channels restoring the same qualitative liquid pattern observed during down-sweep is not clear at first. In that context, an interesting experiment was reported by ALLEN et al. [119]. They investigated pressure-drop and liquid flow rate under two-phase plug flow conditions in a horizontal capillary as function of time. Initially, the pressure difference between inlet and outlet increased linearly with time while no liquid was leaving the capillary. After a critical pressure difference was reached, the liquid flow rate increased abruptly. At the same time, the pressure difference between inlet and outlet was dramatically reduced. The greater the critical

pressure difference, the larger was the amount of removed liquid, which points towards the presence of more liquid inside the capillary. Obviously, there is a relation between the amount of liquid (or cluster size) and the required force to accelerate the clusters. A basic understanding of this can be obtained by considering a simplified problem. The simplest approximation of forces acting on a liquid cluster is regarding the cluster as solid. In order to accelerate a residual cluster, the force acting on the cluster—induced either by the gas flow via drag while passing a droplet or by the pressure drop between inlet and outlet side of a plug—has to be large enough to overcome the friction force. The friction force is proportional to the forces acting perpendicular to the surface. If gravity is neglected, only adhesion forces work at the surface. Since adhesion acts between surface molecules, the resulting force should be proportional to the number of surface molecules and therefore proportional to the surface area. Hence, the force needed to accelerate a residual block is a function of the wetted surface area, which provides an explanation for the observed hysteresis.

It is remarkable that the presence of larger clusters during up-sweep (decreasing current) is not detrimental to the electrochemical performance, as can be seen from the polarization curve shown at the bottom right of Figure 3.6. Actually, the electrochemical performance is slightly improved during up-sweep, which might be attributed to a reduced surface coverage of the cathode with OH adsorbates [120] and/or a reduced ohmic resistance. In any case, the access of O_2 to the cathode is obviously not significantly hampered. An explanation for the weak coupling between the electrochemical performance and the two-phase flow pattern inside the channels is not easily found. However, two reasons can be put forward:

1. If a channel is clogged, the gas flow is forced either through a non-clogged parallel channel or through the GDL. If clogging of most of the channels occurs, it cannot be expelled that part of the gas flow is forced convectively through the GDL.

2. Careful examination of the images shows that most of the clusters fill the channels only partially. It is possible that the liquid is preferentially accumulated at the walls of the flow field. This would still provide a pathway for the gases, because the GDL surface would be liquid free.

Summarizing the investigations of graphite-made flow fields with serpentine flow distributors, it can be said that the use of graphite yields a higher tendency to accumulate liquid within the channels, because the wicking effect is not as pronounced as for gold-coated surfaces. Yet, there is a rather small correlation between liquid accumulations within the flow fields and electrochemical performance. This is likely to be due to a preferential part-filling of the channels keeping the GDL surface accessible for the gases.

3.2 Liquid accumulations within gas diffusion layers

The accumulation of liquid within the porous structures of the gas diffusion layers (GDLs) is believed to be detrimental to cell performance, because the loss of free pore volume might impede the diffusive transport of oxygen to the electrochemical active surface of the cathodic electrode. Unfortunately, information about the degree of flooding—this is the term commonly referring to liquid accumulations within the GDLs—is not easily obtained. Reports have been given utilizing impedance spectroscopy to obtain information about flooding (e.g., Ref. [121]). Yet, it will be shown in Section 3.5 that the extraction of information about the diffusive oxygen transport from
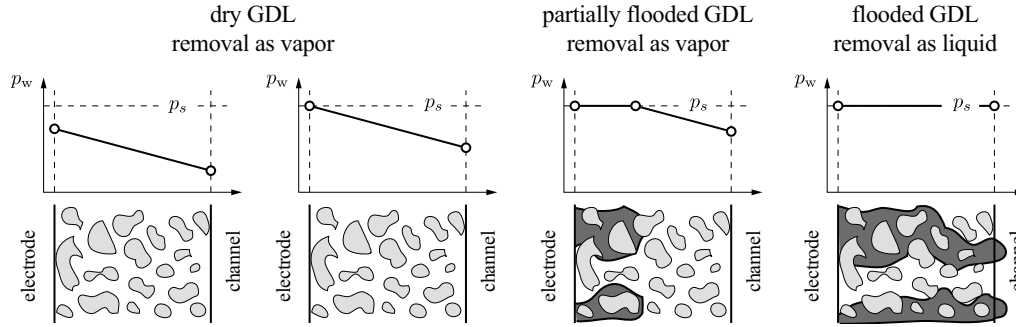
Figure 3.7: Simplistic model describing the water transport through and liquid accumulation within the GDL.

impedance results is complicated by coupling effects, if the cell is operated under technical relevant operating conditions. Neutron imaging provides virtually the only direct experimental access to the liquid within the porous structures, and its importance for fuel cell research mainly originates from this fact.

3.2.1   A simplistic mechanism

Before the discussion will focus on the experimental investigation of GDL flooding, it is worthwhile to formulate a mechanism of water transport through the porous structures as guidance.

The GDL can be seen as a porous layer, where water is entering at the electrode facing side and leaving at the flow field facing side. Under steady-state conditions, the water flux entering the GDL equals the flux leaving the GDL. The production rate of water within the cathodic electrode is proportional to the electrical current. Yet, the exchange of water between anode and cathode cannot be neglected, and whether the water flux through the cathodic GDL is larger or smaller than the water production rate depends on the direction of the net water flux through the membrane[6]. In any case, the water flux passing the GDL may comprise two components: water vapor and liquid.

As local equilibrium prevails, the presence of liquid water requires that the water vapor pressure p_w equals the water saturation pressure $p_s(T)$ correlated to the local temperature. Hence, no liquid water is formed as long as the water vapor pressure is lower than the saturation pressure all over the GDL. This is illustrated by the left-hand diagram of Figure 3.7. The slope of the shown vapor pressure curve is given by Fick's first law

$$\partial_x p_w \propto -\frac{\dot{n}_w}{D_w}, \tag{3.1}$$

where $\dot{n}_w$ and D_w denote the water molar flux through the GDL and the effective diffusion coefficient of water vapor, respectively. Provided the water flux through the GDL does not change, liquid is formed in a certain part of the GDL resulting in an evaporation front somewhere in the bulk of the GDL. This is shown in the third diagram of Figure 3.7. In the flooded part of the GDL, the vapor pressure matches the saturation pressure, and the missing gradient implies a vanishing transport rate of water vapor. Hence, water is first transported in the liquid phase, then evaporated, and is removed from the GDL as vapor. The gradient of the vapor pressure in the non-saturated part of the GDL is again equal to the gradient of the first two diagrams, because $\partial_x p_w$ is

---

[6]The transport rate of water through the membrane depends on the water activity difference between anodic and cathodic side and the current passing through the membrane (electroosmotic drag).

constant under the assumption of equal molar fluxes. Hence, with increasing vapor pressure within the flow field, the saturation limit will be reached nearer to the channel side, and a reduced vapor pressures within the flow field translates into a displacement of the evaporation front towards the electrode.

From this consideration, two important conclusions can be derived: (1) a saturation of the gases within the channels is no necessity to accumulate liquid within the GDL, and (2) the degree of flooding is principally a function of the vapor pressure within the channel. Finally, once the saturation pressure is reached within the channel, the vapor pressure equals the saturation pressure all over the GDL (fourth diagram of Figure 3.7). As there is no vapor pressure gradient, there is no driving force to transport water as vapor. Hence, the total molar flux has to be transported within the liquid phase. This implies that liquid is protruding from the GDL surface and removed from the GDL by either mechanism discussed in Section 3.1. In conclusion, three different regimes can be distinguished:

1. For low vapor pressures within the channels, the saturation pressure is reached nowhere throughout the GDL, and no liquid water is formed.

2. There will be an intermediate range of channel vapor pressures, where liquid can be formed within the GDL, yet not protrude from the GDL surface. Under these conditions, the degree of flooding will depend on the vapor pressure within the channel, and the removal from the GDL is still characterized by gas-phase diffusion.

3. After the gases are saturated within the channels, liquid water will protrude from the GDL surface, and the removal mechanism will change from evaporation/diffusion to droplet removal.

Finally, it should be mentioned that the described mechanism is highly idealized. Although the results related in the Sections 3.3 and 3.4 substantiate the three proposed regimes, the actual water transport through the GDLs is most likely far more complex. The development of a refined understanding would at least require the consideration of aspects like temperature distribution, local non-equilibrium (limited evaporation rate) between liquid and vapor, and capillary effects.

Nonetheless, the simplified picture will provide guidance while the influence of operating conditions and material choice is discussed throughout the next sections. Initially, the discussion will focus on simplified systems (differential cells). This provides the foundation for the exploration of inhomogeneities of liquid content and local performance, which are encountered under technical realistic operating conditions, within the Sections 3.3 and 3.4.

3.2.2 The differential cell approach

System efficiency concerns limit the flow rates applicable to PEFCs under technically realistic operating conditions to near stoichiometric ratios. This entails a significant change of the flow composition as the gases pass over the active area, because: (1) hydrogen and oxygen are consumed, (2) water is produced by the cathodic ORR, and (3) additional water that might penetrate either from anode to cathode or vice versa influences the water content within GDL and flow field. Hence, an inhomogeneous operation over the active area of the cell is very likely. The integral characteristic of a PEFC can be seen as a complicated superposition of local characteristics. These local characteristics have to be investigated in order to develop a refined understanding of the integral characteristics. This can be achieved either by spatially resolved mapping of local characteristics (cf. Sections 3.3 and 3.4) or by investigating simplified systems. The first approach
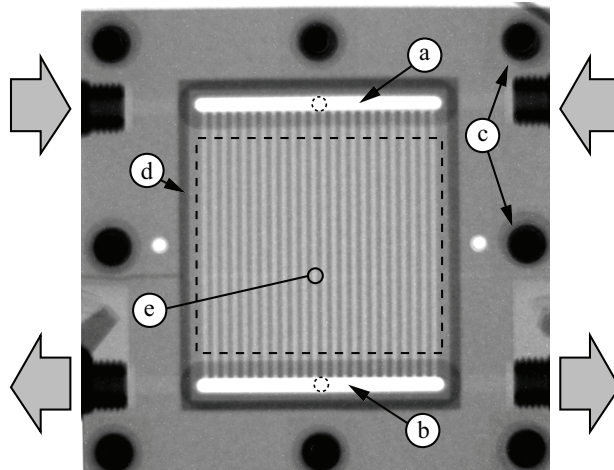
Figure 3.8: Neutron image of a differential cell with 25 cm² active area; the active area is indicated by a dashed box; other features are: (a) inlet manifold, (b) outlet manifold, (c) screws, (d) gasket, (e) temperature sensing point; entry and withdrawal of the gases indicated by arrows.

implies elaborate experimental setups (cf. Section 2.3) but offers the advantage of directness. If the focus is not on the PEFC as a technical device but on the local processes involved, it is highly desirable to simplify the system by avoiding inhomogeneities or, in other words, by ensuring equal gas compositions all over the active area.

A neutron image showing the interior of such a simplified cell is given in Figure 3.8. The manufactured cell[7] consists of two 1.5 mm thick graphite plates with 24 parallel channels. The channels are connected at inlet and outlet by manifolds. The gases are fed to the cell from the top and enter the manifold in the center (dashed circle). Likewise, the gases leave the cell through a hole in the center of the lower manifold. The MEA is placed between these two plates and a gasket seals the MEA against ambient. The active area is 25 cm². Two gold-coated aluminium plates with a thickness of 2 cm each serve as end plates and current collectors. The cell is clamped by eight screws positioned at the perimeter of the cell. A homogeneous compression pressure is ensured by fastening the screws with a torque wrench. Two horizontally aligned heating cartridges are located at the top and the bottom (not visible in Figure 3.8). They were controlled by a thermocouple positioned in the center of the cell. Misalignment of the cell is avoided by two positioning pins located at the center of the left and right side of the cell (white circles in Figure 3.8). The parallel flow field has a rib to channel ratio of one. The depth of the channels is 0.6 mm, and the width is 1 mm. Anodic and cathodic flow field are identical for the sake of simplicity. The parallel flow field was chosen because this geometry allows the operation under very high flow rates—a prerequisite for homogeneous operation—with the lowest possible pressure drop.

3.2.3   Comparison of GDL materials

The differential cell introduced within the last section is a convenient environment to study the influence of GDL material choice. For that purpose, three different GDL materials (two papers

---

[7]cf. first paragraph on page 89

Property		Type A	Type B	Type C
substrate		paper	paper	cloth
thickness (uncompressed)	[μm]	300	300	400
porosity (uncompressed)	[%]	68	75	78
PTFE-content GDL	[%]	17	5	0
PTFE-content MPL	[%]	31	23	38

Table 3.1: Properties of investigated GDL materials.

and a cloth) have been applied to the cathodic side. Main figures characterizing the investigated materials[8] are given in Table 3.1. All GDLs were equipped with a micro porous layer (MPL) linking the GDL to the electrode. For all experiments GDL type A was applied at the anode, and the use of the same catalyst-coated membrane (CCM) enabled the use of similar electrodes for all experiments. The influence of material choice towards liquid content and electrochemical performance will be analyzed by the variation of oxygen partial pressure and humidity. The electrochemical performance is characterized by taking polarization curves, and the liquid content within the GDL is obtained by simultaneous neutron imaging. Before every experiment, the cells are dried with nitrogen until the high frequency resistance (at $1\,\mathrm{kHz}$) gained at least one order of magnitude indicating that even the membrane is significantly dried. At the end of the drying procedure, images serving as references for the subsequent experiment were taken.

3.2.3.1 Sensitivity towards oxygen partial pressure

The oxygen partial pressure within the cathodic flow field was varied by feeding different gas compositions. The used dry gas compositions are: $100\,\%$ O_2 (pure oxygen), $21\,\%$ O_2 in N_2 (air), and 13.3% O_2 in N_2 (diluted air). The anodic supply was always pure hydrogen. Both gas feeds were pre-humidified to a relative humidity of $80\,\%$ by passing the gas feeds through a humidifier.

Oxygen operation. The diagram (a) displayed in Figure 3.9 compares the obtained polarization curves under oxygen operation. It becomes apparent that the cathodic GDL material has no impact on the electrochemical performance despite a small variation at OCV, because the transport of oxygen through the GDL is not rate-limiting. Further on, all GDLs hold a certain amount of liquid, which implies a good hydration of the membrane and, therefore, similar ohmic resistances. This indicates that in neither case a substantial percentage of the active sites is deactivated by liquid coverage. The insensitivity of electrochemical performance is advantageous for a first screening of GDL materials. Particularly, the heat release from the reactions is comparable, and the possible influence of different temperature gradients over the thickness of the GDLs is avoided at the same current density. The diagram (b) shows the liquid content of the whole active area as function of current density for the compared GDL materials. This was possible, because no liquid was observed within the channels. Hence, all GDL materials operate under condition 3 of Figure 3.7: liquid is advancing within the GDL until the evaporation rate matches the production rate, and water is removed from the GDL in vapor state. For each material, an increase in liquid content as function of current density was found, which seems natural considering the higher production rate of water. Yet, there are also significant differences between the materials. The cloth-type material (Type C) shows significantly less liquid in comparison to the two paper-types (A and B). Despite the completely different morphology of the two paper-type GDLs, the total liquid content is comparable. Yet, the partition of water under ribs and channels is different. This can be seen by comparing the displayed neutron images, which reflect the liquid content within the GDL at $1200\,\mathrm{mA/cm^2}$. While the GDLs A and C exhibit a nearly homogeneous liquid content, the Type B is characterized by a strong separation of rib and channel area. Nearly all water is accumulated under the ribs for this GDL.

On the basis of the compared materials and limited number of experiments, it seems that the substrate (paper or cloth) has a significant influence on the amount of liquid inside the GDL. A variation of PTFE content and/or porosity does not significantly influence the total amount of liquid but the distribution of liquid.

---

[8]cf. first paragraph on page 89
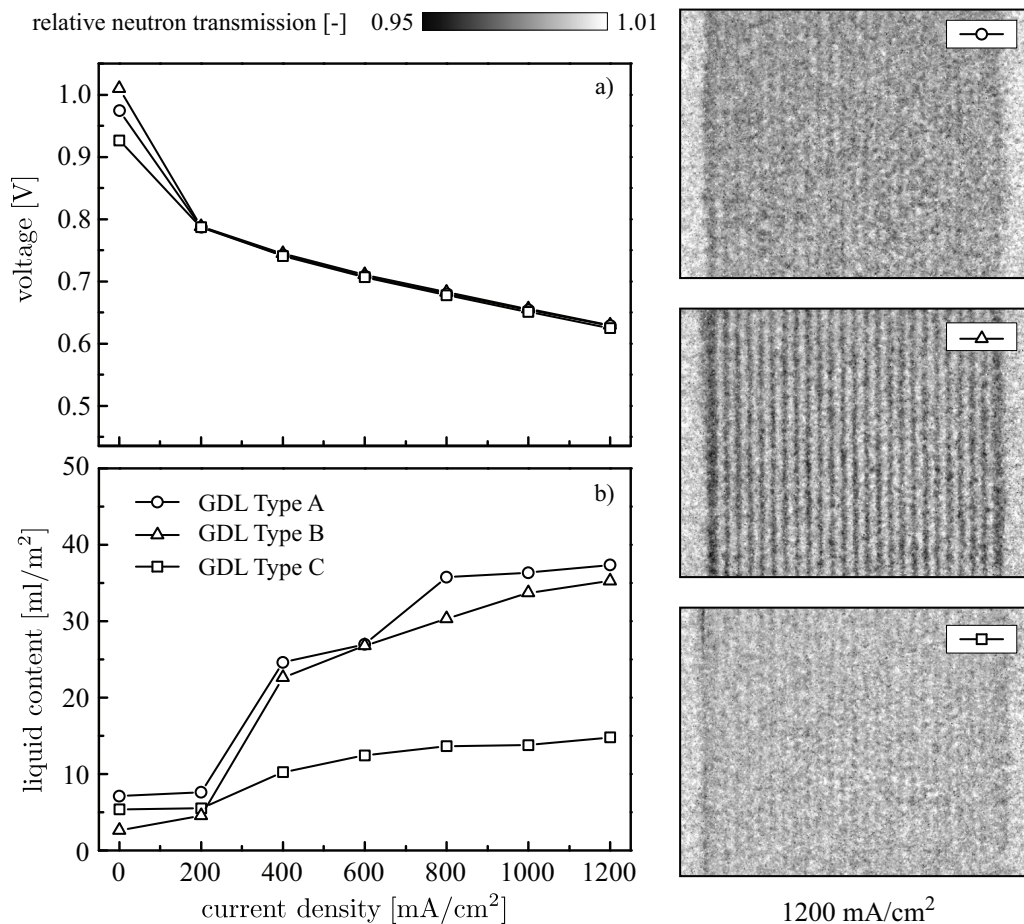
Figure 3.9: Polarization curves (a) and liquid content (b) as function of current density under oxygen operation for three different GDL materials applied to the cathode; selected neutron images are shown at the right; the cells were operated at 70 °C at near ambient pressure; the anodic supply is hydrogen with a stoichiometry of 18; the cathodic supply is oxygen with a stoichiometry of 150; the relative humidity of both feeds is 80 %.

Reduced oxygen partial pressure. While the supply of pure oxygen essentially decouples the electrochemical performance from the accumulation of liquid inside the porous structures, a reduced oxygen partial pressure results in a stronger relation due to the diffusive and therefore limited transport of oxygen in the remaining free pore volume. The liquid content separated into rib and channel area is depicted in Figure 3.10 for the three GDL materials and investigated oxygen partial pressures. Also shown are the corresponding polarization curves. The supply gas relative humidity was 80 %. The separation was achieved by masking [61], and the quantification below the channels was possible because in neither case liquid was observed within the channels. In addition, the calculated liquid volumes are low enough to justify the assumption that the liquid is not protruding into the channels at the GDL surface. The same trends regarding the liquid content as seen under oxygen operation are observed. This is indicating a relatively low sensitivity of the liquid content and distribution towards the oxygen concentration. The highest liquid content under the ribs is observed for GDL Type B, whereas Type C holds the least liquid. This might not be expected, if the polarization curves are compared, because virtually identical electrochemical performance is obtained. This insensitivity is surprising, especially if the result of GDL Type A is considered. This GDL holds less water under the ribs than Type B, but at the same time a substantial fraction of the GDL under the channel is liquid-filled, and the electrochemical performance is much more sensitive to the supplied oxygen concentration. The insensitivity of
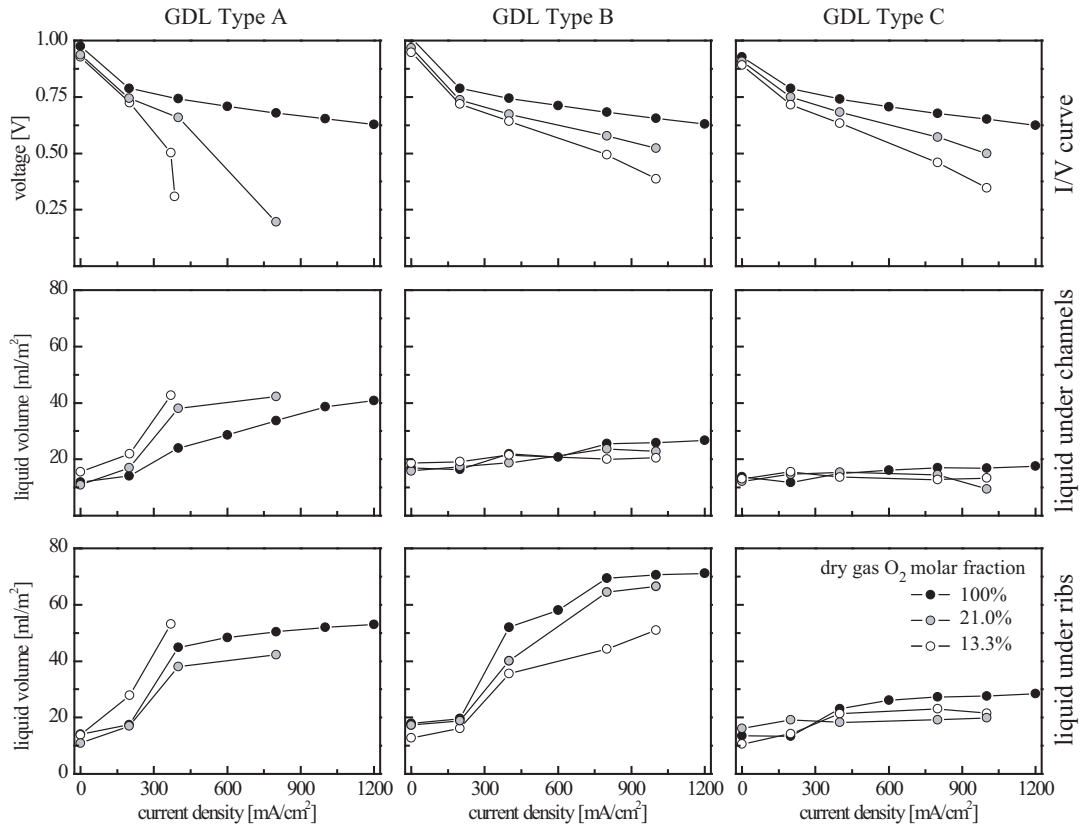
Figure 3.10: Influence of oxygen molar fraction on liquid content separated into rib (lower row) and channel area (middle row), and electrochemical performance (upper row) for different GDL materials applied at the cathode; the cell temperature is 70 °C; the relative humidity of anodic and cathodic gas feed is 80 %; the anodic stoichiometry of H_2 is 18 for oxygen and air operation and 7 for diluted air; the cathodic stoichiometry is 150 for oxygen, 30 for air, and 19 for diluted air.

GDL Type B might be attributed to the inhomogeneity of liquid content under ribs and channels. Theoretical work of KULIKOVSKY et al. [14] or JENG et al. [122] indicates that the rib area is not effectively used in the high current domain due to the increased diffusion length of oxygen even if a loss of porosity due to flooding is not considered. If the current density under the ribs is already much less than under the channels for a liquid-free GDL, flooding under the ribs would have only a weak impact on performance, provided the GDL under the channels is not flooded. This fact could provide a possible explanation for the observed insensitivity even though they based their calculations on a porosity value well below those specified in Table 3.1. Furthermore, recent results of FREUNBERGER et al. [15] seem to support this. They measured the current density distribution under ribs and channels in a specialized cell with an active area of $1\,\mathrm{cm}^2$, finding a derogation of the current generation under the ribs for high current densities. Calculations of NATARAJAN and VAN NGUYEN—who parameterized their model with a porosity much closer to those of the investigated materials—predict the strong separation of liquid inside the GDL observed for Type B [123]. At the same time, however, their results suggest a strong impact on electrochemical performance. Therefore, this explanation is likely to be somewhat oversimplified. The relation between liquid content and effective oxygen diffusivity—an aspect touched upon within Section 3.2.4—would be needed to develop a refined understanding of the observed insensitivity. Moreover, the relation between liquid within GDL and MPL, which was theoretically considered by PASAOGULLARI and WANG [124], might have bearings on the relation between liquid content within the GDL and the electrochemical performance.
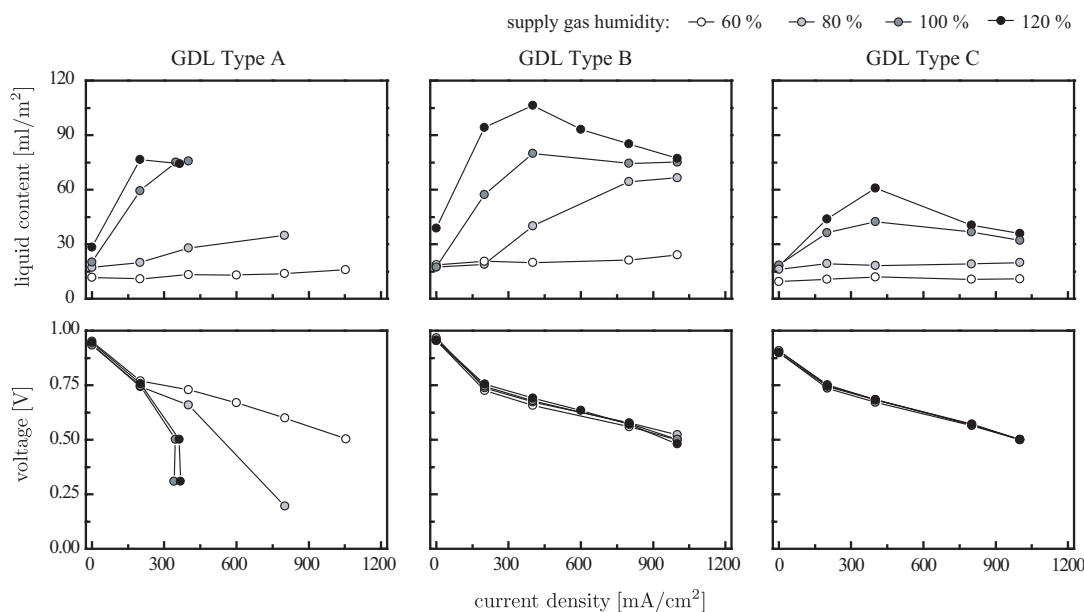
Figure 3.11: Liquid accumulation under the ribs and electrochemical performance as a function of supply gas humidity; the cells were operated at 70 °C at near ambient pressure; the anodic stoichiometry is 19; the cathodic supply is air with a stoichiometry of 30.

3.2.3.2 Sensitivity towards humidity

The liquid accumulation under the ribs as a function of supply gas humidity is displayed in Figure 3.11. A humidity of 120 % is to be understood as follows: the humidifier was set to a temperature above cell temperature; hence, liquid was brought into the cell, because the inlet gas temperature was equal to the cell temperature. In agreement with the simplified scheme depicted in Figure 3.7, liquid inside the channels was observed under fully and over-saturated conditions, and the water content quantification had to be confined to the rib area by masking. Virtually no liquid is present for all three GDL types, if the humidity is below or at 60 %. Largely, the offset in liquid content of about $10 \, \text{ml/m}^2$ can be attributed to membrane hydration. Hence, the removal rate in vapor state is sufficiently large for all GDLs, and the cells operate under condition 1 of the mechanism depicted in Figure 3.7. An interesting trend is observed for the GDLs Type B and C. As long as unsaturated gases are fed to the cell, the liquid content is either constant or gradually increasing with current density. If fully or over-humidified gas is fed to the cells, the liquid content is highest in the middle current density range (around $400 \, \text{mA/cm}^2$). At a first glance, this seems to contradict the proposed transport mechanism, because with increasing current density the production rate increases and the liquid content within a GDL is expected to follow the same trend. Yet, it has to be kept in mind that neutron imaging is a transmitting technique, and hence the cumulative liquid of anode and cathode is detected. The maxima are most likely due to the presence of liquid within the anodic GDLs, which decreases with increasing current density due to the electroosmotic drag. This would indicate that the electroosmotic drag not only counter-balances the permeation of water from cathode to anode under humid conditions but causes a net water flux from anode to cathode even if the cathode is flooded. As depicted in Section 3.6 on page 150, first results from high-resolution neutron imaging indicate that no liquid is present within the anodic GDL at higher current densities despite the supply with fully humidified hydrogen. Although these experiments support the given explanation, the possible influence of flow rate change due to the stoichiometric operation cannot be completely disregarded. Under fully or over-humidified conditions, the liquid removal mechanism is dominated by droplet removal (condition four in Figure 3.7). Hence, the
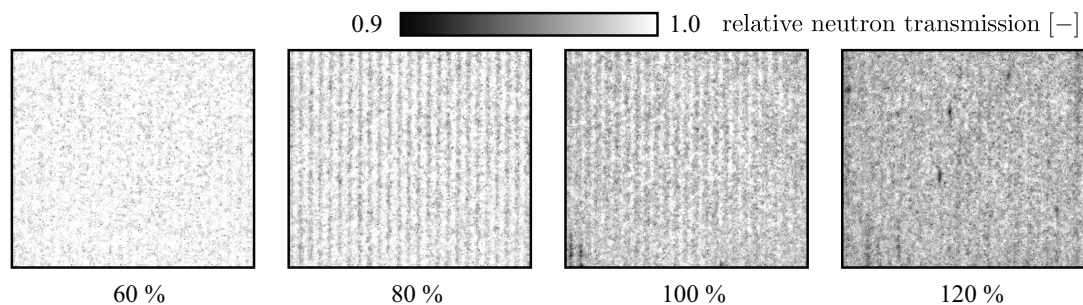
Figure 3.12: Neutron images showing the liquid content under ribs and channels as function of humidity for GDL Type B; operating conditions are the same as given in Figure 3.11; the current density is $1200 \, \mathrm{mA/cm^2}$.

increase of flow rate with current density might support the removal of droplets and by this reduce the liquid content within the cathodic GDL for higher current densities. However, as will be shown below, this effect is rather small.

The polarization curves obtained at 60 % humidity coincide, which is slightly surprising given the differences in porosity and thickness of the compared GDL materials. Obviously, the oxygen diffusion through the GDL is not the dominating rate-determining step as long as the GDL is liquid-free. Again, GDL Type A is characterized by the highest sensitivity of the electrochemical performance to the supply gas humidity. Under fully and over-humidified conditions a limiting current density of approximately $380 \, \mathrm{mA/cm^2}$ is observed in conjunction with a liquid content of about $80 \, \mathrm{ml/m^2}$. The same amount of liquid does not significantly impede the electrochemical performance in the case of GDL Type B, which can be concluded from the diagram in center of the lower row of Figure 3.11. With increasing humidity a slightly reduced ohmic resistance results in a marginal performance gain in the medium current density range (around $600 \, \mathrm{mA/cm^2}$). Yet, the performance loss in the high current density range (around $1000 \, \mathrm{mA/cm^2}$) is likewise marginal, although a substantial amount of liquid is present. In that context, it is worth noting that the strong partition of liquid that was observed for this GDL type at a humidity of 80 % is gradually decreasing with increasing humidity. This is clearly evident from the neutron images shown in Figure 3.12. The possible explanation that the electrochemical insensitivity stems from the partitioning of liquid given in the last section is hence considerably weakened. The liquid content is homogeneous under over-humidified conditions as can be seen from the right image in Figure 3.12. Yet still, the electrochemical performance is only slightly impeded. This strengthens the motivation to find the reason for the insensitivity either in differences in the effective diffusivity or in the relation of liquid content within GDL and MPL or electrode. Finally, the GDL Type C is even less sensitive towards the supply gas humidity, which is in agreement with the observed low tendency to accumulate liquid.

3.2.3.3 The influence of the cathodic flow rate

As discussed within the last section, the flow rate within the channels might have an influence on the liquid accumulation within the GDL, because the removal rate of droplets from the GDL surface is a function of the flow rate. This was investigated for the GDL Types A and C (cf. Table 3.1 on page 100) by changing the cathodic flow rate over a wide range while maintaining the same current density and supply feed humidities. Fully humidified gases were supplied to ensure the droplet removal as dominating transport mechanism (cf. Figure 3.7 on page 98). Pure oxygen was favored as cathodic supply for this purpose, because this allows varying the flow rate in a wider
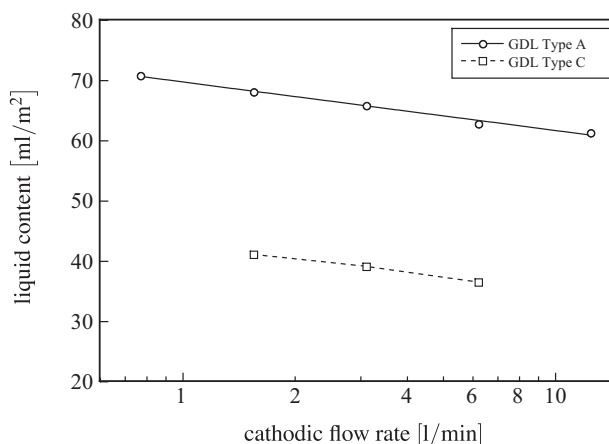
Figure 3.13: The influence of the cathodic flow rate onto the liquid accumulation within different GDLs; the cell temperature is 70 °C; the current density is 1000 mA/cm^2; anodic flow rate is 3.13 l/min; relative humidity of both feeds is 100 %.

range without significantly influencing the electrochemical performance. The cells were operated at 1000 mA/cm^2, and the detected liquid content under the ribs as function of flow rate is shown in Figure 3.13. The oxygen flow rate was varied over more than one order of magnitude. Yet for both GDLs, the liquid content within the GDL changes only by about 10 ml/m^2. In the logarithmic scaling of the plot, the liquid content change is proportional to the flow rate. Notably, the slope of the curves is comparable for both materials, although the absolute values are quite different. Interestingly, the logarithmic relation is in good agreement with the dependence of the droplet detachment diameter determined by ZHANG et al. [118] for a particular paper-type GDL. The relation, however, between liquid content within the GDL and flow rate is too weak to be the main cause of the strong maxima in liquid content at intermediate current densities that were discussed in Section 3.2.3.2, which strengthens the given explanation based on a changing liquid content within the anodic GDL.

The interplay between liquid within the GDL and the channels might be further explored by investigating the relation between liquid within the channels and GDL. Unfortunately, the liquid content within the channels cannot be measured precisely due to instrumental broadening and the superposition of liquid within GDL and channel within the radiograms. An estimate, however, can be obtained by assuming a homogeneous liquid content within the GDLs under channel and ribs. This is a reasonable assumption for the GDL Types A and C as shown in Section 3.2.3.1. With this assumption, the liquid content within the channels is estimated by obtaining the total liquid content within the cell (calculated by considering the whole area: channels and ribs) and subtraction of the liquid content within the GDL as obtained from the rib area only. As shown in Figure 3.14, plotting the liquid content within the GDL against the liquid content within the channels displays a linear relationship. It is worth noting that extrapolation yields a liquid content different from zero for the GDL even for vanishing liquid content within the flow fields. Or in other words, even for a perfect removal from the channel, the requirement of liquid transport within the GDL still results in significant flooding. This shows that the removal from the GDL surface is influencing but not necessarily dominating the liquid transport rate.

In conclusion, it can be stated that under fully humidified conditions the removal of liquid from the GDL is influenced by the removal of droplets within the channel, which is in agreement with the mechanism proposed at the beginning of Section 3.1. The liquid content within the GDL, therefore, depends on the gas flow rate. The dependence, however, is rather weak showing that the droplet removal is not dominating but merely contributing to the net removal rate.

106
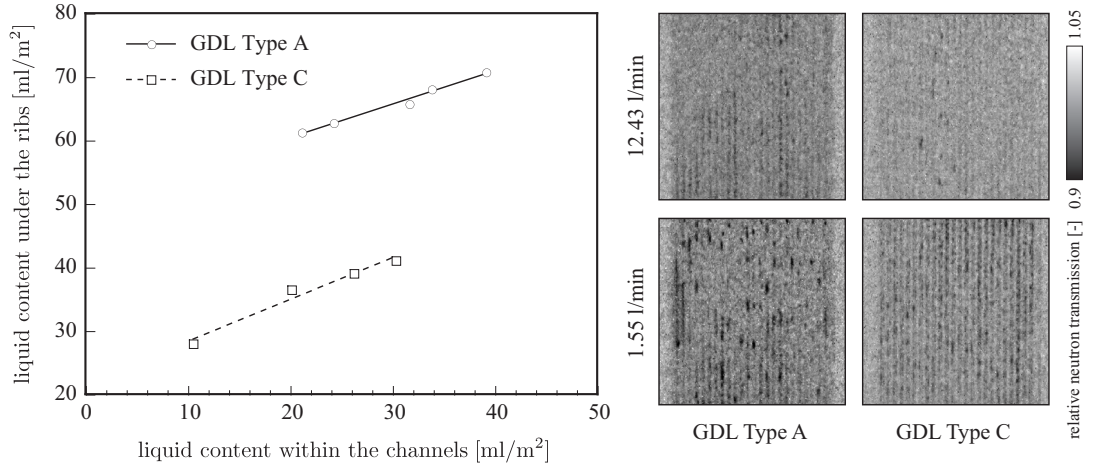
Figure 3.14: Relation between liquid inside the GDL and flow field; the data has been obtained from the same neutron images that form the basis of Figure 3.13; selected neutron images are shown at the right-hand side of the diagram.

3.2.4 Flooding and the effective diffusivity

So far, the accumulation of liquid within the porous structures and its relation to the electrochemical performance was analyzed. The coupling essentially originates from the dependence of the reaction rate on the oxygen concentration at the cathodic electrochemical active surface (cf. Equation (1.45) on page 16). If liquid within the GDL is hampering the transport of oxygen towards the electrode, the oxygen concentration at the electrode surface is reduced, and the resulting current for a given overpotential is diminished. In consequence, it is natural to ask for the relation between the degree of flooding and the resulting mass transport hindrance with respect to oxygen transport towards the electrode.

3.2.4.1 The limiting current density as measure for the effective diffusivity

Unfortunately, it is highly complicated, if not impossible, to measure the oxygen concentration at the electrode surface directly. Therefore, information about the oxygen transport resistance is sought indirectly by investigating the limiting current density. The limiting current density (in its classical definition) was already introduced by Equation (1.51) on page 17. This definition considers only the GDL as mass transport resistance, which is obviously not true as oxygen has to penetrate the electrode in order to be available at electrochemical active surface throughout the electrode. Hence, the limiting current density will be revised from a theoretical perspective leading to a generalized definition of the effective diffusivity. The considerations expand upon the work of EIKERLING and KORNYSHEV [32, 46] and will largely follow their nomenclature.

A popular model of porous gas diffusion electrodes is the agglomerate model, where the electrode is described as a random collection of rigid spheres (the agglomerates), which are optionally covered by an electrolyte film. Between those agglomerates, small meso-pores are formed providing pathways for the oxygen to diffuse through the thickness of the electrode. This is illustrated in Figure 3.15. If the electrode structure is neglected in a first order approximation, the oxygen partial pressure within the gas-filled pores is given by:

$$\partial_{z,z} p' - \frac{J^\circ}{I_k} \cdot p'(z) = 0 \tag{3.2}$$

Herein, $p' = p(z)/p^\circ$ is the dimensionless oxygen partial pressure normalized to a reference pressure
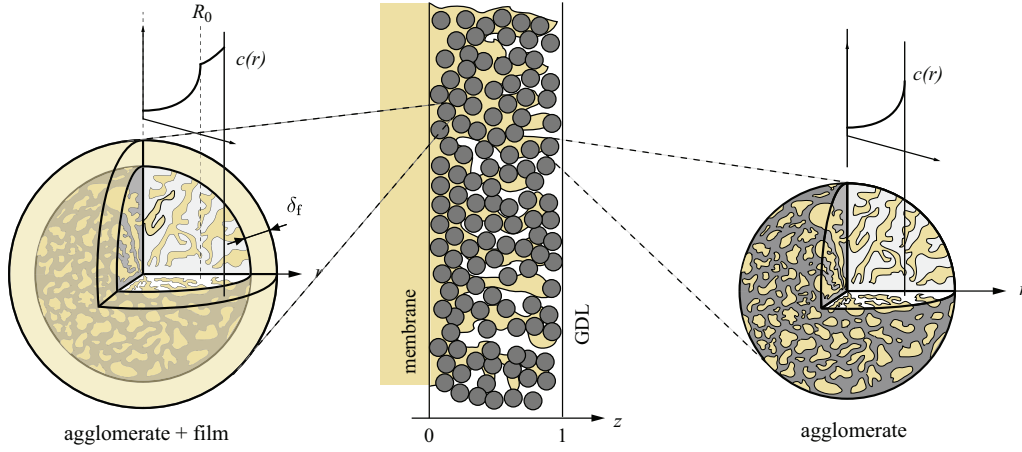
Figure 3.15: Illustration of the agglomerate model to describe porous gas diffusion electrodes.

p°, z is the normalized thickness coordinate of the electrode ranging from $z = 0$ at the membrane-electrode interface to $z = 1$ at the electrode-GDL interface, J° is the current density associated with the pressure p° (the current density resulting from a constant oxygen partial pressure p° within all meso-pores), and I_k is a parameter characterizing the oxygen transport within the gas-phase of the electrode. Assuming KNUDSEN diffusion to be the dominating transport mechanism, I_k would be given by

$$I_k = \frac{4 \cdot \mathcal{F} \cdot \epsilon \cdot D_k}{R \cdot T \cdot l} \cdot p^\circ, \tag{3.3}$$

where l denotes the thickness of the electrode, ϵ its porosity, and D_k the oxygen diffusion coefficient. The oxygen partial pressure as a function of the electrode thickness is obtained by integrating Equation (3.2) with the boundary conditions $\partial_z p' = 0$ at $z = 0$ and $p' = p'(1)$ at $z = 1$, which leads to

$$\frac{p'(z)}{p'(1)} = \frac{\cosh(\gamma \cdot z)}{\cosh(\gamma)} \quad \text{with} \quad \gamma = \sqrt{\frac{J^\circ}{I_k}}. \tag{3.4}$$

The resulting current density is found from

$$j = \int_0^1 p'(z) \cdot J^\circ \cdot dz = I_k \cdot \gamma \cdot \tanh(\gamma) \cdot p'(1). \tag{3.5}$$

To obtain an expression for J°, the oxygen diffusion into the agglomerates has to be accounted for. The oxygen concentration as function of the radius of the agglomerate obeys:

$$\frac{1}{r^2} \cdot \partial_r \left(r^2 \cdot \partial_r c' \right) - \kappa^2 \cdot c' = 0 \quad \text{with} \quad \kappa^2 = \frac{j_k(\eta)}{I_a} \tag{3.6}$$

Herein, r denotes the normalized radius of the agglomerate, c' the normalized concentration within the agglomerate ($c'(r = 1) = 1$), and κ is a parameter consisting of a kinetic and a mass transport term. For example, assuming TAFEL kinetics would lead to $j_k(\eta) = i^* \cdot \exp\{\eta/b\}$, where η and i^* are the overpotential and exchange current density, respectively. In similarity to Equation (3.3), the mass transport term is given by

$$I_a = \frac{4 \cdot \mathcal{F} \cdot \epsilon_a \cdot D_a \cdot H}{R_0^2} \cdot p^\circ, \tag{3.7}$$

where ϵ_a is the volume fraction of the electrolyte or liquid water containing phase within the agglomerate; D_a is the corresponding oxygen diffusion coefficient, and H is HENRYs constant linking the oxygen concentration within the electrolyte/water phase to the oxygen partial pressure sur-

rounding the agglomerate; R_0 denotes the radius of the agglomerate. Integration of Equation (3.6) with $\partial_r c' = 0$ at $r = 0$ and $c' = 1$ at $r = 1$ leads to

$$c'(r) = \frac{\sinh(r \cdot \kappa)}{r \cdot \sinh(\kappa)}, \tag{3.8}$$

and the electric current generated by a sphere is obtained by integrating the current generated at a given radius over the whole agglomerate:

$$J_a = \int_0^1 I_a \cdot \kappa^2 \cdot c'(r) \cdot \underbrace{4\pi \cdot r^2 \cdot dr}_{dV} = 4\pi \cdot I_a \cdot \left[\frac{\kappa}{\tanh(\kappa)} - 1 \right] \tag{3.9}$$

Finally, J_a has to be multiplied by n, where n is the number of agglomerates per unit volume within the electrode. This leads to

$$J = 3 \cdot (1 - \epsilon) \cdot I_a \cdot \left[\frac{\kappa}{\tanh(\kappa)} - 1 \right]. \tag{3.10}$$

Up to here, the possible coverage of the agglomerate with a film (either electrolyte or liquid water) was not considered. However, it is easily shown that this can be respected by correcting J according to

$$J^\circ = J \cdot \left[1 + \frac{J}{J_{\max}} \right]^{-1}, \tag{3.11}$$

where $J_{\max}$ is the maximal current density that can be generated before the oxygen concentration at the interface between agglomerate and film becomes zero. For a spherical coverage of an agglomerate with a film of thickness δ_f results

$$J_{\max} = 3 \cdot I_a \cdot \frac{1 - \epsilon}{\epsilon_a} \cdot \left\{ \left(\frac{R_0 + \delta_f}{R_0} \right)^3 - \left(\frac{R_0 + \delta_f}{R_0} \right)^2 \right\}^{-1}. \tag{3.12}$$

Obtaining an expression for $p'(1)$ in Equation (3.5) is the final step, completing the system of equations. It is easily shown that

$$j = j_{\max} \cdot (1 - p'(1)), \tag{3.13}$$

if the reference pressure p° is chosen to be the oxygen partial pressure at the boundary between GDL and channel. Herein, $j_{\max}$ is the maximal current density that can be generated before the concentration at the interface between electrode and GDL becomes zero (classical definition of the limiting current density), which under the assumption of FICK's diffusion through the GDL would be given by

$$j_{\max} = \frac{\epsilon_g}{\tau_g} \cdot \frac{4 \cdot \mathcal{F} \cdot D_g}{R \cdot T \cdot \delta_g} \cdot p^\circ. \tag{3.14}$$

Herein, ϵ_g and τ_g denote the porosity and tortuosity, respectively; D_g is the oxygen diffusion coefficient, and δ_g symbolizes the thickness of the electrode. Finally, this leads to

$$j = \left\{ \frac{1}{I_k \cdot \gamma \cdot \tanh(\gamma)} + \frac{1}{j_{\max}} \right\}^{-1} \tag{3.15}$$

as expression for the current density. An expression for the limiting current density is found by letting

$$j_{\lim} = \lim_{\eta \to \infty} j = \lim_{\eta \to \infty} \left\{ \frac{1}{I_k \cdot \gamma \cdot \tanh(\gamma)} + \frac{1}{j_{\max}} \right\}^{-1}. \tag{3.16}$$

For $\eta \to \infty$ also κ tends towards infinity due to Equation (3.6). If κ tends to infinity, J° equals $J_{\max}$ because Equation (3.10) tends towards infinity, which gives $\gamma = \sqrt{J_{\max}/I_k}$ due to Equation (3.4).

Introduction of this expression for γ into Equation (3.15) leads to the following expression for the limiting current density:

$$j_{\lim} = \left\{ \frac{1}{\sqrt{J_{\max} \cdot I_k} \cdot \tanh\left(\sqrt{\frac{J_{\max}}{I_k}}\right)} + \frac{1}{j_{\max}} \right\}^{-1} \tag{3.17}$$

Two important conclusion can be extracted from Equation (3.16):

1. The limiting current density is influenced by oxygen diffusion through the GDL (characterized by $j_{\max}$), through the meso-pores (gas phase) of the electrode (characterized by I_k), and the possible diffusion through a film covering the agglomerates (characterized by $J_{\max}$), and

2. the limiting current density will be proportional to the oxygen concentration within the channel.

While the first conclusion is obvious, the second needs to be explained in more detail. It becomes apparent from the Equations (3.3), (3.7), (3.12), and (3.15) that all parameters within Equation (3.17) are proportional to the oxygen concentration within the channels p°. Hence, the limiting current density itself is proportional to the oxygen concentration within the channels. This allows to define the effective diffusivity K in terms of the limiting current density according to

$$K = \frac{R \cdot T}{p^\circ} \cdot \frac{j_{\lim}}{4 \cdot \mathcal{F}}. \tag{3.18}$$

Yet if defined according to Equation (3.18), the effective diffusivity is a characteristic of the whole MEA[9] rather than the GDL only, because the limiting current density is influenced by oxygen transport through GDL, MPL, and electrode.

3.2.4.2   Measurement of the effective diffusivity

Equation (3.18) presents a way to obtain the effective diffusivity: the limiting current density is obtained for various oxygen partial pressures and normalized with the applied oxygen partial pressure. For that purpose, the cells are operated in potentiostatic mode at a rather low voltage (200 mV). Nonetheless, it has to be shown whether the resulting current is indeed the limiting current. This is done by varying the voltage in a certain range. If operating in the limiting current regime, the current must not depend on the cell voltage. The result of such a validation is shown in Figure 3.16 for the three GDL materials (see Table 3.1) that were already analyzed in Section 3.2.3. Unfortunately, only GDL Type A shows a clear limiting current density behavior. For the GDL Types B and C, the current still varies significantly with the cell voltage indicating that the limiting current density is not reached. As the experimental setup is not suitable for obtaining the limiting current density for those GDLs, the discussion will focus on GDL Type A.

The diagram of Figure 3.17 (a) shows the current density (at 200 mV) as a function of the oxygen molar fraction and supply gas humidity. The diagram (b) shows the corresponding liquid content obtained from the rib area. The theoretically expected linear dependence of the limiting current density on the oxygen molar fraction is found for fully humidified conditions and, with exception of the highest current density, for a relative humidity of 60 %. If the gases are supplied with 80 % humidity, the relation between oxygen concentration and limiting current density is highly

---

[9]If possible inhomogeneities under channel and rib are considered [16], the effective diffusivity might also be influenced by the actual cell hardware (e.g., channel and/or rib width).
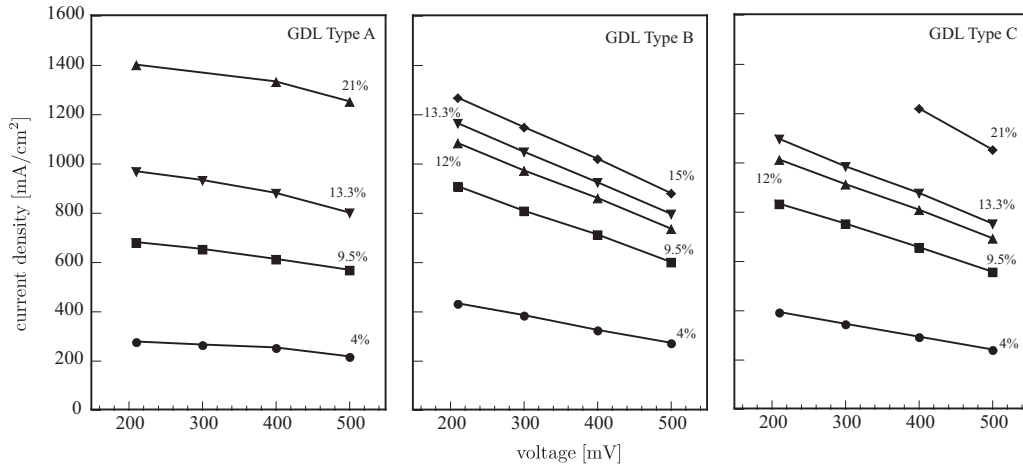
Figure 3.16: Voltage dependence of the electrical current at low cell voltages as function of the oxygen molar fraction within the cathodic feed; the cells were operated at 70 °C at near ambient pressure; the relative humidity of both feeds is 60 %; properties of the compared materials are given in Table 3.1.

non-linear. This behavior is easily understood by considering diagram (b). For fully humidified conditions, the liquid content is virtually constant as function of current density or oxygen molar fraction. Also for a relative humidity of 60 %, this is fulfilled with the exception of the highest oxygen molar fraction. In consequence, the effective diffusivity does not change resulting in the linear relation between limiting current and oxygen molar fraction. Furthermore, the different slopes are evidence of the detrimental impact of liquid within the porous structures. If the cell is supplied with gases that are prehumidified to 80 % relative humidity, the liquid content is increasing with current density. This was expectable considering the results of Section 3.2.3.2. Consequently, the effective diffusivity changes with current density resulting in the non-linear trend.

The diagrams (a) and (b) are combined in diagram (c) by plotting the effective diffusivity as
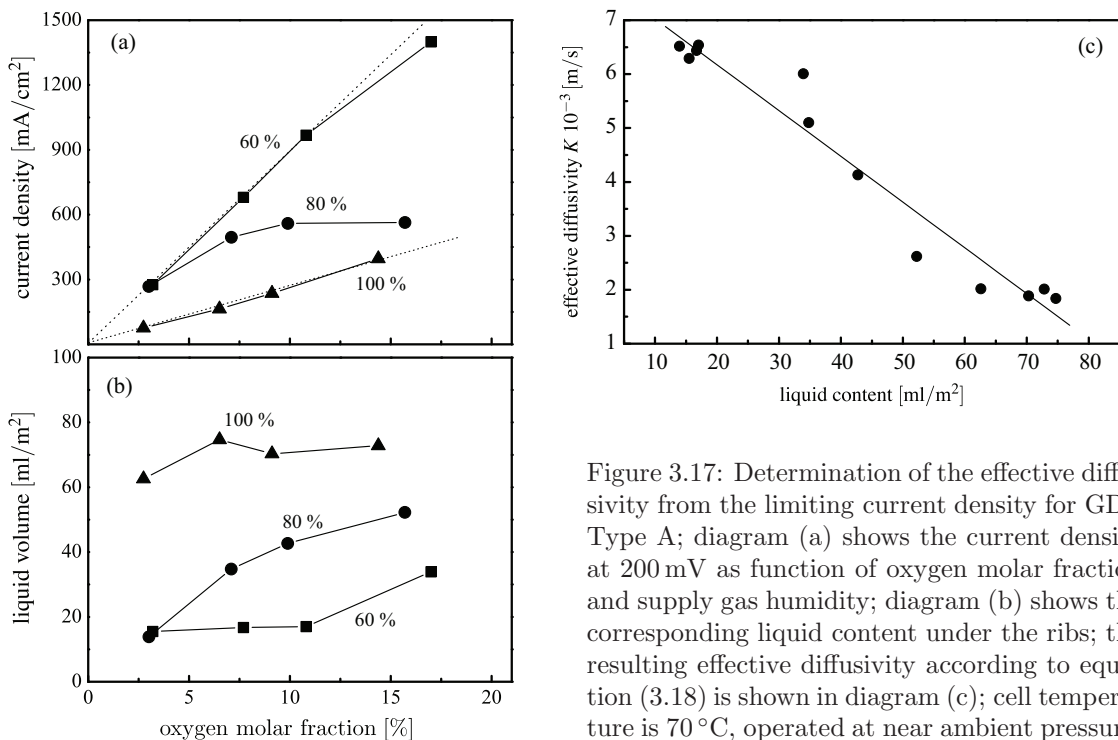
Figure 3.17: Determination of the effective diffusivity from the limiting current density for GDL Type A; diagram (a) shows the current density at 200 mV as function of oxygen molar fraction and supply gas humidity; diagram (b) shows the corresponding liquid content under the ribs; the resulting effective diffusivity according to equation (3.18) is shown in diagram (c); cell temperature is 70 °C, operated at near ambient pressure.

111

function of the liquid content. When studying the plot, it has to be kept in mind that the liquid content contains an offset of about $15\,\mathrm{ml/m^2}$, which is attributed to membrane hydration. Hence, for liquid-free[10] porous structures an effective diffusivity of about $6.5\,\mathrm{mm/s}$ is found, which strongly declines to about $1.5\,\mathrm{mm/s}$ if the porous structures are filled with $80\,\mathrm{ml/m^2}$. Due to the scatter accompanying the data, it is not possible to extract an exact relation between liquid content and effective diffusivity, and the shown linear regression is intended more as guidance for the eye than to imply a linear correlation. The liquid-free effective diffusivity seems surprisingly low. Assuming planar diffusion through the GDL as only contributing effect, the effective diffusivity can be expected to be around $30\,\mathrm{mm/s}$ from FICKs first law[11]. The least known characteristic of a GDL needed to calculate the effective diffusivity is the tortuosity. Especially, modeling work is frequently based on rather high values[12] to achieve limiting currents that are in agreement with experiment—inter alia [122, 125–127]. Lattice gas simulations [128, 129] and analytical geometry considerations [130, 131], however, suggest values of about two or lower, and first results of *ex situ* measurements [132] point in the same direction. Taking the theoretic considerations described within the last section into account, the discrepancy indicates that other components might likewise influence the overall oxygen transport resistance towards the electrochemical active sites. A complete discussion would need at least the additional consideration of electrode morphology, MPL, and possible inhomogeneities under channels and Ribs [15].

3.3 Liquid distribution within GDLs and local performance

After the relation between GDL material choice, liquid accumulation, and electrochemical performance was analyzed under simplifying experimental conditions within Section 3.2, the question of how these results relate to cells working under technically more realistic constrains will be addressed within this section. Three aspects need consideration: (1) the cell size should be comparable to common, technically used designs, (2) the operating conditions, and here especially the stoichiometric ratios of the supply feeds, have to be technically realistic, and (3) the set of applied diagnostic methods has to adequately resolve the expectable spatial inhomogeneities.

3.3.1 Cell design for simultaneous neutron imaging and current distribution measurement

To obtain the local current generation, the segmented cell approach described in Section 2.3.1.1 was favored. However, the simultaneous requirement of good neutron transparency imposes some constrains not common for other segmented cells. Being based on the cell design utilized for the study depicted in Section 3.1, the cells consisted of graphite-made flow fields with a serpentine structure and $100\,\mathrm{cm^2}$ active area. Yet, a segmented current collector was embedded on one side. The end plate housing the segmented collector was anodized rather than gold-coated, insulating the end plate from the current collector. Further on, the end plate was structured such that a precise positioning of the segments was ensured. A sketch of the experimental setup is depicted in Figure 3.18. A neutron image (referenced to an openbeam image) shows the interior of the cell. The different current collector segments are indicated by boxes. The segmentation layout was chosen such that the flow path (as guided by the serpentine structure) passes each segment subsequently

---

[10]Strictly speaking: for liquid contents below the detection limit
[11]Estimate based on the following values: oxygen diffusion coefficient $2.73\cdot10^{-5}\,\mathrm{m^2/s}$, GDL thickness $240\,\mathrm{\mu m}$, GDL porosity $60\,\%$, and GDL tortuosity 2.
[12]Alternatively, many authors parameterize their models with porosity values as low as 0.2.
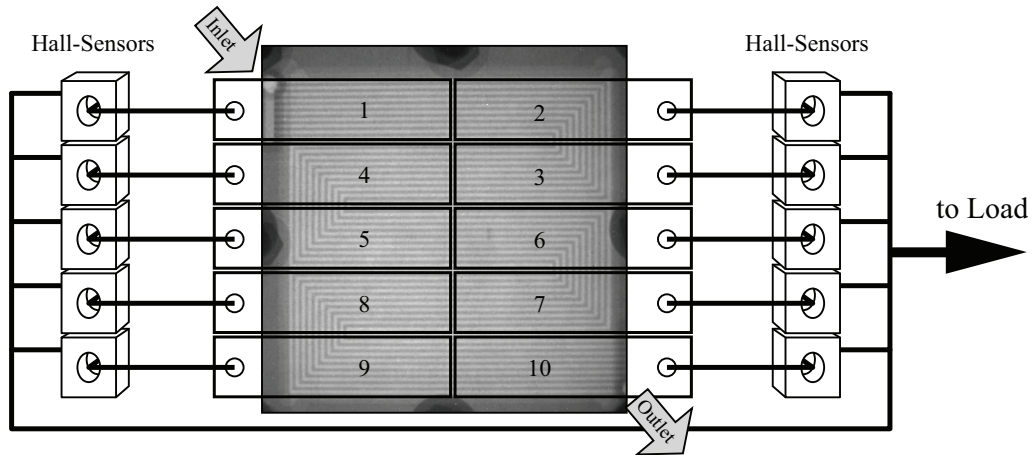
Figure 3.18: Experimental setup for simultaneous neutron imaging and current density measurement within a cell of $100\,cm^2$ active area with serpentine flow field.

without crossing an individual segment twice. The gold-coated current collector sheets protruded from the cell at the left and right. The individually collected currents were passed through cables to a multi-channel current sensor consisting of an array of Hall sensors. The non-segmented side as well as the flow field geometry and material are similar to the non-segmented serpentine cells with graphite-made flow field described in Section 3.1.1. For the sake of simplicity, the flow field itself was not segmented on either side. Hence, the current measured by a segment differs from the current generated within the area spanning the individual segments. Although the ohmic resistance of the outer measurement circuit was minimized by the use of Hall sensors and careful cell design and assembly, a certain error due to lateral currents cannot be avoided as estimated in Section 2.3.1.2. Nonetheless, the current density distribution is preserved well enough to study the relations between local liquid and current distribution.

3.3.2 The influence of operating conditions

The influence of the cathodic stoichiometric ratio and inlet humidity will be explored first. A MEA comprising the same type of CCM as used for the differential cell measurements and GDL Type A (cf. Table 3.1 on page 3.1) on both sides will be investigated, because the results obtained with the differential cells indicate that this material combination entails the strongest correlation between liquid content and electrochemical performance.

The cells were investigated by obtaining galvanostatically controlled polarization curves under stoichiometric operation. Following the usual procedure, the cells were dried before every experiment by purging with dry nitrogen and images taken at the end of the purge served as reference images for the subsequent experiment. The cells were operated at NEUTRAs measurement position one, and the standard CCD-detector was favored as detector system.

The current density as function of position along the serpentine flow path together with the corresponding liquid content within the GDL is shown in Figure 3.18 for a stoichiometric ratio of 1.5 (both feeds) and a relative humidity of $50\,\%$ at the inlets. The current density is shown in diagram (a), and the liquid content as obtained from the land area is shown by diagram (b). Corresponding neutron images are shown at the right for illustration. On the basis of the liquid profiles, the whole area can be subdivided into three regions: (I) a region where no liquid is present within the cell near the inlet, (II) a transient region, where the liquid content is increasing along the serpentine flow path, and (III) a region near the outlet, where the liquid content is virtually constant along
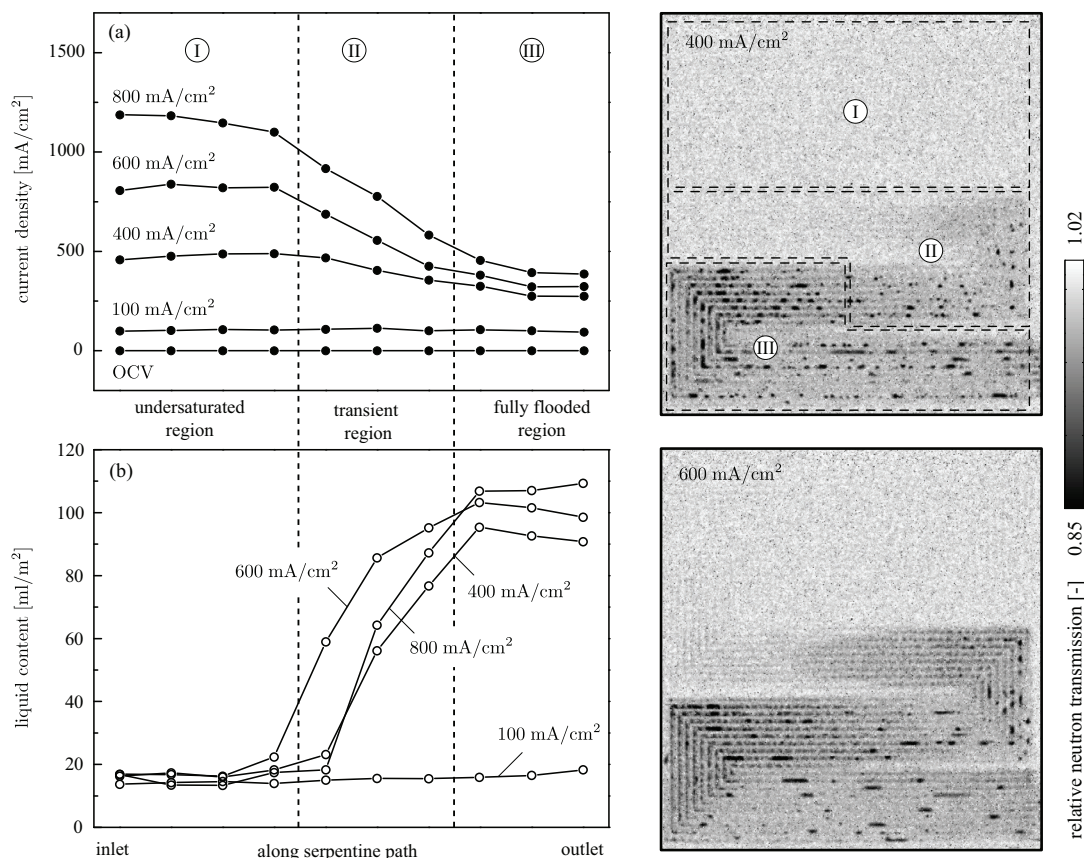
Figure 3.19: Current density and liquid content as function of position along a serpentine flow field; diagram (a) shows the current density distribution, and the corresponding liquid content is depicted in diagram (b); selected neutron images are shown to the right for illustration; the cell was operated at 70 °C under near ambient pressure; anodic stoichiometry is 1.5; cathodic stoichiometry is 1.5; relative humidity of both feeds is 50 %; the GDL Type A serves at the anode and the cathode, respectively.

the serpentine. This profile is qualitatively in agreement with the simplistic mechanism depicted in Figure 3.7 on page 98. Near the inlet, the relative humidity within the channels is low enough to avoid condensation (sufficiently large water vapor gradient between electrode and channels). Recalling the differential cell results, it is expectable that the inlet is dry, because no liquid is expected for relative humidities below 60 % (within the channels). The product water, however, humidifies the gas flow, and the dry region is followed by a transient region with increasing liquid content along the flow path. Following the simplistic mechanism, this region corresponds to the case where the saturation pressure is still not reached within the channels, yet a sufficiently large vapor pressure gradient over the GDL cannot be established without reaching the saturation pressure within the GDL. The increase in liquid content, therefore, is related to an increasing vapor pressure within the channels. Finally, the liquid content within the GDL stabilizes near the outlet reaching a maximum value of about $100 \, \mathrm{ml/m^2}$. The liquid profile is reflected within the current density distribution—especially at higher current densities, where mass transport starts to dominate the electrochemical performance. Region (I) is characterized by the highest current densities. This stems from the fact that the highest oxygen concentrations and the highest effective diffusivity coincide. Careful observation shows that the inlet segment is slightly depleted in performance for an average current density of $400 \, \mathrm{mA/cm^2}$ and $600 \, \mathrm{mA/cm^2}$. This slight performance deterioration is obviously not related to oxygen mass transport but originates from the humidity dependence of the electrolyte conductivity. Yet, the deteriorative impact of a dry inlet conditions is not very pro-
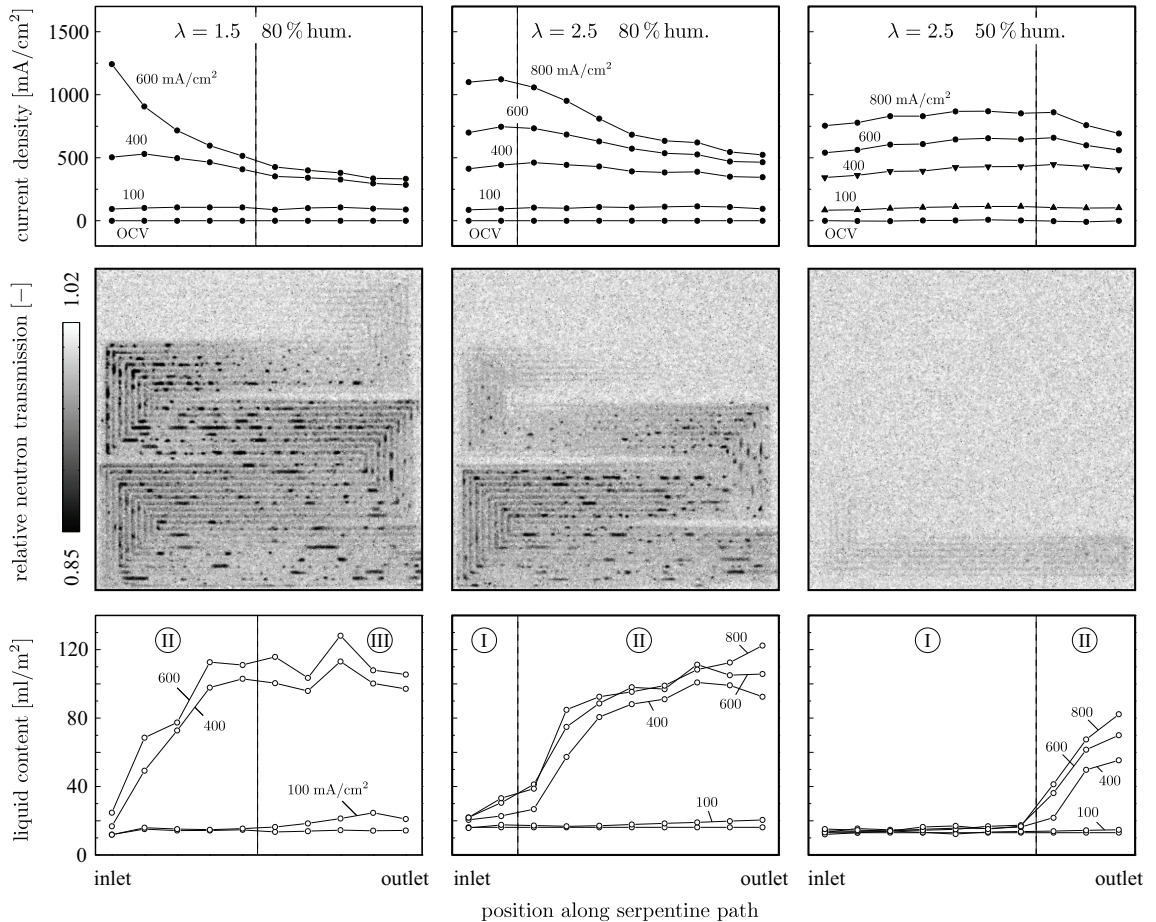
Figure 3.20: Influence of operating conditions onto local current density and liquid content; the diagrams of the upper row show the current density at different average current densities, the neutron images shown of the middle row correspond to an average current density of $400\,\mathrm{mA/cm^2}$, and diagrams showing the liquid content within the GDL are lined-up in the lower row; the cell was operated at $70\,^\circ$C under near ambient pressure; anodic stoichiometry is 1.5; the inlet humidity of the anode equals that of the cathode; the GDL Type A serves at the anode and the cathode, respectively.

nounced here. This might be different for other MEA materials as will be shown in Section 3.4.2. Consequently, the current density is slightly decreasing (due to the reducing oxygen concentration along the flow path) or virtually constant through-out region (I) (due to the counter-balancing effect of drying at the inlet). Region (II) is characterized by a steep decline in current density along the flow path—considerably steeper than in region (I) and (III). This originates from the combination of oxygen depletion along the flow path and a reducing effective diffusivity due to the increasing liquid content within the GDL. This shows very clearly the deteriorative impact of liquid within this type of GDL. It is worth noting that the decline in current density levels out again in region (III), although at a much lower level than in region (I). The constant liquid content within the fully flooded region is reflected here. Due to this, the reducing oxygen concentration is solely contributing to the decline in current density along the flow path within region (III). However, the overall lower current density within this region compared to the regions (I) and (II) originates not only from oxygen depletion along the flow path but also from a hampered oxygen diffusion through the flooded porous structures.

The influence of changing inlet humidity and the stoichiometric ratio of the cathodic supply becomes apparent from the diagrams lined-up in Figure 3.20. The left column shows the change in liquid content and current distribution, if the inlet humidity is increased from 50 % to 80 %. Only

the segment nearest to the inlet is nearly liquid-free under these conditions, and the liquid profile increases from the inlet to around segment five. The slope of the liquid increase is similar to that observed in region (II) with an inlet humidity of 50 %. In addition, region three, which stretches roughly from segment six to the outlet, shows the same constant maximum liquid content. In consequence, the current density distribution is rapidly decreasing already near the inlet at higher average current densities ($600\,\mathrm{mA/cm^2}$) and levels out to approximately the same low current density near the outlet as observed with an inlet humidity of 50 %. If the cathodic stoichiometry is increased from 1.5 to 2.5 (middle column), the onset of flooding is slightly moved downstream to segment three. Qualitatively, the current density is similar to that of Figure 3.19. The current density within the undersaturated region (I), which roughly stretches over the first two segments, is slightly increasing due to the beneficial impact of the increasing humidity with respect to the ionic conductivity. Region (II) is again characterized by a steep decline in current density resulting from the increasing mass transport hindrance due to the increasing liquid content and reducing oxygen concentration. Near the outlet, the slope of the current density profile levels out. Yet, the current density near the outlet is significantly higher than achieved with a stoichiometry of 1.5 due to the higher oxygen concentration near the outlet resulting from the higher stoichiometric ratio. The right column shows the results obtained by operating the cell with an inlet humidity of 50 % and a cathodic stoichiometry of 2.5. The combination of lower inlet humidity and higher flow rate results in a strong reduction of the flooded portion of the active area, because the gas feed can take up considerably more water vapor before reaching the saturation pressure; the undersaturated region (I) stretches from the inlet to segment seven. Within this region, the current density is gradually increasing. This reveals the beneficial impact of higher humidities to the performance originating from the humidity dependence of the electrolyte conductivity very clearly. The current density passes a maximum near the border between region (I) and (II)—this is generally true for most operating conditions—and declines slightly towards the outlet within region (II). The maximum in current density, therefore, is a consequence of the coincidence of an optimal electrolyte conductivity and sufficient oxygen diffusion through the porous systems near the point where water vapor saturation is reached at the electrode. Upstream of this point, the lower humidity is detrimental to performance because of the reduced electrolyte conductivity. Downstream of this point, performance is hampered due to the limited oxygen transport to the electrode, which is a result of the liquid-filled porous structures and depleted oxygen concentration.

3.3.3 Comparison of GDL materials

For the particular material combination investigated within the last section, the flooding seems to be more detrimental to the electrochemical performance than the drying of the inlet region. Consequently, the results of Section 3.2.3 give reason to expect a less pronounced coupling between local electrochemical performance and flooding, if the cathodic GDL material is changed.

The same types of GDL that have been compared within the differential cells—see Table 3.1 on page 100 for material properties—were utilized as cathodic GDL within the $100\,\mathrm{cm^2}$ cells with segmented current collector, and for all experiments the same type of CCM was used. Further on, the choice of GDL Type A as anodic GDL enabled comparability of the spatially resolved investigations with the results obtained by following the differential cell approach. All cells were operated at NEUTRAs measurement position one and investigated by simultaneously obtaining neutron images and current distributions during galvanostatically controlled polarization curves. Again, the cells were dried before every experiment to obtain reference images and to ensure an equal history of operation. The results shown in Figure 3.21 allow a detailed comparison of the
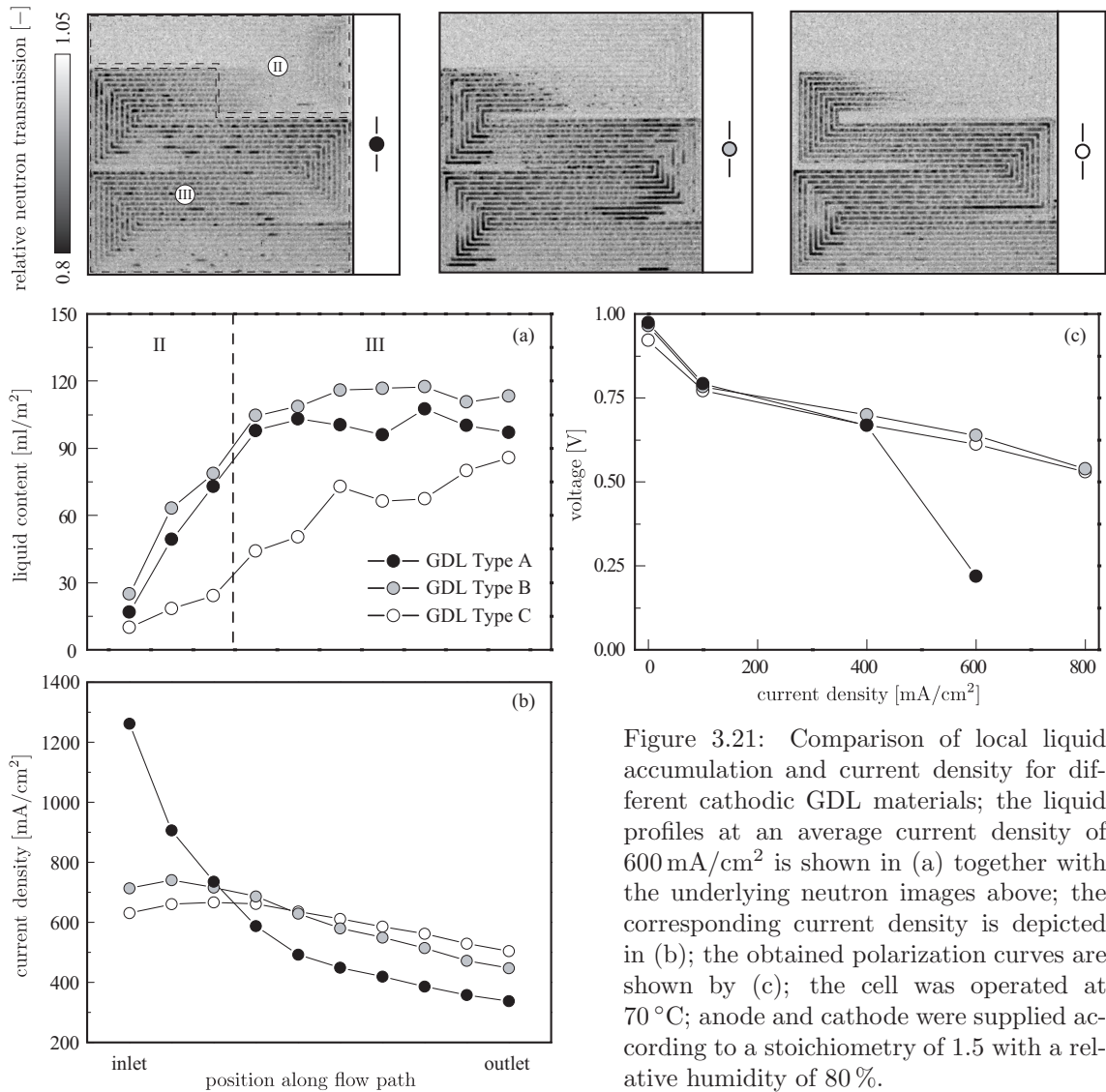
Figure 3.21: Comparison of local liquid accumulation and current density for different cathodic GDL materials; the liquid profiles at an average current density of $600 \, \text{mA/cm}^2$ is shown in (a) together with the underlying neutron images above; the corresponding current density is depicted in (b); the obtained polarization curves are shown by (c); the cell was operated at $70 \, °C$; anode and cathode were supplied according to a stoichiometry of 1.5 with a relative humidity of $80 \, \%$.

three GDL materials. All cells were operated under the same operating conditions: the gases (hydrogen and air) were fed with a relative humidity of $80 \, \%$ according to a stoichiometric ratio of 1.5.

Comparing the polarization curves shown in diagram (c) reveals the same trends as obtained with the differential cells. The GDL Type A shows a significantly hampered electrochemical performance in comparison to the GDL Types B and C at $600 \, \text{mA/cm}^2$, and it was not possible to operate this cell at $800 \, \text{mA/cm}^2$. Further on, the GDL Types B and C show nearly the same electrochemical performance. The utilization of GDL Type B results in a marginal performance gain in the middle current density range. Yet, the loss at $800 \, \text{mA/cm}^2$ is likewise marginal. The liquid content within the GDL (obtained from the land area) at an average current density of $600 \, \text{mA/cm}^2$ is shown in diagram (a), and above the diagrams are the corresponding neutron images. For all three GDLs, only segment one is liquid-free. Both papers (GDL Types A and B) show virtually the same liquid content profiles, which are increasing over the first three to four segments and constant afterwards. This is remarkable considering the different GDL morphology and cell performance at this operating point. Yet, it is in perfect agreement with the behavior observed within the differential cells (cf. Section 3.2.3). Also in compliance with the differential cell investigations is the lower tendency of the cloth-type GDL (Type C) to accumulate liquid and the similar electrochemical performance obtainable by utilizing GDL Type B or C. In contrast to the two paper-type GDLs, it seems

that the cloth-type GDL does not as clearly show a constant liquid content near the outlet. This might be indicative for differences of the liquid transport and removal within cloth and paper. However, it is also possible that the liquid content is stabilizing and that this is concealed by considerable scatter accompanying the data. As the polarization curves might suggest, the current density distribution obtained with GDL Type A notably differs from those obtained with GDL Type B and C. Notwithstanding, a similarity is found as well. Near the outlet (the last four to five segments), the current density is virtually linearly decreasing, whereby the slope is similar for all three GDLs due to the similar decline of the oxygen concentration along the flow path. However, the current density within this region is well below the average value of $600\,\mathrm{mA/cm^2}$ for GDL Type A. The inlet region, which is not as strongly limited by mass transport, has to compensate for the limited current density near the outlet. This results in a strong increase of the current density near the inlet reaching more than twice the average value. This is very costly from the cell voltage point of view. The two other GDL types allow for a significantly higher current density near the outlet; therefore, the inlet region is not forced to produce as much current as in the case of GDL Type A. The current density is highest near the outlet for the cloth-type GDL (Type C), which is agreement with the lower tendency to hold liquid. Yet, also the GDL Type B exhibits a significantly higher current density near the outlet than GDL Type A, although the liquid contents are comparable. The same trend was already observed within the differential cells. For the GDL Types B and C, the maximum current density is again found at the border between the regions. Yet, this time between region (II) and region (III). The slight decline of the inlet region might once more be attributed to the detrimental impact of lower humidity onto electrolyte conductivity.

Taken together, it can be concluded that the active area can be subdivided into three regions: an undersaturated region near the inlet, a region were the liquid content within the GDL is gradually increasing, and a region were the liquid content is reaching a constant maximal level. Whether all three or just two regions are present depends on the operating conditions. The liquid pattern is generally reflected within the current density distribution, although it is biased by the changing oxygen concentration and electrolyte conductivity. The cathodic GDL material has considerable bearing on the current density and liquid distribution. The characteristics observed within the differential cell are reflected on the larger scale of the $100\,\mathrm{cm^2}$ cell: GDL Type A exhibits the strongest relation between liquid and local performance; comparison of GDL Type B with Type A shows a similar behavior in terms of liquid content, yet the electrochemical characteristics are not as strongly impeded by the presence of liquid within GDL Type B; Type C shows generally the lowest tendency to hold liquid, yet the electrochemical performance and current density distribution is quite similar to that obtained with GDL Type B.

3.3.4 Subtleties

Adjacent channels. Examination of the neutron images depicted in the Figures 3.21, 3.19, and 3.20 shows that the liquid content under the lands formed by two adjacent channels after a turning of the serpentine is considerably less than under the parallel channels of the serpentine. This is most likely a consequence of the pressure drop between the adjacent channels. Calculations of PHAROAH indicate that a substantial part of the gas flow is forced convectively through the GDL, if a sufficient pressure drop is established between the channels [133]. This is further supported by velocity field measurements performed by KUCERNAK et al. via laser doppler anemometry [57]. Obviously, this convective flow supports the liquid removal from the GDL, causing a reduced degree of flooding between these channels.
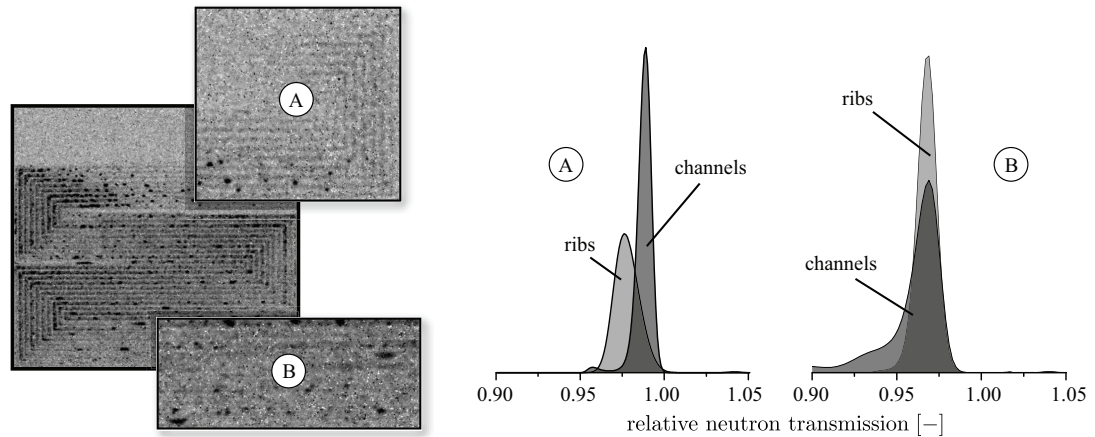
Figure 3.22: The change of liquid partitioning under channels and ribs along the serpentine flow path for GDL Type B; the cell was operated at $70\,°C$; the average current density is $400\,mA/cm^2$; cathodic stoichiometry is 2.5; anodic stoichiometry is 1.5; relative humidity at the inlets is $80\,\%$.

Liquid partitioning within GDL Type B. The partition behavior of GDL Type B within the inhomogeneous environment of the $100\,cm^2$ cell is another interesting subtlety. Within the differential cell, this particular GDL Type exhibited a clear preference to accumulate liquid under the lands of the flow field, while the gas feed within the channel is not fully saturated. This preference is also reflected within the region (II) of the $100\,cm^2$ cells. This can be seen from Figure 3.22, where two histograms obtained from different areas of the cell are compared[13]. The histogram (A) was obtained from an area where liquid starts to accumulate within the GDL (region (II)), and histogram (B) was obtained by regarding the outlet area. The neutron image to the left shows the compared areas as enlargements. Each histogram shows two curves: one for the land area and one for the channel area. These two curves are well separated within region (A), where the curve corresponding to the rib area is shifted to lower values of the relative neutron transmission. Hence, the partitioning occurs within the $100\,cm^2$ cells as well, and the land area exhibits the higher tendency to accumulate liquid within the GDL. Yet, as the gas flow within the channels reaches saturation, the partitioning is diminished and near the outlet a homogeneous liquid content within the GDL under channels and ribs can be assessed. This stems from the well agreeing peak positions of the curves in histogram (B). Hence, the same situation as faced with the differential cells is found within the $100\,cm^2$ cells. Yet, due to the changing gas composition both features (preferential flooding under the lands where the gas flow within the channels is not fully humidified and homogeneous flooding under highly humid conditions) are present within the cell at the same time.

3.4 The influence of flow direction

The last section was dedicated to the investigation of inhomogeneities occuring within PEFCs under technically realistic operating conditions—meaning near stoichiometric operation. The influence of liquid within the porous structures on the local electrochemical performance was investigated in detail. Yet, all experiments have been performed by passing the gases in co-flow through the cell. The implications of changing the direction of either flow will be explored within this section. The influence of the inhomogeneous distribution of relevant species (H_2O, O_2, and H_2) along the flow path within PEFCs is well recognized as performance influencing within the literature.

---

[13]The depicted histograms are deconvoluted according to Section 2.2.6.3.
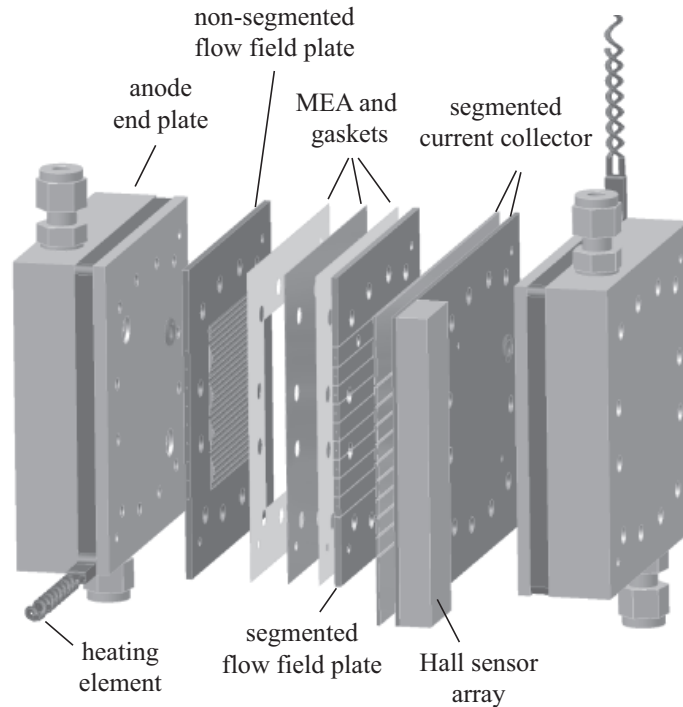
Figure 3.23: Segmented polymer electrolyte fuel cell for simultaneous locally resolved impdeance spectroscopy and neutron imaging; the active area is $29.2\,\mathrm{cm^2}$; adopted from [69].

Being an attractive play ground for fluid dynamics, the majority of studies were performed by computational means and the available theoretical literature is too voluminous to be discussed here; a good starting point for further reading are the reviews by WEBER and NEWMAN [31] and WANG [40]. Surprisingly, the influence of flow direction has not been studied explicitly to a very large extent, especially by experimental means. Striving to dispense with the external humidification system, BÜCHI and SRINIVASAN [134] recognized the close coupling between anode and cathode in terms of water management and elucidated the possibility of internal humidification by proposing an internal water loop (cf. Figure 3.25 on page 123) in counter-flow mode. The first report explicitly investigating the influence of flow direction within H_2/O_2 PEFCs by means of locally resolving EIS was given by SCHNEIDER et al. [117]. They revealed a strong impact of the flow direction on the internal water management and highlighted local performance limitations such as reduced membrane conductivity and electrode drying within the oxygen-fed system. In a joint effort with SCHNEIDER, neutron imaging and locally resolved EIS were simultaneously applied to further inspect the relation between flow direction, internal water management, locally limiting processes, and local performance [69], and the results presented within this and the subsequent section have been obtained in close collaboration.

3.4.1 Measurement cell

For this study, a cell that is based on and comprises enhancements over earlier designs used by SCHNEIDER et al. [96] has been manufactured by SCHNEIDER, merging enhancements regarding the suitability for locally resolved electrochemical diagnostics with the requirements implied by neutron imaging. A sketch of the used cell hardware is depicted in Figure 3.23. The flow fields were made by machining a nine-fold serpentine with three parallel channels into graphite plates of 2 and $3\,\mathrm{mm}$ thickness, respectively. To minimize lateral currents, the cathodic flow field was segmented taking advantage of the gluing technique described in Section 2.3.1.1. To achieve sufficient adhesion between the glued segments, this plate was chosen to be $3\,\mathrm{mm}$ thick. The anodic flow field plate, which was not segmented had a thickness of $2\,\mathrm{mm}$ to ensure sufficient neutron transparency of

the cell. The cathodic current collector comprising nine gold-coated copper straps was fixed on an anodized aluminium plate and introduced between the cathodic flow field and end plate. In contrast to the design depicted in Figure 3.18, Hall sensors were directly attached to the current collector rather than connecting them via cabling to the segments. This further minimizes the resistance of the measurement circuit and, therefore, lateral currents (cf. Section 2.3.1.2 and Ref. [96]); this is essential for the accuracy of the ac measurements. The end plates were manufactured from three centimeter thick aluminum blocks and gold-coated. While the cathodic end plate was insulated from the cell by the segmented current collector, the anodic end plate was in contact with the anodic flow field plate and hence served as current collector. The cell temperature was controlled by heaters located at the perimeter of the cell permitting the neutron beam to pass unperturbed through the active area.

Membrane electrode assemblies were prepared from Nafion 112 membranes and ETEK ELAT (V3.1) Pt/C electrodes with a platinum loading of $0.5\,\mathrm{mg/cm^2}$ and a carbon-cloth as GDL. This type of gas diffusion electrode was utilized for both, anode and cathode. The MEA was hot-pressed at a temperature of $120\,°C$ and a pressure of $2.2\,\mathrm{MPa}$ for three minutes. The thickness of the PTFE gaskets sealing the cell was $250\,\mathrm{\mu m}$ each.

3.4.2 Comparison of co and counter flow operation

The diagrams of Figure 3.24 provide an overview of the local cell behavior under co and counter flow operation. The left column shows the liquid content, high frequency resistance, and current density in co flow operation. The right column shows the results obtained under counter flow operation. The high frequency resistance was obtained at $10\,\mathrm{kHz}$. At this frequency, only ohmic resistances contribute to the impedance, and as the membrane is far less conductive than the electronic conductors (GDL and flow field), this value is indicative for the hydration state of the membrane.

In co flow mode, both gases were fed with a relative humidity of $80\,\%$ at the top right and exit the cell at the bottom left. The results are similar to those of Section 3.3. As the gases were fed undersaturated, there is a region where no liquid is present within the porous structures. This region stretches roughly over the first three segments[14]. Afterwards, the liquid content is monotonically increasing towards the outlet. The maximum liquid content of about $60\,\mathrm{ml/m^2}$ is similar to the low flooding level observed for the cloth-type GDL during the GDL material comparison (cf. Section 3.3.3). The liquid content profile is remarkably well reflected by the high frequency resistance. A rather high membrane resistance of about $140\,\mathrm{m\Omega cm^2}$ is measured within the segment nearest to the inlet and reduces gradually downstream. Within the flooded region, the ohmic resistance is stabilizing at about $70\,\mathrm{m\Omega cm^2}$, which is in good agreement with *ex situ* conductivity measurements of fully hydrated Nafion 112 membranes [135]. This might be indicative for a fully hydrated membrane within the second half of the active area, which would imply the presence of some liquid within the anodic compartment. This reveals a high interaction between anode and cathode with respect to the water household as water seems to pass easily through the membrane. There is a discrepancy between the onset of flooding and the stabilization of the high frequency resistance at $70\,\mathrm{m\Omega cm^2}$ of about two segments. This might be indicative for a region where the cathode is flooded, while the anode is still liquid-free. Under these conditions, it is likely that a gradient in membrane hydration exists, which would lead to an increased overall resistance of the membrane.

---

[14]The offset in liquid content is attributed to the membrane hydration.
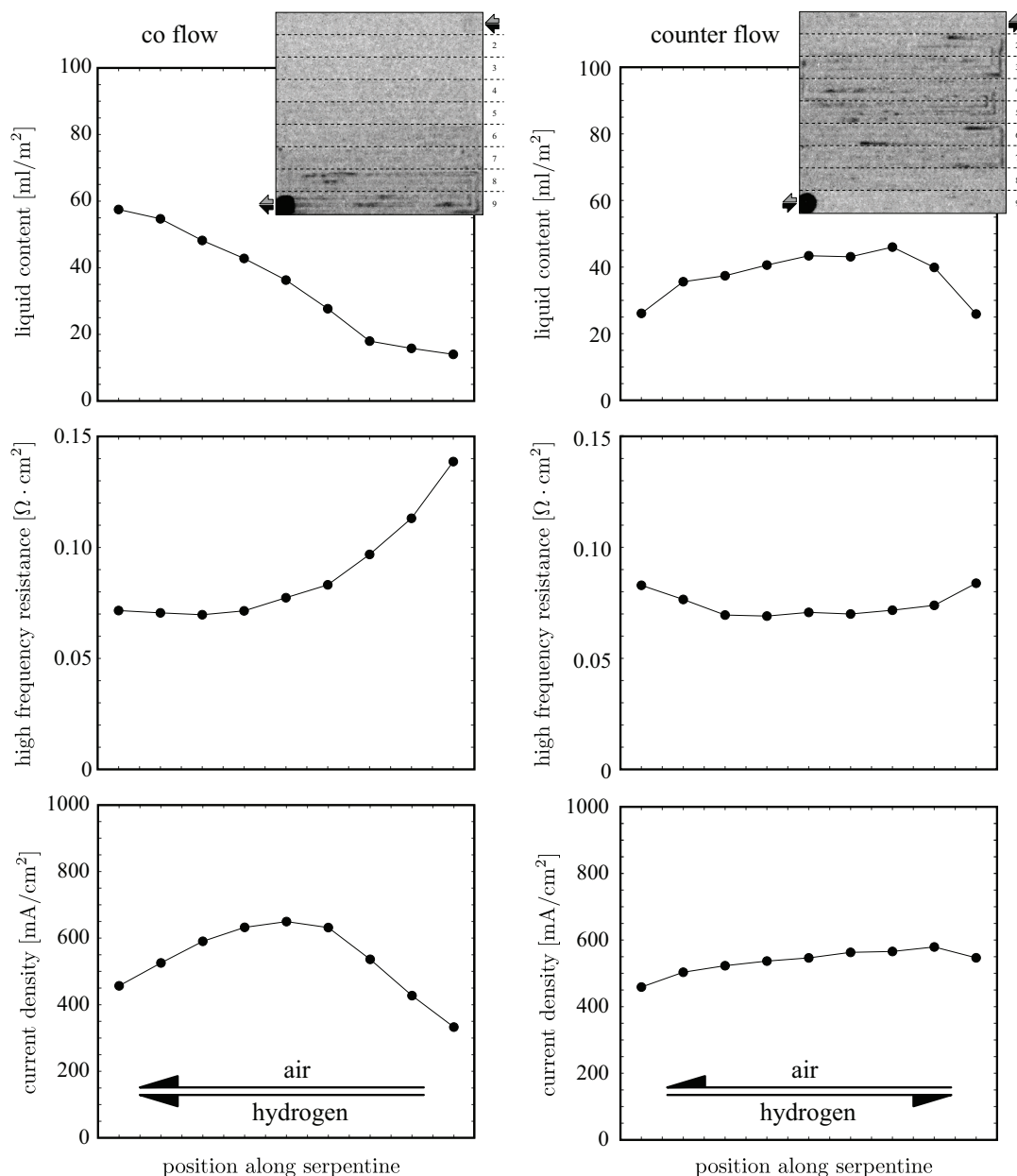
Figure 3.24: The influence of flow direction onto liquid accumulation, electrolyte resistance, and current density distribution; the left column shows co-flow and the right column counter-flow operation, respectively; the liquid content as function of position along the serpentine is shown in the top row; the high frequency resistance at $10 \, \text{kHz}$ is shown in the middle row, and the diagrams of teh bottom row show the current density distribution; the cell was operated at $70 \, °\text{C}$ at near ambient pressure; average current density is $500 \, \text{mA/cm}^2$; both gas feeds were passed with a relative humidity of $80 \, \%$ to the cell; the anodic stoichiometry is 1.5; the cathodic stoichiometry is 2.5.

On the basis of these informations, the current density profile is easily understood. At the inlet the current density is diminished partially due to the detrimental impact of the higher resistance of the not fully hydrated Nafion membrane. The high frequency resistance decreases along the flow path, because the gases are humidified by product water, resulting in a stronger hydration of the electrolyte. Consequently, the current density increases up to the center segment. Here a maximum is passed, because the detrimental influence of limited oxygen diffusion (reduced oxygen concentration near the outlet and hampered accessibility due to flooding) towards the electrochemical active surface starts to dominate resulting in a reduced current density near the outlet. Taken together, this shows very clearly the counter-play between flooding and drying: The inlet region
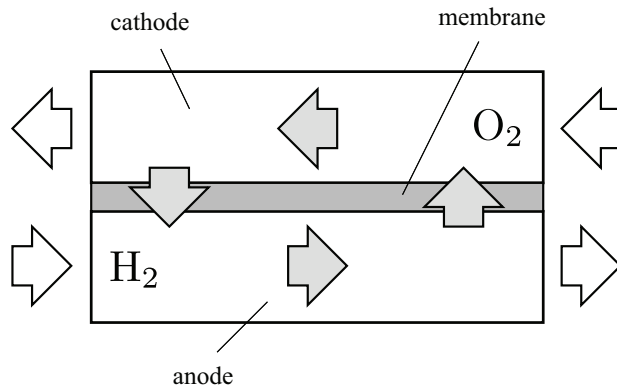
Figure 3.25: Simplified sketch of water fluxes within a PEFC under counter flow operation showing the formation of an internal water loop; after BÜCHI and SRINIVASAN [134].

is limited in electrochemical performance due to drying effects, and the outlet is limited due to hampered oxygen mass transport. Maximal performance is reached in a rather narrow range where good membrane hydration and reasonable oxygen accessibility to the electrode coincide.

If the cell is operated in counter flow mode by passing hydrogen from the bottom left, a notably different situation is faced. The liquid distribution, high frequency resistance, and current density distribution are changed in comparison to co flow operation. The current density near inlet and outlet is significantly improved resulting in a considerably flattened profile. The high frequency resistance reveals that the air inlet does not suffer as much from drying as if both gas feeds enter the cell at this side, because only the segment nearest to the air inlet exhibits a slightly increased ohmic resistance. Further on, the air outlet (which is the hydrogen inlet) is characterized by an increase of the ohmic resistance. Yet, also this side shows only a moderate increase of the ohmic resistance. This is in good agreement with earlier investigations of SCHNEIDER et al., where a similar effect was found for oxygen-fed cells by locally resolved EIS [117]. Over a wide range, the ohmic resistance is virtually constant at a value of about $70\,\mathrm{m\Omega cm^2}$, which is indicative for a high degree of membrane hydration in the center part of the cell. The liquid content rapidly increases from the air inlet and passes a maximum within segment three to four, whereby the maximum liquid content is rather low (approximately $40\,\mathrm{ml/m^2}$). Towards the air outlet, the liquid content decreases again. This results in a higher accessibility of oxygen to the electrode near the outlet, where flooding is critical due to the lower oxygen concentration of the air feed within the channels. In consequence, the slightly higher ohmic resistance near the hydrogen inlet (air outlet) is compensated by better oxygen mass transport; hence, the current density distribution does not show the strong decline that results from co flow operation.

The liquid content profile is a consequence of the close coupling between anode and cathode in terms of water management. As illustrated by Figure 3.25, in counter flow mode an internal water flux loop is formed [134]. Modeling results reported by BERG et al. [136] in 2004 reflect the internal water flux loop proposed by BÜCHI and SRINIVASAN [134] on the basis of water balance measurements, and SCHNEIDER et al. were the first to report experimental evidence on the basis of spatially resolving diagnostics. They could explain the development of the local impedance response near the cathodic outlet of the investigated oxygen-fed cell with such an internal water loop [117]. Near the air outlet, the wetter air flow is facing a relatively dry anodic supply resulting in a net water flux towards the anode. By this, the anodic flow is humidified and the cathodic flow is dried causing a reduction of the degree of flooding within the cathodic GDL. The water is transported back within the anodic flow towards the air inlet, where now a highly humidified hydrogen stream is facing a drier air stream. Consequently, the net water flux is reversed resulting in a faster humidification of the entering air compared to co flow operation where the air is solely humidified by product water.

Figure 3.26: Local impedance spectra obtained in co flow mode; the frequency was ramped from 10 kHz to 100 mHz; operating conditions as given in Figure 3.24; spectra one corresponds to the segment nearest to the inlet and spectra nine corresponds to the outlet.

This internal water loop has several beneficial consequences: (1) the humidification of the air inlet is supported and the severe drying is avoided; (2) the liquid content near the cathodic outlet is reduced supporting the oxygen transport towards the cathode where it is critical; hence, the current density near the air outlet is not as much hampered by mass transport as in the case of co flow operation; and (3) the internal water loop ensures a good membrane hydration over a wide range of the active area. Taken together, the operation in counter flow mode is superior to co flow operation—in this case amounting to a gain in voltage of 37 mV from 631 mV in co flow mode to 668 mV in counter flow mode—because of a favorable internal water household.

Even more insight can be gained by inspecting the local impedance spectra. Figure 3.26 shows the impedance spectra of each segment as NYQUIST plots for co flow operation. The spectra were recorded by scanning a frequency ramp ranging from 10 kHz to 100 mHz. The spectra correlated with the undersaturated inlet region are shown in the left plot as watersheds. Spectra one corresponds to the segment nearest to the inlet. This spectra comprises a single arc with a linear tail at the high frequency end. This shape of the spectra is qualitatively very typical for a PEFC. Various effects might contribute to this arc. First of all, an electron transfer reaction (BUTLER-VOLMER type) would result in a half-circle due to the parallel double layer charging. EIKERLING et al. [46] showed on a theoretical basis that the impedance spectra of a porous electrode where TAFEL type reactions occur might exhibit a linear tail at the high frequency end due to the finite thickness and conductivity of the electrode. Recent results of KUHN et al. [50] from half cell measurements show that the anode might significantly contribute to the cell spectra—especially under dry conditions. Hence, the observed arc is generally attributed to the performance of the electrodes, where a diminished electrochemical performance (e.g., originating from a reduced conductivity of the ionomer incorporated into the porous electrode) is indicated by an increased arc size. Following the development of the first four spectra, it becomes obvious that the hydration state of the cell is increasing, and this is not only beneficial for the membrane conductivity but also for the performance of the electrodes, as has been reported earlier by SPRINGER et al. [137], CIUREANU [138], and SCHNEIDER et al. [96, 117]. This can be concluded from the reducing size of the arc over the first segments[15]. Already in segment two, a second feature starts to appear within the spectra at the low frequency end: a second arc, which is overlapping the first arc. The size of this arc increases monotonically along the flow path. Within the undersaturated region both arcs

---

[15]The dashed lines are solely intended as guidance for the eye. As will be shown in Section 3.5, mass transport phenomena influence not only the low frequency features but have an impact on the high frequency part as well.
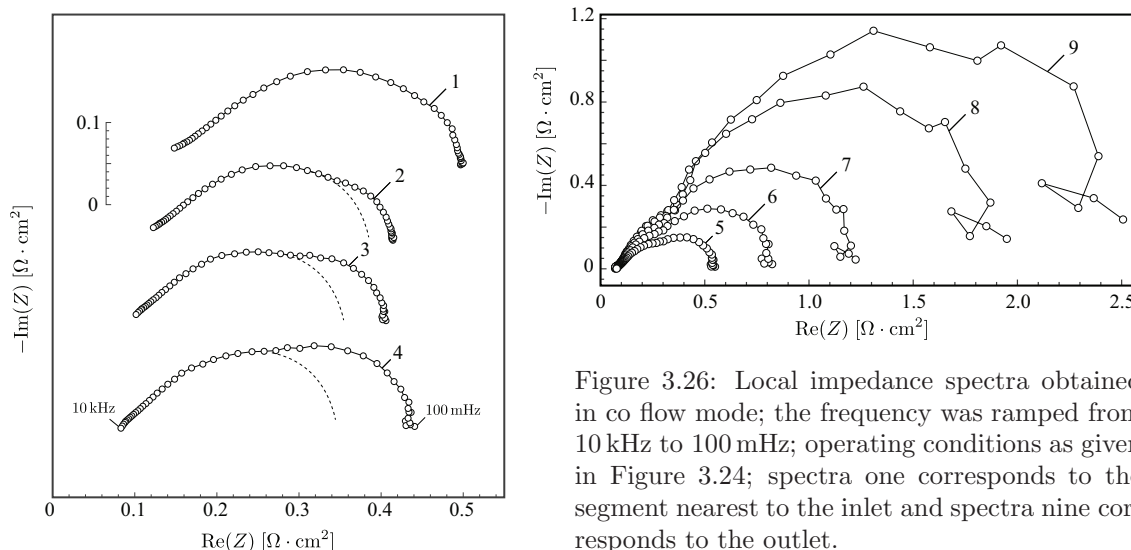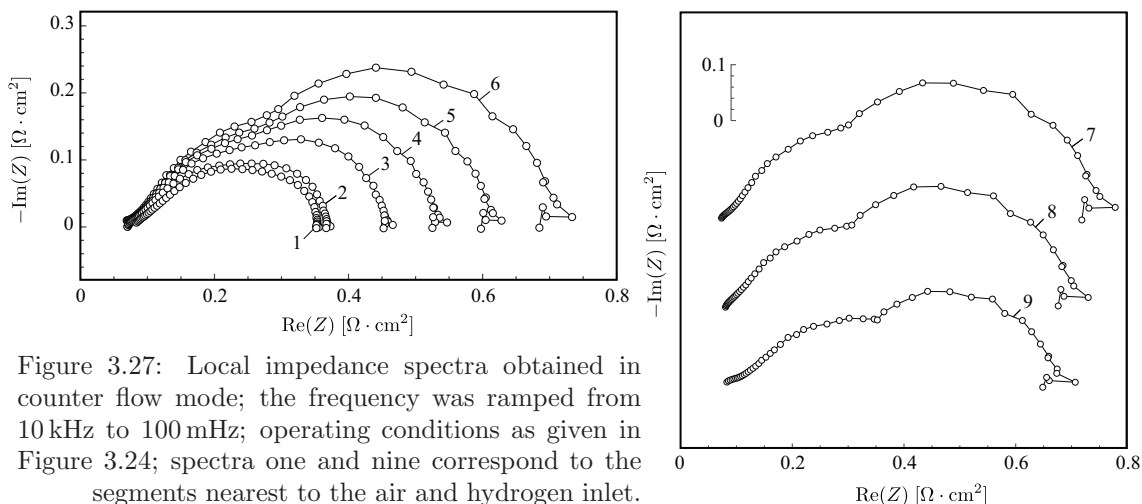
Figure 3.27: Local impedance spectra obtained in counter flow mode; the frequency was ramped from 10 kHz to 100 mHz; operating conditions as given in Figure 3.24; spectra one and nine correspond to the segments nearest to the air and hydrogen inlet.

are more or less equally contributing to the overall spectra. Yet, within the flooded region the low frequency arc starts to dominate the spectra, and reaches approximately three to four times the radius of the higher frequency arc. The nature of the low frequency arc will be explored in detail in Section 3.5. It will be shown that this arc can be attributed to oxygen transport within the gas phase. Yet, it must not be mistaken as a NERNST diffusion, because the oscillation caused by the current perturbation within the gas phase is not confined to the GDL. Nonetheless, the dominance of oxygen transport hampering the electrochemical performance near the outlet is reflected in the spectra by the dominance of the lower frequency arc.

The local impedance spectra as obtained in counter flow operation are depicted in Figure 3.27. The spectra No. 1, obtained from the segment nearest to the air inlet, is qualitatively equal to the co flow spectra (one arc with high frequency tail). Yet, the improved electrochemical performance caused by the internal water loop is reflected by a considerable smaller radius of the arc. Further on, the spectra radius increases monotonically along the flow path showing that the inlet is not as strongly deteriorated by drying effects. As for co flow operation, a second arc in the low frequency part of the spectra is forming along the serpentine. Yet, again the radii of the arcs are notably smaller than observable in co flow operation. This is indicative for a improved oxygen transport towards the electrode, which is in agreement with the lower liquid content obtained from neutron imaging. The largest radius is found for segment seven. Most interestingly, the radii of the lower frequency arcs reduce afterwards. This can be seen from the watershed plot at the right side of Figure 3.27. This is not easily explained. Due to the oxygen depletion along the flow path, a hampered oxygen transport near the outlet would be expected. However, remembering the reduced liquid content near the cathodic outlet (upper right diagram of Figure 3.24), it seems possible that the increased free pore volume compensates for the oxygen depletion resulting in a overall improved oxygen transport rate near the outlet. This would provide an explanation for the reducing arc radius, and the topic will be picked-up again in Section 3.5.6 after a refined understanding of the processes contributing to the low frequency arc is obtained.

3.4.3 Sensitivity towards inlet humidity

The sensitivity of liquid content, high frequency resistance, and current density towards the gas inlet humidity is depicted in Figure 3.28. The upper half shows co flow operation, and the lower half shows counter flow operation, respectively. The liquid content within the GDLs as evaluated from the land area is shown by the left-hand diagrams. The corresponding neutron images are
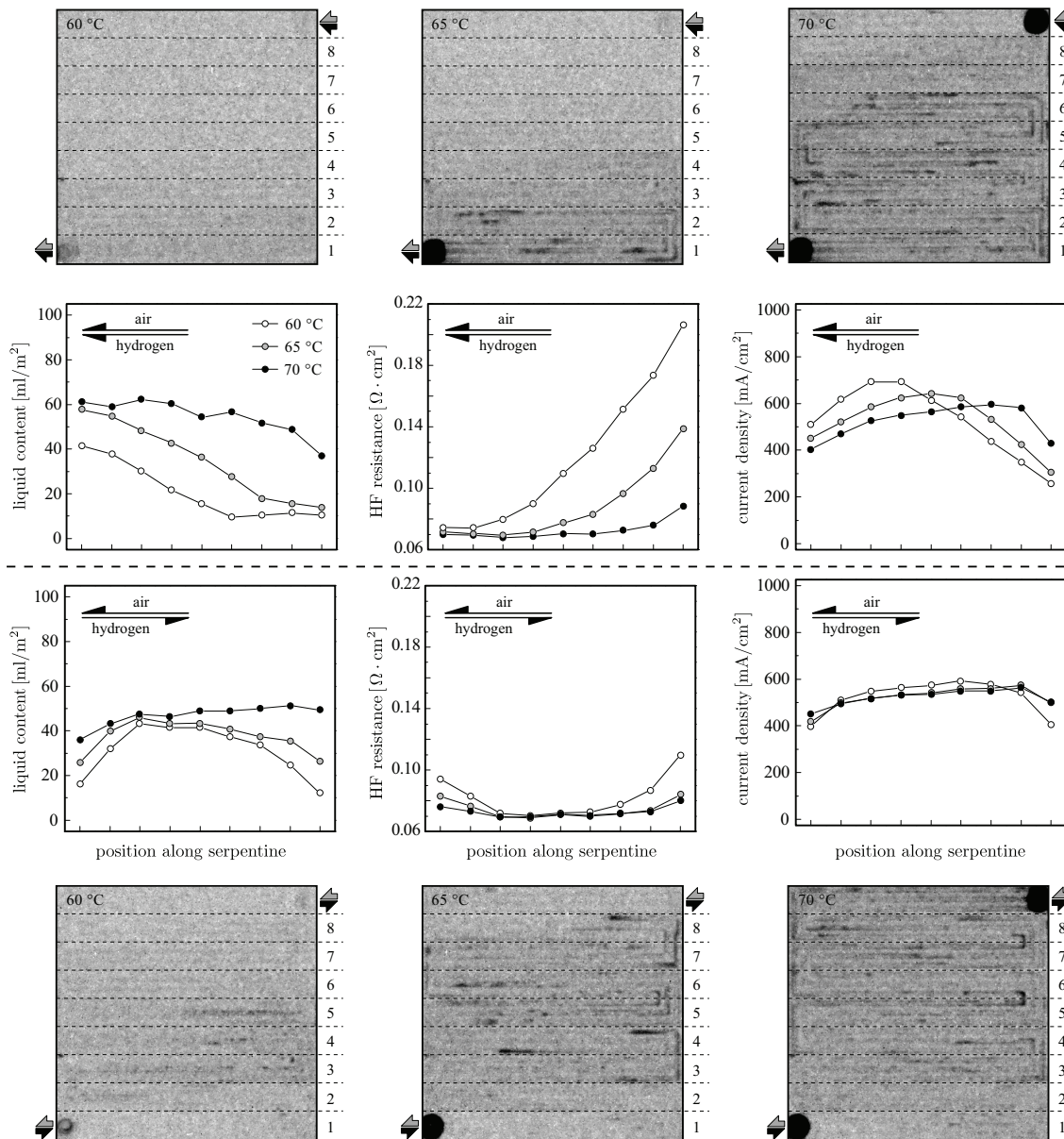
Figure 3.28: Infuence of gas feed humidity onto liquid content, high frequency resistance, and current density; the upper half shows co flow and the lower half counter flow operation; the corresponding neutron images are shown above and below the diagrams, respectively; cell temperature is 70 °C; the humidifiers of both gas feeds had identical set-points; average current density $500 \, \text{mA/cm}^2$; the anodic stoichiometric ratio is 1.5; the cathodic stoichiometric ratio is 2.5; high frequency resistance obtained at 10 kHz.

shown above and below the diagrams, respectively. The middle column shows the high frequency resistance (measured at 10 kHz) of the cell. The current density distribution is shown by the diagrams at the right-hand side.

Under co flow operation, the liquid content gradually increases for every level of feed humidification. Yet, while undersaturated gases are applied a dry region near the inlet is observed, and the liquid content increases with the same slope once the onset of flooding is reached. Under fully humidified conditions, the liquid content does not increase with the same slope, because the maximum liquid content of about $60 \, \text{ml/m}^2$ is already reached after about one third of the active area. The liquid pattern is reflected by the high frequency resistance. If the gases enter the cell with a dew-point of 60°C (64 % relative humidity), the ohmic resistance of the inlet segment is $206 \, \text{m}\Omega \, \text{cm}^2$, which is
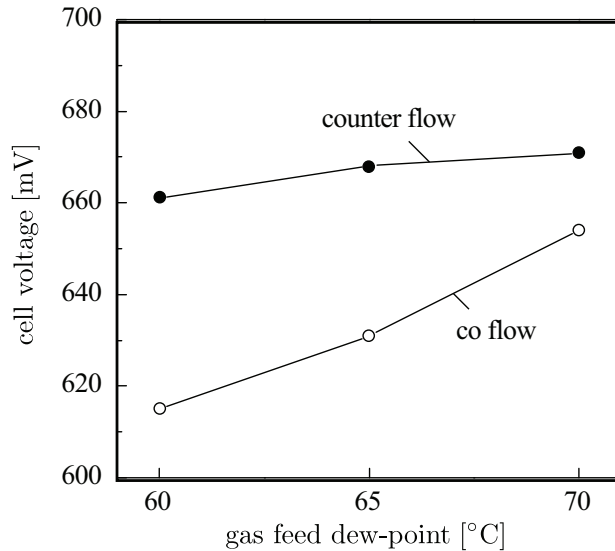
Figure 3.29: Cell voltage as function of supply gas humidity in co and counter flow mode; cell temperature is $70\,°C$; the humidifiers of both gas feeds had identical set-points; the average current density is $500\,mA/cm^2$; the anodic stoichiometric ratio is 1.5; the cathodic stoichiometric ratio is 2.5.

nearly three times the ohmic resistance obtained at the fully wetted outlet. If the dew-point of the gas feeds is raised to $65\,°C$ ($80\,\%$ relative humidity), the ohmic resistance at the inlet is reduced to $140\,m\Omega\,cm^2$, which is still twice the value achievable under fully wetted conditions. In both cases, the ohmic resistance gradually reduces along the serpentine (with the same slope), and reaches the minimum value of $70\,m\Omega\,cm^2$ about two to three segments after the first liquid is detected. Under fully humidified conditions, only a slight increase of the ohmic resistance is detected within the first segment. This is most likely due to some experimental imprecision[16], which caused a slightly lower relative humidity of the inlet feeds. Otherwise, the ohmic resistance is constant at about $70\,m\Omega\,cm^2$. Taken together, a reduction of the supply gas humidity results in a delay of the flooding onset, and at the same time the ionic conductivity is significantly reduced within the undersaturated inlet region. If fully humidified gases are supplied, the liquid content and high frequency resistance are virtually constant and extremal (highest liquid content and lowest ohmic resistance) with the exception of the inlet segment due to some experimental imprecision. This is reflected within the current density. By raising the degree of humidification, the maximum of the current density is shifted towards the inlet, because the drying of the inlet is diminished.

In counter flow operation, the impact of feed gas humidity is not as strong as in co flow mode due to the homogenizing effect of the internal water loop. The current density distribution is virtually not affected, and the ohmic resistance shows a slight sensitivity near the inlets. The center part of the cell—where the internal water loop is effective—is characterized by a constant, low ohmic resistance indicative for fully wetted conditions independent of the inlet gas humidity. The slight increase of the ohmic resistance towards the inlets is matched by the liquid content profile which declines towards the inlets.

Hence, it is not surprising that the cell voltage is less depending on supply gas humidity under counter than in co flow operation. This can be seen from Figure 3.29. Further on, it becomes clear that a higher level of humidification is beneficial for the cell voltage despite the implied higher degree of flooding. Obviously, the gain in terms of ionic conductivity outweighs the loss in oxygen accessibility at the chosen operating point. However, it has to be kept in mind that this cannot be a general conclusion. The chosen operating point of $500\,mA/cm^2$ in average is still in the medium current density range. It is possible that the dominance of oxygen mass transport at higher load operation might result in a different trend.

---

[16]It is very difficult to feed gases with a dew-point that matches the cell temperature exactly, because even the slightest loss in temperature while passing the gases from the humidifier to the cell results in a considerable drop of the relative humidity.

3.5 The low frequency behavior of air-fed PEFCs during electrochemical impedance spectroscopy

As already shown in Section 2.1, the separation of mass transport processes from those of ohmic and kinetic origin is possible by electrochemical impedance spectroscopy (EIS), because these processes occur at different time scales. Mass transport processes are generally slower than those of kinetic origin or charge displacement (ohmic losses). Hence, they influence the impedance response of a fuel cell mainly at the low frequency end. If fully understood, the impedance spectra can principally provide a measure (such as the effective diffusion coefficient) for the oxygen transport towards the electrode. Some attempts to extract this information by applying EIS to PEFCs are reported in the literature. Already in 1996 impedance spectra obtained from air-fed PEFCs were reported by the pioneering work of SPRINGER et al. [137] to contain two features: a higher frequency arc associated with interfacial charge-transfer resistance and catalyst layer properties, and a lower frequency loop determined by gas-phase transport of oxygen. They fitted the experimental data with a model accounting for TAFEL-type kinetics, finite proton conductivity of the electrode, and multi-component diffusion through the GDL (similar to NERNST diffusion). Later on, their model was refined by GUO and WHITE [139] by incorporating the agglomerate model as representation of the electrode morphology. Doing this, they expanded upon the model of JAOUEN and LINDBERGH [43]. However, as sophisticated as the proposed models are, they do not take into account the inhomogeneous operation of PEFCs and consequently are intrinsically one-dimensional and, strictly speaking, only valid for describing the impedance response of differential cells such as that presented in Section 3.2.2. Nonetheless, attempts to interpret experimentally obtained impedance spectra from cells working under technical constrains with one-dimensional models have been made [121, 140].

The first report of impedance measurements accounting for the inhomogeneous operation of a PEFC was given by BRETT et al. [109]. They investigated the development of the local impedance response along the channel of a single channel laboratory scale PEFC and discovered a striking feature of the spectra in the low frequency domain. Like others, they found a second low frequency arc attributed to oxygen transport. As a function of position along the cathodic channel, the capacitive arc gained substantially in size and eventually flipped around the vertical axis pointing towards the negative quadrant. This implies a crossing of the spectra with the negative real axis with vanishing frequency. They were able to correlate this feature with inverting local polarisation curves, where the current passes a maximum and is reduced afterwards even though the electrode polarisation is increased. They attributed this feature to serious reactant starvation yet failed to provide a complete physical picture for the observed phenomena. Further on, no model proposed in the literature so far is able to reflect this feature. Nonetheless, in the light of the pioneering work of BRETT et al., it becomes clear that the impedance spectra obtained from an air-fed PEFC working under technically realistic flow rates (either integral or locally resolved) must not be understood as a simple superposition of independent, local, one-dimensional spectra. This directly points not only to the need of locally resolved measurements but also to the need of a complete understanding of the coupling effects that separate one-dimensional models from the experimentally obtained local impedance response. Recently, we have shown that the phenomena observed by BRETT et al. (back-flipped low frequency arc) also takes place within cells of technical size ($200\,cm^2$ active area) and were able to detect oxygen oscillations within the cathodic effluent during impedance spectroscopy by connecting a second PEFC with the cathodic effluent suggesting that these are the coupling agent [141]. Already on the basis of these results we were able to propose a physical model (cf. Section 3.5.1) explaining the creation and propagation of oxygen concentration oscilla-
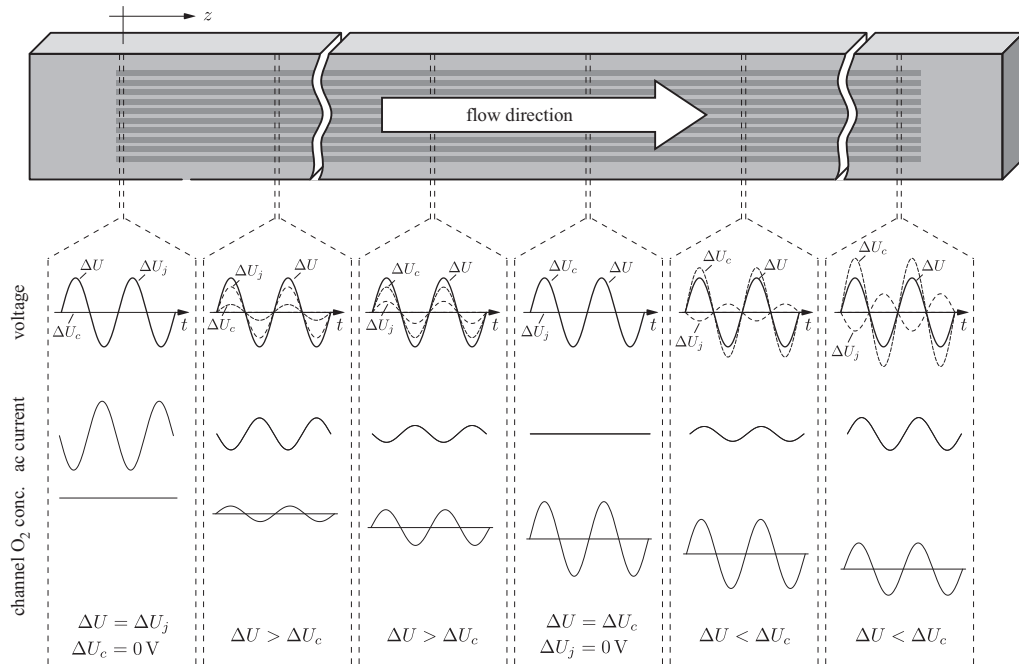
Figure 3.30: Principle sketch of the build-up of a oxygen concentration oscillations within the cathodic gas stream during impedance spectroscopy and the influence to the local impedance; adopted from [141].

tions along the flow path as well as their impact onto the local impedance spectra by inducing a voltage perturbation. Encouraged by these experimental findings, a joint effort was undertaken to develop a complete picture relating the low frequency behavior and the occurrence of oxygen concentration oscillations within the cathodic air stream with each other. The physical model related within Section 3.5.1 was proposed by SCHNEIDER [142], and the mathematical model described in Section 3.5.2, which is the first rigorous, two-dimensional model describing the cathodic impedance response of an air-fed PEFC, was developed in this work [143] to validate and refine the qualitative picture. Finally, rather elaborate experiments proposed by SCHNEIDER were performed jointly to obtain experimental verification [144].

3.5.1 A physical model

To confine the oscillation of the oxygen concentration within the gas-phase caused by the oscillating current to the GDL is a common assumption made while deriving a model to interpret impedance spectra of air-fed PEFCs [121, 126, 137, 139, 140]. If this assumption is relaxed and oscillations are allowed to protrude into the channel, it becomes possible that oxygen oscillations generated at some point within the cell are transported downstream with the gas flow. The schema shown in Figure 3.30 will guide the discussion of the influence of these oscillations to the local spectra. The schema shows slices along the cathode flow path. At each slice, voltage, ac current, and oxygen concentration are depicted as a function of time. For the sake of simplicity, the consideration will be restricted to very low frequencies, where voltages, currents, and concentrations are either in phase ($0°$ phase shift) or out of phase ($180°$ phase shift). At the inlet, a gas feed is entering the cell without any superimposed oscillations. Nonetheless, a small oscillation of the oxygen concentration within the gas phase (cf. Section 2.1) is generated due to the changing rate of consumption; because the cell voltage is oscillating, the faradaic current will oscillate accordingly. At low frequencies (near the steady state), the oxygen oscillation generated at the electrode will be

propagated towards the channel. Hence, a small oxygen concentration oscillation is protruding into and transported with the gas stream. In the schema shown in Figure 3.30, this oxygen oscillation increases along the flow path before entering the second slice. In addition to the oxygen oscillation, the steady-state concentration is diminished due to the consumption within the preceding part of the active area. The oxygen oscillation entering the segment generates a voltage oscillation in this segment even if no external current perturbation is allowed (galvanostatic control). This can be concluded directly from the TAFEL equation. If the oxygen oscillation is symbolized by $\Delta c(t)$, the current density will be given by

$$j = i^* \cdot \left(\frac{c_0 + \Delta c(t)}{c^*} \right) \cdot \exp \left\{ \frac{\eta_0 + \Delta \eta(t)}{b} \right\}. \tag{3.19}$$

Herein, i^* symbolizes the exchange current density, c_0 the unperturbed steady-state oxygen concentration at the electrode, c^* the reference concentration associated with i^*, and η_0 the steady-state over-potential of the electrode. If the current density is fixed to the steady-state value $j = i^* \cdot (c_0/c^*) \cdot \exp(\eta_0/b)$, the resulting voltage perturbation is given by

$$\frac{\Delta \eta(t)}{b} = - \ln \left\{ 1 + \frac{\Delta c(t)}{c_0} \right\}. \tag{3.20}$$

This oxygen concentration induced voltage perturbation is labeled ΔU_c within Figure 3.30. However, in a fuel cell the equipotential criteria requires that the voltage oscillation is equal to the perturbation voltage ΔU at any position. Hence, a faradaic current is needed to account for the difference between the applied voltage perturbation ΔU and the perturbation induced by the entering oxygen concentration oscillation ΔU_c. Yet, the amplitude of the faradaic current will be smaller than without an oxygen concentration oscillation (first slice), because only the voltage difference has to be compensated. Although this ac current attenuation results in an increase of the impedance at nearly vanishing frequencies, the low frequency end of the spectra still resides on the positive real axis, because ac current and perturbation voltage are out of phase (increasing current with decreasing voltage). At the same time, this faradaic current will add to the oxygen oscillation within the flow path. This results in a further build-up of the oxygen oscillation amplitude Δc within the channel along the flow path (third slice) until eventually a critical point is reached. This point, which is shown as the fourth slice within Figure 3.30, is characterized by the equality of the voltage perturbation induced by the oxygen concentration oscillation ΔU_c and the voltage perturbation ΔU applied to the cell. Here, the faradaic current oscillation vanishes, because the applied voltage oscillation is entirely covered by the oxygen concentration oscillation. The low frequency end of the spectra will not lie on the real axis, but tend towards infinity as this point is approached, because the faradaic current oscillation is essentially zero. As no faradaic current oscillation is present at this point, the oxygen oscillation will be passed on without a change of the amplitude. Yet, the steady-state value of the oxygen concentration is reduced nonetheless (the dc current is far from being zero). Due to Equation (3.20), the reduced steady-state oxygen concentration c_0 causes a further increase of ΔU_c downstream the critical point, because ΔU_c is defined by the ratio $\Delta c/c_0$. Now the hypothetical voltage perturbation induced by the oxygen oscillation ΔU_c would be larger than the voltage perturbation applied to the cell ΔU. As sketched by the penultimate slice, a faradaic current is needed to account for the difference. Yet, the faradaic current has to be shifted in phase by $180°$. The inverted ac current causes the low frequency end of the spectra to lie at the negative real axis. Further on, the sign-changed faradaic current will diminish the amplitude of the oxygen concentration near the outlet. Notwithstanding, the oxygen concentration oscillation induced voltage ΔU_c might rise monotonically (last slice), because it is defined by $\Delta c/c_0$, and c_0 decreases monotonically along the flow path. This allows for an increase

of the faradaic current towards the outlet due to the increasing difference between ΔU_c and ΔU, and consequently the low frequency end of the spectra is shifted on the negative half of the real axis from minus infinite towards the origin.

In conclusion, by considering oxygen oscillations within the channels, it becomes possible that the low frequency end of a spectrum is either shifted to higher values on the real positive axis or even located at the negative real axis. As long as the current inversion point is not reached, the oxygen oscillation will cause a shift of the low frequency end of the spectra towards larger values along the positive real axis and tend towards infinity as the current inversion point is approached. After the current inversion point is passed, the low frequency end of the spectrum is found at the negative real axis.

3.5.2 A mathematical model

A simplified model will be derived to investigate the impact of an oscillating oxygen concentration within PEFCs flow fields from a mathematical perspective. As the phenomena originates from mass transport, its influence is most pronounced in the low frequency part of the impedance spectra. Hence, effects stemming from the morphology and finite conductivity of electrode and membrane are neglected for the sake of simplicity. This renders the mathematical model qualitative in the sense that generally the calculated impedances will be smaller than those found experimentally because of the neglect of several deteriorative effects. Nonetheless, features seen experimentally in the low frequency domain will be reflected by the model. The model will account for the following effects:

- Reaction kinetics
  The ORR is assumed to obey TAFEL kinetics, and only the dependence on potential and oxygen concentration will be considered.

- Mass transport within GDL
  The oxygen transport within the GDL is considered to be purely diffusive, and the validity of FICKS first law is assumed. Multi-component diffusion will be neglected for the sake of simplicity.

- Mass transport within channels
  The velocity field within the channels is assumed to be laminar (HAGEN-POISEUILLE parabola). The average flow velocity is regarded as constant along the channel. Hence, the pressure drop is neglected.

Major effects influencing the impedance response of a PEFC that will not be considered for the sake of simplicity are:

- Ohmic resistance of the electrolyte

- Anodic cell reaction

- Effects stemming from the morphology of the gas diffusion electrode (limited conductivity and gas permeability)

- Locally varying properties such as gas permeability (e.g., diminished by the presence of liquid water)

- Possible inhomogeneities due to channel and land area
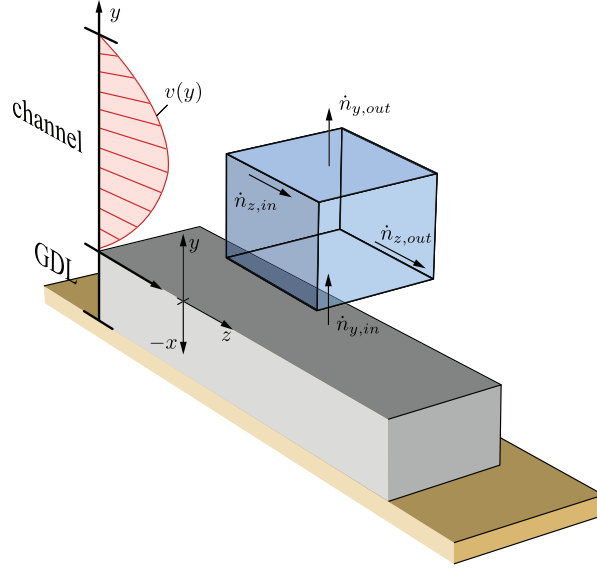
Figure 3.31: Mass balance of oxygen within the flow field channel.

3.5.2.1 The dc case

As the faradaic current is assumed to obey TAFEL kinetics, the current density at a point z along the flow path is given by:

$$j_0(z) = i^* \cdot \frac{c_e(z)}{c^*} \cdot \exp\left\{\frac{\eta_0}{b}\right\} \qquad (3.21)$$

Herein, i^* symbolizes the exchange current density under reference conditions (indicated by the superscript *), $c_e(z)$ the molar concentration of oxygen at the electrode, η_0 the steady-state (dc) over-potential of the electrode, and b the TAFEL slope. The subscript "e" is indicative for the electrode. For the sake of nomenclature consistency with later considerations, the following variable is defined:

$$\kappa = i^* \cdot \exp\left\{\frac{\eta_0}{b}\right\} \qquad (3.22)$$

By this, Equation (3.21) becomes linear in κ and reads

$$j_0(z) = \frac{c_e(z)}{c^*} \cdot \kappa. \qquad (3.23)$$

It is worth noting that due to the disregard of ohmic losses and anodic kinetics, the over-potential η_0 (and consequently κ as well) is independent of z.

The oxygen concentration at the electrode $c_e(z)$ depends on the oxygen concentration at the GDL-channel interface $c_c(z)$, the thickness of the GDL δ_g, the oxygen diffusion coefficient D, and the faradaic current j_0, because FICKs first law requires that

$$c_e(z) = c_c(z) - \frac{j_0(z) \cdot \delta_g}{z \cdot \mathcal{F} \cdot D} = c_c(z) - \frac{j_0(z)}{z \cdot \mathcal{F} \cdot \omega_g \cdot \delta_g} \qquad (3.24)$$

holds, where $\omega_g = D/\delta_g^2$ is the characteristic frequency of oxygen diffusion within the GDL.

To obtain the oxygen concentration at the GDL-channel interface $c_c(z)$, the oxygen transport within the flow field has to be considered. The oxygen mass balance obtained from a control volume within the channel is illustrated by Figure 3.31. Balancing inlet and outlet flows and using TAYLOR expansion leads to the continuum equation:

$$0 = \frac{\partial_y \dot{n}_y}{l} + \frac{\partial_z \dot{n}_z}{l_k} \qquad (3.25)$$

Herein, l and l_k denote the depth and length of the channels, respectively; y and z are the corresponding dimensionless coordinates (normalized to l and l_k, respectively) perpendicular to and along the channel (cf. coordinate plane in Figure 3.31). If convection is considered as the dominating transport process in flow direction (z axis), the molar flux in flow direction is given by:

$$\dot{n}_z = v(y) \cdot c(y, z), \tag{3.26}$$

where $c(y, z)$ symbolizes the oxygen concentration within the channel. Assuming a laminar velocity field, the gas velocity $v(y)$ is given by a HAGEN-POISEUILLE parabola

$$v(y) = 2 \cdot \bar{v} \cdot \left\{ 1 - (2y - 1)^2 \right\}, \tag{3.27}$$

where $\bar{v}$ denotes the average flow velocity. This implies that no convection occurs perpendicular to the flow direction (along the y axis). Hence, the transport of oxygen in that direction is sufficiently described by FICKs law:

$$\dot{n}_y = -\frac{D}{l} \cdot \partial_y c(y, z) \tag{3.28}$$

Combination of the Equations (3.25), (3.26), and (3.28) leads to

$$0 = -\frac{v(y)}{l_k} \cdot \partial_z c(y, z) + \omega_c \cdot \partial_{y,y} c(y, z). \tag{3.29}$$

Herein, the characteristic frequency of oxygen diffusion within the channel is given by $\omega_c = D/l^2$. For a complete problem description, three boundary conditions are required. Assuming an ideally mixed gas at the inlet, the oxygen concentration will be uniform over the depth of the channels, which leads to

$$y, z = 0 : \quad c = c_{in}. \tag{3.30}$$

Conveniently, the reference concentration c^* is arbitrarily chosen to be equal to the inlet concentration c_{in}. The wall at $y = 1$ implies a vanishing oxygen flux perpendicular to the flow direction, and

$$y = 1, z : \quad \partial_y c = 0 \tag{3.31}$$

is found as second boundary condition. At the interface between channel and GDL ($y = 0$), the molar flux perpendicular to the flow direction equals the molar flux within the GDL which in the dc case is proportional to the faradaic current. This leads to

$$x = 1, y = 0, z : \quad \partial_x c = \frac{\omega_c \cdot \beta}{\omega_g} \partial_y c \tag{3.32}$$

Herein, $\beta = \delta_g/l$ is the ratio of GDL thickness to channel depth. The normalized coordinate x describes the position within the GDL (see the coordinate plane of Figure 3.31). The oxygen concentration gradient within the GDL is simply $\partial_x c = j_0/(z \cdot \mathcal{F} \cdot \omega_g \cdot \delta_g)$. The Equations (3.23, 3.29-3.32) form a linear system, if Equation (3.29) is discretized by finite differences. Hence, it is efficiently solved by matrix inversion yielding j_0 as function of the position along the channel z. Finally, the current density j_0 is based on the area possessed by the flow field channels. In order to reference to the geometric MEA area, the current density has to be corrected with a factor ϵ according to

$$j = j_0/(\epsilon + 1). \tag{3.33}$$

In the approximation of negligible differences between channel and rib ϵ is just the rib-to-channel ratio.

3.5.2.2 The ac case

The derivation of an ac model will expand upon the kinetic equation (Eq. (3.21)). A sinusoidal perturbation $\Delta\eta$ will lead to a sinusoidal response of the faradaic current Δj. Likewise, the oxygen concentration at the electrode will oscillate, which might be symbolized by the perturbation Δc_e. Hence, Equation (3.21) becomes

$$j_0 + \Delta j = i^* \cdot \frac{c_e + \Delta c_e}{c^*} \cdot \exp\left\{\frac{\eta_0 + \Delta\eta}{b}\right\}, \tag{3.34}$$

if the coordinate dependence of the different terms is skipped for the bravery of notation. For small perturbations $\Delta\eta$, the exponential term can be linearized around η_0, which leads to

$$j_0 + \Delta j = \underbrace{i^* \cdot \exp\left\{\frac{\eta_0}{b}\right\}}_{=\kappa} \cdot \frac{c_e + \Delta c_e}{c^*} \cdot \left(1 + \frac{\Delta\eta}{b}\right). \tag{3.35}$$

As Equation (3.35) is linear in the variables Δj, $\Delta\eta$, and Δc_e, it is easily transformed into FOURIER space, which leads to

$$\delta j = \frac{1}{R_{ct}} \cdot \delta\eta + \frac{\kappa}{c^*} \cdot \delta c_e, \tag{3.36}$$

if higher order terms are neglected, and the FOURIER transforms of the perturbations are symbolized by a preceding δ (e.g., $\mathcal{F}\{\Delta j\} = \delta j$). For the sake of consistency with classical notation, the charge transfer resistance might be defined as the first order derivative of the over-potential with respect to the faradaic current, which gives

$$\frac{1}{R_{ct}} = \partial_\eta j_0 = \frac{\kappa}{b} \cdot (c_e/c^*). \tag{3.37}$$

Mass conservation within the GDL requires that

$$\partial_t(c + \Delta c) = -\omega_g \cdot \partial_{x,x}(c + \Delta c) \tag{3.38}$$

holds, where c denotes the steady-state oxygen concentration and Δc the corresponding perturbation within the GDL. Both are functions of the coordinate x; yet, only Δc exhibits a temporal dependence. In FOURIER space this reads

$$0 = \partial_{x,x}(\delta c) + i \cdot \frac{\omega}{\omega_g} \cdot \delta c, \tag{3.39}$$

if the imaginary unit is symbolized by i. Further on, the perturbation frequency is denoted by ω. As equilibrium at the electrode prevails, the gradient of the concentration field is related to the current density by

$$x = 0: \quad \partial_x(\delta c) = -\frac{\delta j}{z \cdot \mathcal{F} \cdot \omega_g \cdot \delta_g}. \tag{3.40}$$

The assumption of finite diffusion would lead to $\delta c = 0$ at $x = 1$, which is the underlying assumption of a NERNST impedance (cf. Section 2.1). This requirement will be relaxed by setting

$$x = 1, y = 0: \quad \delta c = \delta c_c, \tag{3.41}$$

where δc_c is the oscillation of the oxygen concentration at the GDL-channel interface. This allows to express the oxygen concentration oscillation at the electrode δc_e as a function of δj and δc_c,

because Equation (3.39) together with the boundary conditions (Eq. (3.40,3.41)) requires that

$$\delta c_{\mathrm{e}} = \frac{\delta c_{\mathrm{c}}}{\cosh(\tau)} - \frac{\delta j}{z \cdot \mathcal{F} \cdot \omega_{\mathrm{g}} \cdot \delta_{\mathrm{g}}} \cdot \frac{\tanh(\tau)}{\tau} \tag{3.42}$$

with $\tau = \sqrt{\mathrm{i} \cdot \omega / \omega_{\mathrm{g}}}$ holds.

The concentration oscillation at the GDL-channel interface δc_{c} is found from mass conservation. Within the time domain, the time-dependent conservation equation reads

$$\partial_t c = -\frac{v(y)}{l_{\mathrm{k}}} \cdot \partial_z c + \omega_{\mathrm{c}} \cdot \partial_{y,y} c, \tag{3.43}$$

and transformation into FOURIER space results in

$$0 = -\frac{v(y)}{l_{\mathrm{k}}} \cdot \partial_z(\delta c) + \omega_{\mathrm{c}} \cdot \partial_{y,y}(\delta c) - \mathrm{i} \cdot \omega \cdot \delta c. \tag{3.44}$$

In analogy to the dc case, the boundary conditions are found to be:

$$y, z = 0: \qquad \delta c = 0 \tag{3.45}$$

$$y = 1, z: \qquad 0 = \partial_y(\delta c) \tag{3.46}$$

$$y = 0, z: \qquad \partial_x(\delta c) = \frac{\omega_{\mathrm{c}} \cdot \beta}{\omega_{\mathrm{g}}} \partial_y(\delta c) \tag{3.47}$$

The gradient of the oxygen concentration oscillation within the GDL at the GDL-channel interface is given by

$$\partial_x(\delta c) = \delta c_{\mathrm{c}} \cdot \tau \cdot \tanh(\tau) + \frac{\delta j}{z \cdot \mathcal{F} \cdot \omega_{\mathrm{g}} \cdot \delta_{\mathrm{g}} \cdot \cosh(\tau)}. \tag{3.48}$$

Respecting the boundary conditions (Eq. (3.40, 3.41)), this is found by integrating Equation (3.39) and taking the first spatial derivative at $x = 1$.

In resemblance to the dc case, the Equations (3.36, 3.44-3.48) form a complex-valued linear system, if Equation (3.44) is discretized by finite differences, and hence conveniently solved numerically by matrix inversion. After solving the linear system, δj is known as a function of position along the flow path (z coordinate). Knowing the faradaic ac current δj, the impedance is calculated by

$$Z_0(z) = \frac{\delta \eta}{\delta j(z) + \mathrm{i} \cdot \omega \cdot C_{dl} \cdot \delta \eta}, \tag{3.49}$$

and hence the inevitable charging of the double layer, which is characterized by its capacitance C_{dl}, is accounted for. In resemblance to the dc case, the impedance is corrected for the geometric area by

$$Z = Z_0 \cdot (\epsilon + 1). \tag{3.50}$$

The model will be parameterized with the values given in Table 3.2, which were either calculated from the geometry of the cell described within the next section or estimated on the basis of typical literature values.

3.5.3 Experimental

A linear cell approach was chosen to obtain experimental evidence for the physical model (cf. Section 3.5.1 and Ref. [141]) by a more defined experimental setup than used before [141]. The linear cell approach bears two advantages: (1) by avoiding serpentines, it is ensured that substantial

Symbol	Value	Unit	Description
b	30	mV	Tafel slope
C_{dl}	1000	F/m^2	Double layer capacitance
$\delta\eta$	10	mV	Amplitude of voltage perturbation
ω_g	80	Hz	Characteristic frequency of oxygen diffusion within GDL
ω_c	100	Hz	Characteristic frequency of oxygen diffusion within channel
c^*	5.13	mol/m^3	Inlet concentration of oxygen
δ_g	250	µm	Thickness of the GDL
l_k	31.5	cm	Length of the flow field
ε	1	-	Rib to channel ratio
β	2	-	Ratio of the channel depth and GDL thickness

Table 3.2: Parameter values of the mathematical model.

convection through the GDL (between the channels) is avoided, and (2) the linear design enables easy segmentation along the flow path. A drawing of the used cell hardware designed jointly with SCHNEIDER is given in Figure 3.32. The cell consists of two aluminum blocks with a thickness of 4 cm each. These serve as end plates to ensure a homogeneous compression and isothermal conditions. The current collectors, flow fields, and MEA were sandwiched by these electrically insulated end plates. Each flow field consisted of a segmented graphite block with a thickness of about 1 cm each into which a ten channel parallel flow field was machined. To achieve sufficient electrical insulation between the segments while maintaining gas tightness, the gluing technology described in Section 2.3.1.1 was utilized. The segmented current collector was placed at the cathodic side. It consisted of nine copper sheets that were coated with a gold layer to minimize contact resistances. The electrical current was measured by an array of Hall sensors that was lined-up at
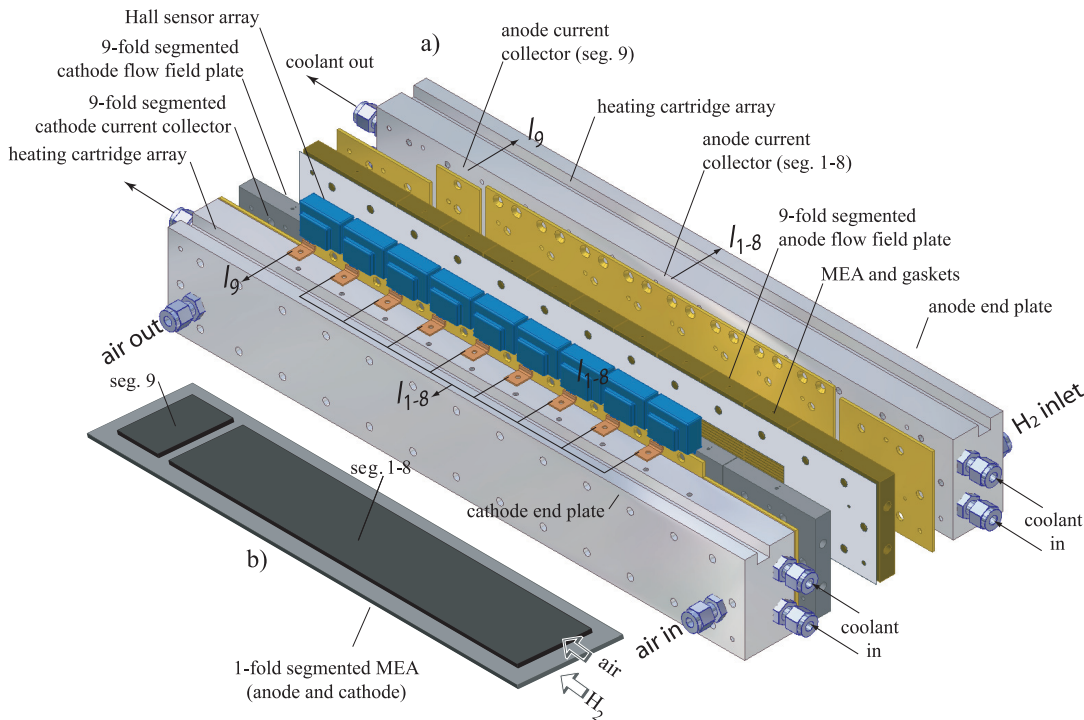

Figure 3.32: Linear polymer electrolyte fuel cell with nine-fold segmented graphite-made flow fields (a) and partially segmented MEA (b); the total active area is 63 cm^2; the flow fields consist of ten parallel channels with a width of 1 mm each; the distance between two channels is 1 mm and the depth of a channel is 0.5 mm; adopted from [142].

the top of the cell. Afterwards, the individual segment currents were combined by a rather thick gold-coated copper plate (not shown in Figure 3.32) before passing the current to an external load circuit. This ensured minimal voltage differences between the segments (around $1\,\mathrm{mV}$) even for largely varying segment currents. The design provided the possibility of disconnecting each segment from the common copper plate, which is essential for some of the experiments described within the next section. The anodic current collector was of similar design yet without segmentation; only the last segment could be disconnected from the common current collector. The cell temperature was regulated by heated water provided by a thermostat connected to four tubes within the aluminum end plates; two at each side—one above and one below the active area. The cell temperature was monitored by a thermocouple located within the graphite-made flow field plates. The cell was clamped by 28 screws at the perimeter of the cell. To ensure a homogeneous compression, the screws were fastened with a torque-wrench.

The MEA was manufactured by stacking two equal porous Pt electrodes supported on a carbon-cloth provided by E-Tek (V2.1 with an precious metal loading of $0.5\,\mathrm{mg/cm^2}$ supported on graphite) with a Nafion 112 membrane in-between. The MEA was unsegmented through-out the segments one to eight. Yet, between the segments eight and nine a gap of about $2\,\mathrm{mm}$ allowed for a complete electric decoupling of segment nine[17]. This is illustrated in diagram (b) of Figure 3.32. This electrical insulation of the last segment allows for a range of experimental configurations (see Figure 3.33) enabling the elaborate experiments proposed by SCHNEIDER [144]. The MEA was sealed against ambiance by two PTFE gaskets, with a thickness of $200\,\mathrm{\mu m}$ on the anodic and $250\,\mathrm{\mu m}$ on the cathodic side. An assembled cell was operated for several days before experiments were performed to achieve optimal and stable electrochemical performance. The cell was operated at $70\,^\circ\mathrm{C}$ at ambient pressure. Both gas feeds (air and hydrogen) were pre-humidified by passing them through bubbler[18]. These were kept at a temperature of $72\,^\circ\mathrm{C}$. To avoid condensation, the tubes connecting the humidifiers with the cell were heated to $80\,^\circ\mathrm{C}$. Unless stated otherwise, the cell was operated galvanostatically at an average current density of $500\,\mathrm{mA/cm^2}$.

3.5.4   The oxygen concentration oscillation induced voltage perturbation

A voltage perturbation at the electrode induced by oxygen concentration oscillations that are transported within the cathodic flow field ΔU_c is a central aspect of the argumentation given in Section 3.5.1 and experimentally substantiated by the experiments related in Ref. [141]. Within the mathematical framework, this additivity of voltage perturbations can also be shown by rearranging Equation (3.36) after relacement of δc_e according to Equation (3.42). This leads to

$$\delta\eta = \underbrace{\delta j \cdot R_{ct} \cdot \left(1 + \frac{\kappa/c^*}{z \cdot \mathcal{F} \cdot \omega_\mathrm{g} \cdot \delta_\mathrm{g}} \cdot \frac{\tanh(\tau)}{\tau} \right)}_{\text{current induced}} - \underbrace{\frac{b}{\cosh(\tau)} \cdot \frac{\delta c_\mathrm{c}}{c_\mathrm{e}}}_{\text{ox. conc. induced}}, \tag{3.51}$$

where the first term reflects the voltage perturbation ΔU_j originating from the faradaic ac current, and the second term resembles the oxygen concentration induced voltage perturbation ΔU_c. This highlights the proper description of the physical phenomena (cf. Section 3.5.1 and Ref. [141]) by the mathematical model (cf. Section 3.5.2). The linear cell was operated in the Modes A and B sketched in Figure 3.33 to characterize this induced voltage perturbation ΔU_c. Under normal operation, segment No. 9 was connected in parallel to the rest of the MEA and hence operated as integral part of the cell. This is shown as Mode A. To detect the oxygen concentration oscillation

---

[17]The membrane was not segmented to ensure gas tightness between anode and cathode.

[18]A bubbler is a heated vessel containing water. Entering the bubbler at the bottom via a frit, the gas takes up vapor while advancing to the water surface. The humidified gas is extracted at the top of the vessel.
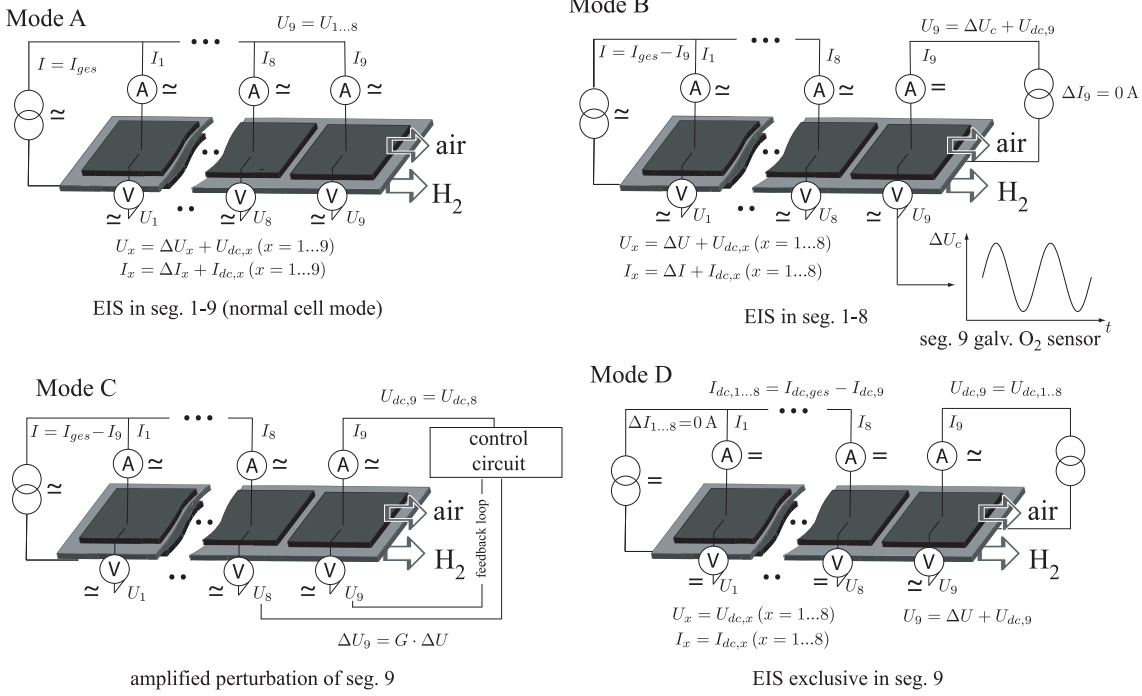
Figure 3.33: Operation modes proposed by SCHNEIDER of the linear PEFC to characterize the local impact of ΔU_c and validate the schema presented in Figure 3.30; Mode A shows the electrical connection for standard local impedance spectroscopy; Mode B shows the electrical connection while operating segment nine as galvanostatic oxygen sensor; Mode C shows the setup for amplified perturbation within segment No. 9; the configuration to apply EIS solely to segment No. 9 is shown as Mode D; adopted from [142].

induced voltage ΔU_c, segment nine was connected to a separate galvanostat. This is shown as Mode B. The segments No. 1 to No. 8 were operated as usual. This setup allows operating segment No. 9 galvanostatically while performing impedance measurements within the preceding eight segments. Hence, an oxygen concentration oscillation was generated by the first eight segments, which then was passed on to segment No. 9 by the gas feed. The induced voltage oscillation was measured by an ac voltmeter connected to segment No. 9.

From the mathematical perspective, this galvanostatic operation of the outlet segment is described by expanding the model of Section 3.5.2.2 with

$$z = 1: \quad 0 = \delta j + \mathrm{i} \cdot \omega \cdot C_{dl} \cdot \delta \eta_c, \tag{3.52}$$

which means that the ac current is zero at $z = 1$. As an additional equation enters the system of equations, the number of variables is increased by one. Naturally, this additional variable is the induced voltage perturbation $\delta \eta_c$ under galvanostatic control.

The diagrams of Figure 3.34 display the amplitude and phase of the induced voltage perturbation as obtained from experiment (ΔU_c). The result of the mathematical model ($\delta \eta_c$) is given in Figure 3.35. The experimentally obtained amplitude is normalized to the amplitude of the ac voltage $\Delta U_{1\ldots8}$ resulting from the current perturbation applied to the segments one to eight. A similar normalization was performed with the modeling results; $\delta \eta$ is the ac voltage for $z < 1$. The phases are also relative to the ac cell voltage. For frequencies larger than about 10 Hz, the amplitude of the induced voltage ΔU_c is reduced to less than ten percent of the ac cell voltage ΔU throughout the range of investigated stoichiometries. The same trend is reflected by the mathematical model, although the calculated attenuation is slightly less pronounced. The attenuation stems from the
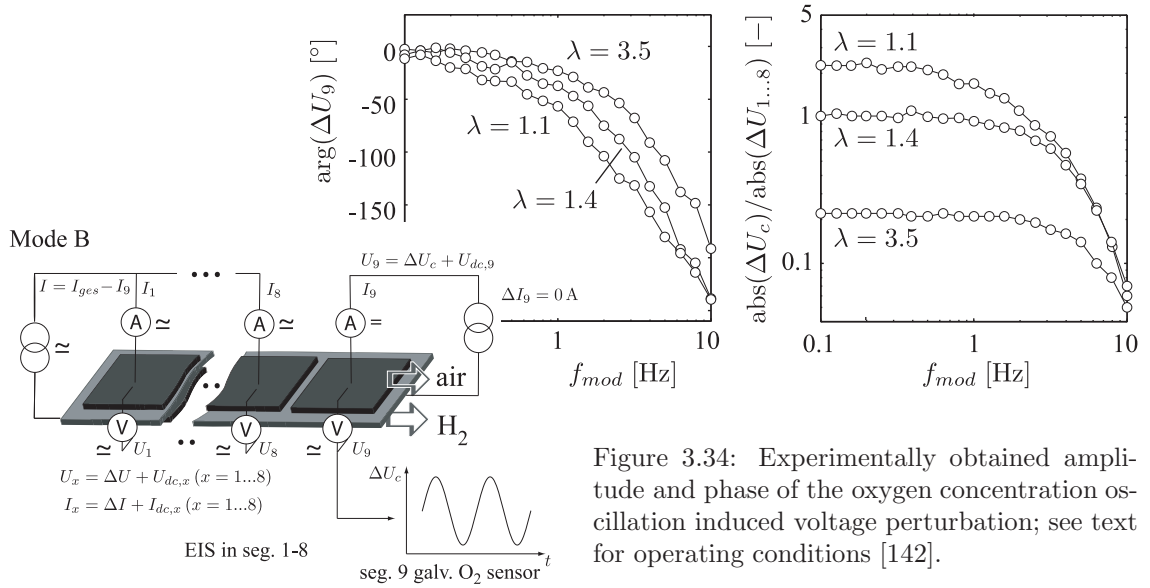
Figure 3.34: Experimentally obtained amplitude and phase of the oxygen concentration oscillation induced voltage perturbation; see text for operating conditions [142].
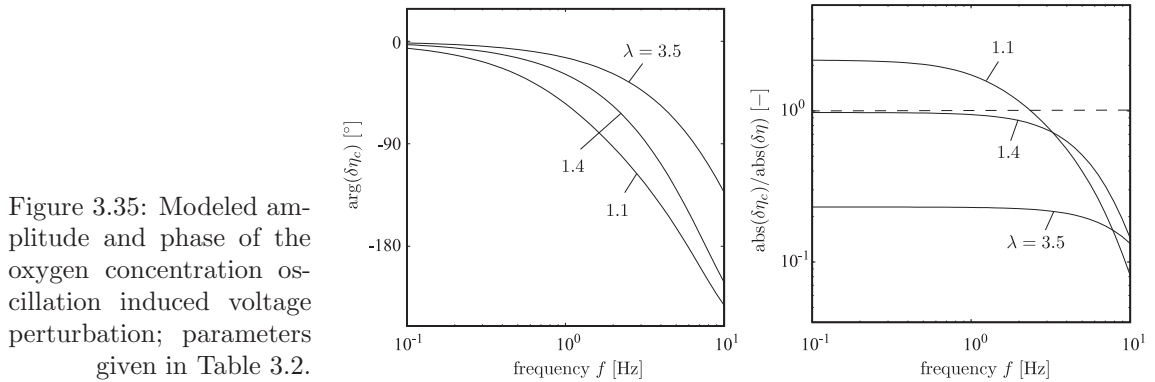
Figure 3.35: Modeled amplitude and phase of the oxygen concentration oscillation induced voltage perturbation; parameters given in Table 3.2.

damping of the oxygen oscillations by the GDL at higher frequencies. However, at a frequency as low as 0.1 Hz, the amplitude of the induced voltage perturbation stabilizes and both voltages are in phase, which is important because the qualitative considerations of Section 3.5.1 were based on that assumption.

At the low frequency end, the relative amplitude depends on the air stoichiometry. A ratio of nearly one is obtained for $\lambda = 1.4$ (i.e., the amplitude of the oxygen induced voltage ΔU_c nearly matches the ac cell voltage ΔU). The ratio is diminished by increasing λ, and for lower λ the induced voltage ΔU_c exceeds the ac cell voltage ΔU.

The λ dependence of the voltage ratio at low frequencies has two sources: the dc concentration and the ac concentration near the outlet—both vary by changing the stoichiometric ratio. The diagrams shown in Figure 3.36 clarify this. The calculated dc oxygen concentration c_e and the amplitude of the oxygen oscillation δc_e at the electrode are plotted as function of the cathodic stoichiometric ratio λ within the left-hand diagram. The right-hand plot shows the ratio of these values. The calculation was performed at a frequency of 0.1 Hz and with an ac voltage of $\delta \eta = 0.01$ V. As the ac values scale with the perturbation amplitude $\delta \eta$, only the qualitative trend should be discussed. The left plot shows that both—the dc and the amplitude of the ac concentration—decline with reducing stoichiometry. While this is natural for the dc case, it is not as easily understood for the ac case. However, as will be shown later, the operation under lower stoichiometric ratios implies larger impedances and hence lower faradaic ac currents. This directly translates into a lower amplitude of the oxygen concentration oscillation[19]. Yet, the ratio of both abs$(\delta c_e)/c_e$, which is shown in the

[19]Furthermore, the amplitude of oxygen oscillations passes a maximum along the flow path at lower stoichiometries,
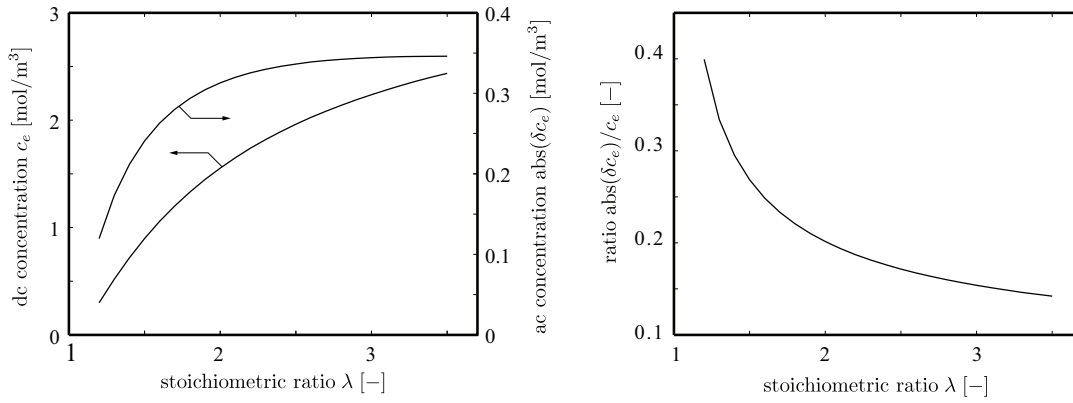
Figure 3.36: Dependence of the outlet oxygen concentration (ac, dc and the ratio thereof) onto the stoichiometric ratio; calculated with the parameters given in Table 3.2 at a frequency of 0.1 Hz; ac values scale with the perturbation amplitude $\delta\eta$ [143].

right-hand diagram, is increasing with reducing stoichiometry λ. It is the ratio of ac and dc value which finally determines the induced voltage. This was already explained in Section 3.5.1 and can easily be seen from the Equations (3.20) on page 130 and (3.51) on page 138, respectively.

Another important implication resulting from the physical schema (cf. Section 3.5.1 and Ref. [141]) relates the ac current to the ratio of the oxygen concentration induced voltage ΔU_c and the perturbation amplitude ΔU. It was argued that the equality of ΔU_c and ΔU will result in a vanishing ac current. Furthermore, it was concluded that the ac current will change sign (180 ° phase shift at vanishing frequencies) if ΔU_c exceeds ΔU. To verify this, the following experiment was performed. The cell was operated in normal impedance mode (Mode A of Figure 3.33) and impedance spectra were recorded. In addition, the amplitude of the ac current generated by segment nine was recorded at 0.1 Hz. Afterwards, the segment was disconnected and operated as oxygen sensor (Mode B in Figure 3.33), where the dc current and voltage of the last segment were maintained. In this mode, impedance measurements were performed at 0.1 Hz within the segments one to eight, and the ac voltage of segment nine was recorded (amplitude and phase) to obtain a measure for ΔU_c. This was repeated for different air stoichiometries. In addition, the corresponding values were calculated with the mathematical model using the parameters given in Table 3.2. To obtain the ratio of the ac current density at the outlet and the average ac current density amplitude $\mathrm{abs}(\delta j_\mathrm{o})/\langle\mathrm{abs}(\delta j)\rangle$, the model as described in Section 3.5.2.2 was used. The subscript "o" is indicative for the outlet ($z = 1$). To calculate the ratio of the oxygen concentration oscillation induced voltage and the perturbation voltage $\delta\eta_c/\delta\eta$, the adoptions described at the beginning of this section (cf. Eq. (3.52)) were applied at the outlet.

The diagrams of the Figures 3.37 and 3.38 compare the results. The experimental results are shown in Figure 3.37, and the modeling results are depicted by Figure 3.38. In both cases, the dependence of the amplitudes of the ac current ratio and ac voltage ratio at 0.1 Hz is plotted as a function of the supplied air stoichiometry at the right-hand side. The corresponding local impedance spectra are shown on the left-hand side. As indicated by Equation (3.20), the ac voltage ratio shows qualitatively the same trend as the ratio of the ac oxygen concentration amplitude and the dc oxygen concentration (see the right-hand diagram of Figure 3.36). At an air stoichiometry of 3.5, the oxygen concentration oscillation induced voltage is about 20 % of the total voltage perturbation. This ratio increases rapidly with decreasing stoichiometry. At an air stoichiometry of about 1.4 to 1.5, the ratio approaches unity, and for lower air stoichiometries the oxygen concentration oscillation

---

which also contributes to the decline of $\mathrm{abs}(\delta c_\mathrm{e})$ at the outlet with reducing stoichiometry.
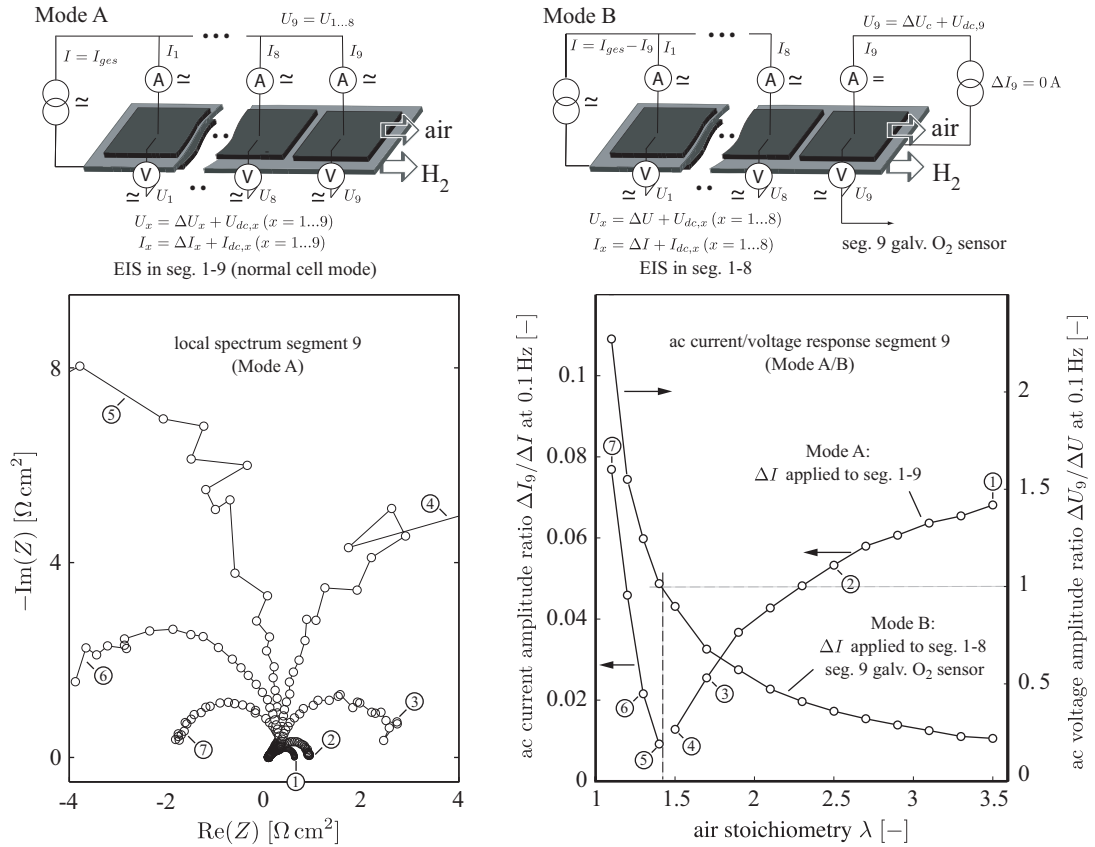
Figure 3.37: Experimentally obtained correlation between the oxygen concentration oscillation induced voltage (Mode B) and the ac current (Mode A) as a function of the air stoichiometry; see Section 3.5.3 for the experimental conditions; local spectra of segment nine obtained while operating the cell in Mode A are shown to the left; the ac current (Mode A) and amplitude of the oxygen concentration oscillation induced voltage as measured in Mode B at $0.1\,\mathrm{Hz}$ are shown on the right; the impedance spectra range from $0.1\,\mathrm{Hz}$ to $5\,\mathrm{kHz}$; adopted from [142].
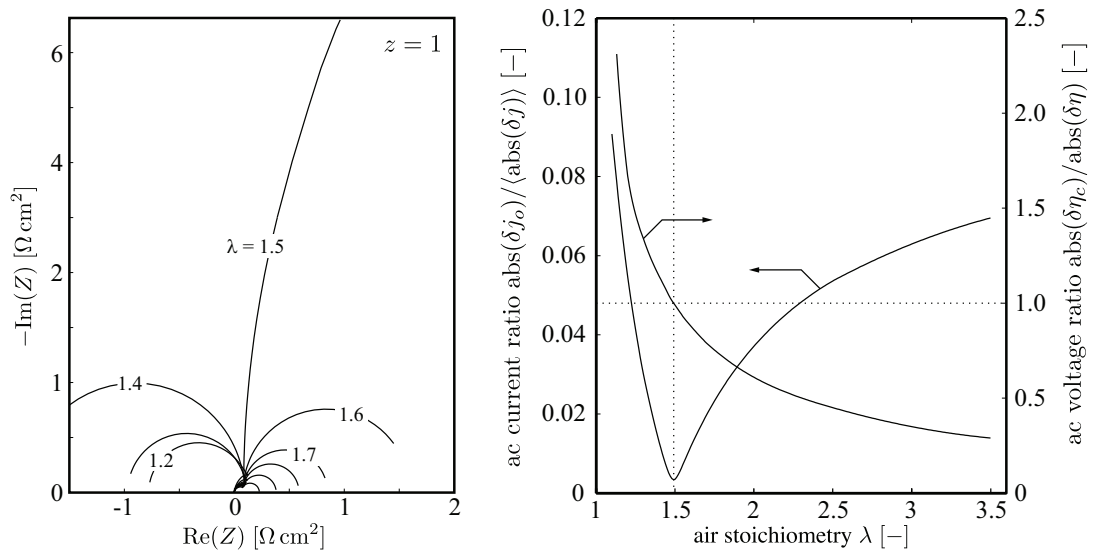
Figure 3.38: Modeled correlation between the oxygen concentration oscillation induced voltage and the ac current as a function of the air stoichiometry; the left hand diagram shows local spectra at $z = 1$ (normal model); the right-hand diagram compares the amplitude of the local ac current (normal model) and the oxygen concentration oscillation induced voltage $\delta\eta_c$ (adapted model defined by Equation (3.52)); model parameters given in Table 3.2; the impedance spectra range from $0.1\,\mathrm{Hz}$ to $5\,\mathrm{kHz}$.

induced voltage amplitude exceeds the amplitude of the total perturbation voltage. Exactly at the stoichiometry that results in unity of the voltage ratio, the ac current ratio features a minimum, which is near to yet not exactly zero. The qualitative model of Section 3.5.1 correlates the unity of the voltage amplitude ratio with a zero current amplitude. This minor discrepancy originates from the finite frequency of 0.1 Hz chosen for experiment and modeling, while the schema depicted in Figure 3.30 was based on considerations valid for the limiting case of vanishing frequency. With increasing stoichiometry, the ac current ratio increases and ac voltage and current are out of phase. This results in a reduction of the low frequency arc of the local spectra, because the low frequency end of the spectra points towards the positive real axis. If the air stoichiometry is reduced below the critical ratio of 1.4 to 1.5, the ratio of the ac current amplitudes is likewise increasing, which naturally causes a reduction of the radii of the corresponding local spectra. Yet, the arcs point towards the negative real axis. This is evidence that indeed the ac current is in phase with the ac voltage as was predicted by reasoning.

By the experiment just described, the ac voltage ratio $\Delta U_c/\Delta U$ was varied indirectly by changing the stoichiometric ratio. The direct change of ΔU (or $\delta\eta$ in the modeling case) while maintaining a constant ΔU_c is another approach. However, changing ΔU globally (for the whole cell area) implies a proportional change of ΔU_c, as both values scale with each other. Otherwise, the independence of the impedance on the actual perturbation amplitude (linearity of the system) would be violated. Hence, the change has to be done locally. If the perturbation amplitude is solely changed at the outlet, ΔU_c at the outlet is nearly not influenced. While this is easily done in modeling, such a variation of the local voltage perturbation amplitude is experimentally not as straightforward, because the phase must be maintained. The experimental configuration depicted in Figure 3.39 (a) was realized to change the amplitude of the local ac voltage amplitude by a factor G (gain) while maintaining the same phase and dc voltage over all the active area. The voltage of the cell (segments one to eight) is passed to an electronic device, which amplifies the ac part of the voltage while maintaining the dc level. The amplified signal controls a potentiostat, which is connected to segment No. 9. This arrangement ensures a matching dc voltage and phase of the voltage perturbation in all segments and allows the variation of the voltage perturbation amplitude of segment nine independently at the same time. Validating the mathematical model further, this change of the voltage perturbation amplitude at the outlet is realized by varying the perturbation voltage $\delta\eta$ only at $z = 1$ (symbolized by $\delta\eta_o$).

The diagrams of Figure 3.39 display the sensitivity of the local spectra at the outlet as obtained experimentally. The local spectra are shown in (c); the left diagram corresponds to an air stoichiometry of 1.4, and the right spectra of (c) reflect the operation under a stoichiometry of 2.5. The corresponding local spectra at $z = 1$ as obtained by modeling are shown in Figure 3.40. In any respect, the change of the local perturbation amplitude at the outlet (i.e., ΔU_9 experimentally and $\delta\eta_o$ computationally) exhibits a striking influence onto the local spectra. If the voltage perturbation amplitude ΔU_9 is increased relative to the amplitude applied to the rest of the cell ΔU_{1-8}, the low frequency arc is diminished at higher stoichiometry ($\lambda = 2.5$), and it folds back into the positive quadrant in the case of lower stoichiometry ($\lambda = 1.1$). It should be emphasized that at the same time the high-frequency part of the spectra shows no sensitivity to the local change of the perturbation amplitude.

The sensitivity in the low-frequency domain is not only explainable by the model described in Section 3.5.1 but also reflected by the mathematical model. The sketches of (b) in Figure 3.39 illustrate the relations between the amplitudes of the ac voltages, the ac currents, and the oxygen concentration oscillations (for the limiting case of vanishing frequency). In the case of lower SR ($\lambda = 1.1$), the oxygen concentration oscillation induced ac voltage slightly exceeds the base

Figure 3.39: Experimentally obtained sensitivity of the local spectra at the outlet towards a local change of the perturbation voltage amplitude; experimental configuration is shown in (a); the left-hand diagram correspond to a stoichiometry of 1.4, and the right-hand diagram reflect the operation at an air stoichiometry of 2.5; the sketches of (b) illustrate the relation between the ac voltage ration, the ac current, and the oxygen concentration; experimental conditions as described in Section 3.5.3 [142].
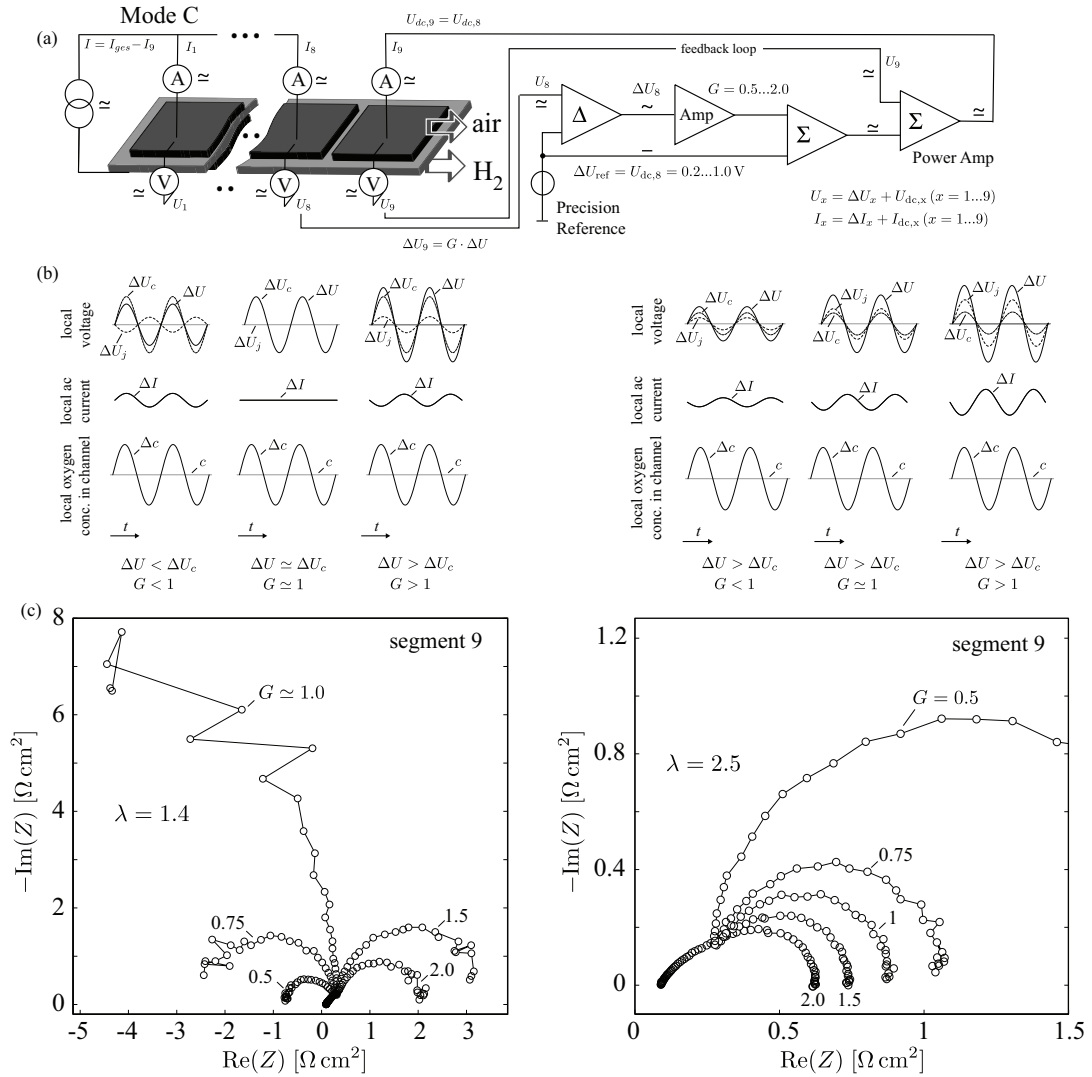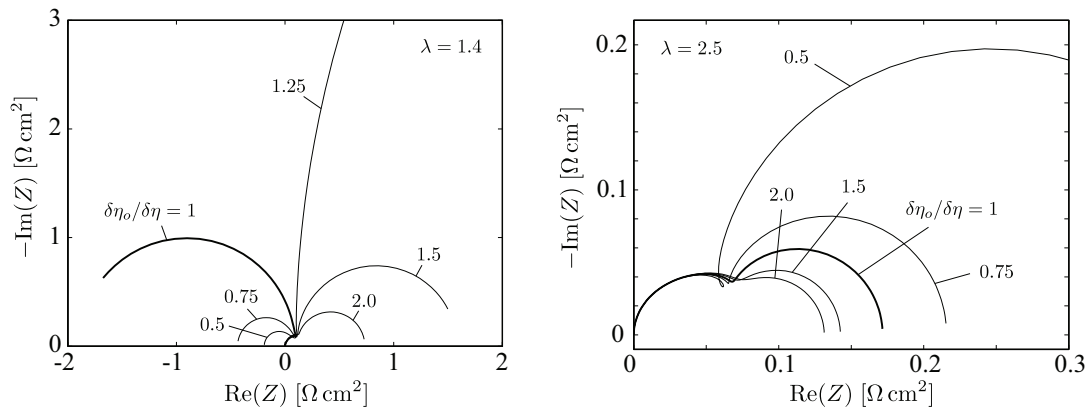

Figure 3.40: Modeled sensitivity of the local spectra at the outlet towards a local change of the perturbation voltage amplitude; the left-hand diagrams correspond to a stoichiometry of 1.4, and the right-hand diagrams reflect the operation at an air stoichiometry of 2.5; used parameters are found in Table 3.2.

143

perturbation amplitude at $\Delta U_9 / \Delta U_{1-8} = 1$. This stems from the folding of the spectra into the negative quadrant. By increasing ΔU_9 (experiment) or $\delta \eta_o$ (modeling), the ratio of oxygen induced voltage perturbation and applied voltage perturbation at the outlet (i.e., $\Delta U_9 / \Delta U_{1-8}$ and $\delta \eta_o / \delta \eta$, respectively) becomes smaller than one resulting in a phase shift of the faradaic current, which manifests itself in the spectra by an low-frequency arc that is pointing towards the positive real axis. If the voltage perturbation at the outlet is further increased, the difference between oxygen concentration oscillation induced voltage perturbation and applied voltage perturbation is increased. This causes a higher faradaic current and is reflected in the spectra by a reduced low-frequency arc. The opposite is true, if the voltage perturbation amplitude ΔU_9 is reduced. In the case of higher SR ($\lambda = 2.5$), the difference between oxygen induced voltage perturbation ΔU_c and applied voltage perturbation ΔU_9 is reduced. Consequently, the spectra feature an increasing low-frequency arc, because less faradaic current must account for the difference. In the case of lower SR, the oxygen concentration induced voltage perturbation ΔU_c is already exceeding the applied voltage perturbation for $\Delta U_9 / \Delta U_{1-8} = 1$. Hence, the difference between oxygen induced voltage perturbation and applied voltage perturbation increases by decreasing the applied voltage perturbation. This translates into an increase of the faradaic current[20], which implies a reducing radius of the flipped low-frequency arc.

3.5.5 The local build-up and influence of oxygen oscillations within the channels

The build-up of oxygen oscillations within the channel is a continuous process along the channels, where amplitude and phase are changing as a function of position z along the flow path. Only at the inlet, the amplitude is vanishing due to the constant oxygen concentration of the feed gas. The left plot of Figure 3.41 shows the calculated amplitude of the oxygen concentration oscillation at the GDL-channel interface ($y = 0$) as function of the position along the flow path. In the case of higher SR ($\lambda = 2.5$), the oxygen concentration oscillation is monotonically increasing towards the outlet. The series of plots at the right-hand side of Figure 3.41 visualize the ac part of the oxygen concentration δc for different perturbation frequencies at different positions (middle of the cell $z = 0.5$ and outlet $z = 1$). Shown is the coss-sectional view perpendicular to the z-axis. The upper half of the plots is associated with the higher SR of $\lambda = 2.5$. At higher frequencies (89 Hz), the oxygen oscillation is still confined to the GDL. Yet, already at 8.9 Hz a significant oscillation within the channels is calculated. The oxygen concentration oscillation is increasing with reduction of the perturbation frequency (0.1 Hz). Nonetheless, the amplitude is always highest at the electrode for $\lambda = 2.5$. A different picture is obtained at $\lambda = 1.1$. The amplitude of the oscillation at the GDL-channel interface passes a maximum along the channel (left diagram) between $z = 0.4$ and $z = 0.5$. In this region, the amplitude of the oxygen concentration oscillation is virtually constant over the thickness of the GDL and depth of the channel at the low frequency end (0.1 Hz). Due to Equation (3.40), this implies a vanishing faradaic ac current—an aspect that will be picked-up later. Further downstream, the amplitude of the oxygen concentration oscillation within the channels exceeds that at the electrode, which is related to the decline along the channel at the GDL-channel interface and is in conjunction with a phase shift of the faradaic ac current as will be discussed in the next paragraph. An interesting behavior is found at intermediate frequencies (8.9 Hz). Here, the amplitude is not monotonically increasing or decreasing over the thickness of the GDL but passes a minimum. This reflects the damping effect of the GDL, which obviously is less important at lower frequencies. Hence, the electrode is somewhat shielded from the oscillation

---

[20] It is worth recalling that the ac current is in phase with the ac voltage here.
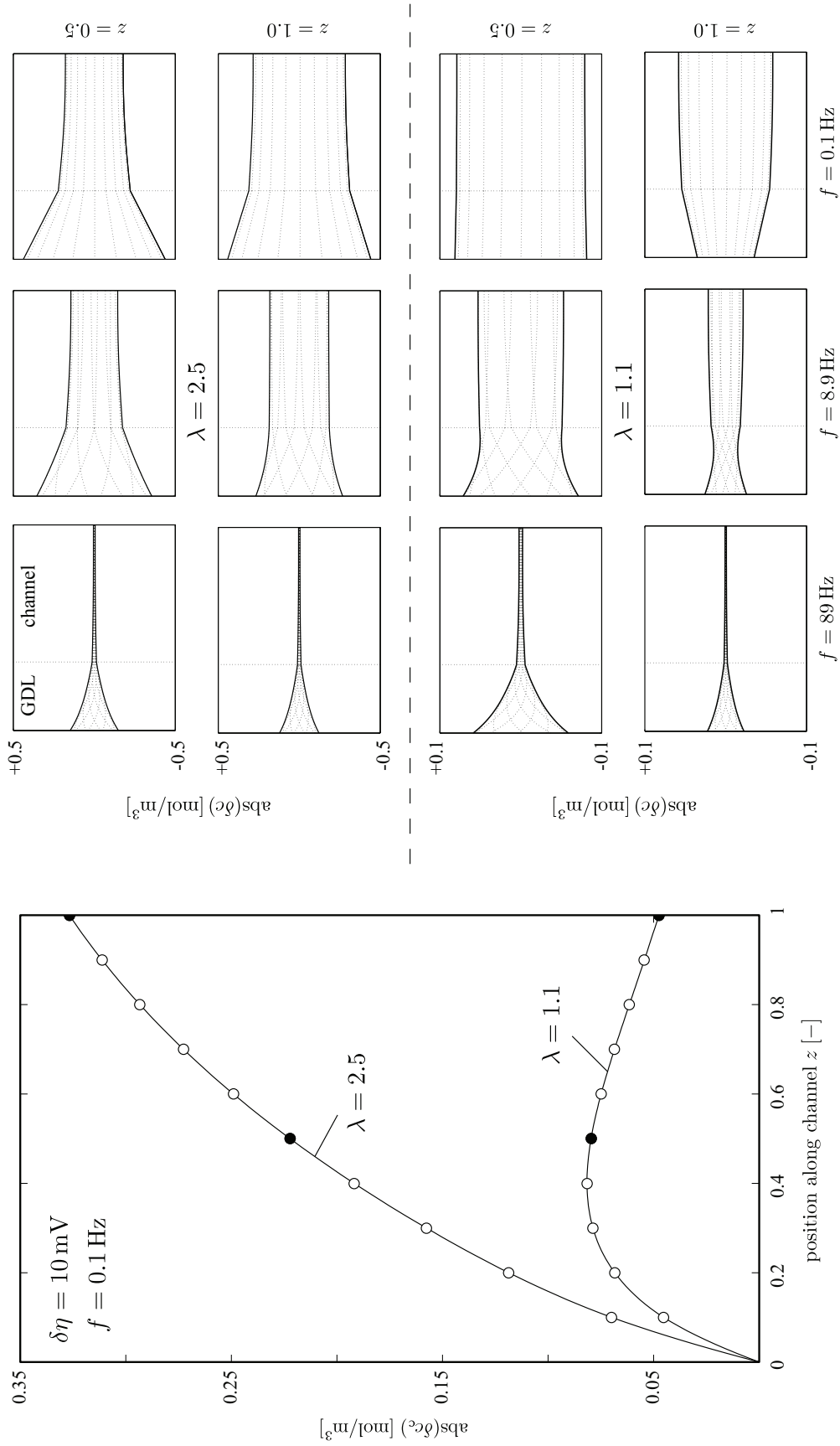
Figure 3.41: Calculated amplitude of the oxygen concentration oscillation as a function of position along the channel z; the left-hand diagram shows the amplitude at the GDL-channel interface for two stoichiometries as a function of the position along the channel; the diagrams to the right show the oxygen concentration oscillation in cross-sectional direction within the middle and at the outlet of the cell, respectively; the dashed lines reflect the ac oxygen concentration voltage perturbation amplitude $\delta\eta = 10\,\mathrm{mV}$ [143].
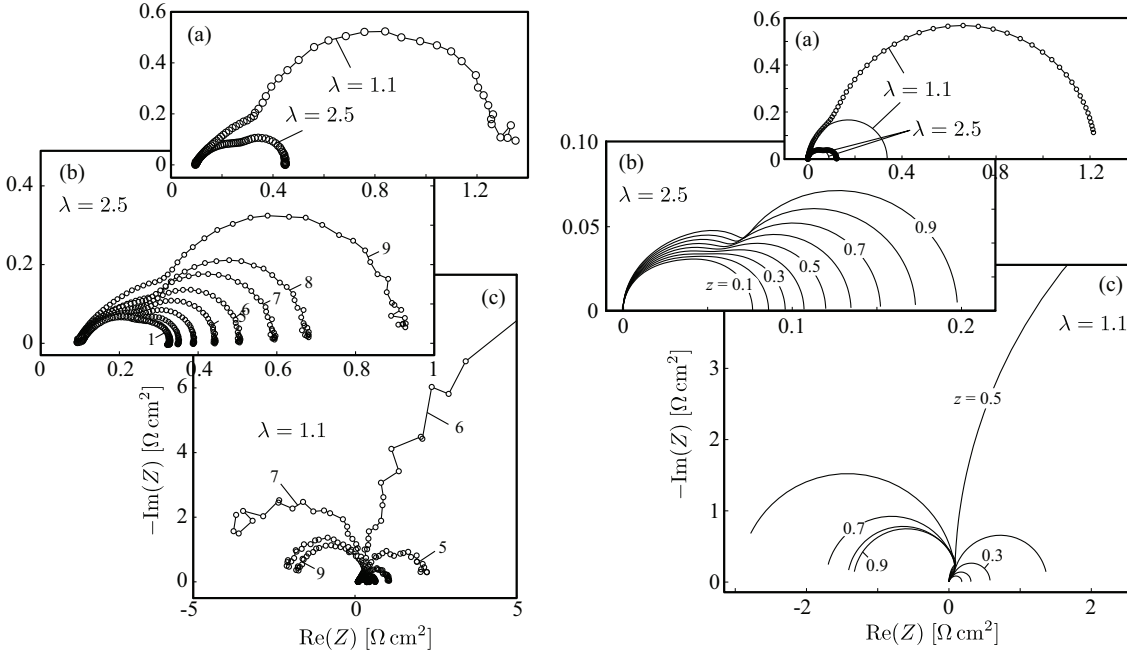
Figure 3.42: Integral and local impedance spectra for two stoichiometric ratios; experimental results are shown at the left; modeling results are shown at the right; (a) shows the integral spectra; the local spectra corresponding to a stoichiometry of 2.5 are shown in (b), and those corresponding to a stoichiometry of 1.1 are given in (c); the modulation frequency ranges from 0.1 Hz to 5 kHz; adopted from [142, 143].

within the channels, and at the same time the additional oxygen oscillation originating from the electrode is mitigated towards the channel. The superposition of both effects causes the minimum of the amplitude in the bulk of the GDL. Finally, the confinement of the oxygen concentration oscillation to the GDL at higher frequencies (89 Hz) is also seen for $\lambda = 1.1$.

Naturally, the oscillation of the oxygen concentration within the channels has an influence on the local impedance spectra and, consequently, is reflected in the integral spectra as well. Integral and local spectra are lined-up for two different stoichiometric ratios in Figure 3.42. Experimental findings are shown in the left part of the Figure, and spectra originating from modeling occupy the right half. The spectra of the diagrams (a) are the sum spectra. The modeling results show two spectra for each stoichiometry; those displayed by circles are calculated with the full model, and the spectra displayed by lines are calculated with the assumption of a finite diffusion length. This means the boundary condition at the GDL-channel interface (Eq. (3.47)) is replaced by $\delta c = 0$ at $y = 0$, and the model basically resembles a set of Randles-cells with NERNST diffusion connected in parallel. Experimentally, a distinct low frequency arc is found in the sum spectra for both stoichiometries. This arc is found by modeling as well, if the full model is used. Only one arc is found under the assumption of finite diffusion, which strongly indicates that the experimentally observable low frequency behavior is dominated by the coupled effect of semi-infinite diffusion and channel coupling along the flow path. The local spectra obtained at $\lambda = 2.5$ feature the low frequency arc, which is growing in size along the flow path. Yet, also the first arc is growing in size along the flow path. The higher frequency part of the experimental spectra is composed of several superimposed effects, while the high frequency arc radii of the modeled spectra are mainly related to the charge transfer resistance and a NERNST diffusion like term—both increase with reducing dc oxygen concentration. Hence, the oxygen depletion along the flow path is reflected in this part of the spectra as well. This will be discussed in more detail at the end of this section. Obviously, the ratio $\Delta U_c / \Delta U$ is always smaller than one, if the cell is operated at an stoichiometry of 2.5,

as can be seen from the right-hand diagrams on page 141 and can be concluded from the fact that the low frequency end of the spectra is always pointing towards the positive real axis. This is mainly due to the higher dc oxygen concentration along the flow path. Recall that the oxygen concentration oscillation induced voltage perturbation ΔU_c is determined by the ratio $\Delta c_e/c_0$ at the electrode. As the amplitude of the oxygen concentration oscillation is higher than at low stoichiometric operation (left diagram of Figure 3.41), ΔU_c can be kept below the perturbation amplitude ΔU only by sufficiently high values of c_0. If the cell is operated with an air stoichiometry of 1.1, ΔU_c exceeds ΔU in the outlet region (segments seven to nine in the experiment, and for $z > 0.55$ in the model). This can be concluded directly from the flipped low frequency arc of the spectra. Furthermore, the ratio $\Delta U_c/\Delta U$ is continuously increasing along the flow path, which stems from the fact that the low frequency arc is increasing while pointing towards the positive real axis, then passing infinity, and finally decreasing while pointing towards the negative real axis. As the modeling suggests, the amplitude of the oxygen concentration oscillation within the channels is decreasing in the outlet part of the cell (left diagram of Figure 3.41). Yet, the damping of the amplitude of the oxygen concentration oscillation[21] is over-compensated by the depletion of the dc oxygen concentration along the flow path. In consequence, $\Delta U_c/\Delta U$ is monotonically increasing although the oxygen concentration oscillation within the channels is attenuated towards the outlet.

Finally, to highlight the influence of the channel coupling and build-up of oxygen concentration oscillations within the channels to the local spectra, the attention will focus on the outlet again. The impedance response obtained without the build-up of oxygen concentration oscillations along the flow path will be compared with the impedance response resulting from the presence of oxygen concentration oscillations within the outlet. Experimentally, the build-up of oxygen concentration oscillations is circumvented by operating the segments one to eight in dc mode and performing EIS solely in segment nine (Mode D in Figure 3.33). From a modeling perspective, this is best done by comparing calculated spectra, which were obtained with the assumption of finite diffusion ($\delta c_c = 0$) with those originating from the full model derived in Section 3.5.2.2.

The spectra of the Figures 3.43 and 3.44 compare the impedance response at the outlet with and without the build-up of oxygen concentration oscillations within the channels as obtained from experiment and calculation, respectively. Depicted are the spectra for three different air stoichiometries. If the build-up of oxygen concentration oscillations is missing (Mode D for the experiments and finite diffusion for the model), the spectra feature only one arc despite the chosen stoichiometry. The experimentally obtained arcs are asymmetrical with a high frequency tail. The absence of this feature in the modeled spectra, which resemble almost a half-circle, is most natural, because effects such as agglomerate diffusion and finite conductivity of the electrode have been neglected. In the light of the work of EIKERLING et al. [46], the neglect of an ionic potential gradient over the thickness of the electrode might contribute to this discrepancy between experiment and model. They have shown on a theoretical basis that the finite conductivity of the ionomer within the electrode will result in a straight line at the high frequency end. In addition, the influence of the anodic electrode to the overall spectra should be considered (cf. Ref. [50]) as contributing to the qualitative discrepancy between experiment and model in the high frequency domain. However, the striking feature is found in the low frequency part of the spectra, and here the agreement between experiment and model is impressive. At higher stoichiometry ($\lambda = 2.5$), the spectra with and without build-up of oxygen concentration oscillations within the channels are separated from each other by the formation of a second low frequency arc. The total absence of this feature in the case of missing oxygen concentration oscillations within the channels is evidence of the dominance of this process (semi-finite diffusion and build-up along the channel) in this part of the spectra.

---

[21]It may be recalled that this is a consequence of the ac current being in phase with the voltage.

Figure 3.43: Experimentally obtained local impedance spectra at the outlet showing the influence of the oxygen oscillations within the channels onto the spectra for three different air stoichiometries; operating conditions are described in Section 3.5.3; the modulation frequency ranges from 0.1 Hz to 5 kHz [142].
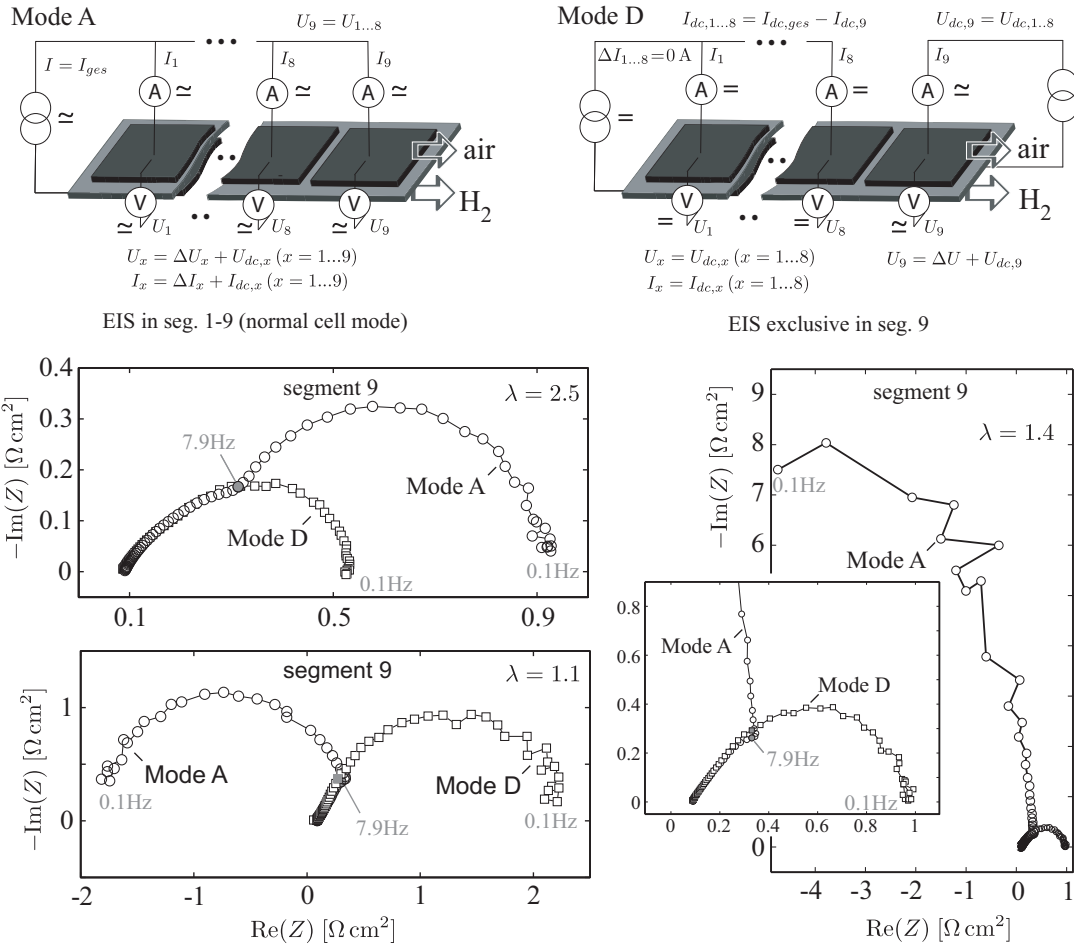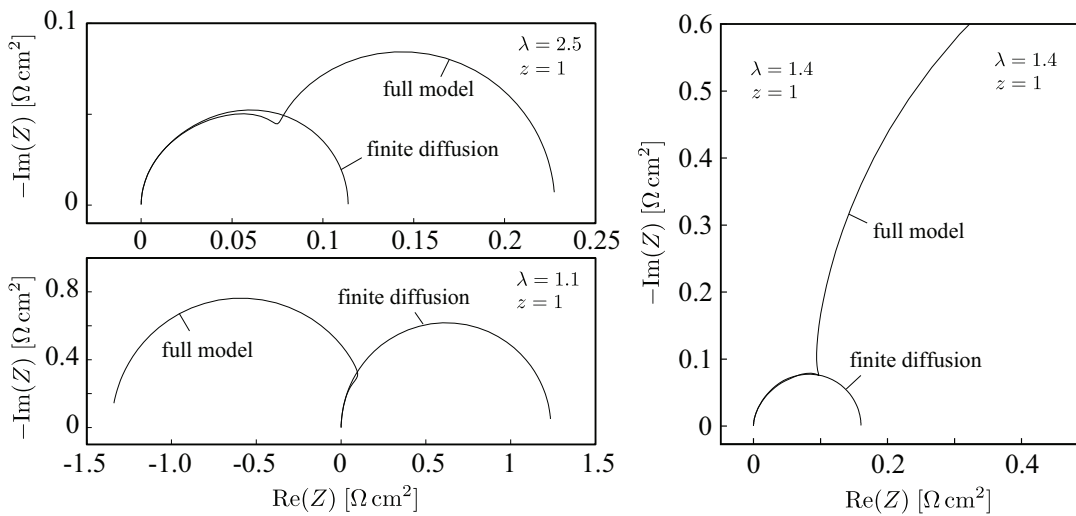

Figure 3.44: Modeled local impedance spectra at the outlet showing the influence of the oxygen oscillations within the channels onto the spectra for three different air stoichiometries; results are based on the parameters given in Table 3.2; the modulation frequency ranges from 0.1 Hz to 5 kHz [143].

Furthermore, the high frequency arc is affected as well. A slight difference can be seen clearly in the modeled spectra and is confirmed by the experimental findings. The high frequency arc is slightly depleted by the build-up of oxygen concentration oscillations along the channel. This is in agreement with the results shown in Figure 3.34 on page 139. At frequencies around $10\,\mathrm{Hz}$, the oxygen concentration oscillation induced voltage ΔU_c starts gaining substantial amplitude; yet, the phase is still vastly different from the perturbation voltage. Due to this discrepancy in phase, ΔU_c is not diminishing the faradaic current but adding to it—even though the amplitude is smaller than the perturbation amplitude. This leads to lower impedances, which explains the slight depletion of the high frequency arc. The same impact is also found for lower stoichiometries ($\lambda = 1.1$). The low frequency arc, which is bended towards the negative real axis because ΔU_c exceeds ΔU, is completely missing without the build-up of oxygen concentration oscillations along the flow path; and the diminishing impact of ΔU_c to the high frequency arc is likewise present. At intermediate stoichiometries ($\lambda = 1.4$), the low frequency arc dominates the spectra. Although experiment and modeled spectra tend towards different quadrants, the agreement is still excellent and consistent with the findings presented by the Figures 3.37 and 3.38. It was shown that air stoichiometries of about 1.4 to 1.5 are critical in the sense that at the outlet the oxygen concentration induced voltage ΔU_c nearly matches the perturbation amplitude ΔU. As the enormous radius of the low frequency arc solely stems from the nearly vanishing residual voltage ($\Delta U - \Delta U_c$), the spectra obtained by circumventing the build-up of oxygen concentration oscillations within the channels feature again just one arc.

Finally, while comparing the spectra without oxygen concentration oscillations for the different air stoichiometries, it is worth noting that the radii of the arcs increase with reducing stoichiometry. This shows the influence of the dc oxygen concentration. At least for the modeled spectra, it can be shown that these spectra virtually resemble a Randles-cell with a NERNST element in series to the charge transfer resistance. This becomes evident from Equation (3.51), which apart from the δc_c containing term[22] basically is the mathematical definition of such an equivalent circuit. Hence, the radii comprise a contribution from charge transfer and gas phase diffusion. Yet, both scale with the reciprocal of the dc oxygen concentration because R_{ct} scales with the reciprocal of the dc oxygen concentration in front of the electrode (see Equation (3.37)). For the experimentally obtained spectra, the situation might not be as simple because of the possible manifold contributions; this was briefly outlined several times throughout the last pages.

3.5.6 Varying effective diffusivity

In the light of this refined understanding of the processes contributing to the low frequency part of the spectra, it is worth recalling the findings presented in Section 3.4.2. There it was shown that the low frequency arc is first gaining and then decreasing in size along the flow path in counter flow mode (Figure 3.27 on page 125). At the same time, the liquid content within the GDL is reduced near the outlet and hence coincides with the decrease of the low frequency arc. The question arises whether a changing effective oxygen diffusion coefficient within the GDL might cause such an effect or not. To investigate the impact of a changing effective oxygen diffusion along the channels (e.g., caused by a changing liquid content within the GDL), the mathematical model is parameterized with a changing characteristic frequency ω_g along the channel. The upper right diagram of Figure 3.45 shows an arbitrarily chosen profile of the characteristic frequency of oxygen diffusion within the GDL. This parabola has been chosen with the qualitative liquid profile along the flow path in counter flow mode in mind (see Figure 3.24 on page 122); as the liquid content

---

[22]Recall that δc_c was set artificially to zero for the calculation of these spectra.
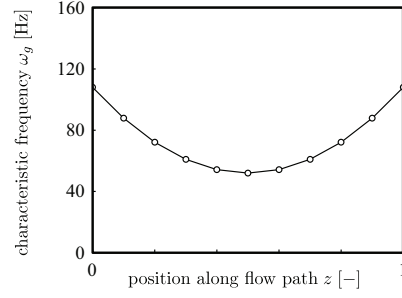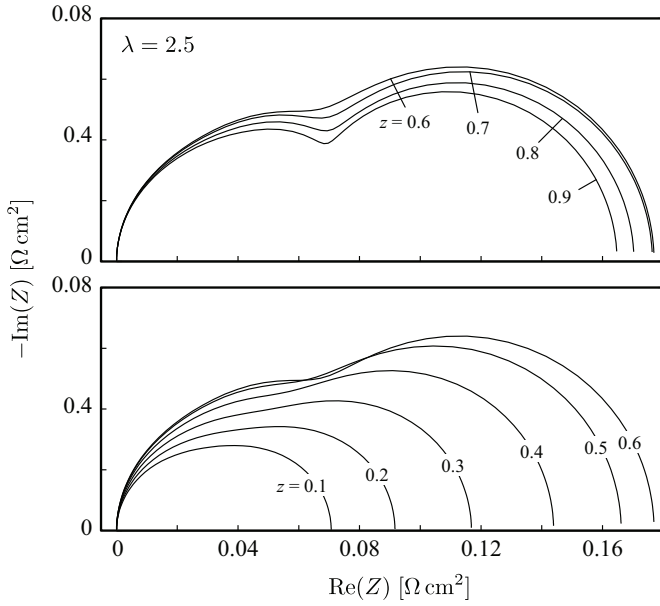
Figure 3.45: Sensitivity of local impedance spectra towards a locally changing characteristic frequency of oxygen diffusion within the GDL ω_g; calculated local spectra are shown to the left, and the arbitrarily chosen ω_g profile is depicted above; the frequency ranges from 5 kHz to 0.1 Hz.

is highest in the center of the cell, the ω_g-profile passes a minimum there and increases towards inlet and outlet. To calculate the spectra shown at the left of Figure 3.45, the parameters given in Table 3.2 were kept with the exception of the varying ω_g, and the spectra are calculated for an air stoichiometry of $\lambda = 2.5$ and an average current density of $500\,\mathrm{mA/cm^2}$ to ensure comparability with the experiments described in Section 3.4.2 and the findings of Section 3.5.5. In similarity to the calculations with constant ω_g, a low frequency arc is forming within the local spectra up to $z = 0.6$. Yet, the radii of the low frequency arc are decreasing for $z > 0.6$, which resembles the experimental findings of Section 3.4.2. This might further support the conclusion of a beneficial impact of the internal water loop towards oxygen transport—by diminishing the liquid content within the GDL—at the outlet in counter flow mode.

3.6 Cross-sectional liquid detection

Being a transmitting technique, neutron imaging cannot discriminate between liquid within the anode and the cathode, if the cell is investigated by passing the beam perpendicular to the active area through the cell. Yet, as has been highlighted in Section 3.4, there is a close coupling between water transport within cathode and anode. Hence, it is highly desirable to develop a experimental setup capable of discriminating between anode and cathode. Relying on neutron imaging, this can be achieved by rotating the cell by ninety degrees. However, this implies the need of a significantly increased spatial resolution, because a typical MEA is less than a millimeter thick.

3.6.1 High resolution imaging of the cross-sectional view

Detector choice. With the standard CCD detector setup, a spatial resolution of about $100\,\mu\mathrm{m}$ can be achieved (not counting the broadening incurred by the beam divergence and the scintillator). This is not sufficient for the cross-sectional investigation. From Table 2.3 on page 38, it becomes obvious that imaging plates (IPs) are the most appropriate detector choice due to the high spatial resolution of up to $12.5\,\mu\mathrm{m}$ per pixel. Unfortunately, the use of imaging plates bears some drawbacks as well:
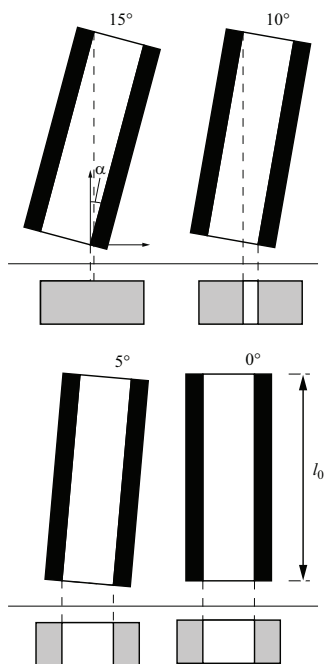
Figure 3.46: Principle of cell alignment by finding the maximal neutron transmission as function of the rotation angle.
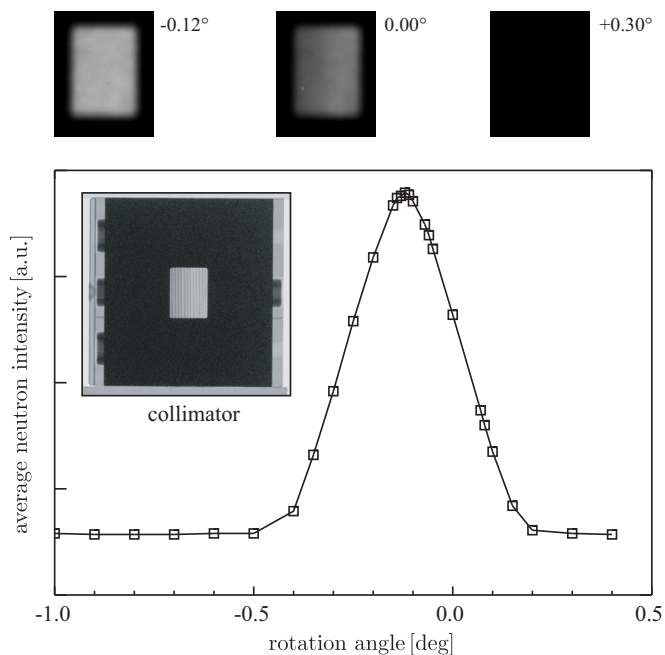
Figure 3.47: Example of sample alignment for high-resolution cross-sectional imaging; sample is a collimator consisting of an array of Gd-coated Mylar foils each $10\,\mu m$ thick; CCD images are shown above the diagram; IP image is shown as inset.

1. Imaging plates are not space invariant. This means that referencing as described in Section 2.2.1 is not possible, because it is highly complicated to position two IPs at the very same point during exposure and read-out within the scanner, especially in combination with the high spatial resolution.

2. The linearity of IPs is not as good as achievable with the CCD-detector for practical reasons. For example, during the transfer of the IP to the scanner, the IP might be exposed to a small amount of light (even if performed in a dark-room). Because, the IP is sensitive to light, this might change the intensity of the resulting image.

Cell alignment. A critical point while investigating the cross-sectional view of a fuel cell is the alignment of the cell. Due to the large penetration length, even a slight tilting of the cell relative to the beam direction results in a strong overlap of anodic and cathodic compartment on the detection plane. Hence, the cell has to be aligned precisely prior to the experiments. An objective and fast procedure is exemplified by the Figures 3.46 and 3.47. The Figure 3.46 illustrates the principle. If an object consisting of a material layer framed by two opaque layers is rotated, the projection length of the central layer at the detection plane is maximal, if the object is parallel to the beam. If the average neutron intensity of an area sufficiently large to include the central layer is obtained as function of the rotation angle, the value is maximal at the angle, where the sample is parallel. Taking the average as measure entails the applicability of the standard CCD detector for alignment, because a high spatial resolution is not required. To test the alignment procedure, a collimator consisting of several $10\,\mu m$ thick Mylar foils was rotated. The average neutron transmission as function of the rotation angle is shown in Figure 3.47 together with selected CCD images. The Mylar foils were coated with Gd to increase the neutron absorbtion of the thin foils. A high resolution IP image of the collimator is shown as inset. The relative neutron transmission features a clear maximum at $-0.12\,°$. Hence, the average neutron transmission obtained from an appropriate
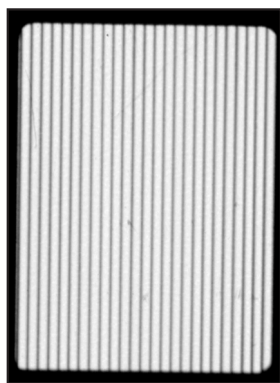
Figure 3.48: Profile of the neutron intensity indicating the inherent resolution of the IP detector for high resolution neutron imaging; the underlying image is shown above.
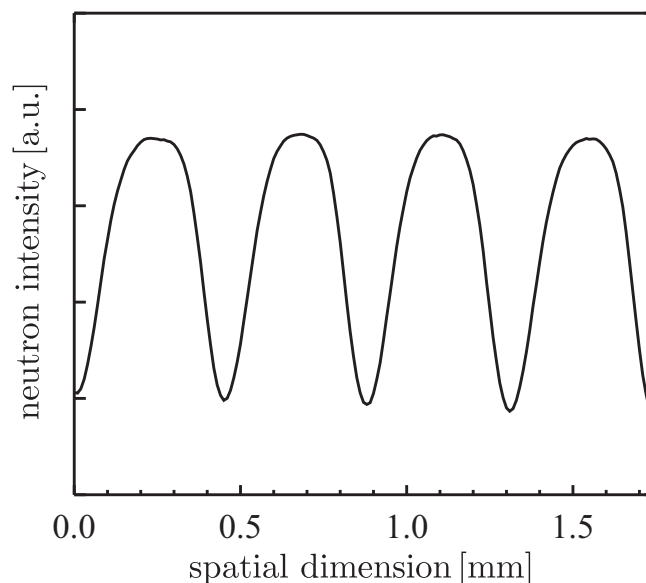
area provides a reliable measure of the sample alignment. Furthermore, the possible use of the standard CCD detector allows for a fast alignment.

Inherent resolution. Although the IP can be scanned with a resolution of $12.5\,\mu m$, the intrinsic resolution is somewhat lower because of the inherent IP resolution limited by the secondary particle spread (cf. Section 2.2.2.4) and the finite collimation of the beam. The neutron intensity profile over the width of the collimator is shown in Figure 3.48. The collimator was investigated at NEUTRAs measurement position three because of the higher L/D ratio. Nonetheless, the profile unveils a rather wide spread ($> 100\,\mu m$) of the peaks caused by the foils. Monte Carlo simulations performed by HASSANEIN [145] indicate that this spread stems mainly from the not perfectly collimated beam.

Another obstacle origins from the necessity to penetrate the sealing of the cell. Usual sealing materials contain a substantial amount of hydrogen. This entails a disturbance of the neutron beam—first by entering the cell and secondly by leaving the cell. This strongly reduces the image quality, as can be seen by comparing the images of Figure 3.49. The upper row shows the neutron image and profile of the cross-sectional view of the $25\,cm^2$ cell described in Section 3.2.2 without sealing (non-operative cell). The MEA is framed by graphite flow fields, which cause the black blocks. Within the images the two GDLs and the membrane are clearly seen. The profile plot shows two peaks—each associated with a GDL. These are separated by a minimum caused by the membrane. Hence, the MEA components are clearly separated, although the inherent resolution is well below the capacity of the detector. The lower row shows the cross-sectional view of the operative cell (including sealing). Due to the deteriorative influence of the sealing, the different MEA layers are indistinguishable, and the overall image quality is significantly reduced. The right-hand diagrams show corresponding cross-sectional intensity profiles. The two peaks of the upper profile are caused by the GDLs, which exhibit significantly less attenuation than the membrane. Hence, the minimum between these peaks is caused by the membrane. Due to the deteriorated quality of the lower image (operative cell), this separation of features is not as clearly recognizable, and a broadened profile is obtained.

removed sealing

operative cell
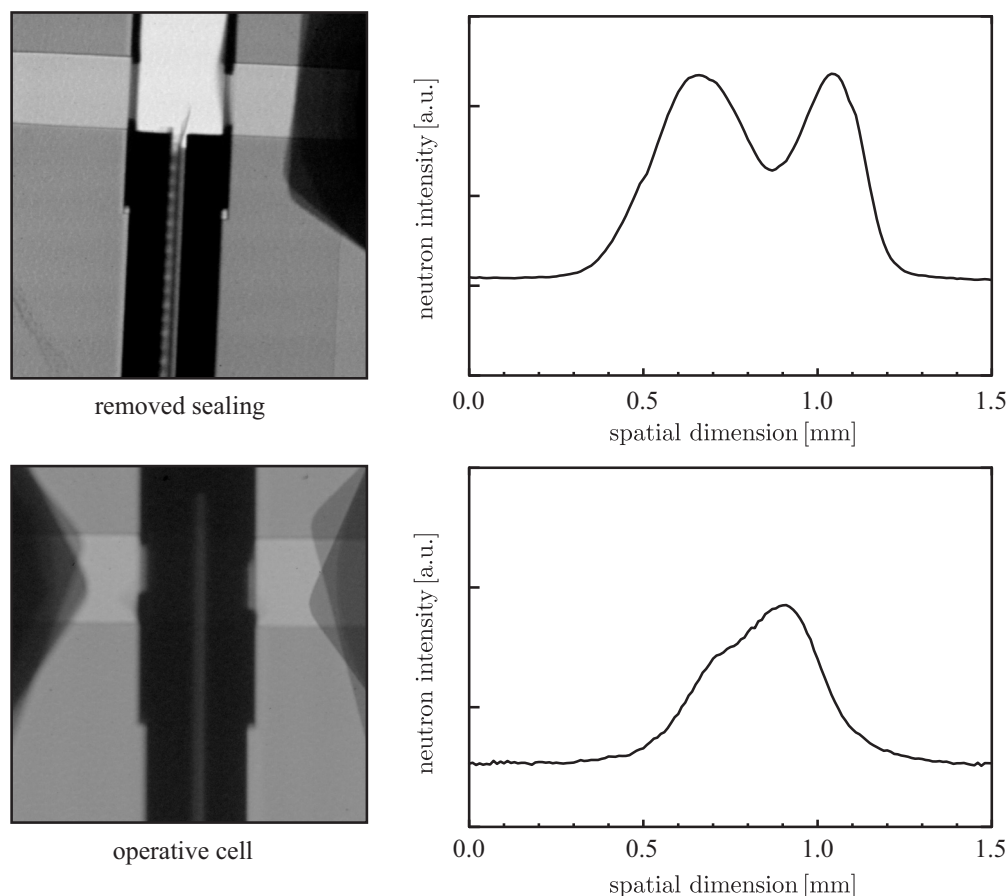
Figure 3.49: Deteriorative influence of hydrogen containing sealing materials onto the image quality of cross-sectional neutron images.

3.6.2 Proof of principle

The differential cell[23] described in Section 3.2.2 was utilized for first experiments intending the validation of the measurement principle. As made clear within the last section, the image quality obtained from this non-optimized cell can be expected to be far from optimal. Yet, even with this setup it is possible to separate liquid accumulations within the anodic and the cathodic compartment. This becomes apparent from the neutron intensity profiles shown in Figure 3.50. The profile labeled as dry was obtained while purging the cell with dry nitrogen. Hence, the porous structures contained no liquid, and the membrane was significantly dried as well. The profile is asymmetric around the membrane due to the presence of an additional insulating sheet. This sheet ensured that the flow fields are not electrically connected at the perimeter of the cell. The second profile was obtained while feeding the cell with humidified gases yet without generating current (OCV). The neutron intensity is reduced in comparison the dry case. By dividing both profiles, it becomes apparent that the reduction of neutron transmission is strongest in the membrane layer. The profile obtained by division is shown in the lower diagram of Figure 3.50. This indicates that the lower neutron transmission originates from membrane hydration. This is in agreement with quantitative results from the trough-plane view were always an offset of about $10 - 20 \, \text{ml/m}^2$ is found. Due to the broadening incurred by the detrimental impact of the sealing and the inherent resolution, the profile is altered over all the MEA area. Yet, the relative profile is symmetrical around the membrane layer. If current is generated, the change of the relative profiles is asymmetric with a much stronger decline of the neutron transmission within the cathodic compartment. Shown in

---

[23]cf. first paragraph on page 89
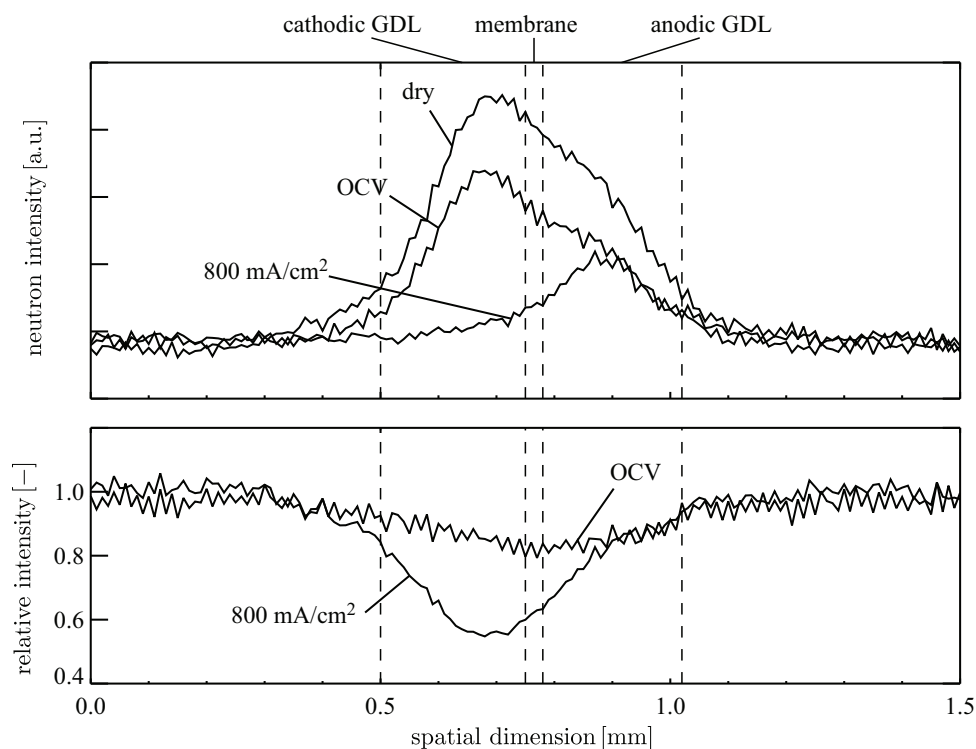
Figure 3.50: Neutron intensity profiles of the cross-sectional view under various operating conditions; the cell temperature is $70\,°C$; the anode was supplied with hydrogen according to a stoichiometric ratio of 18; the cathode was operated with oxygen according to a stoichiometric ratio of 150; both gas feeds entered the cell with a relative humidity of $80\,\%$; in the dry case the cell was flushed with $4\,l/min$ dry nitrogen at both sides; the underlying images were recorded with imaging plates.

Figure 3.50 is the case of $800\,mA/cm^2$. This asymmetry is a strong indication of a preferential accumulation of liquid within the cathodic compartment. The part of the profile corresponding to the anodic compartment is much less changed in comparison to load-free operation. This is evidence that at least the majority of liquid is located within the cathodic compartment—if not all liquid water.

In conclusion, these first results are very promising. Even without an optimized cell design, it was possible to qualitatively show the preferential accumulation of liquid within the cathodic compartment (at the investigated operating conditions). In the future, it is intended to improve the quality of the results by adapting the cell design. Mainly, a change of the sealing material will contribute to less broadened profiles. For the studies shown here, the time to scan an IP was about an hour, which limits strongly the number of investigations. A change of the scanner will reduce the time for read-out to some few minutes, which then allows the investigation of a wider field of operating conditions. Especially, the operation with over-saturated gases and current densities around $400\,mA/cm^2$ is of high interest due to the findings described in Section 3.2.3.2. Finally, the adjustable collimation ratio of the beam provided by ICON will help to reduce the broadening of the profiles.

Chapter 4

Direct methanol fuel cells

The investigation of mass transport related phenomena within DMFCs will focus on two aspects: the formation of a carbon dioxide rich gasous phase within the anodic flow field, and the permeation of water and methanol through the polymer electrolyte. Utilizing neutron imaging, information about the two-phase flow within the anodic flow field is gained. A more traditional diagnostic approach is followed to investigate the transport of methanol and water through the electrolyte. Here, first the influence of the electrolyte thickness is analysed for standard electrolyte materials, and, intending the reduction of the methanol permeation towards the cathodic electrode, a novel, alternative membrane material is explored afterwards.

Contributions of various co-workers were indispensable to obtain the results related within this chapter. Without the previous work of A.B. Geiger, the recent progress in investigating the formation of carbon-dioxide clusters within DMFCs would not have been possible, and part of the results shown in Section 4.1 were obtained jointly.

Various students contributed to the results related in Section 4.2. B. Köllmann (TU Clausthal, Germany) contributed to the used infrastructure by realizing a continuous methanol concentration control of the anodic feed loop as his diploma work [146]. During an internship, S. Loher (ETH Zürich, Switzerland) supported the measurements validating the perimeter-placed DHE as reference electrode. The results related in Section 4.2.3 contain contributions of V. Bammerlin (ETH Zürich, Switzerland) [147], and S. Deubelbeiss (ETH Zürich, Switzerland) contributed during an internship to the study depicted in Section 4.2.2.

The results related in Section 4.3 originate from a cooperation with Pemeas GmbH (Germany). Taking advantage of the diagnostic methods described in Section 2.4, membranes provided by Pemeas GmbH were characterized at PSI, and many fruitful discussions as well as a close cooperation were essential to the success of the project. Further on, L. Gubler participated in the project by performing and organizing part of the experiments, and students contributing to the project were G. Cassina (ETH Zürich, Switzerland) and M. Rubio-Munoz (Univ. de Murcia, Spain).
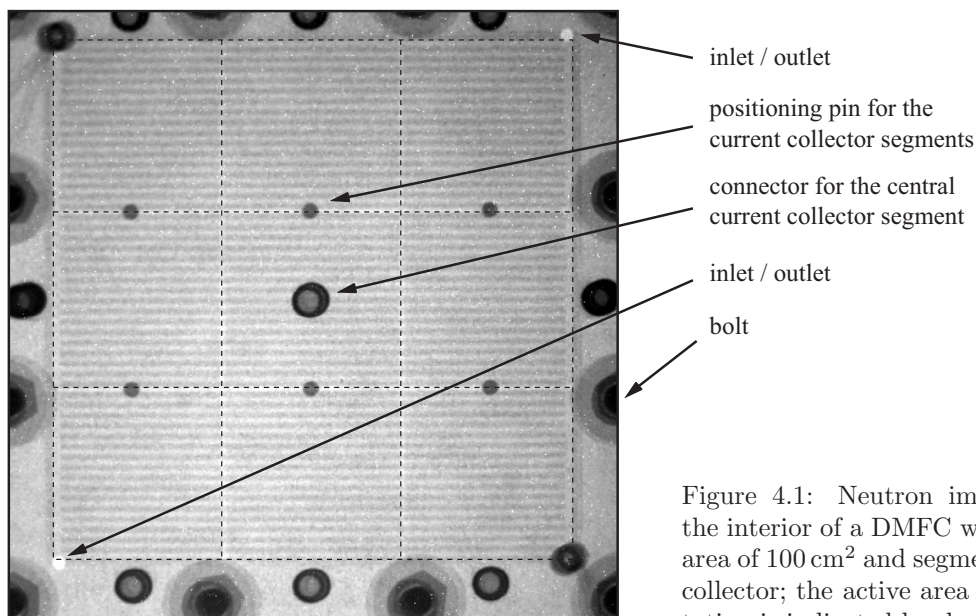
Figure 4.1: Neutron image showing the interior of a DMFC with an active area of $100\,cm^2$ and segmented current collector; the active area and segmentation is indicated by dashed lines.

4.1 Two-phase flow within the anodic flow field

Water-methanol solutions have a limited solubility for carbon dioxide—the anodic main reaction product of a DMFC. Hence, the formation of a CO_2-rich gaseous phase within the anodic, liquid feed is very likely. This formation of a two-phase flow pattern is believed to exhibit at deteriorative impact on the cell performance by hampering the distribution of methanol [56]. Consequently, several recent studies aimed for the investigation of bubble formation and transport within the anodic flow distributor. Mainly, the transparent cell approach described in section 2.1 was utilized to gain experimental access to the anodic flow channels [56, 148–153], and several mathematical models were proposed accounting for the two-phase flow within the anodic compartment, inter alia [56, 154]. The two-phase flow distribution in the anodic flow channels of a DMFC, however, depends on numerous parameters; therefore, the substantial change of the cell hardware implied by transparent cells might interfere with the two-phase flow distribution. This calls for a less intrusive approach such as neutron imaging, although optical methods best neutron imaging in terms of spatial and temporal resolution, to complement the suite of diagnostic methods.

4.1.1 Experimental

Cell design. To investigate the two-phase flow within the anodic flow field, a square cell with an active area of $100\,cm^2$ was chosen. The utilized cell hardware, which consists of two $2\,cm$ thick aluminun end pates with $2\,mm$ thick graphite-made flow fields, originated from earlier work of A.B. GEIGER [155]. A neutron image showing the interior of the cell is depicted in Figure 4.1. The cell featured a segmented current collector on one side, dividing the active area into nine segments (3×3 array) of equal size. By connecting each segment to an Hall sensor array [97], the local current generation could be obtained simultaneous to the radiographical measurements.

MEA and experimental conditions. The investigated MEAs consisted of two porous electrodes on carbon-paper and a Nafion 117 membrane. The anodic active layer consisted of Pt/Ru particles supported on graphite with a precious metal loading of $1.5\,mg/cm^2$, and the cathodic electrode was made of unsupported Pt black ($4.0\,mg/cm^2$). Two PTFE sheets with a thickness of

250 μm each were used as gaskets. All radiographical experiments were performed at NEUTRAs measurement position one (nearest to the source). If not stated otherwise, the anode was supplied with 1 M methanol solution, which is supplied from a tank to the cell by a gear pump. Prior to entering the cell, the methanol solution was heated to cell temperature. The anodic effluent was collected in a separate tank and was hence not recirculated. The cathodic oxidant (i.e, either air or pure oxygen) was provided by gas cylinders and directly passed to the cell (unhumidified). The cells were investigated by recording galvanostatically controlled polarisation curves. At every operating point, an equilibration time of several minutes was granted prior to taking images. As will be shown more clearly below, the used exposure-time of 0.5 s was a trade-off between image quality and temporal resolution. The cell was operated at 90 °C, and both sides where kept at a pressure of 2 bar(a).

4.1.2 Data treatment

The data treatment applied while investigating DMFCs resembles the processing of PEFC data (e.g., referencing is used to extract the attenuation due to the changing liquid content within the channels). Yet, some aspects particular to the quantification of the void fraction within the channels of a DMFC separate the data treatment from the general considerations related in Section 2.2 (cf. Ref. [62]). These will be highlighted hereinafter.

Thresholding. While investigating gaseous carbon dioxide clusters inside the anodic flow field, it is useful to neglect the possibility of partially filled channels and porous structures and to differentiate only three cases: (1) liquid on one side of the cell, (2) liquid on both sides of the cell, and (3) liquid on neither side. Provided the channel depth δ_{ch} of anodic and cathodic flow field are equal, the attenuation of a liquid-filled channel $a_{\text{ch}} = \delta_{\text{ch}} \cdot \Sigma$ would be nearly the same on each side[1]. Ideally, the anodic flow field is completely filled with liquid under load-free operation (OCV), while the cathodic flow field contains no liquid. Taking this operating condition as reference, the relative neutron transmission can take three discrete values:

$$x(i) = \exp\left\{(1-i) \cdot a_{\text{ch}}\right\} \quad i \in [0, 1, 2].$$

$$(4.1)$$

Therefore, values of $x > 1$ are correlated with liquid on neither side, values of $x < 1$ indicate the presence of liquid on both sides, and values of $x = 1$ result for liquid in one flow field. This discretization of the relative neutron transmission, principally, enables the use of a threshold to quantify the void fraction. Naturally, this is an over-simplification leading to semi-quantitative results [62]. Owing to the noise accompanying the images (cf. Section 2.2.5), the obtainable referenced neutron images are characterized by a continuous distribution of relative neutron transmissions. This is exemplified in Figure 4.2, where a referenced neutron image from an operational DMFC under load is depicted together with the corresponding histogram. The medium gray shades indicate areas where no change in comparison to the reference image is detected. Beside the ribs formed by the flow field structure—in this chase fifty parallel channels—channels with liquid on one side contribute to this area, which is represented within the histogram by the large peak around $x = 1$. The lighter strips formed by gaseous clusters inside the anodic flow field are reflected within the histogram by the "shoulder" at higher relative neutron transmissions. The accumulation of liquid on the cathodic side was avoided as far as possible (cf. Section 4.1.3). Hence, the referenced image contains only values around $x = 1$ and above. As investigated in detail in Section 2.2.5.1,

---

[1]This neglects the different attenuation of methanol. Yet, as the anodic feed is highly diluted, this is a justified approximation.
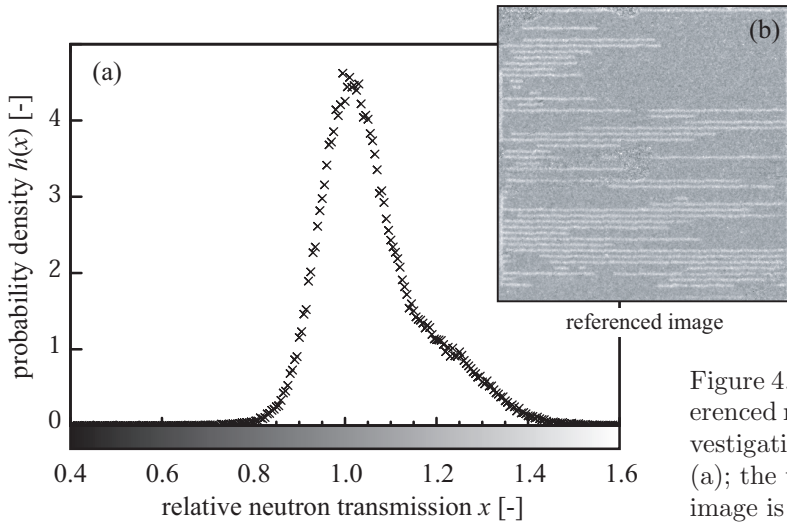
Figure 4.2: Histrogram of a typical referenced neutron image from DMFC investigations; the histogram is shown in (a); the underlying referenced neutron image is shown in (b).

the image noise is dominated by shot-noise, and in resemblance to the model experiments depicted in Section 2.2.6.3, this results in a continuous distribution of the measurable relative neutron transmission even if the attenuation of the sample is discrete.

The considerable noise level implied by the rather short exposure-time needed to achieve sufficient temporal resolution limits the applicability of thresholding for quantifying the void fraction (i.e., the percentage of gas-filled channels). An adequate threshold value is not easily defined, because relative neutron transmissions around 1.1 could origin either from a gas-filled or a liquid-filled region. To emphasis this, the relation between threshold value and resulting void-fraction is depicted in Figure 4.3 together with selected binary images. The quantitative result depends strongly on the choice of the threshold value. Consequently, this approach provides only semi-quantitative information—yet, the full spatial resolution is preserved.

Statistical quantification. By omitting the spatial information, the application of statistical methods becomes available. As shown in Section 2.2.6.3, the histogram can be understood as the biased probability density of relative neutron transmissions convoluted with a noise function or distribution. Hence, the true probability distribution is obtainable by deconvolution. Due to the restrictions introduced by Equation (4.1), this is not needed, because the relative neutron transmission x is restricted to three discrete values. Therefore, the convolution forming the measurable histogram simplifies to a sum of three appropriately scaled noise distributions, and the histogram can be reflected by

$$\tilde{h}(x) = \sum_{i=0,1,2} g_i\left(x, \langle x \rangle_i, \sigma_i\right), \tag{4.2}$$
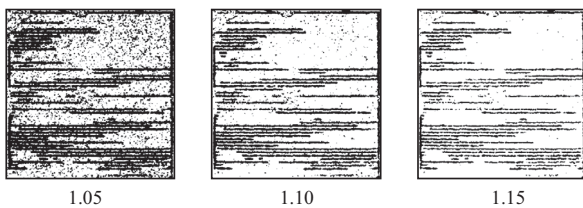
Figure 4.3: Threshold sensitivity of void-fraction quantification; underlying binary images for selected thresholds are shown above; the underlying image is shown in Figure 4.2.
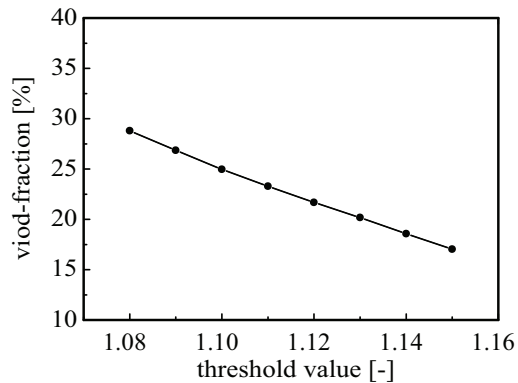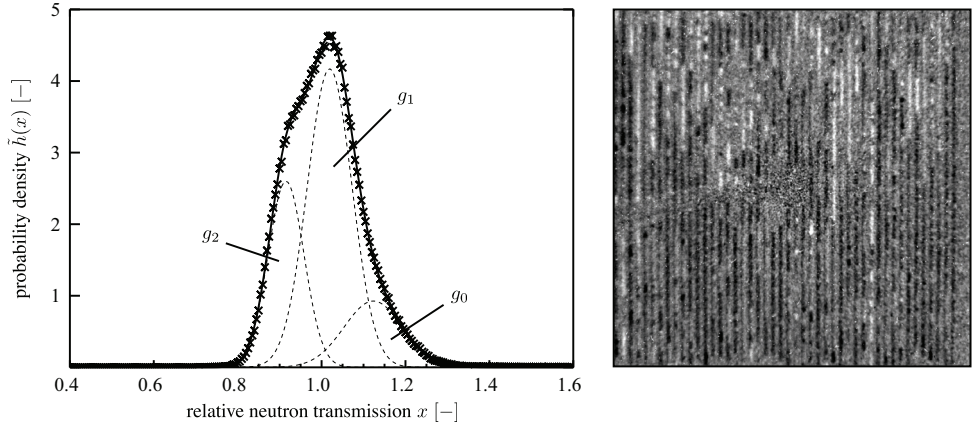
Figure 4.4: Fit of the relative neutron transmission probability density of an image featuring a heavily water-clogged DMFC with Equation (4.2); g_2 corresponds to black, g_1 to medium gray, and g_0 to light gray shades in the image.

where the g_i are well approximated by a scaled GAUSSIAN distribution with mean $\langle x \rangle_i$ and standard deviation σ_i (cf. section 2.2.5.2). To improve the reliability of the parameters obtained by fitting experimental histograms with Equation (4.2), it is useful to incorporate the relations described in Section 2.2.5.2. Especially, the relation between the average and the standard deviation (cf. Equation (2.67) on page 49) allows reducing the number of independent variables, because the number of independent standard deviations is reduced from three to one.

The fitting procedure is exemplified in Figure 4.4, where the histogram of the right-hand image is fitted with Equation (4.2). Being obtained from a heavily water-clogged cell, the image contains a considerable amount of dark gray to black strips ($x \ll 1$). These indicate areas where both flow-fields are liquid-filled. Medium gray shades are indicative of a relative neutron transmission around one, and the light gray to white strips ($x \gg 1$) are associated with areas where both flow fields are gas-filled. Therefore, all three GAUSSIANS contribute substantially to the overall histogram: g_1 for the unchanged area (ribs and liquid inside one flow field), g_0 for the area occupied by gas clusters on both sides, and g_2 for the area where liquid is present in both flow fields.

Further on, this points towards an intrinsic limitation of radiographical methods. The area represented by g_1 comprises three contributions: (1) the rib area, (2) the area where liquid is present within the anodic flow field while the cathodic flow field is gas-filled, and (3) the area where liquid is present within the cathodic flow field while the anodic flow field is gas-filled. Though the rib-area is easily excluded by masking, the cases (2) and (3) remain indistinguishable permitting the concealment of anodic gas-clusters by liquid within the cathodic flow field.

4.1.3 Concealment of gas clusters by cathodic water

To explore the possible concealment of gaseous carbon dioxide clusters by liquid water within the cathodic flow field, the cathodic flow field geometry was varied. The investigated setups were: (a) a one channel serpentine, and (b) a flow field made of fifty parallel channels. In both cases a parallel flow field with fifty channels formed the anodic flow distributor. The channel width and depth was 1 mm in either case. The rib width was likewise 1 mm yielding a rib-to-channel ratio of one.

Liquid is more efficiently removed from the cathode by choosing a one-channel serpentine, since all the mass flow is forced along a single path. This can be concluded by discussing Figure 4.5, where
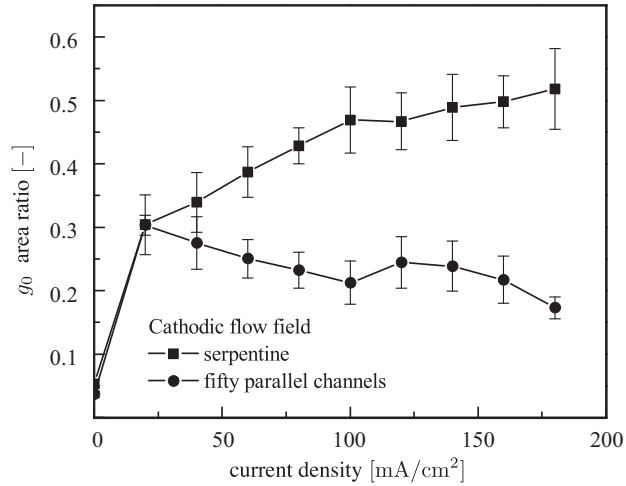
Figure 4.5: Area ratio of the g_0 signal indicating the portion of the image, where both flow fields are gas-filled; fifty parallel channels form the anodic flow field; cell temperature is $90\,°C$; anodic feed is $12\,ml/min$ 1 M methanol solution; cathodic feed is $1.5\,l/min$ dry oxygen.

the area ratio of the g_0 signal is plotted as a function of the current density for the two investigated setups. If the serpentine is used, the area ratio of the g_0 signal is increasing monotonically with current density, which is a direct measure for the produced carbon dioxide. At a current density of $200\,mA/cm^2$, the g_0 signal occupies $50\,\%$ of the image. The g_0 value cannot exceed that number, because half of the area is associated with the ribs. Hence, nearly the entire anodic flow field is gas-filled, and no liquid water is blocking the cathodic flow field. If the same flow field geometry that is used at the anode is used as cathodic flow field as well, the g_0 signal increases at very low current densities; yet, for higher current densities the signal decreases again. This is most likely due to liquid inside the cathodic flow field. This directly shows that this geometry is inferior to the single channel serpentine in terms of liquid removal capacity. Furthermore, no clear information about the amount of gaseous carbon dioxide inside the anode can be obtained, because part of it is concealed by liquid water within the cathode. However, considering the unchanged anodic compartment, it might be allowed as a rough guess to assume a comparable void fraction within the anodic flow field for setup (a) and (b).

4.1.4 Void fraction and flow rate

To further investigate the anodic two-phase flow, setup (a) with the serpentine cathodic flow field was used intending the mitigation of carbon dioxide clusters concealment by liquid within the cathodic flow field as far as possible. An increase the anodic flow rate should result in a reduced void fraction within the anodic flow field. This intuitive assumption is sound, as can be concluded from Figure 4.6. The rib area was disregarded. Therefore, a value of 1.0 translates into a completely gas-filled anodic flow field. Surprisingly, a relatively high percentage of the gas channels is already gas-filled at very low current densities $(20\,mA/cm^2)$. This indicates that not all channels are supplied equally. It seems that non-moving carbon dioxide clusters block some channels, and the majority of the mass flow is passed through the remaining channels. Nonetheless, an increase of the anodic flow rate by more than a factor of three considerably reduces the average void fraction. Yet, still a relatively large fraction of the flow field is occupied by gaseous clusters.

From the performance point of view, a variation of the anodic flow rate has a bivalent impact. As is evident from Figure 4.7, a lower flow rate benefits the electrochemical performance at lower current densities; yet, a severe limiting current density is experienced as well. At a first glance, this mass transport hindrance might be attributed to a reduced average methanol concentration within the flow channels due to depletion along the flow path. Yet, even at $200\,mA/cm^2$ the cell is provided with nearly five times the amount of methanol needed for the electrochemical conversion ($\lambda \simeq 5$) if
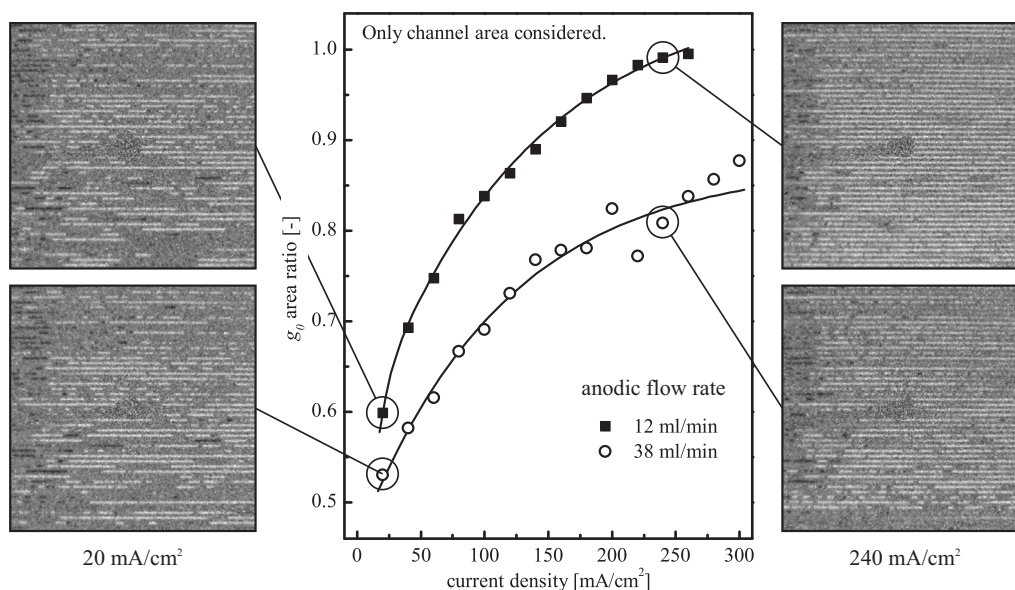
Figure 4.6: Influence of the anodic flow rate onto the amount of void fraction inside the anodic flow field as indicated by the g_0 area ratio; cell temperature is 90 °C; anodic feed is 1 M methanol solution; cathodic feed is 1.5 l/min; fifty parallel channels are used as anodic flow field, and a single channel serpentine served as cathodic flow field.

fed with 12 ml/min of 1 M methanol solution. Hence, the methanol concentration within the effluent is depleted by roughly 20 % compared to the inlet feed[2], and a reduction of the average methanol concentration is unlikely to be the main cause of the experienced limiting current density. This leaves the disturbed distribution of the methanol solution as possible reason for the deteriorated limiting current density. However, considering the radiographical result—virtually all channels are gas-filled at 200 mA/cm^2—it is surprising that the cell is able to generate even this amount of current. As shown by SCOTT et al. [149], who studied the limiting current density of a DMFC, the gaseous clusters might contain methanol and water vapor beside carbon dioxide giving rise to the assumption that methanol transport via the gaseous phase might substantially contribute to the overall transport rate. This might explain the ability to significantly generate current while the anodic flow field is nearly completely filled with gaseous clusters. Although an increase of the void fraction generally impedes the methanol transport towards the electrode and, therefore, limits the current density, a deteriorative influence with respect to the electrochemical performance is not necessarily implied for lower current densities. In fact, the hampered methanol transport towards

---

[2]not counting the methanol that is crossing the membrane (cross-over).
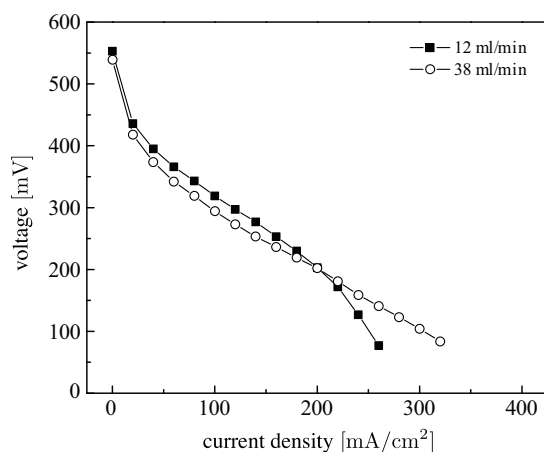
Figure 4.7: Polarisation curves corresponding to Figure 4.6 showing the influence of flow rate; cell temperature is 90 °C; anodic feed is 1 M methanol solution; cathodic feed is 1.5 l/min O_2; fifty parallel channels are used as anodic flow field, whereas a single channel serpentine served as cathodic flow field.
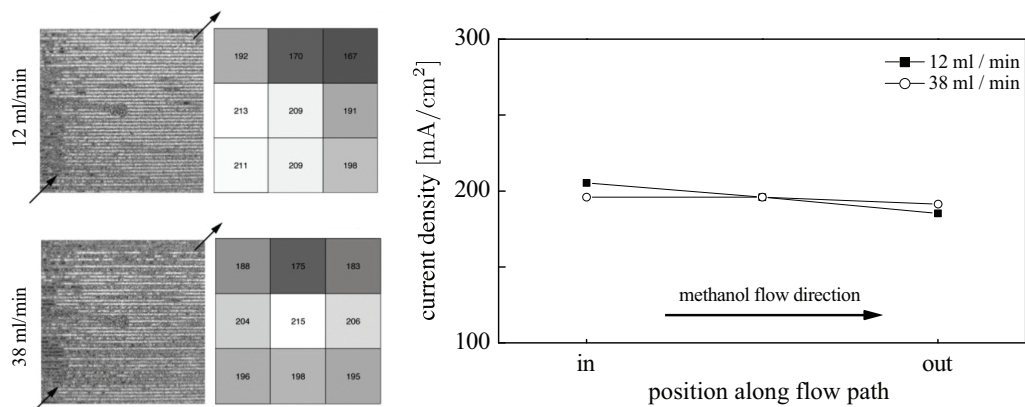
Figure 4.8: Line-up of neutron images and current density maps for two different anodic flow rates; neutron images and current density maps are shown at the left-hand side, the right-hand diagram shows the average current density of each column; operating conditions as for Figure 4.5.

the anode is beneficial to the electrochemical performance at low current densities, which might be attributed to a lower methanol permeation rate towards the cathode. Based on theoretical considerations, KULIKOVSKY argues similarly yet sees a beneficial impact of reduced methanol permeation only if accompanied with insufficient oxygen supply [154].

Finally, the discussion might shortly touch upon the influence on the current density distribution. The left part of Figure 4.8 shows neutron images and current density maps at an average current density of $200\,\mathrm{mA/cm^2}$ for the compared anodic flow rates. The right diagram shows the vertical average of the current density maps (averaged columns). In general, the current density maps are rather homogeneous (about $10\,\%$ deviation from the average), and only a very slight decline is found in flow direction (right diagram) for the lower flow rate. Considering the accumulation of produced carbon dioxide along the flow path, an increased void fraction might be expected downstream. Yet, such a trend is not seen or at least not very pronounced for the chosen setup and operating conditions. Together with the rather low depletion of methanol along the flow path[3], this might explain the nearly homogeneous current density distribution along the methanol flow path. However, this must not lead to the general conclusion that the carbon dioxide clusters do not interfere with the cell operation. It can merely be stated that no clear trend of the void fraction is found along the flow path, and hence a detrimental or beneficial impact onto the local current density along the anodic flow path cannot be seen.

4.2 Transport of methanol and water across the MEA

4.2.1 Experimental

Selected aspects of the coupled transport of methanol and water within DMFCs were investigated by taking advantage of a small-scale single cell[4] with an active area of $29\,\mathrm{cm^2}$. The anodic and cathodic flow field were made by machining $1\,\mathrm{mm}$ wide channels into $1\,\mathrm{cm}$ thick graphite plates forming a single channel serpentine. Providing the means to evaluate the polarisation of each electrode, a DHE was incorporated at the perimeter of the cell (cf. Section 2.4). Though the membrane thickness was varied for the experiments presented in Section 4.2.3, the MEA components

---

[3]Recall that even for the low flow rate the stoichiometric ratio is nearly 5 at $200\,\mathrm{mA/cm^2}$.
[4]Being a standard design for *in situ* material characterization at PSI, a detailed description of this cell type is found in Ref. [12, Section 3.2.2].

(i.e., electrodes, GDLs, and membrane material) match those used for the investigations related in Section 4.1. If not stated otherwise, the cell was operated at 90 °C at a pressure of 2 bar(a).

4.2.2 Compression of the MEA

Within Section 4.1.4 the current density distribution was shown to be largely independent on the depletion of methanol along the anodic flow path. Yet, at the same time the polarisation curves showed a limiting current density. This suggests a mass transport limitation in cross-sectional direction. As oxygen was used as cathodic supply, it is likely that the current density is limited due to the diffusive transport of methanol through the anodic GDL. Targeting on the sensitivity of the electrochemical performance towards this transport process, cells with PTFE gaskets[5]. of different thickness and, therefore, different compression of the MEA were investigated.

Theoretical considerations. By changing the thickness, the diffusive transport through a GDL is affected in two ways: (1) the diffusion length is varied, and (2) the implied porosity and tortuosity change affects the effective diffusion coefficient. Both effects counteract each other; while a reduced diffusion length is beneficial for the mass transport, the reduction of porosity and increase of tortuosity with augmenting compression is detrimental. This is reflected by FICK's first law, which reads

$$\dot{n} = \frac{\epsilon}{\tau} \cdot D \cdot \frac{\Delta c}{\delta} \tag{4.3}$$

in its one-dimensional form. Herein, the porosity and tortuosity are symbolized by ϵ and τ, respectively. The diffusion length is denoted by δ, and the diffusion coefficient is given by D. Further on, Δc is the concentration difference over the thickness δ and $\dot{n}$ the resulting molar flux, respectively.

The porosity of the compressed GDL is given by the ratio of free pore volume V_f to the total volume V_t, and the total volume is the sum of free volume and the volume occupied by the solid material V_m. Consequently,

$$\epsilon = \frac{V_f}{V_t} = 1 - \frac{V_m}{V_t} \tag{4.4}$$

defines the porosity. If the solid material is considered incompressible, V_m will be independent of the degree of compression, which allows to express the porosity as a function of the ratio δ/δ_0

$$\epsilon = 1 - (1 - \epsilon_0) \cdot \frac{\delta_0}{\delta}, \tag{4.5}$$

where δ and δ_0 denote the thickness of the compressed and uncompressed GDL, respectively. Furthermore, ϵ_0 denotes the porosity of the uncompressed GDL. If the change of tortuosity is neglected as a first order approximation (cf. Ref. [132] for the dependence of the tortuosity on the compression), the following expression can be derived:

$$\frac{\dot{n}}{\dot{n}_0} = \frac{\epsilon}{\epsilon_0} \cdot \frac{\delta_0}{\delta} = \left[\frac{1}{\epsilon_0} - \frac{1 - \epsilon_0}{\epsilon_0} \cdot \frac{\delta_0}{\delta} \right] \cdot \frac{\delta_0}{\delta} \tag{4.6}$$

The diagram of Figure 4.9 shows the relative molar flux $\dot{n}/\dot{n}_0$ as given by Equation (4.6) as a function of the GDL compression $1 - \delta/\delta_0$ for different porosities of the uncompressed GDL. An average compression of the GDL (around 20 %) results in a slight increase of the relative molar flux. Hence, the reduced diffusion length outweighs the reduction of the porosity. If the compression is further increased, a maximum is passed. The maximum relative molar flux as a function of the compression depends on the porosity of the uncompressed GDL. Although aspects

---

[5]Being virtually incompressible, PTFE gaskets allow to assemble cells with a known thickness of the GDLs.
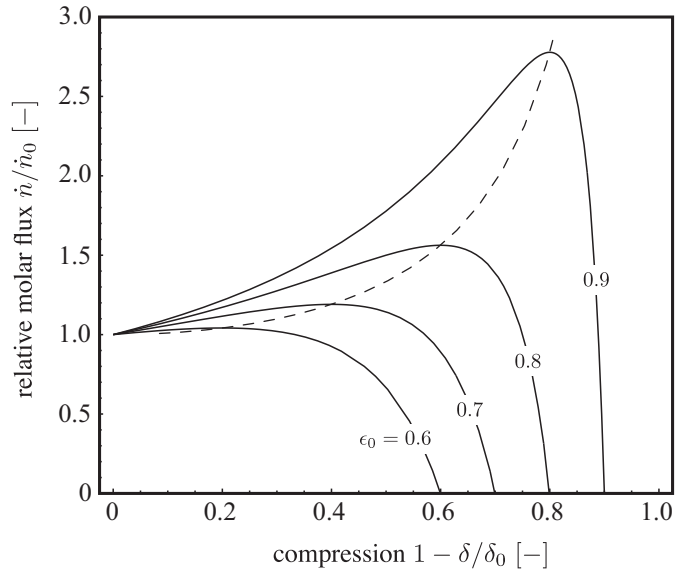
Figure 4.9: Relative molar flux as function of GDL compression as given by Equation (4.6).

like contact resistance and mechanical integrity require consideration while determining the optimal compression, it can be shown that from a mass transport perspective the optimum compression is given by

$$1 - \frac{\delta}{\delta_0} = 2 \cdot \epsilon_0 - 1. \tag{4.7}$$

If the GDL is compressed beyond this value, the strongly diminished porosity outweighs the reduction in diffusion length, which results in a steep decline of the relative molar flux. Hence, given a uncompressed porosity of 70 %, which is a common value for many GDL materials, it can be expected that a compression of up to about 40 % will lead to a moderate improvement from a mass transport perspective, while a stronger compression will be detrimental.

Electrochemical performance. Polarisation curves obtained with similar MEAs yet gaskets ranging from 150 μm to 250 μm thickness are compared in Figure 4.10. The polarisation of the single electrodes as obtained with the DHE arrangement described in Section 2.4 are shown in the inset
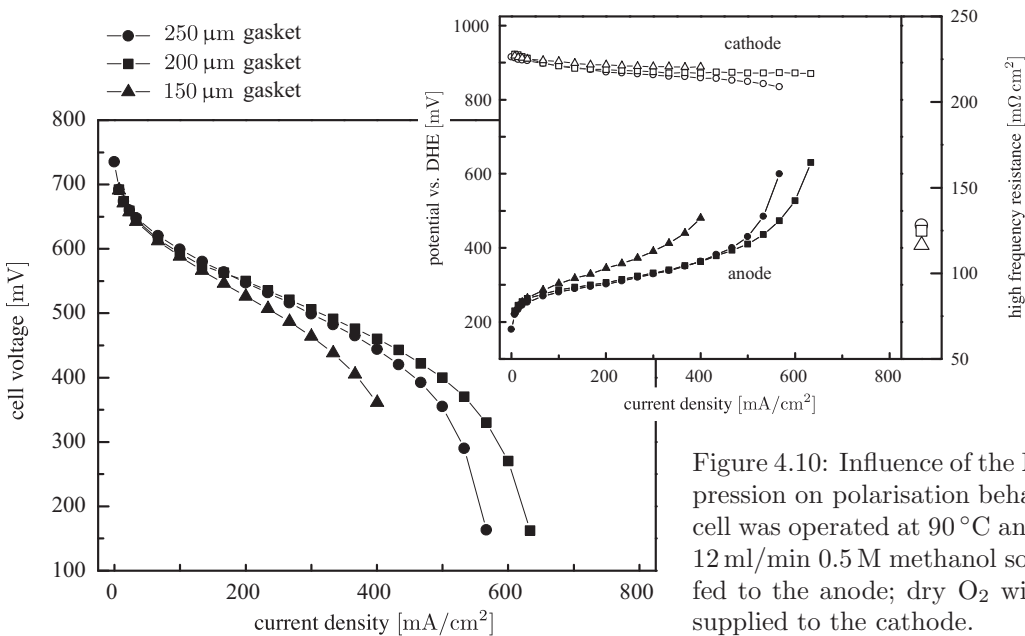
Figure 4.10: Influence of the MEA compression on polarisation behaviour; the cell was operated at 90 °C and 2 bar(a); 12 ml/min 0.5 M methanol solution was fed to the anode; dry O_2 with $\lambda = 15$ supplied to the cathode.

diagram. At the right side of the inset diagram, the ohmic resistance (measured by superimposing a fast auxiliary current pulse) obtained at OCV is depicted. Nafion 115 was used as electrolyte. The cathode was supplied with dry oxygen according to a stoichiometry of $\lambda = 15$ to avoid a cathodic mass transport hindrance as far as possible. The anode was supplied with 20 ml/min 0.5 M methanol solution. Corroborating the existence of an optimal compression, the comparison of the polarisation curves shows that the use of a 200 µm thick gaskets allows for the highest limiting current density. The use of a 250 µm thick gasket results in a slightly diminished limiting current density, and a 150 µm thick gasket leads to a significantly diminished limiting current density. It is worth noting that the ohmic resistance is virtually identical for all three MEAs; the sensitivity of the electrochemical performance towards the MEA compression, therefore, must not be attributed to a changing contact resistance. As comparison of the single electrode polarisations (cf. inset of Figure 4.10) shows, the sensitivity of the cell polarisation curves mainly originates from the anode. Within the accuracy limit of the DHE measurements, the electrochemical performance of the cathode is virtually unaffected by a change of the MEA compression. Considering the cathodic supply with pure oxygen at a high stoichiometric ratio, this is not surprising because the supply of the cathodic active layer with oxygen is not limited by diffusion.

Further on, the cathodic polarization does not show the typical BUTLER-VOLMER-type polarisation curve characteristic of an exponential dependence between polarisation and current density, a subtlety worth noting. The usual steep potential decline at small current densities seems missing. This is a consequence of the electrolyte allowing for methanol permeation through the membrane (i.e., methanol cross-over). Even though no external current is generated at OCV, the electrode potential departs from equilibrium because the methanol reaching the cathodic active surface is readily oxidized. The electrical currents originating from methanol oxidation and oxygen reduction, respectively, merely compensate each other at OCV. Generally, the electric current generated by oxygen reduction matches the sum of cell current and methanol cross-over current. As explained qualitatively in Section 1.3.2.4, this causes a mixed potential and explains the missing steep voltage decline at low current densities.

The electrochemical behavior at higher current densities is in qualitative agreement with the simple consideration described in the last section. Owing to a reduced diffusion length, an increase of the compression is first beneficial to the electrochemical performance at higher current densities; yet, a further increase of the compression results in a diminished electrochemical performance in this region because of the reduced porosity.

4.2.3 Variation of the electrolyte thickness

Because of the considerable methanol permeability of Nafion—the standard electrolyte material— a substantial amount of methanol reaches the cathode, where it is readily oxidized. This bears two major implications: (1) the fuel efficiency is reduced, because the crossing methanol does not participate in the current generation, and (2) the oxidation of methanol at the cathode consumes additional oxygen. This is especially problematic if the device is operated with air, because the transport of oxygen towards the cathode might be limited as well. Feeding strongly diluted methanol solutions is one possibility to reduce the methanol cross-over. Yet given the limited methanol transport through the anodic GDL towards the electrode (cf. Section 4.2.2), this implies a serious limitation in current density. Another approach pointing in the same direction relies on the increased mass transport resistance implied by employing thicker membranes, and in fact the most commonly used electrolyte for DMFC applications is the rather thick Nafion 117 membrane. However, to clarify the limits of this traditional approach, the coupled transport of methanol and
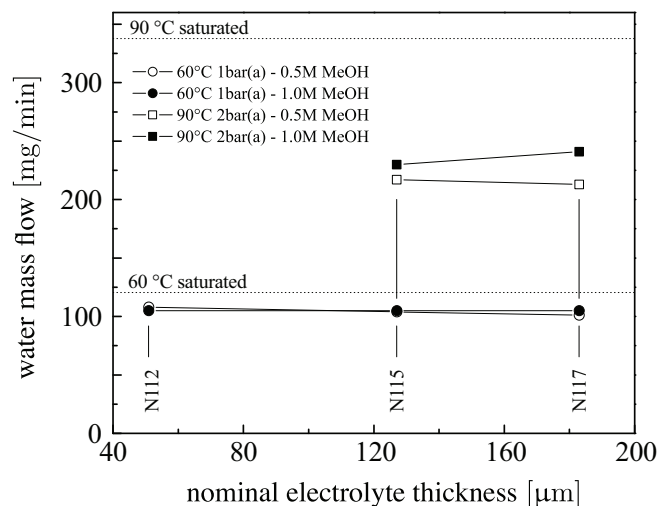
Figure 4.11: Water mass flow within the cathodic effluent at OCV as a function of Nafion thickness; 20 ml/min methanol solution supplied to the anode; cathode supplied with 600 ml/min dry air; the water mass flow resulting from a saturated effluent is indicated by dashed lines.

water through Nafion membranes of different thickness will be investigated.

4.2.3.1 Water transport

The water transport through Nafion membranes is driven by two processes: (1) a gradient in water content causes a convective flux principally obeying D'Arcys law, and (2) the protons drag water molecules thorough the electrolyte by carrying a solvation shell [11]. Evidently, the convective transport is a function of the hydraulic pressure gradient within the aqueous phase, and the thickness of the electrolyte influences the flux for a given gradient. The electro-osmotic drag is mainly a function of the current density; yet, the drag coefficient[6] is a function of the water content, because the number of water molecules forming the solvation shell around a proton is a function of the water content (cf. Ref. [11] for details).

Water permeation rate at OCV and electrolyte thickness. The discussion will start with and is based on a rather simple yet meaningful experiment. Three similar cells (cf. Section 4.1.1 for experimental details) were assembled: one utilizing a Nafion 112 membrane, one with Nafion 115, and one with Nafion 117 as electrolyte. Beside utilizing the same cell hardware, the electrodes and GDLs were of the same kind for all cells. The anode was supplied with 20 ml/min methanol solution (either 0.5 M or 1.0 M), which was heated to cell temperature before entering the cell. Operating at OCV, the water transport via electroosmosis was avoided. On the cathodic side, the cells were supplied with 600 ml/min dry air. By cooling the cathodic effluent to room temperature, most of the water within the gas stream was condensed, and after separating the liquid water from the gas stream, the water mass per unit time within the effluent was measured by weighing the liquid mass accumulated in a certain period of time (around one hour) and dividing by the accumulation time.

As the cell was supplied with dry gases, all water carried in the cathodic effluent origins either directly from the anode or is formed at the cathode by oxidizing the crossing methanol. The water accumulation rate is depicted in Figure 4.11 as a function of electrolyte thickness for two operating temperatures. Strikingly, no sensitivity of the water mass flow carried within the cathodic effluent towards the electrolyte thickness is found. The graphs corresponding to a cell temperature of 60 °C are virtually horizontal, and also at 90 °C no sensitivity significantly larger than the experimental scatter is found. Further on, the influence of the methanol concentration on the accumulated

---

[6]Basically, the average number of water molecules carried by a proton within its solvation shell.

water mass per unit time is small and practically negligible, although a substantial amount of water might stem from the cathodic methanol oxidation[7]. The observed insensitivity of the water permeation rate with respect to the membrane thickness suggests that neither Nafion membrane[8] is substantially limiting the water permeation from anode to cathode, which points towards the cathodic compartment as the main mass transport resistance for water permeation.

Hypothesis and mathematical formulation. The dashed lines in Figure 4.11 show the water mass flow resulting from a saturated effluent. As these lines are above the measured mass flows, the cathodic effluent carries all water as vapor. Further on, the insensitivity towards the Nafion thickness suggests a negligible water content gradient within the membrane (i.e., a fully swollen membrane throughout the thickness of the electrolyte). This indicates the presence of a liquid phase within the porous structures of the cathode (electrode and/or GDL) even at OCV. Taken together, the evaporation and diffusive transport of water vapor is most likely the process limiting the water flux from anode to cathode at OCV.

Hence, the molar water flux (vapor) $\dot{n}_l$ perpendicular to the gas flow (i.e., through the GDL) at a position z along the cathodic flow path is proportional to the difference between water vapor pressure within the gas stream of the flow field p_w and the saturation pressure p_s:

$$\dot{n}_l(z) \propto p_s(T) - p_w(z) \tag{4.8}$$

Water vapor accumulates along the cathodic flow path, and the conservation equation leads to

$$\partial_z \dot{n}_w(z) = \beta \cdot \delta \cdot (p_s(T) - p_w(z)) = \beta \cdot \delta \cdot \left(p_s(T) - p \cdot \frac{\dot{n}_w}{\dot{n}_w + \dot{n}_{in}} \right). \tag{4.9}$$

Herein, $\dot{n}_w$ denotes the molar flow of water vapor carried by cathodic gas stream within the flow field, $p_s(T)$ the water vapor saturation pressure, p_w the water vapor pressure within the cathodic gas stream, p the total system pressure, and $\dot{n}_{in}$ the molar flow of nitrogen and oxygen[9]. Further on, the factor β stems from the proportional relation of Equation (4.8), and δ is a characteristic length. In a zero order approximation, δ equals the total width of all flow field channels; yet, due to the geometric simplicity of the mathematical representation, δ is not strictly defined as this. With L being the length of the cathodic flow path, integration of Equation (4.9) over $z = [0...L]$ with $\dot{n}_w(0) = 0$ (dry gas feed) as boundary condition results in

$$\frac{\dot{n}_w}{\dot{n}_{in}} = \frac{p_s}{p - p_s} \cdot \left[1 + \frac{p}{p_s} \cdot \mathcal{W} \left(-\frac{p_s}{p} \cdot \exp \left(-\frac{p_s}{p} - \left(\frac{p - p_s}{p} \right)^2 \cdot \frac{\beta \cdot p}{\dot{n}_{in}/A} \right) \right) \right], \tag{4.10}$$

where $\mathcal{W}(x)$ denotes LAMBERT's W-function[10] and $\dot{n}_w$ symbolizes the molar flow of water vapor leaving the cell. For the benefit of notation, this is not indicated by further indices. Furthermore, δ was chosen such that $\delta \cdot L$ equals the active cell area A. It is worth noticing that Equation (4.10) simplifies to

$$\frac{\dot{n}_w}{\dot{n}_{in}} = \frac{p_s}{p - p_s} \tag{4.11}$$

in the limiting case of $\beta \cdot p \ll \dot{n}_{in}/A$ (i.e., a fully saturated gas stream at the outlet).

---

[7]From the methanol permeation rates shown in Figure 4.14 on page 171, it is easily calculated that up to 30 % (1 M methanol, 60 °C, Nafion 112) of the accumulated water originates from the cathodic methanol oxidation.

[8]Consider that Nafion within a DMFC is virtually fully swollen due to the liquid feed at the anode.

[9]This is regarded as constant over the length of the flow path neglecting the consumption of oxygen by the cathodic methanol oxidation.

[10]The LAMBERT W-function is the inverse function of $f(W) = W \cdot \exp(W)$, which is also known as omega function or product logarithm.
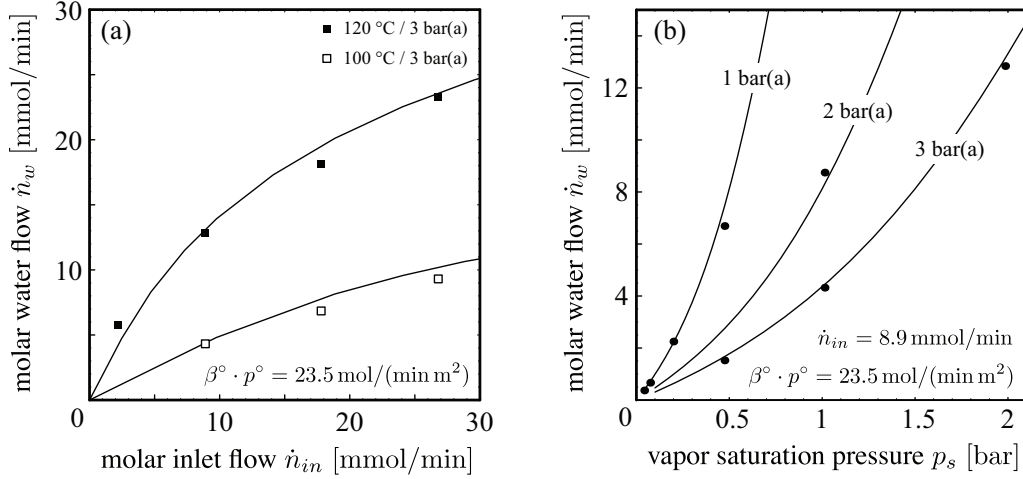
Figure 4.12: Dependence of the molar water flow transported within the cathodic effluent at OCV; the variation of the flow rate supplied to the cathode is shown in (a) for two operating temperatures; the variation of the cell temperature for constant supply flow rate is shown in (b) by plotting the molar water flow as function of vapor saturation pressure; symbols indicate measurements, and lines reflect the theoretical prediction according to Equation (4.14) with $\beta^\circ \cdot p^\circ = 23.5\,\mathrm{mol}/(\mathrm{min}\,\mathrm{m}^2)$ as parameter.

The dependence on operating conditions. The molar water flow leaving the cathode is coupled with the molar flow of nitrogen and oxygen entering the cathode, the total pressure, and the cell temperature by Equation (4.9). While explicitly containing the molar flow $\dot{n}_{\mathrm{in}}$ and the total pressure p, the temperature enters Equation (4.9) indirectly via the saturation pressure p_s and via β. While the temperature dependence of p_s is obvious, the relation between β and the operating conditions needs further explanation. If the diffusion of water vapor through the cathodic porous structure is the limiting mass transport effect, β is coupled with the diffusion coefficient D via $\beta \propto D/(R \cdot T)$. By the kinetic gas theory, a relation between the diffusion coefficient, temperature, and pressure is established. According to the kinetic gas theory, the diffusion coefficient follows

$$D \propto \frac{T^{3/2}}{p}. \tag{4.12}$$

In consequence, β should exhibit the following dependence:

$$\beta = \beta^\circ \cdot \frac{\sqrt{T/T^\circ}}{p/p^\circ}, \tag{4.13}$$

where the superscript $^\circ$ indicates arbitrary reference conditions. Introduction of Equation (4.13) into Equation (4.9) finally leads to

$$\frac{\dot{n}_{\mathrm{w}}}{\dot{n}_{\mathrm{in}}} = \frac{p_s}{p - p_s} \cdot \left[1 + \frac{p}{p_s} \cdot \mathcal{W}\left(-\frac{p_s}{p} \cdot \exp\left(-\frac{p_s}{p} - \left(\frac{p - p_s}{p}\right)^2 \cdot \frac{\beta^\circ \cdot p^\circ}{\dot{n}_{\mathrm{in}}/A} \cdot \sqrt{\frac{T}{T^\circ}} \right) \right) \right], \tag{4.14}$$

where β° is a parameter that is independent of pressure, temperature, and flow rate.

Comprising just one parameter beside the operating conditions, Equation (4.14) is reliably validated by a variation of operating conditions. This is shown in Figure 4.12. While the dependence of the water flow carried within the cathodic effluent on the inlet flow rate (dry gases) for constant temperature is shown in diagram (a), the influence of the operating temperature is shown in diagram (b) by plotting the molar water flow as a function of the vapor saturation pressure[11] for a

---

[11]Consider that the vapor pressure is a function of temperature only.
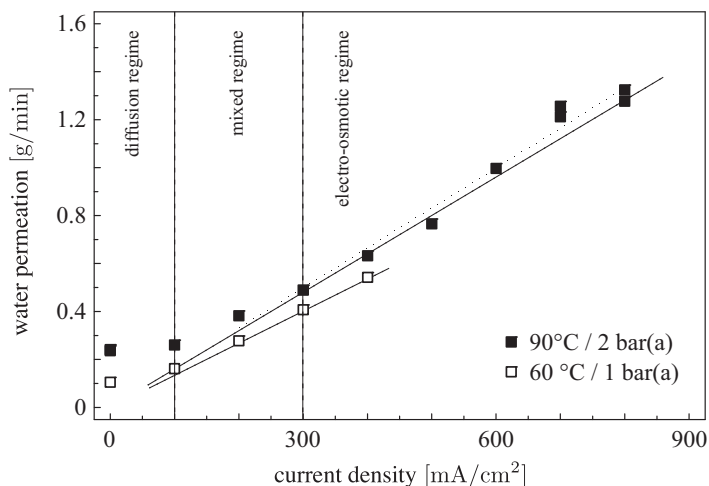
Figure 4.13: Net water permeation from anode to cathode as function of current density; fuel flow 20 ml/min 1.0 M methanol; cathodic supply is oxygen with a stoichiometric ratio of 14.3 (minimum flow rate 600 ml/min); electrolyte is Nafion 117.

constant supply flow rate $\dot{n}_{in}$. Measured data is indicated by various symbols, and calculated values according to Equation (4.14) are shown by lines. For the calculation of all lines, the same parameter $\beta^\circ \cdot p^\circ = 23.5 \, \mathrm{mol}/(\mathrm{min}\,\mathrm{m}^2)$ is used in combination with the proper values for p, T, and p_s. A value of 373.15 K was used for the reference temperature T°. The remarkable agreement between measurement and calculation strongly suggests that indeed the water permeation from anode to cathode is limited by evaporation and diffusion of water vapor within the cathodic compartment at OCV. Again it is worth mentioning that this and the results presented by Figure 4.11 imply the presence of a liquid aqueous phase within the cathodic porous structures even at OCV, which is also in agreement with the findings of Section 4.1.3, where a high tendency to accumulate liquid within the cathodic flow field was found.

Electro-osmotic drag. If current is generated, the protons carry a certain amount of water molecules through the membrane by maintaining a solvation shell. This is a well investigated effect and copious data is available for standard materials such as Nafion—inter alia Ref. [156–159]. Hence, the discussion will only shortly linger on the topic for the sake of completeness. If the permeated water flow is plotted as a function of current density, three regions are distinguishable. This is exemplified in Figure 4.13, where the net water permeation is shown as a function of current density for a Nafion 117 membrane operated in the $29 \, \mathrm{cm}^2$ cell with serpentine flow field. For low current densities ($< 100 \, \mathrm{mA/cm}^2$), the water permeation rate tends towards a finite value defined by the processes discussed within the last paragraph. The permeation rate depends only slightly on the current density in this region. The opposite is true for large current densities ($> 300 \, \mathrm{mA/cm}^2$). Emphasizing the dominance of the electro-osmotic drag, the permeation rate increases linearly with current density within this region. In this context, it should be mentioned that the water permeation rate at higher current densities easily exceeds several times the capacity of the cathodic gas flow to hold water vapor, which again is in agreement with the findings related in Section 4.1.3. These two regimes are separated by a transition region, where both regimes—diffusion limitation and drag control—overlap.

Conclusion. In the case of Nafion, the cathodic compartment controls the permeation rate at OCV, because the evaporation and diffusive vapor transport towards the cathodic flow field is the limiting mass transport process. This implies the presence of liquid within the cathodic porous structures even at OCV. Furthermore, the upper limit of the permeation rate is given by the water vapor uptake capacity of the cathodic gas flow. This limit is easily exceeded once current is generated, and the permeation rate can reach several times the uptake capacity of the gas flow

169

because of the linear scaling with current density originating from the electro-osmotic drag. Hence, the cathode of a DMFC is easily flooded with liquid water. Finally, a change of the electrolyte (Nafion) thickness is not a viable approach to limit the considerable water permeation from anode to cathode.

4.2.3.2 Methanol transport

Theoretical consideration. In the light of the results regarding the water transport, a simplified mathematical description of the methanol permeation can be derived. Again, the discussion will be limited to the operation at OCV. The methanol transport through the nano-porous network of the Nafion membrane is driven by two processes: (1) methanol is carried convectively within the water flow crossing the membrane (i.e., transport of the solution), and (2) due to the cathodic methanol oxidation, a gradient in methanol concentration is established over the thickness of the membrane leading to a superimposed diffusion within the nano-porous network. Hence, the methanol flow through the membrane is given by

$$\dot{n}_{\mathrm{m}} = -D_{\mathrm{m}} \cdot \partial_x c_{\mathrm{m}} + \frac{c_{\mathrm{m}}}{c_{\mathrm{m}} + c_{\mathrm{w}}} \cdot \dot{n}_{\mathrm{w}} \tag{4.15}$$

from a mathematical perspective. Due to mass conservation within the membrane $\partial_x \dot{n}_{\mathrm{m}} = 0$ holds, which leads to

$$0 = -D_{\mathrm{m}} \cdot \partial_{x,x} c_{\mathrm{m}} + \frac{\dot{n}_{\mathrm{w}}}{c_{\mathrm{w}}} \cdot \partial_x c_{\mathrm{m}}, \tag{4.16}$$

provided $c_{\mathrm{m}} \ll c_{\mathrm{w}}$ is valid throughout the membrane. An analytical solution of Equation (4.16) exists, if the methanol concentration is vanishing on the cathodic side ($c_{\mathrm{m}} = 0$), which is a reasonable assumption considering the fast methanol oxidation at the cathode. As expression for the methanol permeation rate

$$\dot{n}_{\mathrm{m}} = \dot{n}_{\mathrm{w}} \cdot \frac{c_{\mathrm{m}}}{c_{\mathrm{w}}} \cdot \left\{ 1 + \left[\exp\left(\frac{\dot{n}_{\mathrm{w}}}{c_{\mathrm{w}} \cdot D_{\mathrm{m}}} \cdot \delta_{\mathrm{m}} \right) - 1 \right]^{-1} \right\} \tag{4.17}$$

is found, if the water concentration within the nano-porous network is considered as constant. Herein, c_{m} denotes the methanol concentration at he anode-membrane interface, δ_{m} the membrane thickness, D_{m} the effective methanol diffusion coefficient within the membrane, and $\dot{n}_{\mathrm{w}}$ the molar water permeation flux.

To reflect the conditions within a DMFC, the diffusion through the anodic porous structures needs consideration as well. Although derived with the membrane in mind, Equation (4.17) is valid for any diffusive process within porous structures with superimposed convection and, hence, is likewise applicable to account for the anodic porous structures. Consequently, a "series" of porous systems (expressed by Equation (4.17)) can be used to include the methanol transport through the anodic porous structures. This leads to

$$\dot{n}_{\mathrm{m}} = \dot{n}_{\mathrm{w}} \cdot \frac{c_{\mathrm{m}}}{c_{\mathrm{w}}} \cdot \left(\sum_i \frac{1}{K_i} \right)^{-1} \quad \text{with} \quad K_i = 1 + \left[\exp\left(\frac{\dot{n}_{\mathrm{w}}}{c_{\mathrm{w}} \cdot D_i} \cdot \delta_i \right) - 1 \right]^{-1}, \tag{4.18}$$

with c_{m} being the methanol concentration at the anodic channel-GDL interface. Furthermore, D_i and δ_i are the effective diffusion coefficient and length of the i-th layer, respectively.

Methanol permeation rate at OCV and electrolyte thickness. The methanol permeation rate as a function of Nafion thickness is shown in Figure 4.14. Again, Nafion 112, Nafion 115, and
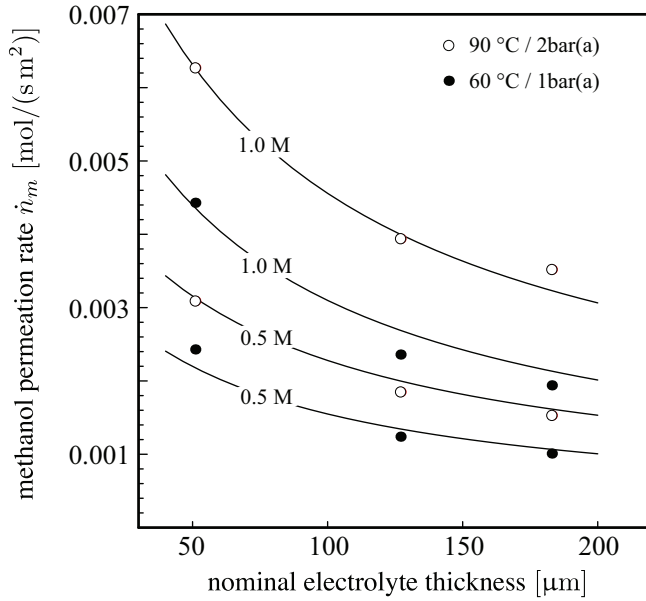
Figure 4.14: Methanol permeation rate at OCV as a function of Nafion thickness; fuel flow 20 ml/min; cathodic supply is oxygen with 600 ml/min; measured methanol permeation rate based on the carbon dioxide concentration within the cathodic effluent.

Nafion 117 were used as electrolytes in combination with equal cell hardware, MEA components, and sealings. The methanol permeation rate was determined from the carbon dioxide concentration within the cathodic effluent assuming 100 % oxidation of methanol at the cathode. The symbols indicate measurements and the lines are calculated with Equation (4.18). Obviously, a higher feed concentration of methanol c_{m} results in a higher permeation rate. Likewise, an increase in temperature results in a higher permeation rate. The methanol permeation rate is reduced by increasing the membrane thickness. Yet, it is worth noting that the relationship between permeation rate and electrolyte thickness is not linear. First of all, the permeation rate does not tend towards zero with increasing electrolyte thickness. This is a consequence of the convective transport. Even if the diffusive transport is diminished by increasing the diffusion length (thicker membrane), the convective transport together with the water—remember that this is not a function of the membrane thickness—results is a finite cross-over. The application of Nafion membranes even thicker than Nafion 117, therefore, bears only limited improvements in terms of methanol cross-over. On the other side, the permeation rate increases rapidly with reducing membrane thickness, especially for higher methanol feed concentrations.

The shown lines in Figure 4.14 were fitted to the measured data with

$$\dot{n}_{\mathrm{m}} = \dot{n}_{\mathrm{w}} \cdot \frac{c_{\mathrm{m}}}{c_{\mathrm{w}}} \cdot \left(\frac{1}{K_{\mathrm{a}}} + \frac{1}{K_{\mathrm{m}}} \right)^{-1} \quad \text{with} \quad K_{\mathrm{m}} = 1 + \left[\exp \left(\frac{\dot{n}_{\mathrm{w}}}{c_{\mathrm{w}} \cdot D_{\mathrm{m}}} \cdot \delta_{\mathrm{m}} \right) - 1 \right]^{-1}. \qquad (4.19)$$

Herein, K_{a} denotes a constant comprising the effective diffusion coefficient and the diffusion length through the anodic porous structures. This is the parameter that has been fitted to the data. As the methanol diffusion coefficient in Nafion is known from literature [160,161], the transport resistance K_{m} associated with the membrane can be calculated. This leaves just one fitting parameter, which improves the reliability considerably. Generally, the parameter K_{a} will be temperature dependent because of the temperature dependence of the diffusion coefficient. Yet, a dependence on the methanol concentration cannot be justified in the range of investigated methanol concentrations. Hence, the same K_{a} value has to reflect the methanol permeation rate obtained for 0.5 M and 1.0 M feed concentration at the same temperature. This is fulfilled with reasonable accuracy, as a comparison of the lines and symbols of Figure 4.14 shows. The least square fit gave the following values:

$T\,[^\circ\mathrm{C}]$	$K_\mathrm{a}\,[-]$	$D\,[\mathrm{m}^2\cdot\mathrm{s}^{-1}]$
60	13.7	$1.52\cdot 10^{-9}$
90	19.6	$2.20\cdot 10^{-9}$

The shown diffusion coefficients were calculated from K_a by assuming a diffusion length of $200\,\mu\mathrm{m}$. They are in reasonable agreement with tabled values, where the diffusion coefficient of methanol in water is stated to be $1.28\cdot 10^{-9}\,\mathrm{m}^2/\mathrm{s}$ at $15\,^\circ\mathrm{C}$ [162, page 6-194].

Conclusion. The methanol permeation rate depends on the electrolyte (Nafion) thickness; yet, the relation is not linear, which origins from the superposition of convective and diffusive transport. A simplistic representation of the membrane as nano-porous system is able to reproduce the experimental observation with reasonable accuracy. Due to the convective transport, the permeation rate does not tend towards zero with ever increasing membrane thickness. Hence, thicker Nafion membranes are not a promising route to reduce the permeation of water and methanol.

4.2.3.3 Electrochemical performance

To investigate the influence of Nafion thickness from the performance point of view, galvanostatically controlled polarisation curves have been measured. During this, a side-placed DHE was utilized to obtain information about the single electrode polarisations, and the pulse technique was applied to acquire the ohmic resistance and enable the ohmic compensation of the potential measurements against the DHE. The carbon dioxide concentration within the cathodic effluent was measured by an infrared sensor giving an estimate for the methanol permeation rate.

The left and right column of Figure 4.15 compare the electrochemical performance and methanol permeation at $60\,^\circ\mathrm{C}$ and $90\,^\circ\mathrm{C}$ cell temperature, respectively, for Nafion 112 and Nafion 117. The system was operated at $2\,\mathrm{bar(a)}$ pressure and $90\,^\circ\mathrm{C}$, and at $1\,\mathrm{bar(a)}$ and $60\,^\circ\mathrm{C}$. In both cases, $1\,\mathrm{M}$ methanol was supplied with a flow rate of $20\,\mathrm{ml/min}$, and the cathode was operated with dry oxygen according to a stoichiometry of 15 ($200\,\mathrm{ml/min}$ minimum). The upper row (diagrams (a)) show the cell polarisation curves as obtained and with the ohmic loss subtracted. Interestingly, nearly the same polarisation curves are obtained at $60\,^\circ\mathrm{C}$ despite the used membrane. Yet, the comparison of the IR-free polarisation curves reveals an inferior performance for the Nafion 112. Obviously, the lower ohmic loss of the Nafion 112 membrane is compensated by some other effect. The single electrode polarisation curves (diagram (b) - left side) reveal a deteriorated electrochemical performance of the cathode, while the anode polarisation is virtually identical for both membranes. Obviously, the higher methanol permeation rate of Nafion 112 is limiting the cathodic performance at this temperature. This is interesting, because a performance loss caused by insufficient oxygen supply is unlikely due to the operation with oxygen. Taken together, the beneficial impact of the thinner membrane in terms of ohmic losses is compensated by a deteriorated performance of the cathodic half cell reaction.

At higher temperature ($90\,^\circ\mathrm{C}$), a slightly different picture is obtained. Under these operating conditions, the MEA comprising Nafion 112 outperforms the Nafion 117 based MEA (diagram (a) - right side), although the methanol cross-over is significantly higher (diagram (c) - right side). The superior performance of the Nafion 112 based MEA origins solely from the reduced ohmic loss. This becomes apparent already from the well agreeing IR-free polarisation curves and is even further emphasized by the single electrode polarisations, which show virtually no sensitivity towards the chosen membrane. Obviously, the electrochemical performance of the cathode is not
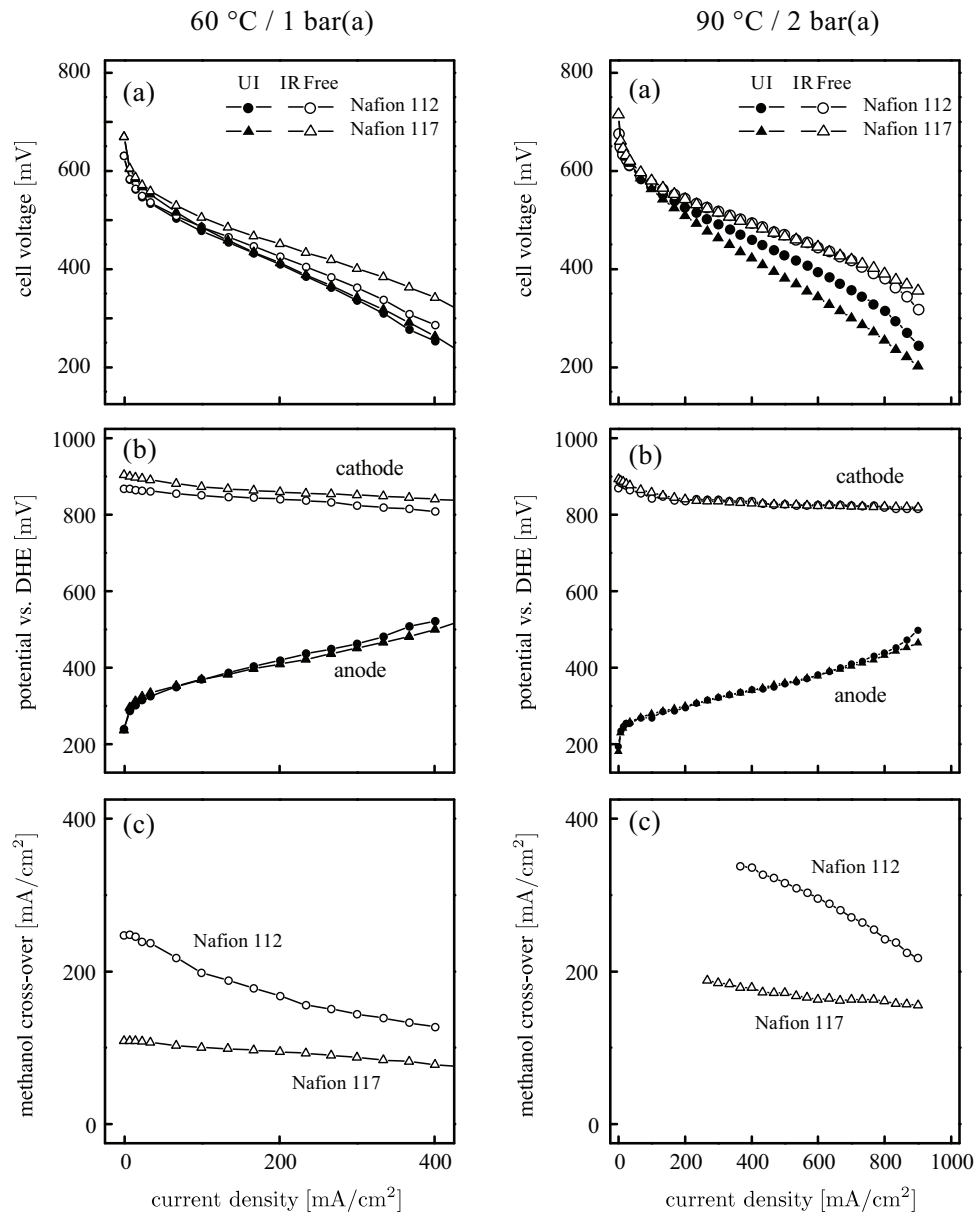
Figure 4.15: Electrochemical performance as a function of electrolyte thickness (Nafion); the left-hand diagrams correspond to 60 °C and 1 bar(a), and the right-hand diagrams reflect the operation at 90 °C and 2 bar(a); fuel flow 20 ml/min 1 M methanol; cathodic supply is dry oxygen with a stoichiometry of 15; the diagrams in (a) show the obtained and IR-corrected polarisation curves; the corresponding single electrode polarisations are shown in (b); the methanol permeation rate is depicted in (c) as oxidation current density.

hampered at this elevated temperature by a higher methanol cross-over rate as long as the oxygen supply is sufficient.

4.3   A Polybenzimidazole based membrane for the DMFC

Compiling the findings of section 4.2.3 into one statement—the capability of Nafion to minimize the water and methanol permeation through the electrolyte is limited due to the coupled transport and high electro-osmotic drag—it is logical to call for alternative electrolyte materials to overcome these limitations, which stimulated the investigation of several promising materials including modified Nafion structures [163–165], radiation-grafted membranes [4, 161], and blends [166].

However, the majority of novel electrolyte materials considered for DMFC application rely on the traditional sulfonic acid groups as proton donor-acceptor and hence depend on a high hydration level to provide sufficient conductivity. This is a challenging dilemma, if the water permeation rate is to be minimized at the same time. As the group around KREUER illustrated recently by investigating model compounds, phosphonic acid is an interesting alternative, as it provides high proton conductivity in the dry state at elevated temperatures, and a moderate water uptake at higher relative humidities even allows for reasonable conductivities at lower temperature [5]. Taking advantage of the water-free, high temperature conductivity of phosphoric acid, acid-doped polybenzimidazole (PBI)—a polymer known for its excellent oxidative and thermal stability— was used by WAINRIGHT et al. [167] as electrolyte for PEFCs with remarkable electrochemical performance at 200 °C. Although they reported some bonding between the doped phosphoric acid and the PBI, this spacer-like approach (i.e., a liquid electrolyte within a porous membrane) is not directly applicable to a DMFC; the presence of an aqueous phase would result in a rather fast decline in proton conductivity. It was shown by LI et al. that only two molecules of phosphoric acid are bonded to each repeating unit of PBI and hence the majority of doped acid is "free acid", which is readily washed-out by an aqueous phase [168].

Finally, the use of phosphoric acid bears implications of kinetic origin. Taking advantage of FTIR spectroscopy, HABIB and BOCKRIS revealed a strong tendency of H_3PO_4 to form an adsorbate layer at Pt surfaces [169]. As the adsorbate formation was strongest around 800 mV vs. NHE, a serious hindrance of the ORR might be expected if phosphoric acid is present at the cathodic electrode—especially at the low operating temperatures attractive for DMFC applications.

Taken together, a viable approach utilizing PBI as electrolyte has to fulfill two constrains: (1) the proton conduction mechanism should be based on a phosphoric acid-like proton donor-acceptor to decouple proton and water transport; yet, the acid has to be immobilized to prevent washing-out. (2) the cathodic electrode should be shielded from the acid to circumvent the hampering influence of an adsorbate layer to the cathodic ORR.

4.3.1   Material choice, MEA manufacturing, and experimental

Celtec-V is the trade name of a PBI based polymer blend developed by Pemeas GmbH. The blend incorporates polyvinylphosphonic acid (PVPA) into a PBI matrix. The interpenetrating PVPA is immobilized within the PBI matrix by cross-linking and covalent bonding [170]. This membrane blend perfectly fulfills the first criterion and, therefore, is attractive for DMFC application. The targeted operating temperature of DMFCs (well below 100 °C) provides liberty in terms of electrode morphology to comply with the second criterion (shielding of the electrodes); MEAs were manufactured by hot-pressing Celtec-V membranes with Nafion-containing, standard DMFC electrodes. Hence, the electrochemical active surface of the electrode is in contact with sulfonic acid rather than phosphonic acid, which should circumvent the possible hampering of the cathodic reaction. To provide adequate comparison, a second set of MEAs was manufactured utilizing identical electrodes and Nafion 117 as electrolyte.

Both types of MEAs were operated under identical conditions (same cell hardware and test bench). An active area of 30 cm^2 was considered sufficient for the material comparison. The cell consisted of graphite-made flow fields with a single-channel serpentine. The cell was clamped by stainless steel end plates, and electrical heating cartridges were used to control the cell temperature. PTFE-sheets were used as sealings, and the cell was clamped by eight screws (fastened with a torque wrench) at the perimeter of the cell.
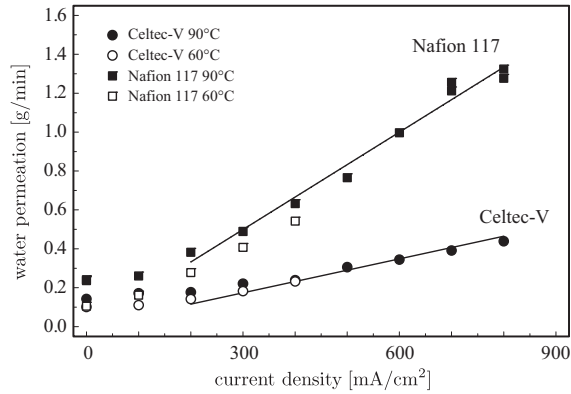
Figure 4.16: Net water permeation from anode to cathode in working single cells; the active area is $30\,cm^2$; fuel flow $20\,ml/min$ $1.0\,M$ methanol; dry oxygen according to a stroichiometry of 14.3 ($600\,ml/min$ minimum) supplied to the cathode; pressure is $2\,bar(a)$ at $90\,°C$ and $1\,bar(a)$ at $60\,°C$; the lines show the result of a linear regression estimating the electroosmotic drag coefficient.

4.3.2 Mass transport across the membrane

Water transport. The net water permeation rate from anode to cathode as a function of current density is depicted in Figure 4.16. Compared are the results obtained with Nafion 117 and Celtec-V as electrolyte at $60\,°C$ and $90\,°C$, respectively. For both electrolytes, a linear dependence between net water permeation and current density is found for current densities larger than $300\,mA/cm^2$. This suggests a dominanance of the electroosmotic drag at high current densities for Celtec-V as well as for Nafion 117. However, the net drag coefficient (the number of water molecules per proton) of Celtec-V is significantly smaller. Values for the drag coefficient are extracted from the net water permeation rate by linear regression neglecting values at lower current density. This is illustrated by the regression lines in Figure 4.16, and the following values were obtained:

$T\,[°C]$	Nafion 117	Celtec-V
60	4.05 ± 0.05	0.70 ± 0.04
90	5.08 ± 0.27	1.09 ± 0.33

As the electroosmotic drag of Celtec-V is reduced approximately by a factor of five compared to Nafion, significantly less flooding can be expected within the cathodic compartment if Celtec-V is utilized. However, at low current densities (convection dominated regime) Celtec-V does not lead to such a significant reduction of the water permeation rate, which might be indicative of a relatively high water content within the membrane.

Methanol permeation. Besides a noteworthy electro-osmotic drag reduction, Celtec-V also bears significant advantages in terms of methanol permeation. The cross-over current density[12] for

---

[12]The methanol permeation rate was transformed into a current density via Faraday's law.
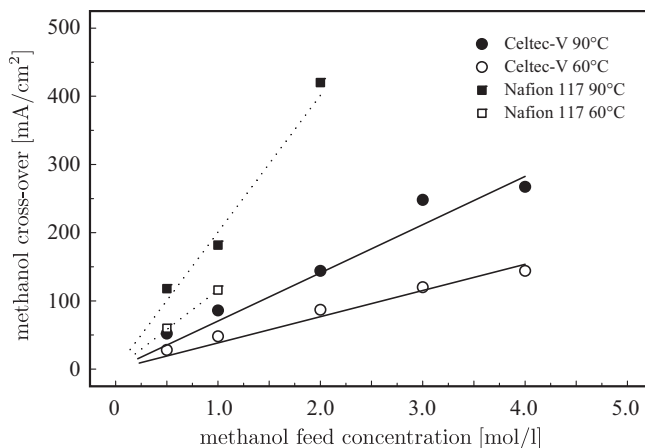

Figure 4.17: Methanol cross-over current density at OCV for different methanol feed concentrations; the active area is $30\,cm^2$; fuel flow $20\,ml/min$ for Celtec-V and $12\,ml/min$ for Nafion 117; $200\,ml/min$ supplied to the cathode, except $600\,ml/min$ for Celtec-V at $90\,°C$ and $3.0/4.0\,M$ methanol; pressure is $2\,bar(a)$ at $90\,°C$ and $1\,bar(a)$ at $60\,°C$.

Figure 4.18: Cyclic coltammograms of the cathode; 200 ml/min hydrogen supplied to the anode, and 200 ml/min nitrogen supplied to the cathode; the cell was operated at 60 °C and 1 bar(a) pressure; the gray area indicates the hydrogen desorption area considered to estimate the electrochemical catalyst surface.
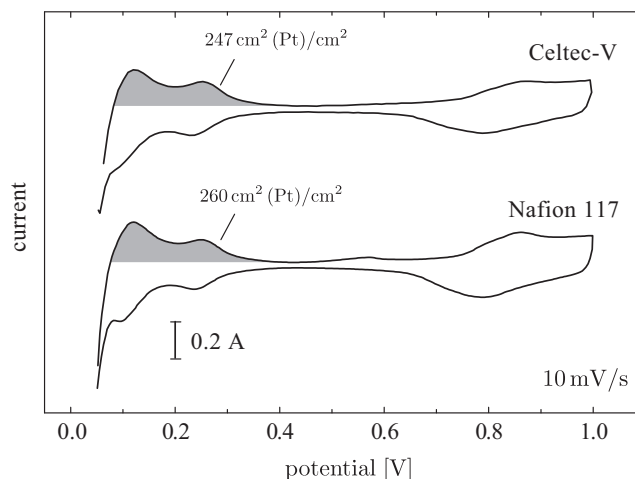
different methanol feed concentrations is shown in Figure 4.17; filled symbols show measured data at 90 °C and measurements performed at 60 °C are shown by empty symbols, respectively. All measurements were performed at OCV to emphazise the differences in diffusive/convective transport and to exclude the influence of the different water permeation rates at higher current densities (cf. last paragraph). The methanol cross-over was calculated from the carbon dioxide concentration within the cathodic effluent. In any case, a fairly linear relation between methanol cross-over and feed concentration is found, which is not surprising—at least in the case of Nafion—due to the diffusive/convective transport at OCV (cf. Equation (4.17)). Despite the chosen operting temperature, a remarkable reduction of the cross-over rate is attained with Celtec-V. The reduction of the diffusive/convective transport enables the operation with relatively high methanol feed concentrations while keeping a reasonable methanol cross-over rate; for example, feeding a cell with Celtec-V as electrolyte with 3.0 M methanol and feeding a cell with Nafion 117 with 1.0 M methanol results in approximately the same cross-over. As will be shown in the next section, this is of utmost importance from the performance point of view. Yet, even more important might be either the gain in fuel efficiency (for the same feed concentration) or the gain in volumetric energy density of the fuel implied by higher methanol concentrations, especially if the likely application of DMFCs as energy converter for portable applications is considered.

4.3.3 Electrochemical characterisation

4.3.3.1 The electrode attachment to the electrolyte

The motivation to sandwich Nafion-containing electrodes with a PVPA containing electrolyte was given by the introductory words of Section 4.3. However, the question whether the combination of two vastly different proton-conducting materials is possible without loosing active area crosses one's mind, immediately.

To investigate the cathodic accessibility of Pt, cyclic voltammetry was used. The assembled cells (one set based on Nafion 117 and another set based on Celtec-V) were supplied with hydrogen at the anode and nitrogen at the cathode; both gas feeds were fed fully humidified to the cell, which was operated at 60 °C at 1 bar(a). The potential was sweeped from 50 mV to 1 V with a rate of 10 mV/s. The hydrogen-flushed anode simultaneously served as counter and reference electrode. The recorded cyclic voltamograms (CVs) are shown in Figure 4.18. Both CVs are qualitatively similar showing clearly the H-UPD region in the potential range of $50 - 300$ mV, the Pt oxide formation above 600 mV, and the double layer region in between. At a first glance, this similarity
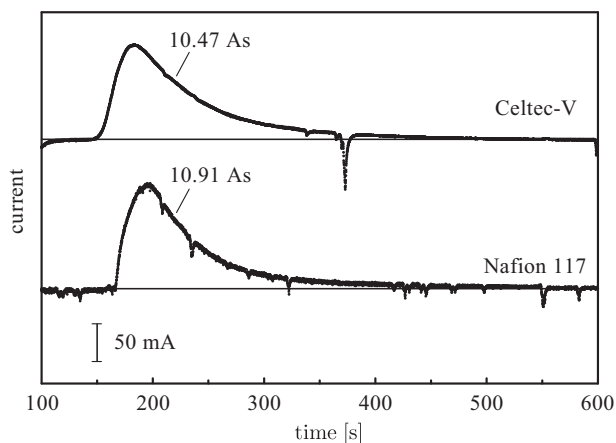
Figure 4.19: Chrono-amperometric estimation of the electrochemical active anode surface; 500 ml/min hydrogen supplied to the cathode; anode purged with water, then the anodic feed was changed to 0.5 M methanol solution at 20 ml/min; the cell was operated at 60 °C and 1 bar(a) pressure.

of the CVs might appear surprising because of the different electrolytes. Yet, after recalling that the same *Nafion-containing* electrodes were used, this is most natural, and the similarity of the CVs might merely provide reassurance that the cathode is shielded from the PVPA within the Celtec-V membrane. Finally, the active area is estimated by evaluating the hydrogen desorption charge (gray area in the CVs). Assuming a specific charge of $210\,\mu As/cm^2$, the desorption charge can be converted into an specific, electrochemical active surface. This yields $247\,cm^2(Pt)/cm^2$ active surface for the Celtec-V based MEA and $260\,cm^2(Pt)/cm^2$ for the Nafion based MEA. As the discrepancy is less than 10 %, a good connection between the Nafion containing cathode and the Celtec-V membrane exists.

The electrochemical active surface area of the anode was characterized by a chrono-amperometric technique. Intending a relatively stable reference potential, the cathode was supplied with hydrogen (500 ml/min) and served as reference and counter electrode. The anode was first flushed with water and subsequently cleaned by several potential shifts. Afterwards, the anode was set to a potential of 60 mV vs. the hydrogen flushed cathode. Methanol is dehydrogenated at that potential; yet, the final oxidation of CO-like adsobates is hindered resulting in an adlayer covering the electrode. This is reflected in the current-time plots of Figure 4.19. After methanol enters the cell, the current rapidly increases due to the dehydrogenation at the clean electrochemical active surface. This results in an increasing amount of CO-like adsorbates blocking the active sites. Consequently, the current passes a maximum and decreases as the surface coverage tends towards unity (i.e., full coverage of the active surface with adsorbates). The collected charge serves as a measure for the total electrochemical active area. The cumulative charge is about 10 As for the Celtec-V comprising MEA as well as for the Nafion 117 reference. This proves that also the anode is attached to the Celtec-V membrane without a significant loss of active surface.

4.3.3.2 Electrochemical performance

The electrochemical performance of the cells was tested by taking galvanostatically controlled polarisation curves. Taking advantage of the reference electrode arrangement described in Section 2.4, the loss contributions were split into anodic polarisation, cathodic polarisation, and ohmic losses. The cell voltage as function of current density obtained at 90 °C with 2 bar(a) pressure is plotted in diagram (a) of Figure 4.20 together with the methanol cross-over current density. The cells were operated with oxygen and 1 M methanol solution. Under these operating conditions, the Celtec-V based MEA is outperformed by the Nafion 117 reference, where the lower net performance is the result of several effects. Firstly, the ohmic resistance of the Celtec-V membrane is considerably higher ($276\,m\Omega\,cm^2$ for Celtec-V vs. $168\,m\Omega\,cm^2$ for Nafion 117) resulting in 1.6 times the ohmic
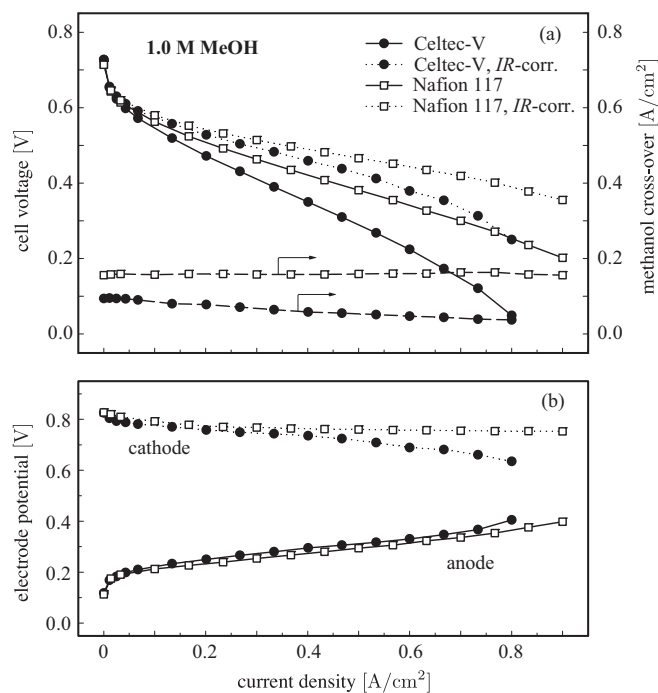
Figure 4.20: Polarisation curves including ohmic resistance corrected cell voltage and resolved anode and cathode potentials, respectively; cell temperature is 90 °C, fuel flow is 20 ml/min 1 M methanol; dry oxygen supplied to the cathode according a stoichiometry of 14.3 (200 ml/min minimum); the pressure is 2 bar(a).

loss compared to Nafion 117. Secondly, in the higher current density region ($> 400 \, \text{mA/cm}^2$), the IR-free voltage obtained from the Celtec-V based MEA significantly falls short of the Nafion 117 based reference. The comparison of the single electrode polarisations depicted in diagram (b) of Figure 4.20 shows that the anodic polarisation is virtually identical for both membrane types. In consequence, the additional voltage loss (i.e., in addition to the higher ohmic loss) originates from the cathode, which is clearly reflected in the cathodic polarisations given in diagram (b). Obviously, the lower methanol cross-over (about 50 % compared to Nafion 117 / diagram (a)), does not result in a cathodic performance gain. A beneficial impact of the reduced methanol cross-over was not expected under oxygen operation, because no impact of the cross-over rate on the cathodic polarisation was found from the variation of Nafion thickness (cf. right side of Figure 4.15 on page 173). Although an explanation for the lower performance is not easily found, two possible explanations seem likely: (1) the much lower water permeation rate might result in a considerably dryer cathodic environment, and because the chosen type of electrode was tailored for the wet conditions resulting from Nafion, this might be deleterious to the performance; (2) although no detrimental impact of PVPA was found within the CVs (cf. Figure 4.18), it cannot be excluded that some free PVPA is present at the cathodic electrochemical active surface resulting in a loss of active sites due to adsorption.

Operation under different methanol feed concentrations. Polarisation curves obtained with different methanol feed concentrations are compared in Figure 4.21. The cells were operated at 90 °C and 2 bar(a) pressure. Shown are the respective cell voltages (continuous lines) together with the corresponding methanol cross-over current densities (dashed lines). If the cells are operated with low methanol feed concentrations (0.5 M methanol), the Nafion 117 based MEA is superior to the Celtec-V alternative for the reasons explained within the last paragraph (i.e., the lower ohmic loss and the slightly better cathodic polarisation). If the feed concentration is increased to 1 M methanol, a comparable performance (at least up to $300 \, \text{mA/cm}^2$) is obtained. This is remarkable, because for quite similar operating conditions—despite the fact that pure oxygen was used rather than air—the Celtec-V alternative was shown to yield inferior performance within the last paragraph. Obviously, the coincidence of higher cross-over rates and limited transport
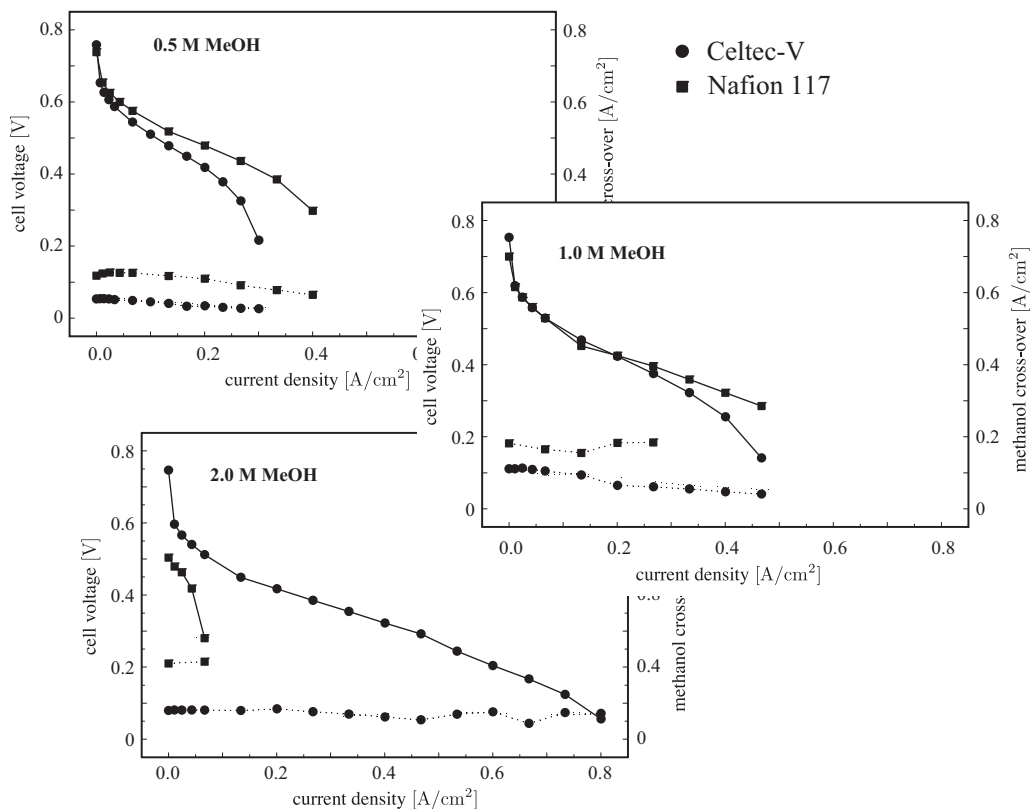
Figure 4.21: Polarisation curves for different methanol feed concentrations; fuel flow 20 ml/min for Celtec-V and 12 ml/min for Nafion 117; cathodic supply is dry air according a stoichiometry of 3 (200 ml/min minimum); the cells were operated at 90 °C and 2 bar(a) pressure.

of oxygen towards the cathodic electrode starts to impede the performance of the Nafion 117 based MEA making the Celtec-V alternative competitive from the performance point of view. At higher methanol feed concentrations (2 M methanol), the electrochemical performance of the Nafion 117 based MEA is extremely poor. Obviously, the methanol cross-over rate is so high that the cathodic methanol oxidation requires so much oxygen that the cell voltage declines rather rapidly even at modest current densities. In contrast thereto, the lower methanol permeability of the Celtec-V membrane enables a fairly good electrochemical performance at these high methanol feed concentrations, and the Celtec-V based MEA clearly outperforms the Nafion 117 reference.

Long-term stability. As already mentioned, a major limitation of traditional acid-doped PBI originates from the high amount of "free acid", which is readily washed-out from the system in the presence of liquid water. This was addressed by employing cross-linked PVPA, which is also covalently bonded to the PBI matrix, as acid. However, the concern for long-term stability (best indicated by the ohmic resistance of the electrolyte) remains. Hence, the durability of the Celtec-V membrane was tested by operating a cell for several hundreds of hours under dynamic load conditions: the cell was operated for 2 h at 400 mV, for 2 h at 200 mV, for 2 h at 400 mV, and finally for 10 min at OCV before the cycle was started again. During that time, 0.5 M methanol solution was recycled. Because not controlled on-line, the concentration reduced over time due to consumption. Intermittently, the mixture was replaced and the methanol depletion between the exchange intervals was minimized by employing a rather large storage vessel. The diagram of Figure 4.22 shows the current density at the different voltages together with the ohmic resistance[13] as a function of operation time. The symbols represent the average current density during each

---

[13]Obtained by the fast auxiliary pulse technique

Figure 4.22: Durability experiment using a dynamic load profile; fuel flow 20 ml/min 0.5 M methanol recycled and occasionally replaced; cell operated at 90 °C and 2 bar(a) pressure; dry air supplied with stoichiometry 3 (200 ml/min minimum).
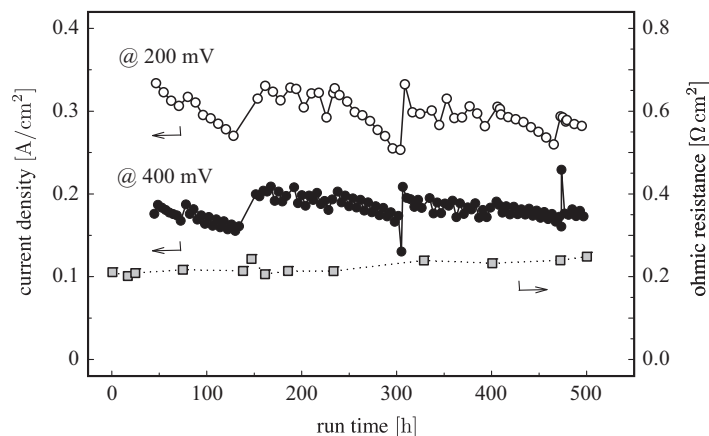
constant potential interval. It can be seen that the ohmic resistance of the cell only increases marginally with time. Linear regression yields a rate of $74 \pm 17\,\mu\Omega\,cm^2/h$. Hence, the loss of acid from the PBI matrix is strongly mitigated by the use of cross-linked PVPA, and even in the harsh environment of a DMFC, operation over several hundreds of hours is possible without diminishing conductivity of the membrane.

Summary. Celtec-V is an alternative polymer electrolyte with attractive properties for DMFC application. Due to the protonic transport within PVPA interpenetrating a PBI matrix, Celtec-V stands out with a very low electro-osmotic drag coefficient and a significant lower methanol permeability (compared to Nafion 117). However, at the current state of development, Nafion 117 allows for a lower ohmic resistance. In consequence, Nafion 117 based MEAs show better electrochemical performance at low methanol feed concentrations, where the parasitic consumption of oxygen by crossing methanol does not impede the electrochemical performance too dramatically. Yet, under operation with higher methanol feed concentrations—and hence more serious competition for oxygen at the cathode—Celtec-V based MEAs easily outperform Nafion 117 based MEAs, especially under air operation. Finally, the cross-linked and covalently bonded PVPA seems to be sufficiently immobilized within the PBI matrix, and operation over several hundreds of hours without a major loss in conductivity was demonstrated.

Chapter 5

Summary and conclusions

This work deals with selected aspects of mass transport phenomena in PEFCs and DMFCs. Emphasis is placed on the implications originating from the occurrence of two-phase flow within these devices. Optimality of supply, distribution, and removal of the fuel, the oxidant, and the reaction products is of utmost importance for the stability, efficiency, and durability of the devices. Being a prerequisite for high current densities while maintaining sufficient voltage, mass transport optimization contributes to the development of cost effective as well as compact designs and hence competitive fuel cells. Although intending a contribution which ultimately leads to optimized cells of technical scale—meaning stacks—the work is confined to the investigation of single cells, because one cannot hope for an intelligent optimization at the stack level without a detailed understanding of the fundamental aspects.

The water household of a PEFC affects its operation mainly by two effects: (1) owing to the operation temperature of a PEFC, water might condensate within the device, and liquid water within the porous structures and flow distributors might impede the access of the gaseous reactants to the electrodes, leading to starvation effects; (2) a high proton conductivity relies on a high hydration level of the membrane and the ionomer incorporated into the porous gas diffusion electrode. Hence, a dilemma is encountered. On the one hand, a highly humid operating environment is beneficial from the conductivity point of view but might lead to serious flooding. On the other hand, flooding is mitigated by operating under low humidity conditions, yet a seriously impeded proton conductivity will lead to serious performance deterioration. In consequence, a delicate balance has to be maintained—ideally over the whole active area—in order to achieve optimal performance.

A slightly different situation is faced in DMFCs. As the anodic fuel is fed as liquid, a DMFC is usually not impeded by drying effects. Nonetheless, the formation of a gaseous CO_2-rich phase within the anodic compartment interferes with the transport of methanol towards the anode. Furthermore, the high permeability of the membrane with respect to methanol and water impedes the operation and efficiency of the device. The oxidation of methanol at the cathode reduces the fuel efficiency and might interfere with the cathodic oxygen reduction either by blocking the electrode (at lower operating temperatures) or by parasitic consumption of oxygen. The formation of a liquid phase within the cathode—giving rise to the same detrimental impact on oxygen supply as in a PEFC—is very likely because of the high water flux through the membrane and the additional water produced by the cathodic oxidation of methanol.

Exploration of two-phase flow phenomena in fuel cells requires suitable *in situ* diagnostics and extensive experimental studies, because the theoretical description of two-phase flow is highly

complicated, up to now insufficiently accurate, and to a good extent characterized by empirical correlations. In consequence, this work relies to a large extent on experiments and the development and/or employment of appropriate diagnostics. Neutron imaging, probably the best-suited *in situ* method to detect liquid water within PEFCs and DMFCs, is of outstanding importance. Being a transmitting technique, neutron imaging allows the detection of liquid within the flow fields and porous structures. A detailed analysis of all methodological aspects important for fuel cell investigations enabled the improvement of this novel technique and made *quantitative* investigations possible. Appropriate post-processing (e.g., the compensation of instrumental broadening and the quantification beyond the limitation given by the signal-to-noise ratio) is developed, analyzed, and demonstrated to overcome experimental limitations.

In the course of the experimental investigation of PEFCs, the intense interaction and interdependency of liquid water accumulation in the cell components and electrochemical performance has been elucidated to some extent, thus deepening the understanding of flooding phenomena.

The accumulation of liquid in the flow fields is studied by inspecting the liquid water distribution along polarization curves. A hysteresis in terms of liquid content and distribution was found. In comparison to accessing an operating point from lower current (i.e., increasing the current), a higher tendency to accumulate large slugs within the flow field channels was found, if an operating point is accessed from higher load. Yet, the hysteresis has no detrimental impact on the electrochemical performance, which is explained with a preferential part-filling of the channels.

Different flow field geometries are compared, highlighting the inability of interdigitated geometries to remove liquid from the structure connected to the inlet. As these flow fields do not provide a continuous pathway from inlet to outlet, liquid has to be forced convectively through the GDLs. Yet, the pressure drop between inlet and outlet structure is insufficient to achieve this. Serpentine structures, although superior in terms of liquid removal, bear a higher sensitivity of the electrochemical performance with respect to liquid accumulations within the GDLs, because neither gas nor liquid is convectively forced through the GDLs, and hence the transport of oxygen towards the electrode has to rely on diffusion.

Utilizing a simplifying differential cell, it is shown that the choice of GDL material has considerable bearings on the relation between liquid accumulation, operating conditions, and electrochemical performance. Flooding of a substantial percentage of the GDL can be tolerated without serious hampering the electrochemical performance for one material, while the same degree of flooding bears a serious performance deterioration for another material. This suggests that the relation between flooding in the GDL and the electrode, which is presently not accessible by neutron imaging, might have relevance for the sensitivity of the electrochemical performance towards GDL flooding.

Combining neutron imaging with spatially resolved current density measurements, the inhomogeneity of liquid content under technically realistic operating conditions is investigated and related to the local performance. Depending on the operating conditions, up to three different regimes are present within a cell operated in co flow mode. Feeding undersaturated gases, a dry inlet region is encountered, and depending on the MEA materials, drying effects might limit the performance in that region. Liquid is likely to be present within the GDLs and flow fields near the outlets, and the electrochemical performance is hampered by insufficient oxygen supply to the cathode. A third region between these two is characterized by a moderate liquid content within the GDLs, while no liquid is observed within the flow fields. As the gas flow is not saturated within the flow field, liquid is evaporating from the GDL and removed as vapor in that region. Usually, the highest current density is found somewhere near the border between the dry and this region, because sufficient

oxygen access to the electrode and a high hydration state of the membrane coexist there.

Operation in counter flow mode is superior to co flow operation due to the beneficial impact of an internal water loop. Near the hydrogen inlet, the net water flux is directed from cathode to anode, resulting in a faster internal humidification of the anodic feed and a reduced flooding of the cathode. Near the hydrogen outlet, the net water flux is reversed leading to a faster humidification of the cathodic inlet feed. In comparison to co flow operation, counter flow operation has two beneficial consequences: (1) the inlet feeds are faster humidified, mitigating drying effects near the inlets, and (2) the cathodic outlet is less likely flooded, allowing for a higher oxygen transport rate near the cathodic outlet.

Even more insight is gained by simultaneous application of neutron imaging and locally resolved impedance spectroscopy. Local limiting processes can be identified and related to the local liquid content and electrochemical performance. It is shown that oxygen concentration oscillations evoked by the alternating faradaic current are not confined to the GDL and transported within the cathodic flow field. Thereby, a coupling downstream the cathodic flow field is established, which has to be respected while interpreting the local impedance response.

In the course of the experimental investigation of DMFCs, the formation of a CO_2-rich gaseous phase within the anodic flow field is investigated and related to the electrochemical performance. The bearings of a variation of the electrolyte thickness (Nafion) on the water and methanol permeation are investigated, and a novel MEA concept based on an alternative membrane material is evaluated.

By applying neutron imaging to DMFCs, it is shown that a gaseous CO_2-rich phase is formed in the anodic flow field, even at very low current densities. Although limiting the current density by hampering the access of methanol to the anode, this gaseous phase is beneficial for the electrochemical performance in the low current density range for the same reason. Furthermore, the high tendency of the cathodic compartment to contain liquid is shown by changing the cathodic flow field structure.

The water flux across the membrane (Nafion) at OCV is not influenced by a variation of the electrolyte thickness. A Nafion membrane, therefore, provides no significant transport resistance, and at OCV the permeation rate is determined by the cathodic compartment. A non-linear dependence of the methanol cross-over on the electrolyte thickness (Nafion) is found at OCV. This originates from a super-position of a convective and a diffusive transport process. Methanol is transported convectively across the membrane within the water flux. Because methanol is readily oxidized at the cathode, a concentration gradient is established, leading to a super-imposed diffusive transport. Due to the convective component, the methanol cross-over does not tend towards zero with increasing electrolyte thickness. As a consequence, a further increase of the electrolyte thickness (i.e., beyond the thickness of Nafion 117) is no viable approach to minimize the methanol cross-over.

Taking advantage of a perimeter-placed reference electrode, the single electrode polarization is investigated. No sensitivity of the cathodic polarization is found with respect to the methanol permeation rate at elevated temperatures provided sufficient oxygen is accessing the electrode.

Celtec-V, a polybenzimidazole based polymer blend incorporating polyvinylphosphonic acid developed by Pemeas GmbH (Germany), is attractive for DMFC application, because it provides anhydrous proton conductivity. In comparison to Nafion 117, this membrane allows for a significantly reduced permeation of methanol and water, thus enabling stable operation and higher electrochemical performance if operated with high methanol feed concentrations.

The present work was carried out at the Electrochemistry Laboratory of the Paul Scherrer Institut in Villigen (Switzerland).

SUMMARY AND CONCLUSIONS

Bibliography

[1] J. Houghton. *Climate Change 2001 - IPCC Third Assessment Report.* Cambridge University Press, 2001.

[2] L. Spector. Bye-Bye, Bateries? *PC World*, 2003.

[3] M. Eikerling, A. A. Kornyshev, A. M. Kuznetsov, J. Ulstrup and S. Walbran. Mechanisms of proton conductance in polymer electrolyte membranes. *Journal of Physical Chemistry B*, 105(17) 3646–3662, 2001.

[4] L. Gubler, S. A. Gürsel and G. G. Scherer. Radiation Grafted Membranes for Polymer Electrolyte Fuel Cells. *Fuel Cells*, InPress, 2005.

[5] M. Schuster, T. Rager, A. Noda, K. D. Kreuer and J. Maier. About Choice of the Protogenic Group in PEM Separator Materials for Intermediate Temperature, Low Humidity Operation: A Critical Comparison of Sulfonic Acid, Phosphonic Acid and Imidazole Functionalized Model Compounds. *Fuel Cells*, 5(3) 355–365, 2004.

[6] E. Gülzow and T. Kaz. New results of PEFC electrodes produced by the DLR dry preparation technique. *Journal of Power Sources*, 106(1-2) 122–125, 2002.

[7] M. K. Debe. Novel catalysts, catalysts support and catalysts coated membrane methods. In W. Vielstich, H. A. Gasteiger and A. Lamm (Edt.), *Handbook of Fuel Cells - Fundamentals, Technology and Application*, volume 3: Fuel Cell Technology and Applications, pages 576–589. John Wiley and Sons, 2003.

[8] M. F. Mathias, J. Roth, J. Fleming and W. Lehnert. Diffusion media materials and characterisation. In W. Vielstich, H. A. Gasteiger and A. Lamm (Edt.), *Handbook of Fuel Cells - Fundamentals, Technology and Applications*, volume 3: Fuel Cell Technology and Applications, pages 517–537. John Wiley and Sons, 2003.

[9] J. McBreen. Voltammetric Studies of Electrodes in Contact with Ionomeric Membranes. *Journal of The Electrochemical Society*, 132(5) 1112–1116, 1985.

[10] F. N. Büchi and G. G. Scherer. Investigation of the transversal water profile in nafion membranes in polymer electrolyte fuel cells. *Journal of The Electrochemical Society*, 148(3) A183–A188, 2001.

[11] M. Eikerling, Y. I. Kharkats, A. A. Kornyshev and Y. M. Volfkovich. Phenomenological theory of electro-osmotic effect and water management in polymer electrolyte proton-conducting membranes. *Journal of The Electrochemical Society*, 145(8) 2684–2699, 1998.

[12] B. Andreaus. *Die Polymer-Elektrolyt Brennstoffzelle - Characterisierung ausgewählter Phänomene durch elektrochemische Impedanzspektroskopie.* Ph.D. thesis, École Polytechnique Fédérale de Lausanne, 2002.

[13] C. Wieser. *Stromdichteverteilung und Leistungsverhalten der Polymerelektrolyt-Brennstoffzelle.* Ph.D. thesis, Universität Stuttgart, 2001.

[14] A. A. Kulikovsky, J. Divisek and A. A. Kornyshev. Modeling the cathode compartment of polymer electrolyte fuel cells: Dead and active reaction zones. *Journal of The Electrochemical Society*, 146(11) 3981–3991, 1999.

[15] S. Freunberger, M. Reum, A. Wokaun and F. N. Büchi. Expanding Current Distribution Measurement in PEFCs to Sub-Millimeter Resolution. *Electrochemical Communications*, *submitted for publication*, 2006.

[16] S. Freunberger, M. Reum, J. Evertz, A. Wokaun and F. Büchi. Measuring the Current Distribution with Sub-Millimeter Resolution in PEFCs. *Journal of The Electrochemical Society*, *submitted for publication*, 2006.

[17] P. W. Atkins. *Physikalische Chemie.* VCH Verlagsgesellschaft mbH, 1990.

[18] W. Schmickler. *Grundlagen der Elektrochemie.* Vieweg, 1996.

[19] C. H. Hamann, A. Hamnett and W. Vielstich. *Electrochemistry.* Wiley-VCH, Weinheim, 1th edition, 1998.

[20] N. M. Marković and P. N. Ross. Electrocatalysis at Well-Defined Surfaces: Kinetics of Oxygen Reduction and Hydrogen Oxidation/Evolution on Pt(hkl) Electrodes. In A. Wieckowski (Edt.), *Interfacial Electrochemistry*, page 821. Marcel Dekker, New York, 1999.

[21] M. S. Wilson, J. A. Valerio and S. Gottesfeld. Low platinum loading electrodes for polymer electrolyte fuel cells fabricated using thermoplastic ionomers. *Electrochimica Acta*, 40(3) 355, 1995.

[22] U. Paulus. *Electrocatalysis for Polymer Electrolyte Fuel Cells: Metal Alloys and Model Systems.* Ph.D. thesis, Swiss Federal Institute Of Technology, 2002.

[23] N. M. Marković, T. J. Schmidt, V. Stamenković and P. N. Ross. Oxygen Reduction on Pt and Pt Bimetallic Surfaces: A Selective Review. *Fuel Cells*, 1(2) 105–116, 2001.

[24] F. Jaouen, G. Lindbergh and G. Sundholm. Investigation of mass-transport limitations in the solid polymer fuel cell cathode - I. Mathematical model. *Journal of The Electrochemical Society*, 149(4) A437–A447, 2002.

[25] M. P. Hogarth and T. R. Ralph. Catalysis for Low Temperature Fuel Cells Part III: Challenges for the direct methanol fuel cell. *Platinum Metals Review*, 46(4) 146–164, 2002.

[26] G. T. Burstein, C. J. Barnett, A. R. Kucernak and K. R. Williams. Aspects of the anodic oxidation of methanol. *Catalysis Today*, 38(4) 425, 1997.

[27] A. Hamnett. Mechanism and electrocatalysis in the direct methanol fuel cell. *Catalysis Today*, 38(4) 445, 1997.

[28] W. Vielstich. Electrochemical Energy Conversion - Methanol Fuel Cell as Example. *Journal of the Brazilian Chemical Society*, 14(4) 503–509, 2003.

[29] J. Bockris and H. Wroblowa. Electrocatalysis. *Journal of Electroanalytical Chemistry*, 7(6) 428, 1964.

[30] S. Motoo and M. Watanabe. Electrocatalysis by Sn and Ge ad-atoms. *Journal of Electroanalytical Chemistry*, 69(3) 429, 1976.

[31] A. Z. Weber and J. Newman. Modeling transport in polymer-electrolyte fuel cells. *Chemical Reviews*, 104(10) 4679–4726, 2004.

[32] M. Eikerling and A. A. Kornyshev. Modelling the performance of the cathode catalyst layer of polymer electrolyte fuel cells. *Journal Of Electroanalytical Chemistry*, 453(1-2) 89–106, 1998.

[33] D. Bevers, M. Wöhr, K. Yasuda and K. Oguro. Simulation of a polymer electrolyte fuel cell electrode. *Journal of Applied Electrochemistry*, 27(11) 1254, 1997.

[34] T. E. Springer, M. S. Wilson and S. Gottesfeld. Modeling And Experimental Diagnostics In Polymer Electrolyte Fuel-Cells. *Journal of The Electrochemical Society*, 140(12) 3513–3526, 1993.

[35] B. R. Sivertsen and N. Djilali. CFD-based modelling of proton exchange membrane fuel cells. *Journal of Power Sources*, 141(1) 65–78, 2005.

[36] V. Gurau, H. T. Liu and S. Kakac. Two-dimensional model for proton exchange membrane fuel cells. *AIChE Journal*, 44(11) 2410–2422, 1998.

[37] A. A. Kulikovsky. Two-dimensional numerical modelling of a direct methanol fuel cell. *Journal of Applied Electrochemistry*, 30(9) 1005–1014, 2000.

[38] T. Berning and N. Djilali. A 3D, multiphase, multicomponent model of the cathode and anode of a PEM fuel cell. *Journal of The Electrochemical Society*, 150(12) A1589–A1598, 2003.

[39] Y.-G. Yoon, W.-Y. Lee, G.-G. Park, T.-H. Yang and C.-S. Kim. Effects of channel configurations of flow field plates on the performance of PEMFC. *Electrochimica Acta*, 50(2-3) 709–712, 2004.

[40] C. Y. Wang. Fundamental models for fuel cell engineering. *Chemical Reviews*, 104(10) 4727–4765, 2004.

[41] D. Kramer, A. J. McEvoy, I. Schneider, H. Kuhn, A. Wokaun and G. G. Scherer. Test and measurement methods for fuel cell technology. *Chimia*, 58(12) 851–856, 2004.

[42] F. N. Büchi, A. Marek and G. G. Scherer. In-Situ Membrane Resistance Measurements In Polymer Electrolyte Fuel-Cells By Fast Auxiliary Current Pulses. *Journal of The Electrochemical Society*, 142(6) 1895–1901, 1995.

[43] F. Jaouen and G. Lindbergh. Transient techniques for investigating mass-transport limitations in gas diffusion electrodes - I. Modeling the PEFC cathode. *Journal of The Electrochemical Society*, 150(12) A1699–A1710, 2003.

[44] R. de Levie. Electrochemical Response of Porous and Rough Electrodes. In P. Delahay and C. W. Tobias (Edt.), *Advances in Electrochemistry and Electrochemical Engineering*, volume 6, pages 329–397. Wiley, New York, 1967.

[45] T. Springer and I. Raistrick. Electrical Impedance of a Pore Wall for the Flooded-Agglomerate Model of Porous Gas-Diffusion Electrodes. *Journal of The Electrochemical Society*, 136(6) 1594–1603, 1989.

BIBLIOGRAPHY

[46] M. Eikerling and A. A. Kornyshev. Electrochemical impedance of the cathode catalyst layer in polymer electrolyte fuel cells. *Journal of Electroanalytical Chemistry*, 475(2) 107, 1999.

[47] H. Kuhn, A. Wokaun and G. Scherer. Exploring Single Electrode Reactions in Polymer Electrolyte Fuel Cells. *Electrochimica Acta*, *accepted*, 2006.

[48] K. C. Neyerlin, H. A. Gasteiger, C. K. Mittelsteadt, J. Jorne and W. Gu. Effect of Relative Humidity on Oxygen Reduction Kinetics in a PEMFC. *Journal of The Electrochemical Society*, 152(6) A1073, 2005.

[49] B. Andreaus and G. G. Scherer. Proton-conducting polymer membranes in fuel cells–humidification aspects. *Solid State Ionics*, 168(3-4) 311, 2004.

[50] H. Kuhn, B. Andreaus, A. Wokaun and G. Scherer. Electrochemical impedance spectroscopy applied to polymer electrolyte fuel cells with a pseudo reference electrode arrangement. *Electrochimica Acta*, 51(8-9) 1622–1628, 2006.

[51] Q. Dong, J. Kull and M. M. Mench. Real-time water distribution in a polymer electrolyte fuel cell. *Journal of Power Sources*, 139(1-2) 106, 2005.

[52] H. Yang, T. S. Zhao and Q. Ye. Addition of non-reacting gases to the anode flow field of DMFCs leading to improved performance. *Electrochemistry Communications*, 6(11) 1098–1103, 2004.

[53] A. Hakenjos, H. Muenter, U. Wittstadt and C. Hebling. A PEM fuel cell for combined measurement of current and temperature distribution, and flow field flooding. *Journal of Power Sources*, 131(1-2) 213, 2004.

[54] K. Sugiura, M. Nakata, T. Yodo, Y. Nishiguchi, M. Yamauchi and Y. Itoh. Evaluation of a cathode gas channel with a water absorption layer/waste channel in a PEFC by using visualization technique. *Journal of Power Sources*, In Press, Corrected Proof, 2005.

[55] K. Tüber, D. Pócza and C. Hebling. Visualization of water buildup in the cathode of a transparent PEM fuel cell. *Journal of Power Sources*, 124(2) 403–414, 2003.

[56] K. Sundmacher and K. Scott. Direct methanol polymer electrolyte fuel cell: Analysis of charge and mass transfer in the vapour-liquid-solid system. *Chemical Engineering Science*, 54(13-14) 2927, 1999.

[57] A. R. Kucernak, B. Ladewig, R. Blewitt and J. Shimpton. Laser Doppler Anemometry Study of Reactant Flow in Fuel Cell Channels, 2005.

[58] O. A. Velev, S. Srinivasan, A. Appleby, I. Carron, S. Gunter and A. Sanchez. Real Time Two-Phase Fluid Flow Visualization in Polymer Electrolyte Fuel Cells Using Neutron Radiography. In *The 1997 Joint International Meeting of the Electrochemical Society and the International Society of Electrochemistry*, volume 97-2, pages 232–233, Paris, 1997.

[59] A. B. Geiger, A. Tsukada, E. Lehmann, P. Vontobel, A. Wokaun and G. G. Scherer. In Situ Investigation of Two-Phase Flow Patterns in Flow Fields of PEFC's Using Neutron Radiography. *Fuel Cells*, 2(2) 92–98, 2002.

[60] R. Satija, D. Jacobson, M. Arif and S. Werner. In situ neutron imaging technique for evaluation of water management systems in operating PEM fuel cells. *Journal of Power Sources*, 192(2) 238–245, 2004.

[61] D. Kramer, J. B. Zhang, R. Shimoi, E. Lehmann, A. Wokaun, K. Shinohara and G. G. Scherer. In situ diagnostic of two-phase flow phenomena in polymer electrolyte fuel cells by neutron imaging Part A. Experimental, data treatment, and quantification. *Electrochimica Acta*, 50(13) 2603–2614, 2005.

[62] D. Kramer, E. Lehmann, G. Frei, P. Vontobel, A. Wokaun and G. G. Scherer. An on-line study of fuel cell behavior by thermal neutrons. *Nuclear Instruments and Methods in Physics Research Section A: Accelerators, Spectrometers, Detectors, and Associated Equipment*, 542(1-3) 52–60, 2005.

[63] J. Zhang, D. Kramer, R. Shimoi, Y. Ono, E. Lehmann, A. Wokaun, K. Shinohara and G. G. Scherer. In situ diagnostic of two-phase flow phenomena in polymer electrolyte fuel cells by neutron imaging. *Electrochimica Acta*, 51(13) 2715–2727, 2006.

[64] N. Pekula, K. Heller, P. Chuang, A. Turhan, M. Mench, J. Brenizer and K. Ünlü. Study of water distribution and transport in a polymer electrolyte fuel cell using neutron imaging. *Nuclear Instruments and Methods In Physics Research Section A-Accelerators Spectrometers Detectors And Associated Equipment*, 542(1-3) 134–141, 2005.

[65] A. Turhan, K. Heller, J. Brenizer and M. M. Mench. Quantification of liquid water accumulation and distribution in a polymer electrolyte fuel cell using neutron imaging. *Journal of Power Sources*, in press, 2006.

[66] M. Hickner, N. Siegel, K. Chen, D. McBrayer, D. Hussey, D. Jacobson and M. Arif. Real-time imaging of liquid water in an operating proton exchange membrane fuel cell. *Journal of The Electrochemical Society*, 153(5) A902–A908, 2006.

[67] T. Trabold, J. Owejan, D. Jacobson, M. Arif and P. Huffman. In-situ Investigation of Water Transport in an Operating PEM Fuel Cell Using Neutron Radiography. Part 1 - Experimental Method and Serpentine Flow Field Results. *International Journal of Heat and Mass Transfer*, accepted, 2006.

[68] J. Owejan, T. Trabold, D. Jacobson, D. Baker, D. Hussey and M. Arif. In-situ Investigation of Water Transport in an Operating PEM Fuel Cell Using Neutron Radiography. Part 2 - Transient Water Accumulation in an Interdigitated Cathode Flow Field. *International Journal of Heat and Mass Transfer*, accepted, 2006.

[69] I. A. Schneider, D. Kramer, A. Wokaun and G. G. Scherer. Spatially resolved characterization of PEFCs using simultaneously neutron radiography and locally resolved impedance spectroscopy. *Electrochemistry Communications*, 7(12) 1393–1397, 2005.

[70] E. Lewis and W. Miller. *Computational Methods of Neutron Transport*. John Wiley and Sons, 194.

[71] N. Kardjilov, F. de Beer, R. Hassanein, E. Lehmann and P. Vontobel. Scattering corrections in neutron radiography using point scattered functions. *Nuclear Instruments and Methods in Physics Research Section A: Accelerators, Spectrometers, Detectors and Associated Equipment*, 542(1-3) 336, 2005.

[72] R. Hassanein, E. Lehmann and P. Vontobel. Methods of scattering corrections for quantitative neutron radiography. *Nuclear Instruments and Methods in Physics Research Section A: Accelerators, Spectrometers, Detectors and Associated Equipment*, 542(1-3) 353, 2005.

[73] http://neutra.web.psi.ch, 2006.

[74] P. Von der Hardt and H. Rœttger. *Neutron Radiography Handbook.* D. Reidel Publishing Company, 1981.

[75] M. J. Knitel. *New Inorganic Scintillators and Storage Phosphors for Detection of Thermal Neutrons.* Ph.D. thesis, Technical University Delft, 1998.

[76] E. Lehmann, H. Pleinert, T. Williams and C. Pralong. Application of new radiation detection techniques at the Paul Scherrer Institut, especially at the spallation neutron source. *Nuclear Instruments and Methods in Physics Research Section A: Accelerators, Spectrometers, Detectors and Associated Equipment*, 424(1) 158, 1999.

[77] E. Lehmann, K. Lorenz, E. Steichele and P. Vontobel. Non-destructive testing with neutron phase contrast imaging. *Nuclear Instruments and Methods in Physics Research Section A: Accelerators, Spectrometers, Detectors and Associated Equipment*, 542(1-3) 95, 2005.

[78] E. H. Lehmann, P. Vontobel, G. Frei and C. Bronnimann. Neutron imaging-detector options and practical results. *Nuclear Instruments and Methods in Physics Research Section A: Accelerators, Spectrometers, Detectors and Associated Equipment*, 531(1-2) 228, 2004.

[79] M. Estermann, G. Frei, E. Lehmann and P. Vontobel. The performance of an amorphous silicon flat panel for neutron imaging at the PSI NEUTRA facility. *Nuclear Instruments and Methods in Physics Research Section A: Accelerators, Spectrometers, Detectors and Associated Equipment*, 542(1-3) 253, 2005.

[80] R. G. Gonzales. *Digital image processing.* Addison-Wesley Publishing Co., 1987.

[81] G. Kühne. personal communication, 2006.

[82] The JEFF-3.0 Nuclear Data Library, JEFF Report 19, 2005.

[83] R. Mac Farlane. New thermal neutron scattering files for ENDF/B Release 2 LA-12639-MS (ENDF 356), 1994.

[84] Janis, Java-based nuclear data display program.

[85] M. Jäggi. Eigenschaften und Betriebsbedingungen der Andor Kamera A-DV434-BV. Internship report, Paul Scherrer Institut, 2003.

[86] http://www.mathpages.com. 2006.

[87] G. Frei and E. Lehmann. Optimization of neutron sensitive imaging scintillators. In *8th World Conference on Neutron Radiography*, Gaithersburg, MD, 2006.

[88] C. Xu, I. Aissaoui and S. Jacquey. Algebraic analysis of the Van Cittert iterative method of deconvolution with a general relaxation factor. *Journal of the Optical Society of America A*, 11 2804, 1994.

[89] P. Bandzuch, M. Morhac and J. Kristiak. Study of the Van Cittert and Gold iterative methods of deconvolution and their application in the deconvolution of experimental spectra of positron annihilation. *Nuclear Instruments and Methods in Physics Research Section A: Accelerators, Spectrometers, Detectors and Associated Equipment*, 384(2-3) 506, 1997.

[90] B. Jähne. *Digitale Bildverarbeitung.* Springer-Verlag, Berlin, 6. edition edition, 2005.

[91] G.-W. Jeong and H.-K. Kang. Maximum Likelihood Constrained Deconvolution. I: Algorithm and Qualitative and Quantitative Enhancement in Synthetic Two-Dimensional NMR Spectra. *Concepts in Magnetic Resonance*, 14(6) 402–415, 2002.

[92] M. Morhac, V. Matousek and J. Kliman. Optimized multidimensional nonoscillating deconvolution. *Journal of Computational and Applied Mathematics*, 140 639–658, 2002.

[93] S. J. C. Cleghorn, C. R. Derouin, M. S. Wilson and S. Gottesfeld. A printed circuit board approach to measuring current distribution in a fuel cell. *Journal of Applied Electrochemistry*, 28(7) 663, 1998.

[94] S. Schönbauer, T. Kaz, H. Sander and E. Gülzow. Segmented Bipolar Plate for the Determination of Current Distribution in Polymer Electrolyte Fuel Cells. In D. Stolten (Edt.), *2nd European Fuel Cell Forum*, volume 1, pages 231–237, Lucerne, 2003.

[95] G. Bender, M. S. Wilson and T. A. Zawodzinski. Further refinements in the segmented cell approach to diagnosing performance in polymer electrolyte fuel cells. *Journal of Power Sources*, 123(2) 163, 2003.

[96] I. Schneider, H. Kuhn, A. Wokaun and G. G. Scherer. Fast Locally Resolved Electrochemical Impedance Spectroscopy in Polymer Electrolyte Fuel Cells. *Journal of The Electrochemical Society*, 152(10) A2092–A2103, 2005.

[97] A. B. Geiger, R. Eckl, A. Wokaun and G. G. Scherera. An approach to measuring locally resolved currents in polymer electrolyte fuel cells. *Journal of The Electrochemical Society*, 151(3) A394–A398, 2004.

[98] M. M. Mench, C. Y. Wang and M. Ishikawa. In situ current distribution measurements in polymer electrolyte fuel cells. *Journal of The Electrochemical Society*, 150(8) A1052–A1059, 2003.

[99] SGL Sigracet BMA5 product specification - http://www.sglcarbon.com, 2006.

[100] C. Wieser, A. Helmbold and E. Gulzow. A new technique for two-dimensional current distribution measurements in electrochemical cells. *Journal of Applied Electrochemistry*, 30(7) 803–807, 2000.

[101] F. N. Büchi, A. B. Geiger and R. P. Neto. Dependence of current distribution on water management in PEFC of technical size. *Journal of Power Sources*, 145(1) 62–67, 2005.

[102] E. Gülzow, T. Kaz, R. Reissner, H. Sander, L. Schilling and M. von Bradke. Study of membrane electrode assemblies for direct methanol fuel cells. *Journal of Power Sources*, 105(2) 261–266, 2002.

[103] J. Stumper, S. A. Campbell, D. P. Wilkinson, M. C. Johnson and M. Davis. In-situ methods for the determination of current distributions in PEM fuel cells. *Electrochimica Acta*, 43(24) 3773–3783, 1998.

[104] D. J. L. Brett, S. Atkins, N. P. Brandon, V. Vesovic, N. Vasileiadis and A. R. Kucernak. Measurement of the current distribution along a single flow channel of a solid polymer fuel cell. *Electrochemistry Communications*, 3(11) 628–632, 2001.

[105] Q. Dong, M. M. Mench, S. Cleghorn and U. Beuscher. Distributed performance of polymer electrolyte fuel cells under low-humidity conditions. *Journal of The Electrochemical Society*, 152(11) A2114–A2122, 2005.

[106] A. Hakenjos and C. Hebling. Spatially resolved measurement of PEM fuel cells. *Journal of Power Sources*, 145(2) 307–311, 2005.

BIBLIOGRAPHY

[107] D. Natarajan and T. Van Nguyen. Current distribution in PEM fuel cells. Part 1: Oxygen and fuel flow rate effects. *AIChE Journal*, 51(9) 2587–2598, 2005.

[108] K. H. Hauer, R. Potthast, T. Wuster and D. Stolten. Magnetotomography - a new method for analysing fuel cell performance and quality. *Journal of Power Sources*, 143(1-2) 67–74, 2005.

[109] D. J. L. Brett, S. Atkins, N. P. Brandon, V. Vesovic, N. Vasileiadis and A. Kucernak. Localized impedance measurements along a single channel of a solid polymer fuel cell. *Electrochemical and Solid State Letters*, 6(4) A63–A66, 2003.

[110] H. Kuhn, B. Andreaus, G. G. Scherer and A. Wokaun. Simultaneous Local EIS Measurement in PEFC. In D. Stolten (Edt.), *2nd European Fuel Cell Forum*, volume 1, pages 363–370, Lucerene, 2003.

[111] I. Schneider, H. Kuhn, A. Wokaun and G. G. Scherer. Fast Locally Resolved Electrochemical Impedance Spectroscopy in Polymer Electrolyte Fuel Cells. In *4th Intl. Symp. on Polymer Electrolyte Fuel Cells*, Honolulu, USA, 2004.

[112] I. Schneider, D. Kramer, H. Kuhn, S. Freunberger, A. Wokaun, F. N. Büchi and G. G. Scherer. Advanced in situ diagnostic methods for polymer electrolyte fuel cells. PSI Scientific Report Volume 3, Paul Scherrer Institut, 2005.

[113] H. Maget. In C. Berger (Edt.), *Handbook of Fuel Cell Technology*, page 455. Prentice-Hall, New York, 1968.

[114] W. S. He and T. Van Nguyen. Edge effects on reference electrode measurements in PEM fuel cells. *Journal of The Electrochemical Society*, 151(2) A185–A195, 2004.

[115] S. S. Kocha. Principles of MEA preparation. In W. Vielstich, H. A. Gasteiger and A. Lamm (Edt.), *Handbook of Fuel Cells - Fundamentals, Technology and Application*, volume 3. Wiley, 2003.

[116] Z. Y. Liu, J. S. Wainright, W. W. Huang and R. F. Savinell. Positioning the reference electrode in proton exchange membrane fuel cells: calculations of primary and secondary current distribution. *Electrochimica Acta*, 49(6) 923–935, 2004.

[117] I. A. Schneider, H. Kuhn, A. Wokaun and G. G. Scherer. Study of water balance in a polymer electrolyte fuel cell by locally resolved impedance spectroscopy. *Journal of The Electrochemical Society*, 152(12) A2383–A2389, 2005.

[118] F. Y. Zhang, X. G. Yang and C. Y. Wang. Liquid water removal from a polymer electrolyte fuel cell. *Journal of The Electrochemical Society*, 153(2) A225–A232, 2006.

[119] J. Allen, S. Young Son and K. Kihm. Characterization and control of two-phase flow in microchannels. Technical report, National Center for Microgravity Research on Fluids and Combustion, 2003.

[120] F. A. Uribe and J. T. A. Zawodzinski. A study of polymer electrolyte fuel cell performance at high voltages. Dependence on cathode catalyst layer composition and on voltage conditioning. *Electrochimica Acta*, 47(22-23) 3799, 2002.

[121] M. Ciureanu and R. Roberge. Electrochemical impedance study of PEM fuel cells. Experimental diagnostics and modeling of air cathodes. *Journal of Physical Chemistry B*, 105(17) 3531–3539, 2001.

[122] K. T. Jeng, S. F. Lee, G. F. Tsai and C. H. Wang. Oxygen mass transfer in PEM fuel cell gas diffusion layers. *Journal of Power Sources*, 138(1-2) 41–50, 2004.

[123] D. Natarajan and T. Van Nguyen. A two-dimensional, two-phase, multicomponent, transient model for the cathode of a proton exchange membrane fuel cell using conventional gas distributors. *Journal of The Electrochemical Society*, 148(12) A1324–A1335, 2001.

[124] U. Pasaogullari and C. Y. Wang. Two-phase transport and the role of micro-porous layer in polymer electrolyte fuel cells. *Electrochimica Acta*, 49(25) 4359–4369, 2004.

[125] N. P. Siegel, M. W. Ellis, D. J. Nelson and M. R. von Spakovsky. A two-dimensional computational model of a PEMFC with liquid water transport. *Journal of Power Sources*, 128(2) 173, 2004.

[126] Y. Bultel, K. Wiezell, F. Jaouen, P. Ozil and G. Lindbergh. Investigation of mass transport in gas diffusion layer at the air cathode of a PEMFC. *Electrochimica Acta*, 51(3) 474, 2005.

[127] G. Inoue, Y. Matsukuma and M. Minemoto. Examination of optimal separator shape of polymer electrolyte fuel cell with numerical analysis including the effect of gas flow through gas diffusion layer. *Journal of Power Sources*, In Press, Corrected Proof, 2006.

[128] A. Koponen, M. Kataja and J. Timonen. Permeability and effective porosity of porous media. *Physical Review E*, 56(3) 3319–3325, 1997.

[129] A. Koponen, M. Kataja and J. Timonen. Tortuous flow in porous media. *Physical Review E*, 54(1) 406–410, 1996.

[130] M.-J. Yun, B.-M. Yu, B. Zhang and M.-T. Huang. A Geometry Model for Tortuosity of Streamtubes in Porous Media with Spherical Particles. *Chinese Physical Letters*, 22(6) 1464, 2005.

[131] B.-M. Yu and J.-H. Li. A Geometry Model for Tortuosity of Flow Path in Porous Media. *Chinese Physical Letters*, 21(8) 1569, 2004.

[132] S. A. Freunberger, D. Kramer, F. N. Büchi and G. G. Scherer. Measuring the Effective Relative Diffusivity of Gas Diffusion Media for PEFC. Electrochemistry Laboratory Anual Report 2005, Paul Scherrer Institut, 2006.

[133] J. G. Pharoah. On the permeability of gas diffusion media used in PEM fuel cells. *Journal of Power Sources*, 144(1) 77–82, 2005.

[134] F. N. Büchi and S. Srinivasan. Operating Proton Exchange Membrane Fuel Cells Without External Humidification of the Reactant Gases - Fundamental Aspects. *Journal of The Electrochemical Society*, 144(8) 2767–2772, 1997.

[135] L. Gubler, N. Prost, S. A. Gursel and G. G. Scherer. Proton exchange membranes prepared by radiation grafting of styrene/divinylbenzene onto poly(ethylene-alt-tetrafluoroethylene) for low temperature fuel cells. *Solid State Ionics*, 176(39-40) 2849, 2005.

[136] P. Berg, K. Promislow, J. St Pierre, J. Stumper and B. Wetton. Water management in PEM fuel cells. *Journal of The Electrochemical Society*, 151(3) A341–A353, 2004.

[137] T. E. Springer, T. A. Zawodzinski, M. S. Wilson and S. Gottesfeld. Characterization of polymer electrolyte fuel cells using AC impedance spectroscopy. *Journal of The Electrochemical Society*, 143(2) 587–599, 1996.

BIBLIOGRAPHY

[138] M. Ciureanu. Effects of Nafion (R) dehydration in PEM fuel cells. *Journal of Applied Electrochemistry*, 34(7) 705–714, 2004.

[139] Q. Z. Guo and R. E. White. A steady-state impedance model for a PEMFC cathode. *Journal of The Electrochemical Society*, 151(4) E133–E149, 2004.

[140] M. Boillot, C. Bonnet, N. Jatroudakis, P. Carre, S. Didierjean and F. Lapicque. Effect of gas dilution on PEM fuel cell performance and impedance response. *Fuel Cells*, 6(1) 31–37, 2006.

[141] I. Schneider, S. Freunberger, D. Kramer, A. Wokaun and G. G. Scherer. *to be published*, 2006.

[142] I. Schneider, D. Kramer, A. Wokaun and G. G. Scherer. Oscillations in the Gas Channels - The Forgotten Player in Impedance Spectroscopy in Polymer Electrolyte Fuel Cells Part A. Exploring the Wave. In *210th Meeting of the Electrochemical Society*, Cancun, Mexico, 2006.

[143] D. Kramer, I. Schneider, A. Wokaun and G. G. Scherer. Oscillations in the Gas Channels - The Forgotten Player in Impedance Spectroscopy in Polymer Electrolyte Fuel Cells Part B. Modeling the Wave. In *210th Meeting of the Electrochemical Society*, Cancun, Mexico, 2006.

[144] I. Schneider, D. Kramer, A. Wokaun and G. G. Scherer. *to be published*, 2006.

[145] R. Hassanein. personal communication, 2006.

[146] B. Köllmann. *Entwicklung einer Regelung der Methanolkonzentration in wässriger Lösung und Integration in Teststände zur Charakterisierung von Direkt-Methanol-Brennstoffzellen*. Diplomarbeit, Technische Universität Clausthal, 2003.

[147] V. Bammerlin. *Untersuchung von Elektrolytvariationen in Direkt-Methanol-Brennstoffzellen*. Diplomarbeit, ETH Zürich, 2004.

[148] P. Argyropoulos, K. Scott and W. M. Taama. Gas evolution and power performance in direct methanol fuel cells. *Journal of Applied Electrochemistry*, 29(6) 661–669, 1999.

[149] K. Scott, W. M. Taama, S. Kramer, P. Argyropoulos and K. Sundmacher. Limiting current behaviour of the direct methanol fuel cell. *Electrochimica Acta*, 45(6) 945–957, 1999.

[150] G. Q. Lu and C. Y. Wang. Electrochemical and flow characterization of a direct methanol fuel cell. *Journal of Power Sources*, 134(1) 33–40, 2004.

[151] J. Nordlund and G. Lindbergh. Temperature-dependent kinetics of the anode in the DMFC. *Journal of The Electrochemical Society*, 151(9) A1357–A1362, 2004.

[152] H. Yang, T. S. Zhao and Q. Ye. In situ visualization study of CO2 gas bubble behavior in DMFC anode flow fields. *Journal of Power Sources*, 139(1-2) 79–90, 2005.

[153] G. Q. Lu, P. C. Lim, F. Q. Liu and C. Y. Wang. On mass transport in an air-breathing DMFC stack. *International Journal of Energy Research*, 29(12) 1041–1050, 2005.

[154] A. A. Kulikovsky. Bubbles in the anode channel and performance of a DMFC: Asymptotic solutions. *Electrochimica Acta*, 51(10) 2003–2011, 2006.

[155] A. B. Geiger. *Characterization and Development of Direct Methanol Fuel Cells*. Dissertation, Swiss Federal Institute of Technology, 2002.

[156] J. T. A. Zawodzinski, M. Neeman, L. O. Sillerud and S. Gottesfeld. Determination of Water Diffusion Coefficients in Perfluorosulfonate Ionomeric Membranes. *Journal of Physical Chemistry*, 95(15) 6040–6044, 1991.

[157] J. T. A. Zawodzinski, J. Davey, J. A. Valerio and S. Gottesfeld. The Water Content Dependence of Electro-Osmotic Drag in Proton-Conducting Polymer Electrolytes. *Electrochimica Acta*, 40(3) 297–302, 1994.

[158] X. Ren, W. Henderson and S. Gottesfeld. Electro-osmotic Drag of Water in Ionomeric Membranes - New Measurements employing a Direct Methanol Fuel Cell. *Journal of The Electrochemical Society*, 144(9) L267–L270, 1997.

[159] M. Ise, K. D. Kreuer and J. Maier. Electroosmotic drag in polymer electrolyte membranes: an electrophoretic NMR study. *Solid State Ionics*, 125(1-4) 213–223, 1999.

[160] P. S. Kauranen and E. Skou. Methanol permeability in perfluorosulfonate proton exchange membranes at elevated temperatures. *Journal of Applied Electrochemistry*, 26(9) 909–917, 1996.

[161] K. Scott, W. M. Taama and P. Argyropoulos. Performance of the direct methanol fuel cell with radiation-grafted membranes. *Journal of Membrane Science*, 171(1) 119–130, 2000.

[162] ”Diffusion Coefficients in Liquids at Infinite Dilution”. In D. R. Lide (Edt.), *CRC Handbook of Chemistry and Physics, Internet Version 2006*. Taylor and Francis, Boca Raton, FL, 2006.

[163] P. L. Antonucci, A. S. Aricò, P. Creti, E. Ramunni and V. Antonucci. Investigation of a direct methanol fuel cell based on a composite Nafion-silica electrolyte for high temperature operation. *Solid State Ionics*, 125(1-4) 431–437, 1999.

[164] P. Dimitrova, K. A. Friedrich, U. Stimming and B. Vogt. Modified Nafion-based membranes for use in direct methanol fuel cells. *Solid State Ionics*, 150(1-2) 115–122, 2002.

[165] W. C. Choi, J. D. Kim and S. I. Woo. Modification of proton conducting membrane for reducing methanol crossover in a direct-methanol fuel cell. *Journal of Power Sources*, 96(2) 411–414, 2001.

[166] J. Kerres. Blended and Cross-Linked Ionomer Membranes for Application in Membrane Fuel Cells. *Fuel Cells*, 5(2) 230–247, 2004.

[167] J. S. Wainright, T. Wang, D. Weng, R. F. Savinell and M. Litt. Acid-Doped Polybenzimidazoles: A New Polymer Electrolyte. *Journal of The Electrochemical Society*, 142(7) L121–L123, 1995.

[168] Q. Li, R. He, R. W. Berg, H. A. Hjuler and N. J. Bjerrum. Water uptake and acid doping of polybenzimidazoles as electrolyte membranes for fuel cells. *Solid State Ionics*, 168(1-2) 177–185, 2004.

[169] M. Babib and J. Bockris. In Situ FT-IR Spectroscopic Study of Electrochemical Adsorption of Phosphoric Acid on Platinum. *Journal of The Electrochemical Society*, 130(12) 2510–2512, 1983.

[170] Ö. Ünsal and J. Kiefer. A proton conducting electrolyte membrane obtainable by the steps: (A) swelling of a polymer film with vinyl-containing phosphonic acid-containing liquid and polymerization of the phosphonic acid. Patent number DE10209419-A1 issued by Pemeas GmbH, Germany, 2003.